Large imaging surveys for cosmology: cosmic magnification and photometric calibration

Alexandre Boucaud

UNIVERSITÉ PARIS DIDEROT

École doctorale : Particules, Noyaux, Cosmos

Doctorat de l'université Paris Diderot

Spécialité : Champs, Particules, Matières

Alexandre Boucaud

Large imaging surveys for cosmology: cosmic magnification and photometric calibration

Thèse réalisée au laboratoire Astroparticule et Cosmologie (APC)
sous la direction de MM. James G. Bartlett et Michel Crézé

soutenue le 27 septembre 2013 devant le jury composé de :

M. Pierre Antilogus ..... Examinateur
M. Tim Axelrod ..... Rapporteur
M. James G. Bartlett ..... Directeur de thèse
M. Pierre Binétruy ..... Président
M. Alain Blanchard ..... Rapporteur
M. Michel Crézé ..... Invité
M. Alan Heavens ..... Examinateur

Résumé

Ce travail de thèse se focalise sur l'usage de grands sondages pour extraire de l'information sur la cosmologie. Une photométrie de précision joue un rôle clé dans cette quête à travers la détermination de redshifts photométriques ainsi que la propagation des erreurs dans les résultats cosmologiques ; thème unissant les deux parties de cette thèse.

Après une revue de la cosmologie et des mesures favorisant le modèle ΛCDM, ainsi qu'une description du Large Synoptic Survey Telescope (LSST), la première partie de ce travail se porte sur l'étude de la variation des principaux constituants de l'atmosphère sur la photométrie au sol, au niveau du site du LSST à Cerro Pachón, au Chili. Nous utilisons des données récentes sur l'ozone, la vapeur d'eau et les aérosols pour en construire une simulation de longue durée et estimer quantitativement l'influence des gradients spatiaux et temporels de ces constituants sur la procédure de la calibration du LSST.

La deuxième partie de ce travail débute par une description théorique de l'effet de lentille gravitationnelle, avec un accent sur le lentillage faible. Après une comparaison des avantages et inconvénients inhérents aux mesures de cisaillement cosmique, nous explorons l'utilisation de l'amplification cosmique conjointement à la séparation tomographique en redshift permise par le LSST afin de contraindre les modèles. Nous trouvons que l'amplification cosmique, bien qu'affectée par le clustering intrinsèque, représente une sonde prometteuse du biais des galaxies et de l'énergie noire, complémentaire au cisaillement cosmique, et qui augmente la robustesse des contraintes cosmologiques provenant des mêmes relevés.

mots clés: cosmologie, énergie noire, lentilles gravitationnelles, LSST, amplification cosmique, étalonnage de la photométrie

Abstract

This thesis work focuses on the use of deep, wide field surveys to extract new cosmological information. Precise photometry plays a large role in this quest, through the determination of photometric redshifts and the propagation of photometric errors into the cosmological results. This is a unifying theme which effectively ties both parts of the thesis together.

After a general review of cosmology and the measurements that support the ΛCDM model, and a description of the Large Synoptic Survey Telescope (LSST), the first part of this work deals with the influence of the variation of main atmospheric constituents on ground-based photometry, focusing particularly on the LSST site at Cerro Pachón, Chile. We process all recent available data on ozone, water vapor and aerosols to construct a long-term atmospheric simulation and estimate quantitatively how the spatial and temporal gradients of these constituents would affect LSST calibration process.

The second part of this work starts with a theoretical description of gravitational lensing, concentrating on the weak lensing aspect. After discussing the advantages and difficulties of cosmic shear measurements, we explore the use of cosmic magnification, together with the redshift tomography enabled by the LSST, to constrain cosmological models. We find that cosmic magnification covariance is beset by intrinsic clustering but nevertheless represents a useful probe of galaxy bias and dark energy that complements cosmic shear, and which can increase the robustness of cosmological constraints from lensing surveys.

keywords: cosmology, dark energy, gravitational lensing, LSST, cosmic magnification, photometric calibration

Remerciements

Difficile est la tâche de résumer en une page les contributions individuelles qui ont fait de ces trois dernières années une période qui restera un souvenir des plus agréable. La liste dressée dans ces lignes est loin d'être exhaustive, mais se concentre sur les personnes les plus proches de moimes remerciements s'étendent bien plus largement qu'aux seuls noms cités et sans doute à vous qui me lisez.

Je remercie en premier lieu Pierre Binétruy pour m'avoir acceuilli au sein du laboratoire AstroParticule & Cosmologie.

Je remercie Jim Bartlett pour m'avoir fait découvrir la physique enseignée avec une approche non conventionnelle, lors de mon arrivée à Paris en Licence. J'ai suivi ce professeur atypique et profondément passionné au cours de mes années de Master, et c'est lui qui m'a lancé sur la voie de la cosmologie. J'ai pris un plaisir intense à travailler avec toi. Puisse notre collaboration continuer..

Je remercie chaleureusement Michel Crézé d'avoir pris la patience de m'enseigner la rigueur de l'analyse de données et surtout de m'avoir épaulé en continu sur un sujet qui, sans apparaître *sexy* au premier abord, m'a permis de prendre du recul sur mon travail et de gagner une vision d'ensemble des problématiques liées à la calibration d'une expérience astrophysique au sol, comme le LSST. Sa participation sans faille aux diverses étapes de ma thèse a été un soutien capital.

Je remercie ensuite les membres du groupe LSST, avec lesquels j'ai pris un grand plaisir à travailler ; et plus généralement, je remercie les membres du groupe Cosmologie et Gravitation qui se sont toujours montrés disponibles aux moments cruciaux. Merci notamment à Guillaume et Cécile pour leur écoute et leurs conseils, Eric pour ses bonnes adresses, JC pour son enthousiame, Jean pour sa franchise, Cyrille pour sa disponibilité, Michel et Eric pour les éclats de rire. Sans oublier Yannick, l'âme du groupe, qui a su trouver les mots justes dans les moments difficiles (et l'argent le reste du temps :-).

La bonne humeur durant cette thèse doit énormément aux occupants du bureau 427B ainsi qu'à ses membres satellites et ses visiteurs, qui n'ont fait que grandir pendant ces trois ans. Je pense notamment (et par ordre d'ancienneté) à Sebinouf, Silvia, HBM, Mariana, Jo & Jo, Giulio, Gougouille, Guillaume, Flo, Ben, the BOSS,

Mamatt, Alexis, Julien, Jibril, Anne-Sylvie et Marta. Les trois grands absents de cette liste sont ceux qui tiennent une place toute particulière dans mon esprit. En premier lieu, celle que j'ai eu le plaisir d'avoir en face de moi et à laquelle j'ai rappelé tous les jours ma présence en lui marchant sur les pieds mais qui ne s'est jamais plaint, j'ai dénommé Marianne. George, ensuite, qui a pris physiquement sa place pendant les derniers mois de rédaction et qui, nourri au Starbucks®, a su trouver l'énergie pour me motiver à venir rédiger pendant les beaux weekends de Juillet. Et puis il y a Bobic, l'homme entre autres doué d'une culture footballistique sans égale, qui a su égayer ces années de discussions passionnantes alternant cosmologie, politique et The Wire. Puisses-tu bien préparer le terrain au Chili pour lancer notre futur élevage de chèvres !

Une thèse s'accompagnant de hauts et de bas, une grande médaille revient à mes amis, qui ont toujours été là pour supporter mes lamentations comme pour me faire passer des moments géniaux. Je pense en particulier à Fede, Ivan, Philou et mes deux adorables colocs, Margot et Jérémie. La vie serait moins belle sans vous !

Enfin, ses longues études n'auraient pas été possible sans le soutien infaillible de mes parents et de ma famille, ainsi que les encouragements au quotidien de Chiara. C'est avec toute mon affection que je leur dédie cette thèse.

Alexandre Boucaud

Octobre 2013

Contents

List of Figures

List of Tables

Preface

Big Bang is probably the first term that nowadays comes in mind when evoking the history, and more particularly the early times of the Universe. The reason it is such a great catch-phrase is that it triggers in people's mind the convincing image of an explosion, with a mixture of light, energy, debris and speed.[1] This was the exact intention of its creator, Fred Hoyle, when he released it during a BBC radio broadcast on 28 March 1949. However, his purpose at that time was to emphasize the difference between the model of an expanding Universe defended by Georges Lemaître and described during a 1931 meeting as the hypothesis of the « Atome Primitif »[2] (Lemaître, 1931), and the alternative *steady state* theory of the Universe with no beginning and no end that he spent his life defending (Bondi & Gold, 1948; Hoyle, 1990, for a review).

More than being a simple term, the Big Bang has been adopted as the name of the standard model of cosmology whose complete denomination is « Lambda-CDM concordance model ». This model, which currently prevails in the scientific community, assumes Einstein's General Relativity as the theory of gravity and describes the evolution of the Universe from a very hot and dense state, approximately 14 billion years ago, to its current state. Lambda-CDM (or ΛCDM) stands for Lambda Cold Dark Matter, where Λ refers to Einstein's cosmological constant. In other words, this theory presumes that we live in a Universe where ordinary matter accounts for 5 % of its total energy density, and where the rest is filled with collisionless particles interacting only gravitationally, referred to as dark matter (∼26 %), and completed (∼69 %) with an energy whose origin still needs to be determined, called dark energy, parameterized by the cosmological constant.

The success of the model is based on a series of observational probes that have been measured with high precision over the last two decades. Among the pillars of observational cosmology we can mention:

- **the expansion of the Universe** and the value of the Hubble constant,
- **the cosmic microwave background radiation (CMB)** which is the event of the light decoupling from the hot baryonic soup, predicted by Gamow, Alpher and Herman (Gamow, 1948a,b; Alpher & Herman, 1948), was discovered by two engineers in 1965 (Penzias & Wilson, 1965) and measured with increasing precision since the early nineties

[1] This image is however completely misleading for the general public as it encourages to interpret the Big Bang as a starting point, literally the beginning of the Universe, leading to the metaphysical question of the origin of the Universe. The laws of physics do not apply at energies that would be required by that singularity and therefore scientists face a "wall" called the Planck wall 10^{-43} s after that hypothetical point. Everything past that wall is pure imagination.

[2] Primeval Atom

using satellites like COBE (Smoot et al., 1992; Mather et al., 1994), WMAP (Bennett et al., 2003, 2012) or very recently Planck (Planck Collaboration, 2013a), proving the Cosmological Principle that states that the Universe is isotropic and homogeneous on cosmological scales;

– **the abundance of the light elements in the Universe** calculated via the Big Bang Nucleosynthesis theory developed by Alpher and Gamow (Alpher et al., 1948; Gamow, 1948a), which shows excellent agreement with current measurements. A recent review is given in Steigman (2007);

– **the introduction of cold dark matter**, in the early eighties (Peebles, 1982; Blumenthal et al., 1984) as a non-baryonic alternative to dark matter models. At that time, most scientists thought the matter density in the Universe was unity and favored models with dark matter on the form of neutrinos, the so-called hot dark matter. Some indications in favor of cold dark matter came from galaxy formation models, which were supported the following years by numerical simulations (Davis et al., 1985). This has been confirmed since by high precision cosmological N-body simulations like the Millennium Simulation (Springel et al., 2005) or the more recent DEUS (Alimi et al., 2012);

– **the measurement of distant supernovæ**, in the late nineties (Riess et al., 1998; Perlmutter et al., 1999) showed that the Universe is currently in a phase of accelerated expansion. The supplementary energy needed to push objects away from each other on cosmological distances was labeled dark energy and enters the equations as the cosmological constant.

Like any phenomenological model, this one is not complete. The major issue of the ΛCDM model, and more generally current cosmology, is that 95 % of the present content of the Universe is still of unknown nature. The standard model of particle physics does not predict a particle matching the cold dark matter requirements. However, there is a continuous quest for it (see Saab, 2012, for a review). So far, direct dark matter detection experiments CDMS, (CDMS Collaboration et al., 2013) ; CRESST-II, (Angloher et al., 2012) ; XENON100, (Aprile et al., 2012) ; EDELWEISS, (Armengaud et al., 2011) and DAMA/LIBRA, (Bernabei et al., 2010), have not found conclusive results on the presence of a dark matter particle. Indirect-detection methods, which rather probe the annihilation of dark matter particles may have had more chances. The FermiLAT experiment has recently reported an anomaly in the gamma-ray spectrum (Weniger, 2012; Tempel et al., 2012; Hektor et al., 2013) which might point towards a dark matter particle evidence. The next few years will thus probably be decisive on the subject

of dark matter.

Then there is the cosmological constant problem, i.e. the question of the origin of dark energy and the reason for it started dominating the Universe only very recently. Theorists have sought about the vacuum energy as a possible explanation but so far this hypothesis fails at explaining the huge measured discrepancy between the two quantities today.

We can however learn more about dark energy, for instance by studying its evolution with time. Dark energy drives the accelerated expansion of the Universe, and the ΛCDM model predicts that acceleration started only a few billion years ago. Therefore, supposing the Universe is homogeneous and isotropic, the measure of distances between objects at different times of cosmic evolution provides information on the time dependence of the acceleration and thus on dark energy properties. To that extent, the observation of distant and faint objects (very numerous) is necessary. While this is not an easy task due to the dilution of the traveling light over time, an observed physical effect, referred to as gravitational lensing, can help by focusing the light of sources over very long distances. This effect is key to observe and characterize the properties of distant[3] sources as well as the matter content in between.

Gravitational lensing is the perturbation of light path by matter in the Universe, which affects every photon propagating from a source towards Earth (see Bartelmann, 2010, for a recent review on the subject). In the special event of a source being aligned with a gravitational potential (lens), the light distortion produces giant arcs in the sky, a phenomenon known as strong lensing and first observed by Soucail et al. (1987). There are more subtle effects that only appear statistically, like galaxy shape deformation or CMB lensing (Blanchard & Schneider, 1987), which are referred to as weak lensing effects. They have been observed at the beginning of the nineties (Tyson et al., 1990) but truly detected (in a statistical manner) a decade later (Wittman et al., 2000; Van Waerbeke et al., 2000; Bacon et al., 2001; Rhodes et al., 2001). Weak lensing allows scientists to map out the matter content between the source and us (Kaiser & Squires, 1993), which has been used, e.g., to infer the mass of the Bullet Cluster (Clowe et al., 2007) and show that the source of gravitational potential in this merged cluster is separated from the source of light (emitted by the baryonic matter), revealing indirectly the presence of dark matter.

This thesis work aims at exploring an aspect of weak lensing known as cosmic number magnification. Lensing increases the angular size of extended sources, so while their surface brightness is conserved, the observed flux of these sources in a survey increases, bringing faint

[3] i.e. young

ones into the survey catalog. This effect is weak and requires a high number of sources and a clean redshift separation to be properly detected (Scranton et al., 2005; Hildebrandt et al., 2009, 2011; Morrison et al., 2012). Upcoming surveys like the near-infrared Euclid satellite or the optical Large Synoptic Survey Telescope (LSST), which are partially designed for gravitational lensing measurements, will detect a wealth of sources. This should enhance the signal-to-noise ratio of cosmic magnification measurements. Moreover, the unprecedented depth of the LSST will provide detailed information on the radial repartition of sources, thus making possible the visualization of the Universe in three dimensions (tomography) which will help constrain the evolution of dark energy.

For a ground-based wide-field telescope like the LSST, the flux measurement of sources is affected by systematic errors, the most erratic being the atmosphere variability. To achieve its scientific goals, the LSST requirement on photometric accuracy has been set to one percent for the whole survey. As a matter of comparison, this accuracy has hardly been reached in the past with Sloan Digital Sky Survey data, selecting the nights with best observation conditions (Padmanabhan et al., 2008). This requirement has therefore set a new challenge for the photometric calibration, challenge that can be addressed by rethinking and optimizing the calibration strategy. In particular, a dedicated atmosphere monitoring strategy is necessary in order to account for its intrinsic variability and prevent the error propagation to the source catalogs. In this context, we have separated and studied the atmosphere constituents that contribute the most to atmospheric opacity and implemented an algorithm that realistically simulates long-term variations ($\sim$ 10 years) of these very constituents above LSST site at Cerro Pachón , Chile. This atmospheric simulator is a necessary tool for the calibration group to test and validate both the accuracy of the baseline atmospheric model and the efficiency of the monitoring strategy (that currently uses a spectrophotometric follow up with an auxiliary telescope).

After introducing the main foundations of the standard cosmological model in chapter 1, I will present the instrument and the science goals of the future LSST survey in chapter 2. In chapter 3, I will expose the concepts of photometric calibration of a ground-based instrument, report on the study of atmospheric constituents variability and their impact on the photometry, and describe the atmospheric simulator we have developed. Chapter 4 will introduce the concepts of gravitational lensing and the motivations that lead to the study of the power of cosmic magnification at constraining the cosmological parameters in chapter 5. Eventually, I will put these two subjects in perspective in chapter 6.

CHAPTER 1

Principles of cosmology

Three years from now, in 2016, we will celebrate the century of the publication of Einstein's General Relativity (Einstein, 1916), event that can be considered as the starting point of cosmology. Scientists got really excited by this new concept of a non-static cosmos and it gave rise to many theories and predictions as well as observational campaigns. As every physics field, cosmology has known several bursts in its history, the first being in the 20's and 30's and the latest in the 90's. With time and observational data, a robust model emerged from the theory. Analogously to particle physics, we call it the standard model of cosmology (or the concordance model) and it contains about 10 free parameters.

In the following chapter, I will start with a brief description of spacetime and its metric, before introducing the composition of the Universe. After defining the cosmological distances, I will describe the concepts of structure formation and eventually present the current cosmological probes, constraints, and the remaining challenges.

I A homogeneous and isotropic Universe

In cosmology and astrophysics in general, information travels essentially with light[1] in the form of photons. These photons have a finite speed, c, currently measured with an extreme precision (see e.g. Mohr et al., 2012). That finite velocity implies that everything we see at present has been emitted in the past and thus that we only have access to our past *light cone*, the limited region in spacetime within which a photon can reach us. Still, light travels fast and the photons emitted a few billion years ago give us access to cosmological scales.

I.1 From the cosmological principle to General Relativity

Centuries of astronomical observations have come to gradually establish that the Earth has no special position in the Universe.[2] Our star, the Sun, is itself a very trivial star that sits in the suburbs of our Galaxy, the Milky Way ; itself part of a local group of banal massive galaxies sitting at a random point in the cosmos. In other words, there is no preferred direction around us. Added to the fact that on very large scales, the structures we observe in the cosmos are distributed rather uniformly (see e.g. results from Cole et al., 2005; Planck Collaboration, 2013a), we can reasonably postulate the large scale isotropy and homogeneity of the Universe. This postulate, known as the *cosmological principle*, is an extension of the Copernican principle (valid locally) to very large scales, and will guide the theorists when selecting models.

[1] not to mention cosmic rays, and possibly gravitational waves, which are predicted by General Relativity but have not yet been observed

[2] the anthropic principle states a different philosophical view on that subject

A good basis to start building a cosmological model is to assume that fundamental laws of physics are universal. In other words, every region in space and time should abide by the same laws. So far, every work aiming at detecting a variation in time of the fundamental physics constants has not observed any departure from the current measured values, and that to a very high level of precision. Among the four fundamental interactions, only gravity has an effect on the scales we would like to probe. We thus assume that gravity acts the same way throughout the cosmos and we will make use of General Relativity to determine its spacetime structure.

In that theory, time and space are linked inside a four-dimensional geometry defined by a symmetric tensor: the spacetime metric g. The metric values $g_{\mu\nu}$ can be described in a coordinate system x^μ where $\mu = 0$ represents the time and the indices $\mu = 1, 2, 3$ the three dimensions of space. The square norm in such geometry is defined by

$$\mathrm{d}s^2 = g_{\mu\nu}\,\mathrm{d}x^\mu \mathrm{d}x^\nu \,. \tag{1.1}$$

The main product of General Relativity is to relate the geometry of the Universe, embodied in the metric-dependent Einstein tensor $G_{\mu\nu}$, to its matter/energy content, contained in the energy-momentum tensor $T_{\mu\nu}$. This is done via Einstein's equations,

$$G_{\mu\nu} = \frac{8\pi G}{c^4}\, T_{\mu\nu} \,, \tag{1.2}$$

where, G denotes the gravitational constant and c the speed of light in vacuum. For a more complete description and formulation of General Relativity theory, one can have a look at Dodelson (2003) or Weinberg (2008). These equations basically mean that a source of energy or matter will locally modify the geometry of the four-dimensional spacetime metric g. Therefore the geodesics, the trajectories followed by the photons and defined by $\mathrm{d}s^2 = 0$, will locally also be modified and curved, leading to the gravitational lensing effect we will see in Chapter 5.

Convinced by the eternal nature of the Universe, Einstein tried to solve his equations using a static universe as a boundary condition, bearing no success. To solve this problem, he therefore introduced an additional term Λ, referred to as the *cosmological constant*, compatible with General Relativity (Einstein, 1917). The new equations were

$$G_{\mu\nu} + \Lambda\, g_{\mu\nu} = \frac{8\pi G}{c^4}\, T_{\mu\nu} \,. \tag{1.3}$$

The meaning of this term will be addressed in Section II.

I.2 The expansion of the Universe

In the quest for solving these equations (1.2), the first breakthrough happened in the early twenties when Aleksandr Friedmann proposed a first solution (Friedmann, 1922, 1924) which was that of a dynamic universe. After a controversy between Friedmann and Einstein who wanted the solutions to be static, a rather silent breakthrough[3] came with a paper from a theorist (Lemaître, 1927) and two years later by an experimentalist (Hubble, 1929) where they found observational evidence of local cosmic expansion. Classifying stellar spectra, mostly from bright stars called cepheids, they noticed the Doppler shift caused by the recession of objects was increasing as the objects distance. The Doppler shift being related locally to the velocity of the objects, they discovered that their recessing velocity v_r could be expressed with what we called nowadays the *Hubble law*,

$$v_r = H_0\, d\,, \tag{1.4}$$

where H_0 denotes the Hubble constant and d the object distance from Earth. The recession velocity is thus a combination of the peculiar velocity of the object and the velocity of expansion of the Universe. To disentangle both effects one needs to introduce the comoving coordinate frame, where the comoving observers are at rest, and the comoving distance χ is related to the physical distance d[4] via

$$d = a(t)\,\chi\,, \tag{1.5}$$

where $a(t)$ is the scale factor. The latter is chosen to be unity at present time $a_0 = a(t_0) \equiv 1$ and is a function of time only, because of the assumed homogeneity of space. Calculating again the recession velocity using (1.5) yields

$$v_r = \dot{a}\,\chi = \frac{\dot{a}}{a}\,d = H(a)\,d\,, \tag{1.6}$$

where

$$H(a) \equiv \frac{\dot{a}}{a}\,, \tag{1.7}$$

is the normalized rate of cosmic expansion, or *Hubble rate*. The Hubble constant H_0 introduced in (1.4) is the present value of the Hubble rate $H_0 \equiv H(a_0)$ and is a key parameter for cosmological models. Cosmologists rather use a dimensionless constant to refer to it, in this case h, defined by

$$H_0 = 100\,h\,\mathrm{km\ s^{-1}Mpc^{-1}}\,, \tag{1.8}$$

[3] Lemaître was a Belgian priest, wrote this papers in French and thus it was not broadcast at that time
[4] these distances are well defined if small, i.e. in the nearby universe

so that h is of order unity. The current constraint on the Hubble parameter is given by Planck Collaboration (2013b) and yields a value of

$$H_0^{\text{best}} = 67.3 \pm 1.2 \text{ km s}^{-1}\text{Mpc}^{-1} . \tag{1.9}$$

Cosmological redshift

Despite the scale factor, one other frequently used parameter is the redshift z, defined as the relative shift of observed spectral features at a wavelength λ with respect to the rest frame wavelength λ_0,

$$z \equiv \frac{\lambda_0 - \lambda}{\lambda} , \tag{1.10}$$

because it is more closely related to observables such as stellar spectra. Locally, this can be interpreted as the previous mentioned Doppler shift caused by the recession of objects due to cosmic expansion. Hence, $\mathrm{d}\lambda/\lambda = \mathrm{d}v/c$ and using the Hubble law (1.4) in its infinitesimal form, one can show that

$$\frac{\mathrm{d}\lambda}{\lambda} = \frac{\mathrm{d}a}{a} , \tag{1.11}$$

and in particular that $\lambda/\lambda_0 = a/a_0 = a$. This leads, using (1.10), to the important relation between the scale factor and the redshift

$$a(z) = \frac{1}{1+z} . \tag{1.12}$$

I.3 A solution to General Relativity field equations

After the discovery of the first solutions to Einstein field equations by Friedmann and Lemaître, two other theorists took over the work and proposed (Robertson, 1935, 1936b,a; Walker, 1936) a homogeneous and isotropic metric, known as the FLRW metric, solution of (1.3) and describing an expanding universe. This metric can be expressed in spherical coordinates as

$$\mathrm{d}s^2 = c^2\mathrm{d}t^2 - a^2(t)\left[\frac{\mathrm{d}r^2}{1 - c^2 k\, r^2} + r^2(\mathrm{d}\theta^2 + \sin^2\theta\, \mathrm{d}\phi^2)\right] , \tag{1.13}$$

where t is the cosmic time and k is the curvature of the Universe. Choosing for the energy-momentum tensor a perfect fluid at rest in comoving coordinates, and fully described in terms

of its pressure p and density ρ, it reads

$$T_{\mu\nu} = \begin{pmatrix} c^2\,\rho(a) & 0 & \cdots & 0 \\ 0 & p(a) & \ddots & \vdots \\ \vdots & \ddots & p(a) & 0 \\ 0 & \cdots & 0 & p(a) \end{pmatrix} . \tag{1.14}$$

Inserting this tensor expression into (1.3), one obtains the Friedmann equations

$$\left(\frac{\dot{a}}{a}\right)^2 = H^2(a) = \frac{8\pi G}{3}\rho(a) - \frac{c^2 k}{a^2} + \frac{\Lambda}{3}\,, \tag{1.15}$$

$$\frac{\ddot{a}}{a} = -\frac{4\pi G}{3}\left(\rho(a) + \frac{3}{c^2}\,p(a)\right) + \frac{\Lambda}{3}\,. \tag{1.16}$$

which governs the evolution of the scale factor. These two equations allow us to compute the cosmological expansion history simply knowing the dominant matter component at a given scale a. As we will see in Section II, the relative quantity of different types of matter evolve as the Universe expands, and thus drives the expansion through the relation between their pressure p and their density ρ, also called the equation of state.

Cosmic time and the Planck epoch

So far, the evolution of the Universe is only characterized using the scale factor a. Because a is a function of cosmic time (or redshift), the evolution of observables could, as well, be parameterized using the cosmic time

$$t(a) = \int_0^a \frac{\mathrm{d}a'}{a' H(a')}\,. \tag{1.17}$$

Defining things this way requires adopting an initial time at $a = 0$. We shall avoid defining here what the *initial cosmological time* physically means, and use a detour stating that we observe an expansion today as well as in the past and if we simply extrapolate to early times, this leads to a period of time when the Universe was so dense and hot that the fundamental laws of physics cannot apply anymore. The frontier with that period is called the *Planck wall* ; and if we were to apply the same expansion past it, we would end up with a singularity 10^{-43} s before the Planck wall. We thus take the instant of that extrapolated-but-unknown singularity as a reference time, often named the *Big-Bang*, as the initial cosmic time $t_0 = t(a = 0)$. A particular time is the Hubble time,

$$t_{\mathrm{H}} = \frac{1}{H_0}\,, \tag{1.18}$$

defined as the present cosmic time, which corresponds to the time signals have had to propagate since the Big-Bang.

We shall now see how the content of the Universe has evolved with time.

II Energy content of the Universe

II.1 Energy densities

The densities of the constituents of the cosmos drive the evolution of the scale factor through equation (1.15), which can be rewritten

$$\left(\frac{\dot{a}}{a}\right)^2 = \frac{8\pi G}{3}\left(\rho + \rho_{\rm k} + \rho_\Lambda\right) , \tag{1.19}$$

where

$$\rho = \rho_{\rm r} + \rho_{\rm m} , \tag{1.20}$$

$$\rho_{\rm k} = -\frac{3\,c^2 k}{8\pi G a^2} , \tag{1.21}$$

$$\rho_\Lambda = \frac{\Lambda}{8\pi G} . \tag{1.22}$$

As (1.20) points out, the matter density ρ is the sum of the (non-relativistic) matter density $\rho_{\rm m}$ and the radiation density $\rho_{\rm r}$ that accounts for photons and relativistic neutrinos. These densities being free parameters of cosmological models, it is useful to use instead dimensionless cosmological parameters. To this end, one introduces the *critical density*

$$\rho_{\rm cr} = \frac{3\,H^2}{8\pi G} , \tag{1.23}$$

which can be interpreted as the total density in the Universe provided there is no curvature and no cosmological constant. This critical density is then used to define the dimensionless cosmological parameters

$$\Omega_{\rm x} \equiv \frac{\rho_{\rm x}}{\rho_{\rm cr}} , \tag{1.24}$$

where x can stand for the subscripts r, b, m, k, Λ and T (respectively radiation, baryons, matter, curvature, cosmological constant, and total). There is a specific cosmological parameter for baryons since they play a specific role in structure formation (*cf.* Section IV).

Equation (1.19) can now be expressed with these new parameters

$$\left(\frac{\dot{a}}{a}\right)^2 = H^2 \left(\Omega_\mathrm{m} + \Omega_\mathrm{r} + \Omega_\mathrm{k} + \Omega_\Lambda\right) , \tag{1.25}$$

which leads, at present time, to the relation[5]

$$\Omega_\mathrm{k} = 1 - \Omega_\mathrm{m} - \Omega_\Lambda = 1 - \Omega_\mathrm{T} , \tag{1.26}$$

where Ω_T stands for the sum of the matter content and the cosmological constant and represents the total energy content of the Universe. Equation (1.26) acts as a boundary condition that determines the curvature the Universe knowing its total energy content. Three cases can be distinguished:

$$\begin{aligned}
\Omega_\mathrm{T} > 1 \;&\Leftrightarrow\; k < 0, \quad \text{the Universe is closed,} \\
\Omega_\mathrm{T} = 1 \;&\Leftrightarrow\; k = 0, \quad \text{the Universe is flat,} \\
\Omega_\mathrm{T} < 1 \;&\Leftrightarrow\; k > 0, \quad \text{the Universe is open,}
\end{aligned}$$

and their effect on light propagation is shown in Figure 1.2. All current observations favor the flat geometry, as shown in Figure 1.6

II.2 Evolution eras

Using Friedmann equations (1.15) and (1.16), one can write the *continuity equation*

$$\dot{\rho} + 3\,H\,(\rho + p/c^2) = 0 , \tag{1.27}$$

which describes the evolution of the fluid density with cosmic time. As for any fluid, pressure and density in that equation are linked through an equation of state

$$p = w\,\rho\,c^2 , \tag{1.28}$$

that has to be determined for each constituent. Equation (1.27) can be rewritten as

$$\mathrm{d}\left(\rho(a)\,a^3\,c^2\right) = -p(a)\,\mathrm{d}\left(a^3\right) , \tag{1.29}$$

[5] we can neglect Ω_r because the current radiation is essentially made of a diluted microwave background which does not contribute to the expansion anymore

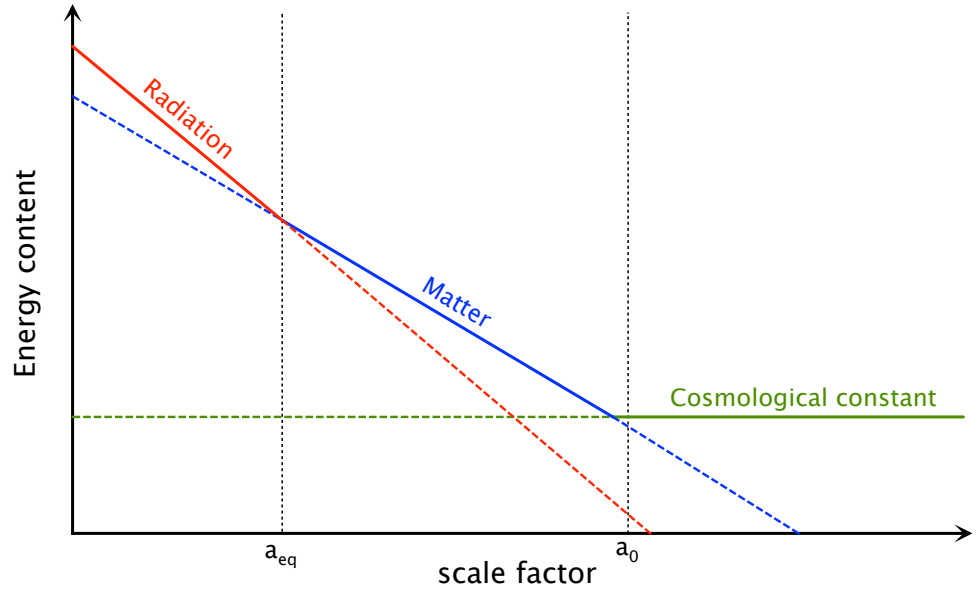

Figure 1.1 – Schematic of the evolution of the Universe's main constituents energy densities as a function of the scale factor. The radiation is plotted in red, the non-relativistic matter in blue and the cosmological constant contribution in green. These are represented in log scale.

which can be identified with the first law of thermodynamics $\mathrm{d}U = -p\,\mathrm{d}V$ where U is the internal energy of the fluid, and V scales with a^3. This equation is then used to access the density evolution and the temporal dependence of the scale factor using (1.19). One can look at every component individually.

Radiation

The equation of state for relativistic matter is $p = \frac{1}{3}\rho c^2$. The solution for the radiation density is

$$\rho_\mathrm{r} \propto a^{-4} \quad \Rightarrow \quad \Omega_\mathrm{r}(a) = \Omega_\mathrm{r}\, a^{-4}\,. \tag{1.30}$$

In addition to the spatial dilution factor of a^{-3}, there is a loss of energy due to cosmological shift which accounts for another factor a^{-1}. Radiation dominated the post inflation era and during that time the scale factor changed to

$$a(t) \propto t^{1/2}\,. \tag{1.31}$$

The radiation contribution for the expansion of the Universe in the concordance model is shown in red in Figure 1.1.

Matter

Non-relativistic matter, which stands for baryons or dust as well as dark matter (see Section IV.3), is made of particles with velocities much smaller than the speed of light. They are considered thermally cold and thus have no pressure. It follows that $\mathrm{d}\left(\rho_\mathrm{m}(a)\,a^3\right) = 0$ and that the matter density scales like

$$\rho_\mathrm{m} \propto a^{-3} \quad \Rightarrow \quad \Omega_\mathrm{m}(a) = \Omega_\mathrm{m}\, a^{-3}\,, \tag{1.32}$$

which simply accounts for the spatial dilution due to the expansion. The matter era took over the radiation driven expansion at a scale factor $a_\mathrm{eq} \simeq 6 \times 10^{-6}$ and dominated until very recently (cf. the matter contribution in blue in Figure 1.1). During that time the Universe expanded like

$$a(t) \propto t^{2/3}\,. \tag{1.33}$$

Cosmological constant

Concerning the cosmological constant, Friedmann equation yields $\dot{a}/a = \sqrt{\Lambda/3} = H$. Therefore

$$a(t) \propto e^{Ht}\,, \tag{1.34}$$

the expansion of the Universe accelerates forever. Observations tend to show we currently live in a cosmological constant dominated universe. The transition from the matter domination is estimated to have happened at a scale factor of $a \simeq 0.78$ which is fairly recent (*cf.* the green line in Figure 1.1).

Curvature

The only possible solution of Friedmann's equation with a domination of the curvature is for an open universe ($k < 0$). In this case, we find a density evolution as

$$\rho_\mathrm{k} \propto a^{-2} \quad \Rightarrow \quad \Omega_\mathrm{k}(a) = \Omega_\mathrm{k}\, a^{-2}\,, \tag{1.35}$$

and a scale factor proportional to the cosmological time

$$a(t) \propto t\,. \tag{1.36}$$

That option is nevertheless ruled out by current observations (cf. page 33 for an overview).

Hubble rate

The Hubble rate enters in a lot of cosmological equations so it is useful to relate it to the energy content of the universe, and vice-versa. Following Peebles (1993, p.312) and Hogg (1999), the evolution of the Hubble rate as a function of the cosmological parameters evolution can be rewritten as

$$H(z) = H_0\, E(z)\,, \tag{1.37}$$

where

$$E(z) = \sqrt{\Omega_\mathrm{r}(z) + \Omega_\mathrm{m}(z) + \Omega_\mathrm{k}(z) + \Omega_\Lambda(z)}\,. \tag{1.38}$$

In the ΛCDM model, this expressions reads

$$E(z) = \sqrt{\Omega_\mathrm{r}\,(1+z)^4 + \Omega_\mathrm{m}\,(1+z)^3 + (1-\Omega_\mathrm{T})\,(1+z)^2 + \Omega_\Lambda}\,. \tag{1.39}$$

III Distance measurements

Comoving distance

As the information in the cosmos travels at the speed of light, time and distance are closely related. The FLRW metric (1.13) applied to a light ray radially incoming simplifies to $c\,\mathrm{d}t = -a\,\mathrm{d}\chi$. A source observed now at $t = t_0$ and whose light has been emitted at $t = t(a)$, is thus situated at a comoving distance χ given by

$$\chi(a) = \int_{t(a)}^{t_0} \frac{c\,\mathrm{d}t'}{a(t')} = \int_a^1 \frac{c\,\mathrm{d}a'}{a'^2 H(a')}\,. \tag{1.40}$$

Since the redshift, defined in (1.10), is very adapted for working at late times and dealing with astrophysical objects, equation (1.40) can also be written as

$$\chi(z) = \int_0^z \frac{c\,\mathrm{d}z'}{H(z')} = \frac{c}{H_0}\int_0^z \frac{\mathrm{d}z'}{E(z')}\,. \tag{1.41}$$

This yields a more practical expression for the line-of-sight comoving distance.

Comoving horizon and Hubble radius

A useful quantity to define is the *comoving horizon distance*

$$\chi_\mathrm{hor}(a) = \int_0^a \frac{c\,\mathrm{d}a'}{a'^2 H(a')} = d_\mathrm{H}\int_0^a \frac{\mathrm{d}a'}{a'^2 E(a')}\,, \tag{1.42}$$

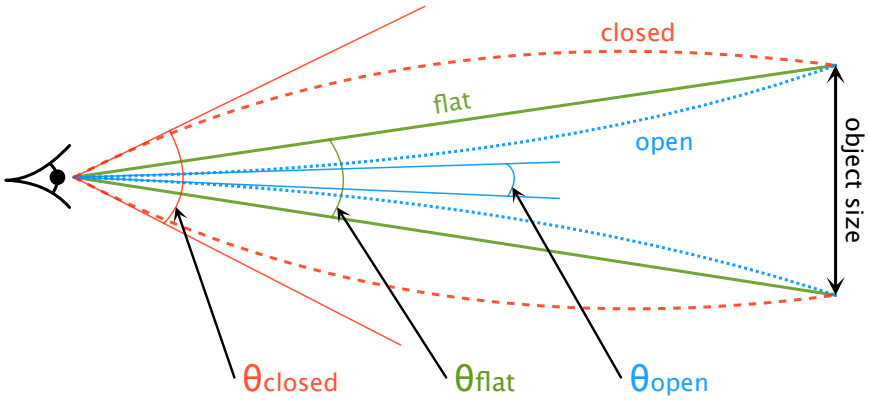

Figure 1.2 – Schematic of light propagation in an open, flat and closed Universe. This plot shows the impact of the curvature of the Universe on the apparent observed angle subtended by an object.

where

$$d_{\rm H} = \frac{c}{H_0} \tag{1.43}$$

is the Hubble distance. The comoving horizon is the comoving distance that light has traveled since $a = 0$ until an epoch a. A sphere of radius $\chi_{\rm hor}$ is therefore the finite volume of space than can have been in causal contact since the Big Bang, due to the finite velocity of light. In gravitational lensing, the upper boundary for the line-of-sight integrals is therefore the comoving horizon distance taken at present time

$$\chi_{\rm H} = \chi_{\rm hor}(a_0) = d_{\rm H} \int_0^1 \frac{{\rm d}a'}{a'^2 E(a')} \,. \tag{1.44}$$

Proper distance

If one desires to measure the distance d between two events, at the same redshift, separated by an angle $\delta\theta$, one needs to compute the transverse comoving distance $d_{\rm M}$, also know as *proper distance*, so that $d = d_{\rm M}\,\delta\theta$.

The difference from the line-of-sight comoving distance comes from the curvature of space-time through its density ratio $\Omega_{\rm k}$, as shown in Figure 1.2. Again, one can distinguish between

three cases,

$$d_{\rm M}(z) = f_k(\chi(z)) = \begin{cases} \dfrac{d_{\rm H}}{\sqrt{\Omega_{\rm k}}} \sinh\left[\dfrac{\sqrt{\Omega_{\rm k}}}{d_{\rm H}}\,\chi(z)\right] & \text{for} \quad \Omega_{\rm k} > 0 \\ \chi(z) & \text{for} \quad \Omega_{\rm k} = 0 \\ \dfrac{d_{\rm H}}{\sqrt{-\Omega_{\rm k}}} \sin\left[\dfrac{\sqrt{-\Omega_{\rm k}}}{d_{\rm H}}\,\chi(z)\right] & \text{for} \quad \Omega_{\rm k} < 0\,, \end{cases} \tag{1.45}$$

where $d_{\rm H}$ is the Hubble distance (see equation (1.43)).

In astronomy, the basic methods of distance determination are of two kinds. The first one uses the relation between the measured angular size or separation of an object and its known physical one ; and the second uses the relation between a measured flux of an object and its known intrinsic luminosity. Etherington (1933) showed that in the case of an expanding spacetime, these methods need some correction.

Angular diameter distance

A way to determine an astronomical distance is to measure the angle θ subtended by an object of known physical size l. Assuming θ is small, the expression for the distance to the object is

$$d_{\rm A} = \frac{l}{\theta}\,, \tag{1.46}$$

where $d_{\rm A}$ is called the angular diameter distance. In an expanding universe, the comoving size of the object is obtained by dividing its size by the scale factor. Hence the angle becomes

$$\theta = \frac{l/a}{d_{\rm M}}\,, \tag{1.47}$$

and comparing with (1.46) we end up with

$$d_{\rm A} = a\, d_{\rm M} = \frac{d_{\rm M}}{(1+z)}\,. \tag{1.48}$$

Contrary to the comoving distance, the angular diameter distance decreases and converges at large redshift.

Luminosity distance

The other method for inferring distances is to measure the observed flux F of an object of known luminosity L, whose expression is

$$F = \frac{L}{4\pi d_{\mathrm{L}}^2}\,, \tag{1.49}$$

where d_{L} is the luminosity distance to the object. A luminosity is a number of photons multiplied by an energy exiting a shell per unit time. In the comoving frame of an expanding universe, the observed energy of photons will be lower than the initial energy by a factor a and the time the photon take to exit the shell is increased by a factor a^{-1}. Therefore the expression for the observed flux becomes

$$F = \frac{L\,a^2}{4\pi d_{\mathrm{M}}^2}\,. \tag{1.50}$$

Again, comparing (1.49) and (1.50) the expression for the luminosity distance becomes

$$d_{\mathrm{L}} = \frac{d_{\mathrm{M}}}{a} = (1+z)\,d_{\mathrm{M}}\,. \tag{1.51}$$

As mentioned in the Dodelson (2003, p. 37), the more dark energy, the larger the cosmological distances. At high redshift, more dark energy means a small matter contribution and thus a smaller expansion rate. Light from distant objects has therefore had more time to propagate towards us and distant sources will appear at present brighter than in a matter dominated universe.

IV Structure formation

The cosmological principle, assuming homogeneity and isotropy, associated with the General Relativity theory, leads to the FLRW metric, and is the main pillar of the current cosmological model. While it is verified at very large scale by CMB measurements, the structures we currently observe in the Universe like galaxies or galaxy clusters, appear in direct contradiction with that principle at small scales. The only way to verify these assumptions is to find a uniform process for these structures to form.

The current shared vision is that the tiny inhomogeneities (within the statistically homogeneous universe) present in the Universe at early times, evolved under the gravitational force, to form more and more massive structures, a scenario called *bottom-up*.[6] This model implies a slightly modified FLRW metric to account for the fluctuations, as well as a quantity of non relativistic and non-baryonic matter, called *dark matter* in order to describe the formation and

[6] as opposed to a *top-down* scenario where bigger structures are formed first and then split into smaller ones.

evolution of these structures.

IV.1 Gravitation and perturbations evolution

If the Universe was strictly homogeneous and isotropic, there would be absolutely no structures in it like stars or galaxies today. There must have been some primordial anisotropies in density than acted as seeds for the creation of all cosmological structures. But as of today, there is no model that is able to explain the formation process of those structures from one end to the other. Despite being really complex, that process occurred mostly during a phase called *dark ages*. It corresponds to an epoch where the cosmos was filled with hydrogen atoms that absorbed light (emitted by young stars), thus impeding its propagation. In the end, this absorption process lead to the complete re-ionization of the cosmos which became « transparent », again.

Nevertheless, scientists tend to agree on a mechanism that ought to be responsible for the structure formation and evolution. This mechanism is referred to as *gravitational instability*.

IV.1.1 Gravitational instability

Starting with an homogeneous Universe with an average density $\bar{\rho}$, in order to describe the density fluctuations in the cosmos, we define the density at a given position $\boldsymbol{x}$ in space

$$\rho(\boldsymbol{x}) = \bar{\rho} + \delta\rho(\boldsymbol{x}) \tag{1.52}$$

where $\delta\rho$ is the deviation from homogeneity. These fluctuations will amplify with time under their own gravity, a phenomenon known as gravitational collapse. A helpful observable is the density contrast

$$\delta(\boldsymbol{x}) = \frac{\delta\rho(\boldsymbol{x})}{\bar{\rho}} \tag{1.53}$$

which is the relative density fluctuation.

Gravitation acts on matter particles as long as they are causally connected. This limits, at a given time, the size of the fluctuations that can collapse. A few instants after the Planck era, the current model favors a short period of extremely fast expansion called inflation. Density fluctuations are created purely stochastically at the end of inflation, but end up out of the horizon, the causal distance in the Universe, due to the quick expansion. Then, as the horizon expands, the fluctuations re-enter progressively the horizon and start interacting.

IV.1.2 Linear evolution

Linearity is an approximation usually admitted for the early phases of evolution models as it implies that gravitational collapse operated independently at all scales. This approximation holds as long as the density contrast δ of the perturbations is lower than unity. The upper limit over which the linear evolution is not valid is still subject to debate, is probably the most currently undecided issue of the structure formation theory.

While the density contrast at recombination (at a redshift of $z \sim 1100$) yields a peak to peak value of the order 10^{-5}, the density contrast of structures in the local Universe (stars, galaxies) is highly superior to 1. Hence the linear approximation is not valid anymore in the local Universe at scales under the size of a galaxy cluster ($\sim 1\,\mathrm{Mpc}$) and it is important to find when, in the past, the density contrast crossed unity, to determine the time (or redshift) and scale of the transition between linear and non- linear regime. For that, we need to compute the evolution of the perturbations.

IV.2 A statistical description

The first step is to relate the previous mentioned density contrast with actual observables. One can translate the concepts of homogeneity and isotropy into statistical probability formulæ:

$$\mathcal{P} = \bar{n}\,\mathrm{d}V \tag{1.54}$$

$$\mathcal{P}_{12}(\mathrm{d}V_1, \mathrm{d}V_2) = \bar{n}^2\ (1 + \xi_{gg}(r))\ \mathrm{d}V_1\,\mathrm{d}V_2\,, \tag{1.55}$$

where $\bar{n}$ is the mean galaxy density per unit volume, $\mathrm{d}V_i$ infinitesimal volume elements and $\xi_{gg}(r)$ the three-dimensional two-point correlation function of galaxies separated by a distance r in space. Equation (1.54) gives the probability of finding a galaxy in a volume $\mathrm{d}V$, and equation (1.55) gives the probability of finding a galaxy in a volume $\mathrm{d}V_1$ and a second in a volume $\mathrm{d}V_2$, both separated by r. Statistical homogeneity is represented by (1.54) while the isotropy lies in the use of the modulus of the separation ($r = \|\boldsymbol{r}\|$) between galaxies in (1.55).

IV.2.1 Correlation function

The correlation function between galaxies can be expressed by means of the *galaxy density contrast*. In a given direction $\boldsymbol{r}$ from us, it is defined by

$$\delta_g(\boldsymbol{r}, t) = \frac{n(\boldsymbol{r}, t) - \bar{n}(t)}{\bar{n}(t)}\,, \tag{1.56}$$

and represents the deviation from the average value in that particular direction. Then, the two-point correlation function between two directions is simply

$$\langle \delta_g(\boldsymbol{r_1}, t)\, \delta_g(\boldsymbol{r_2}, t) \rangle = \xi_{gg}(|\boldsymbol{r_2} - \boldsymbol{r_1}|, t)\,. \tag{1.57}$$

This correlation can be generalized to the mass, with the matter density contrast, already mentioned in (1.53)

$$\delta(\boldsymbol{r}, t) = \frac{\rho(\boldsymbol{r}, t) - \bar{\rho}(t)}{\bar{\rho}(t)} \tag{1.58}$$

where $\bar{\rho}(t)$ is the mean matter density (relativistic + non-relativistic) in the FLRW model. The density fluctuations created at the end of inflation can be described in terms of a Gaussian random field, which means $\delta(\boldsymbol{r}, t)$ is a Gaussian random variable. Its associated two-point correlation function is

$$\langle \delta(\boldsymbol{r_1}, t)\, \delta(\boldsymbol{r_2}, t) \rangle = \xi(|\boldsymbol{r_2} - \boldsymbol{r_1}|, t)\,. \tag{1.59}$$

IV.2.2 Bias factor

There is an obvious relation between the galaxy field and the mass field. The simplest approach is to assume both are equal. However, in general, this cannot be true because we probe the galaxy field using the light we receive from it, but some sources of matter, like dark matter, which are not collisional, do not emit light, and thus cannot be directly mapped out using photons. This is why Kaiser (1984) introduced for the first time the bias factor b

$$\xi_{gg} = b^2\, \xi\,, \tag{1.60}$$

which signifies that the galaxy field is a biased tracer of mass (or the density field). Since it is very hard to measure it properly, and that we do not have hints about its spatial and time behavior, it is generally referred to as a nuisance parameter, currently under strong investigation.

In particular in this thesis work, we inquired about the ability of cosmic magnification measurements with tomography to bring information about the bias at different redshifts (*cf.* Section III).

IV.2.3 Power spectrum

In order to fully characterize the fluctuations in space, studying the evolution of $\delta(\boldsymbol{r}, t)$ in every direction seems impossible and vain. One instead prefers separating the fluctuations at given scales the same way the electromagnetic spectrum is divided in wavelengths. This is achieved

via the Fourier transform, which takes the comoving wavenumber $\boldsymbol{k}$ as parameter.[7] We thus introduce the Fourier transform of the matter density contrast

$$\delta_{\boldsymbol{k}}(t) = \int \mathrm{d}^3 r\, \delta(\boldsymbol{r}, t)\, e^{-i\,\boldsymbol{k}.\boldsymbol{r}}\,. \tag{1.61}$$

The related correlation function in Fourier space is defined by

$$\langle \delta_{\boldsymbol{k}}(t)\, \delta^*_{\boldsymbol{k'}}(t) \rangle = (2\pi)^3\, \delta_{\mathrm{D}}^{(3)}(\boldsymbol{k} - \boldsymbol{k'})\, P_\delta(k, t)\,, \tag{1.62}$$

where $\delta_{\mathrm{D}}^{(3)}$ denotes the three-dimensional Dirac delta distribution and P_δ the matter power spectrum. P_δ is defined as the Fourier transform of the two-point correlation function ξ.

$$P_\delta(k, t) = \int \mathrm{d}^3 r\, \xi(r, t)\, e^{-i\,\boldsymbol{k}.\boldsymbol{r}}\,. \tag{1.63}$$

Since the distribution of the perturbations is assumed to be statistically homogeneous and isotropic, the power spectrum only depends on the modulus of $\boldsymbol{k}$: k. It is a measure of the intensity of the correlation between density fluctuations at a scale $\lambda = 2\pi/k$.

Normalization

A useful parameter that constrains the current level of the fluctuations, in the galaxy power spectrum is called σ_8 and often referred to as the power spectrum normalization. It is the root-mean square of matter fluctuations in a sphere of radius $R = 8\,h^{-1}\mathrm{Mpc}$, supposed to be a linear scale.

$$\sigma_R^2(z) \equiv \int_0^\infty \frac{\mathrm{d}k}{k} \Delta^2(k, z) |\tilde{W}(kR)|^2\,, \tag{1.64}$$

where

$$\tilde{W}(kR) = \frac{3\, j_1(kR)}{kR}\,, \tag{1.65}$$

is the Fourier transform of a normalized top hat window function $W_R(r)$ and j_1[8] is a spherical Bessel function of the first kind, while

$$\Delta^2(k, z) \equiv 4\pi\, P(k, z)\, k^3/(2\pi)^3 \tag{1.66}$$

[7] $k = \|\boldsymbol{k}\|$ is an inverse scale, generally expressed in units $h\,\mathrm{Mpc}^{-1}$

[8] $j_1(x) = \dfrac{\sin x}{x^2} - \dfrac{\cos x}{x}$

is the dimensionless power per wavenumber. The current derived value, given by (Planck Collaboration, 2013b), is

$$\sigma_8 = 0.823 \pm 0.018\,. \tag{1.67}$$

Ergodicity hypothesis

The angular brackets in (1.62) denote the ensemble average, taken over a large number of realizations of the random field. This is obviously not the case in cosmology where we only have a single realization of our observable Universe to play with. To circumvent that issue, cosmologists work under the *ergodic hypothesis*, which states that taking the average over a large number of statistically independent patches of one realization can fairly approximate the average over a large number of realizations. That hypothesis is valid in the case of Gaussian random fields, which we currently observe.

IV.3 Introducing dark matter

We cannot continue our description without mentioning the dark matter. Its very first prediction dates back from the very first steps of cosmology, in the thirties, and is rather associated with astronomy.

IV.3.1 Historical summary

The missing mass problem

Dutch astronomer Jan Oort was studying the motion of stars in the Milky Way (our galaxy) measuring their Doppler shift, and concluded that the visible matter (emitting light) could not, by itself, prevent some of the stellar objects to escape the Galaxy (Oort, 1932). During the same period, American astronomer Fred Zwicky was studying galaxies in the Coma cluster using the same method as Oort and found evidence that additional matter was needed in order to explain the velocity dispersion of these galaxies compared to the apparent gravitational potential (Zwicky, 1933, 1937). That ration between the measured and observed mass was called the mass-to-light ratio M/L and Zwicky computed a value of 10 for the Coma cluster (recent measurements found values up to 300). At that time, they referred to that difference as the « missing mass problem » as it was obviously there but not visible.

Galaxy rotation curves

Thirty years later, another discovery helped constraining that missing mass. It came from measurements of the velocity of stars in spiral galaxies, as a function of the distance to the

galaxy center. Most of the radiating mass being held in the center (galactic bulge), the velocity of stars in the spiral arms should quickly decrease as their distance to the radius in order to maintain a gravitational bound. In the seventies, Vera Rubin measured those velocities and found that the velocity as a function of radial distance was a flat curve (Rubin & Ford Jr, 1970; Rubin et al., 1980). This time, due the measurement precision, not only scientists could imagine the presence of missing mass, but also the distribution of that mass in the form of a halo to properly compensate for the velocity. Studying lots of galaxies, they discovered that a huge number of them contains a dark matter halo that extends far from the visible galaxy boundaries. Rubin's work was soon followed by the same study on elliptical galaxies (Faber & Jackson, 1976) to find the same conclusions.

Later, the interstellar gas around galaxies has also been subject to studies that found that galaxies are gravitationally bound up to a radius 10 times larger than their visible radius, largely increasing the mass-to-light ratio and setting the fraction of dark matter relative to the total gravitating mass to nearly 95 %.

Dark matter and gravitational lensing

Dark matter acts gravitationally exactly as baryonic matter except it does not radiate and is way more abundant. As for the velocity dispersion of galaxies of stars, we see a gravitational effect that baryonic matter alone cannot explain. This is the case for any observed gravitational effect in the cosmos, in particular the deflection of light by gravitational potentials, the so-called gravitational lensing. Due to the huge size of the Universe, this effect is fainter than the one affecting astrophysical objects. That is the reason why though it has been predicted very early, it has been observed rather late, in the eighties, when the instruments gained in performance and resolution. For a longer introduction on gravitational lensing pleaser refer to chapter 4.

Nevertheless, a discovery made in the last decade can be mentioned here, since some scientists have considered it as a smoking gun for dark matter existence. This is the Bullet Cluster case (Clowe et al., 2007). The Bullet cluster is a massive structure resulting of the collision of two galaxy clusters. During the merging process, the baryonic matter mostly in the form of gas collided and heated up. The measurement from X-ray telescopes maps the hot gas, shown in red on Figure 1.3. Gravitational lensing, through its weak statistical effects helped mapping the actual mass of the cluster. This is represented in blue on the same Figure. Assuming galaxy clusters also have their companion dark matter halo, accounting for most of the cluster mass, the best plausible scenario for the Bullet Cluster is that the non collisional dark matter halo of the two parent clusters crossed each other and their kinetic energy kept them going forward, while gravity probably slowed them down.

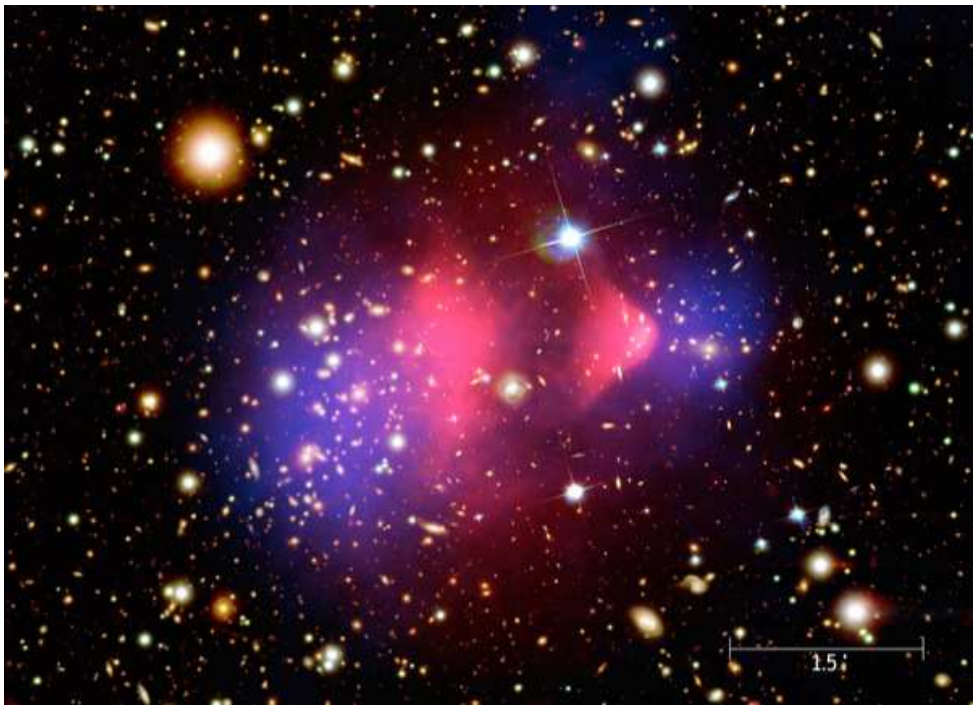

Figure 1.3 – Composite image of the Bullet Cluster. The main image is a visible exposure, and superimposed we find the X-ray gas in red, and the reconstructed mass from weak lensing in blue (image credit D. Clowe for optical and lensing and M. Markevitch for X-ray contours).

A word about the CMB and BAOs

A summary of the dark matter evidence cannot avoid mentioning two very constraining probes, the baryon acoustic oscillations (BAO), whose main feature, a peak at a comoving distance of $d_{\rm BAO} \simeq 150\ h^{-1}$Mpc, could not exist without dark matter. Last but not least, the power spectrum of temperature fluctuations in the radiation at the time of decoupling, also known as CMB temperature spectrum, currently provides the best constraints of the absolute amount of matter in the Universe. These two probes will be discussed in more details in Section V.

IV.3.2 Cold vs. Hot dark matter

Before 1980, people thought the missing mass was ordinary matter hidden or simply non radiating like galactic dust, brown dwarfs, neutron stars, black holes, etc. Early in the beginning of the eighties, new ideas encountered a good acceptance in the community. They stated that dark matter is no ordinary matter but could be in neutrinos or in the form of non-baryonic particles and that this could be tested in laboratory using particle physics instruments like colliders.

Neutrinos were mentioned quite early as possibly accounting for an appreciable contri-

bution to the mean mass density by Gershtein & Zeldovich (1966) and Cowsik & McClelland (1973) found that neutrinos would be a good candidate for dark matter in rich galaxy clusters. The interest around neutrinos grew at that time and especially in the early 1980's. Neutrinos were known to have a low mass and thus should have been relativistic at early time. For that reason the type of dark matter made of neutrino was called *hot dark matter*. Though it is an appropriate model to account for the most massive structures, the relativistic aspect of neutrinos tend to wash out fluctuations the size of galaxies and bellow and thus could not explain the observations.

At the same time, Peebles (1982) followed by Blumenthal et al. (1984) introduced arguments in favor of non-baryonic massive particles that were called *cold dark matter*. Contrary to the hot dark matter, that model agreed more with the observations and is still the standard model of dark matter. The main issue of the cold dark matter theory is that no particle candidate has already been detected.

It is important to note that at the time, the Universe was supposed to be currently dominated by matter and that the cosmological constant/dark energy was not yet accepted. Thus the natural theory was that the Universe was flat with a total matter density $\Omega_{\mathrm{m}} = 1$, that is a Einstein-de Sitter model. The evidence of the acceleration of the expansion of the Universe finally set the current value of the current matter contribution to about 30 %. The current best candidates for dark matter are

- **WIMPs** (Weakly Interacting Massive Particles): lightest stable supersymmetric particles
- **axions**: massive particles solving the strong CP violation in quantum chromodynamics
- **massive neutrinos**.

Detection of dark matter particles

There are currently a high number of experiments aiming at detecting a dark matter particle. They are of two categories, the direct detection experiment that try to measure and detect the events of dark matter interacting with baryonic matter. Due to the supposed extremely small cross-section of dark matter, the reduction of the background noise for these experiments is the main issue they face. The second category is the detection of the light produced by the annihilation of dark matter particles, called indirect detection experiments.

While no direct detection has been claimed so far, the Large Array Telescope (LAT) onboard the Fermi Gamma-ray Space Telescope[9] has recently reported a strong evidence for a monochromatic gamma-ray line with energy $E = 130$ GeV coming from the Galactic center

[9] `http://www-glast.stanford.edu/`

(Weniger, 2012). Soon after, a second line was detected at an energy $E = 110$ GeV. This double peak excess could be interpreted as a signal of dark matter annihilation in two different channels: $\gamma\gamma$ and γZ. The analysis of nearby galaxy cluster signals confirmed the detection (Tempel et al., 2012; Hektor et al., 2013), which, if true, would indicate that dark matter is of particle physics origin (baryonic ?). On the other hand, CMB data strongly pushes for an astrophysical non-baryonic origin. To sum up our knowledge from current observations, one can say that dark matter

- is non relativistic,
- only interacts through the gravitational force,
- has a very small cross-section so that it is non collisional.

N-boby simulations

A word about the simulations, in the mid-eighties, Davis et al. (1985) started a series of numerical simulations of the interactions between particles, and in particular massive cold dark matter particles. Computational power has increased exponentially over the last decades, allowing for extremely heavy numerical simulations with billions of particles (Springel et al., 2005; Alimi et al., 2012). The comparison of the observed large scale structure with the output of these simulations shows a very good agreement with the current ΛCDM model.

IV.3.3 Current estimations

The pure dark matter contribution to the energy density of the Universe has been measured (Planck Collaboration, 2013b) to be

$$\Omega_{\rm c}\, h^2 = 0.1196 \pm 0.0031\,. \tag{1.68}$$

The same measure applied to the baryonic matter (baryonic elements + intergalactic gas) yields a contribution of

$$\Omega_b\, h^2 = 0.02207 \pm 0.00033\,, \tag{1.69}$$

which leads to a total mass density of

$$\Omega_{\rm m}\, h^2 = 0.1423 \pm 0.0029 \quad \text{that is} \quad \Omega_{\rm m} \simeq 0.31 \tag{1.70}$$

The h^2 is the dimensionless Hubble constant and appears in these results to account for the uncertainty on the measurement of the Hubble constant, which is rather big compared to

these ones.

IV.4 The matter power spectrum

Considering dark matter effects, one can now model the evolution of the perturbations from the end of inflation to the end of the linear evolution.

IV.4.1 A history of transitions embedded in a single spectrum

Single-field inflation predicts a scale-invariant power spectrum of the form

$$P_{\rm prim}(k) = A_s\, k^{n_s} \tag{1.71}$$

where A_s is the normalization of the primordial power spectrum at a wavemode $k = 0.002h\,\mathrm{Mpc}^{-1}$ (still linear today) and n_s is the spectral index. A_s can be linked to the integrated normalization of the power spectrum (1.64). Current best σ_8 constraint is inferred from A_s given by CMB measurement. Concerning the spectral index, observations are in good agreement with $n_s \leq 1$ but in general the computation is done under the limiting case $n_s = 1$, also called Harrison-Zeldovitch power spectrum. Starting from this primordial power spectrum, one can follow the evolution of the Universe to predict the the time evolution and the scale dependence of modes k.

Growth of perturbations at a fixed scale

The evolution of perturbations at a fixed scale and under linear regime are schematically described in Figure 1.4. The paragraphs that follow will describe its content.

The expansion during inflation is so fast that at the end of inflation, the Hubble radius is very small and most of the scales are larger than the Hubble radius and thus called *super-horizon*. This means that fluctuations at those scales are not physically related and can grow freely. The growth is linear with time, that is $\propto a^2$ in terms of the scale factor.

The modes that enter the horizon during the radiation dominated era (this is the case for the ones in Figure 1.4) start a physical interaction, that is mostly gravitational. The dark matter distinction arises here. Dark matter perturbations, which interacts only via gravity, stop growing until the equality. Then in the matter dominated era they start growing again at a rate $\propto a$, like the Universe around. Meanwhile the baryons and photons are strongly coupled and their fluctuations start oscillating, the gravitational collapse balancing the radiation pressure. This goes on until recombination where baryons decouple from the photons and start collapsing. The

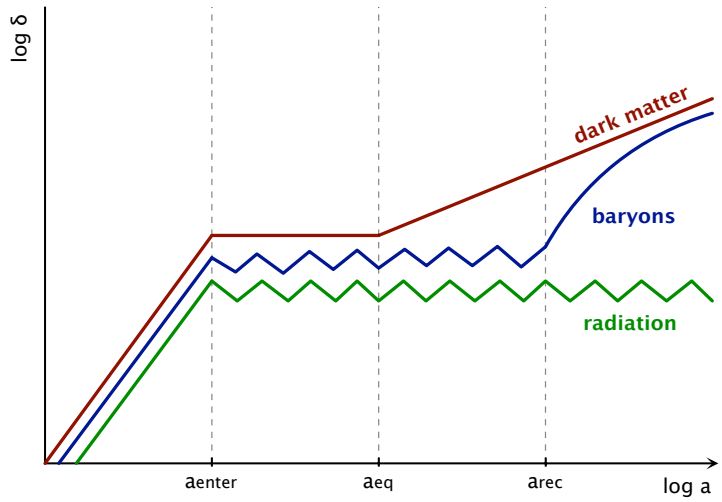

Figure 1.4 – Sketch of the evolution of the density contrast for different energy components and for a given wavenumber. Super-horizon fluctuations ($a < a_{\rm enter}$) grow $\propto a^2$. Then they are frozen during radiation domination ($a_{\rm enter} < a < a_{\rm eq}$) and the baryon-photon plasma starts oscillating. Starting from matter-radiation equality, dark matter fluctuations grow $\propto a$ and baryons and photons stay tightly coupled until the recombination $a_{\rm rec}$. Then the baryons fall into dark matter potential.

presence of already grown dark matter fluctuations tends to speed up the process. The radiation fluctuations are frozen and can thus give us now the amplitude of the baryonic fluctuations at the time of recombination.

A more detailed evolution of the sub-horizon fluctuations can be computed using a Newtonian approach (with continuity, Euler and Poisson equations and pressure neglected) which leads to a homogeneous differential equation for the density contrast

$$\ddot{\delta}(\boldsymbol{x},t) + \frac{2\,\dot{a}}{a}\,\dot{\delta}(\boldsymbol{x},t) - \frac{3\,H_0^2\,\Omega_{\rm m}}{2\,a^3}\,\delta(\boldsymbol{x},t) = 0 \tag{1.72}$$

A detailed calculation can be found in Dodelson (2003). This equation can be solved by separating the space and time dependences: $\delta(\boldsymbol{x},t) = D(t)\Delta(\boldsymbol{x})$. This yields two solutions, one that decays with time (irrelevant here), and one described by the growth factor

$$D_+(a) = \frac{5\,\Omega_{\rm m}}{2}\,E(a)\int_0^a \frac{{\rm d}a'}{(a'\,E(a'))^3} \tag{1.73}$$

where E is the Hubble rate normalized at present, defined in equation (1.38).

The transfer function

If the perturbations followed a linear evolution, the evolution of their power spectrum could be expressed using only the growth factor (1.73). However, the physical transitions occurring in the Universe imprint a scale dependence to that evolution. Among such events, perhaps the most obvious is the density contrast reaching unity, thus breaking down the linearization of equations. One can also mention, as pictured in Figure 1.4,

- the radiation domination era affecting the growth of structure,
- super-horizon fluctuations following their own evolution,
- relativistic species streaming away instead of falling into potential well (photons, neutrinos).

All these transitions are summarized in the transfer function

$$T(k) \equiv \frac{\Phi(k, a_{\rm late})}{\Phi_{\rm Large-scale}(k, a_{\rm late})} \tag{1.74}$$

which is the ratio between a perturbation at wavenumber k now and one that have not been through any transition, at the same wavenumber. On very large scales (i.e. small k), $T(k) \simeq 1$. On small scales, the transfer function is very dependent on the model chosen for dark matter and can therefore help distinguishing between them. For the current CDM model, for large values of k, $T(k) \propto k^{-2}$ while for HDM model (massive neutrinos) the transfer function drops exponentially on small scales. The transition between the two regimes depends on the scale of the comoving horizon at the time of matter- radiation equality $d_{\rm H}(a_{\rm eq})$.

Taking into account all the considerations above, one obtains the expression for the linear matter power spectrum at arbitrary times and for a given wavenumber,

$$P_\delta(k,t) = P_{\rm prim}(k)\, T^2(k)\, D_+^2(t)\,. \tag{1.75}$$

IV.4.2 Non linear corrections

Under some physical scale the linear evolution of matter density fluctuations breaks down and complex structures which have a density contrast $\delta >> 1$ begin to form. The evolution cannot be treated using perturbation theory, this is the nonlinear regime. On the matter power spectrum, this regime takes over at a wavemode $k \simeq 0.2\, h\, {\rm Mpc}^{-1}$.

The standard model for nonlinear evolution is the spherical collapse model by Hamilton et al. (1991) known as the HKLM model, which assumes the non-linear collapsed objects form

isolated and virialised systems decoupled from the expansion of the Universe. This model was extended by Peacock & Dodds (1996), creating the non-linearities from the linear spectrum via a function calibrated with N-body simulations. A different approach was taken by Peacock & Smith (2000); Seljak (2000), considering the decomposition of the density field into individual halos of matter with their own density profile and mass, known as the halo model. The resulting formula, called *halofit*, is a fitting formula based on numerical simulations with a combination of the halo model and HKLM scaling relation (Smith et al., 2003).

V ΛCDM universe: current constraints and science drivers

V.1 Current cosmological probes

V.1.1 CMB: A very old radiation

Most of the radiation we receive on Earth at present does not come from the emission of astrophysical objects. It is actually a relic from the early ages of the Universe, a primordial radiation called cosmic microwave background radiation (CMB). It surrounds us with an extremely uniform temperature (last constrained by Fixsen, 2009) that reads

$$T_{\mathrm{CMB}} = 2.7255 \pm 0.0006\,\mathrm{K}\,. \tag{1.76}$$

This radiation is often called the first picture of the Universe, because the CMB photons are the first photons that escaped the baryon-photon plasma at the moment of recombination, i.e. when the expansion of the Universe allowed the plasma to cool down to a temperature of about 3000 K. This corresponds to a redshift of $z \sim 1100$. At that moment, the electrons that were strongly interacting with the photons, recombine with protons and Helium nuclei to form atoms, therefore letting the photons free to travel the cosmos.

The constant interaction between matter and radiation at that time produced a very homogeneous plasma. This is why the temperature of the CMB is so uniform. But space-born instruments that measured the CMB also measured tiny variations around that value, of the order 10^{-5} (Smoot et al., 1992; Bennett et al., 2003; Planck Collaboration, 2013a). These tiny anisotropies contain a lot of information, especially in the shape and tilt of their power spectrum (see Figure 1.5) ; and are very valuable in order to constrain the cosmological parameters.

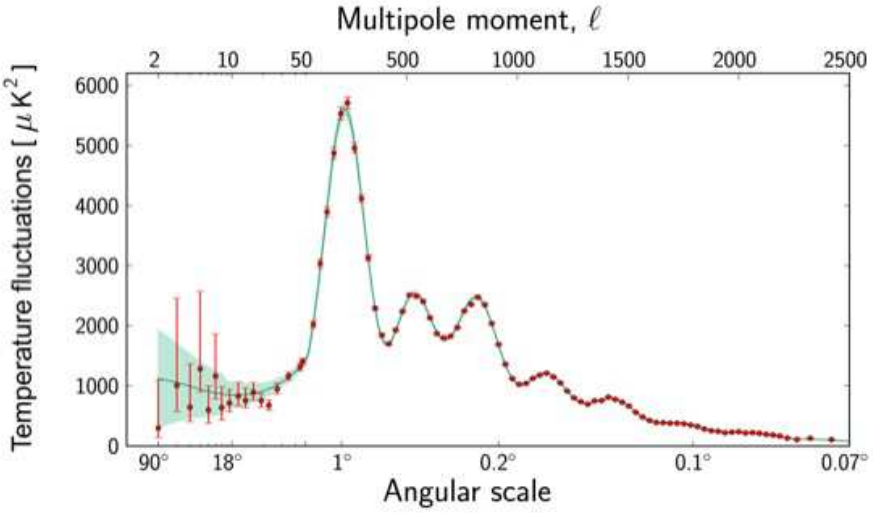

Figure 1.5 – Cosmic Microwave Background temperature anisotropy power spectrum. The green line represents the ΛCDM model fitted to the red *Planck* data points (source Planck Collaboration (2013a)).

V.1.2 Baryon acoustic oscillations

Baryon acoustic oscillations (BAOs), are acoustic waves that propagated in the hot baryon-photon plasma. Non relativistic cold dark matter, present at that time, did not interact with the plasma continued its own evolution. At the time of decoupling, the oscillations froze, the photons then streamed away, and the baryons fell into the existing potential wells. These were located at a distance from the center of each perturbation corresponding to the sound horizon at the time of decoupling $d_{\rm BAO} \simeq 150h^{-1}$Mpc on the one hand, and on the dark matter potentials remained at the center of these perturbations, on the other hand. Without cold dark matter, one should thus find an excess of matter at a scale corresponding to $2 \times d_{\rm BAO}$. That excess has been found by Eisenstein et al. (2005) in SDSS and by Cole et al. (2005) in 2dFDRS at a scale corresponding to $d_{\rm BAO}$, therefore confirming the existence of dark matter.

Once proven, this excess can now be used as a standard ruler in cosmology to measure distances across the epochs and see how the distance varies with, e.g., the redshift. The most recent results have been obtained with the Lymanα quasars from the BOSS experiment (Slosar et al., 2013). A good review on the BAO subject can be found in Weinberg et al. (2013).

V.1.3 Supernovæ

Supernovæ are extremely bright explosions that end the existence of massive stars. One can classify them in two main categories, those that collapse to form neutron stars and emit a lot of neutrinos, but a relatively low number of photons ; and the ones (usually white dwarfs) that accrete matter coming from a binary star and then implode, leading to a thermonuclear combustion of the carbon and oxygen nuclei until ^{56}Ni. The photons escaping are mostly due to the nuclear decay of ^{56}Ni to ^{56}Co and then ^{56}Fe. These are the supernovæ interesting for cosmology, since their exploding process is fairly identical from one to another, and so is the shape of the luminosity curve of the emitted photons that are observed. They are called SN Ia.

These supernovæ are often referred to as *standard candles* as they provide a measurement of the distances in the local Universe due to the simple scaling between the light curves to determine their redshift. Their also are good tracers of the expansion of the Universe and have been used to infer the current acceleration of expansion (*cf.* Section V.2.3) and more generally provide the best constraints for the Hubble parameter H_0. For this reason, supernovæ often appear as joint probes in cosmological parameter constraints.

V.1.4 Clusters

Galaxy clusters are among the most massive structures in the Universe. In the light of the current structure formation scenario, they are the last structures to have form, they thus are young and provide information at low redshift $z < 1$. Cosmological tests based on observations of galaxy clusters have seen tremendous improvement in recent years, setting competitive constraints on cosmological parameters including the amplitude of the matter power spectrum, the mean matter and dark energy densities and the dark energy equation of state, w (Benson et al., 2013; Allen et al., 2011; Rozo et al., 2010; Vikhlinin et al., 2009; Allen et al., 2008). In addition to tests based on measurements of the mass function and clustering of galaxy clusters, there are two complementary ways of using galaxy clusters to measure cosmic distances, via X-ray observations.

The first, pioneered by White et al. (1993), consists in measuring the cluster gas mass fraction, under the assumption that they are so large their matter content should be representative of the matter content of the Universe. Defining the gas mass fraction f_{rmgas} as the ratio between the X-ray mass and the total cluster mass and adding the fraction of stars, one defines the baryon fraction as proportional to the baryon-matter ratio $\Omega_b/\Omega_{\rm m}$, the constant of proportionality being obtained via simulations. The low systematic scatter in f_{rmgas} offers the prospect to probe cosmic acceleration.

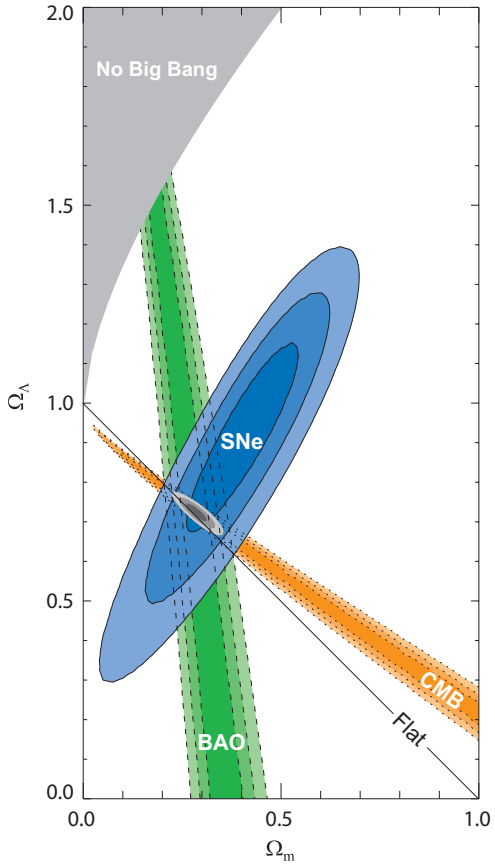

Figure 1.6 – Constraints in the $\Omega_m - \Omega_\Lambda$ plane. Shown are 1-σ, 2-σ, and 3-σ confidence contours in dark, medium, and light shading, respectively. Blue regions correspond to constraints from the Union Supernovæ data set, green regions to constraints from BAOs measured in SDSS, orange regions to constraints from CMB anisotropies (WMAP5 data). The gray regions represent the joint constraints of the three data sets. (source Kowalski et al., 2008).

The second is the cluster count technique. The observed growth rate of galaxy clusters, obtained via the cluster count as a function of redshift, is well constrained by numerical simulation and therefore provides a good cosmological constraints.

V.2 Cosmological results

V.2.1 A flat Universe

Using Friedmann equations, we saw in Section II.1 that the total energy content of the Universe is directly linked to its curvature. In addition, the cosmological principle implies that the curvature should remain spatially constant, so that the Universe has a unique curvature. Until the eighties, where experiments really made a breakthrough in observational cosmology, theorists argued a

lot about the Universe curvature. As Peebles points it out (Peebles, 1993), it was mostly about personal opinion rather than theoretical arguments, but a large trend favored a flat universe model, probably because of its simplicity (Euclidian geometry). While it will remain impossible to demonstrate that our Universe is strictly flat, because of the remaining uncertainty on the measurements, current joint cosmological probes shown on Figure 1.6 and the latest constraints (Planck Collaboration, 2013b)

$$100\,\Omega_{\rm k}^{\rm best} = -0.10 \pm 0.60\,, \tag{1.77}$$

point towards a flat universe. For the remainder of this work, we will assume (otherwise mentioned) that $\Omega_{\rm k} = 0$.

V.2.2 Neutrinos

The CMB helps constraining the number of relativistic neutrino species, as well as their energy density contribution to finally compute the total energy distribution due to radiation

$$\Omega_{\rm r}^{\rm best} = \Omega_\gamma\,[1 + 0.227\,N_\nu] = 2.47 \times 10^{-5}\,h^2 \tag{1.78}$$

where N_ν is the number of relativistic neutrino species (Rich, 2001). Currently this number is compatible with 3 but often measured > 3.

V.2.3 Dark energy and the cosmological constant

Einstein introduced the cosmological constant in the « geometrical » side of his equations because he wanted it to affect the geometry of the Universe. Later observations proved Einstein's intuition wrong and so he removed this term. In the late nineties, two experiments studying supernovæ Ia (Riess et al., 1998; Perlmutter et al., 1999) discovered that the Universe is currently in a phase of accelerated expansion.[10] Such an acceleration could not be driven by matter or radiation due to their dilution and therefore an extra term of energy was needed in Einstein's equations. The cosmological constant has thus been reconsidered, but this time, to account for an additional energy term into the energy momentum tensor.[11] The latest measured value put

[10] Saul Perlmutter, Adam Riess and Brian Schmidt were offered the 2011 Physics Nobel Price for their discovery

[11] In most cosmological models, homogeneity and isotropy are assumed even though we see it is wrong at small scales. Density fluctuations might have lead to structure in spacetime which may affect back the expansion history. This effect called *backreaction* is currently investigated since it could provide an alternative explanation for the effects we associate with the presence of dark energy. While this alternative theory has a certain appeal, the strength of its effects seems to be too low to account for the current observations.

its contribution to

$$\Omega_\Lambda^{\rm best} = 0.685 \pm 0.017\,. \tag{1.79}$$

At present, this is thus the major contribution to the energy density of the universe.

By analogy with the other energy components, the cosmological constant accounts for a perfect fluid whose equation of state is

$$p_\Lambda = -\,\rho_\Lambda\, c^2\,. \tag{1.80}$$

The Universe being essentially made of vacuum, that apparently ever lasting energy, whose effect counteracts gravity, has been considered to be the vacuum energy, the energy coming from the quantum fluctuations of the fundamental fields. This rather « pretty » interpretation however leads to some difficulties. The estimation of the vacuum energy contribution via renormalization theory yields a value $\Lambda = c^3/\,\hbar G \sim 10^{69}\,{\rm m}^{-2}$ that we can compare with the current measurement of the cosmological constant $\Lambda = 3\,\Omega_\Lambda H_0^2/c^2 \sim 10^{-52}\,{\rm m}^{-2}$. With 120 orders of magnitude difference between both fundamental constants, this accounts for the worst prediction error to date. Yet, in an effort to unite quantum field theory and gravitation, theorists still try to reconcile those models.

This negative pressure fluid which origin is currently undetermined is usually referred to as *dark energy* (see Polarski, 2013, for a recent review). In this generalized version, the equation of state of dark energy is

$$p_{\rm de} = w_{\rm de}\,\rho_{\rm de}\,c^2\,. \tag{1.81}$$

where $w_{\rm de}$ is called the dark energy equation of state parameter. Although the absolute density of dark energy is currently measured with a high precision, its evolution with time is fairly unconstrained. This is mainly because dark energy has only been dominating the expansion of the Universe recently. In the ΛCDM model, $w_{\rm de} = -1$ and dark energy is imagined as the effect of a scalar field called the cosmological constant. But the remaining uncertainty enables the consideration of new evolutionary models like wCDM, first introduced by Chevallier & Polarski (2001). In that dynamical dark energy model, the equation of state parameter becomes a function of the redshift

$$w_{\rm de}(z) = w_0 + \frac{z}{1+z}\,w_a \tag{1.82}$$

where w_0 is constant term, and w_a the dynamical one. We now describe the density evolution of dark energy as

$$\rho_{\rm de}(z) = \rho_{\rm de}\,\exp\left(3\int_0^z {\rm d}z'\,\frac{1+w(z')}{1+z'}\right)\,. \tag{1.83}$$

Constraining the evolution of dark energy is one of the main current drivers of observational cosmology (Weinberg et al., 2013). Gravitational lensing, by probing distances which value rely on the cosmological parameters at the time light was emitted or deflected, is a powerful probe of the evolution of the Universe.

V.2.4 Concordance model parameters summary

This is the summary of the latest constraints on the cosmological parameters, mostly given by the *Planck* Collaboration. These are the 1-σ confidence limits estimations using *Planck* and WMAP polarization data (Planck Collaboration, 2013b) ; except for the last three parameters that result from the joint constraints with BAO data and presented at a 2-σ CL. I also added the fiducial values for the set of parameters used in set of Chapter 5.

Parameter	*Planck* + WP (2013)	This work
h	0.673 ± 0.012	0.72.
$\Omega_{\rm m}$	0.315 ± 0.017	0.30.
Ω_Λ	0.685 ± 0.017	0.70.
Ω_b	0.0487 ± 0.0003	0.046.
σ_8	0.829 ± 0.012	0.80.
n_s	0.9603 ± 0.0073	1.00.
$\Omega_{\rm k}$	0.0000 ± 0.0066	0.00.
w_0	-1.13 ± 0.25	-1.00.
w_a	$\lvert w_a\rvert < 1.32$	0.00.

Table 1.1 – Table of the current constraints on the cosmological parameters with the associated uncertainty and the value chosen for this work.

V.3 Cosmology in the next decade: the emergence of weak lensing

With Planck results (Planck Collaboration, 2013a), there is hardly any room left for discoveries concerning the spectrum of CMB temperature anisotropies (except maybe at extremely large scale). However, CMB polarization and CMB lensing can still provide useful cosmological information. While the E-modes of CMB polarization have already been detected, the B-modes (tensor modes) are still to be discovered. If so, they would provide a direct measurement of the amplitude of primordial gravitational waves, emitted at the end of inflation and thus an evidence of the latter. CMB lensing on the other hand, is the mapping of the tiny deflection due to the large scale structure on CMB anisotropies (Das et al., 2013; Van Engelen et al., 2012). It measures the integrated gravitational potential between us and the last scattering

surface (z 1100) and can therefore help constrain the evolution of cosmological parameters and discriminate between cosmological models (see e.g. Marchini et al., 2013; Sievers et al., 2013; Reichardt et al., 2012).

The future of cosmology is probably to look for in all-sky surveys, both in optical and radio. Radio survey will focus on the 21 cm line of hydrogen, which is the only signal that can pass through the dark ages, between recombination and reionization. This will allow a mapping of the early stages of structure formation at redshifts of 10 to 20 and due to that depth, provide a wealth of sources for weak lensing in radio and through cross probes (see e.g. the Square Kilometer Array Group et al. (2011) or LOFAR Kassim et al. (2004). Optical wide-field surveys, like Euclid (Refregier et al., 2010), LSST (Ivezic et al., 2008a) or PanSTARRS (Kaiser et al., 2002), will open the constraining power of weak gravitational lensing to cosmological scales with cosmic shear and cosmic magnification. The wealth of sources offered by these projects will greatly improve the statistical uncertainties and their depth will give the ability to select the populations using tomography, thus allowing the study of the three-dimensional content of the Universe. This will hopefully provide new constraints on the evolution of the cosmological parameters.

CHAPTER 2

Large Synoptic Survey Telescope (LSST)

I An ambitious project

The Large Synoptic Survey Telescope (LSST) is a future wide-field optical telescope operating in Northern Chile to scrutinize the southern sky in six broad photometric bands for ten years. « Synoptic », which refers to the full coverage of a topic, means in this astronomical context that the survey will monitor the whole sky ($20\,000\,\mathrm{deg}^2$) quite simultaneously (on a three day basis). Most of the information given hereafter have been extracted from LSST Science Collaboration (2009), Ivezic et al. (2008b) and Ivezic et al. (2010).

I.1 LSST design

Telescope site

The LSST will be installed on top of the Cerro Pachón mountain, in the Northern Chilean desert, right in between the Pacific ocean and the Andes. Its exact coordinates are in longitude λ and latitude φ

$$\lambda = 70°44'57.8'' \; W\,,$$
$$\varphi = 30°14'39.6'' \; S\,.$$

The top of the El Peñón peak has been leveled off in the last three years to enable the LSST facility to be built there, at 2647 m from the sea level. An artist view of both the telescope and the facility are shown on Figure 2.1. One can see on the right picture the sketch of the auxiliary telescope called « Calypso », which has already been built on the adjacent mountain. This site was chosen for its particularly good seeing conditions.

Telescope design

The telescope design is a three-mirror anastigmat, also called a Mersenne-Schmidt, which proposes a mirror configuration that reduces optical aberrations. The mirror characteristics as well as the corrective lenses are detailed on Figure 2.2. The primary mirror, already build, reach a diameter size of 8.4 m, including the 5.0 m tertiary mirror embedded at its center.

Combined with a field-of-view of $9.8\,\mathrm{deg}^2$, these mirrors will enable the LSST to reach an unprecedented depth for a wide-field survey, right above that of the CFHTLS Deep survey covering a field of $4\,\mathrm{deg}^2$.

A good way to compare surveys is to use the étendue: $A\Omega$, defined as the collecting area A times the field-of-view Ω of the survey, which has the units of $\mathrm{m}^2\,\mathrm{deg}^2$. The étendue can be

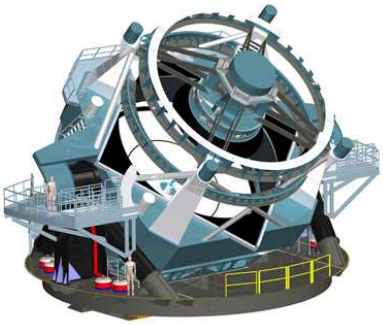

(a) The telescope.

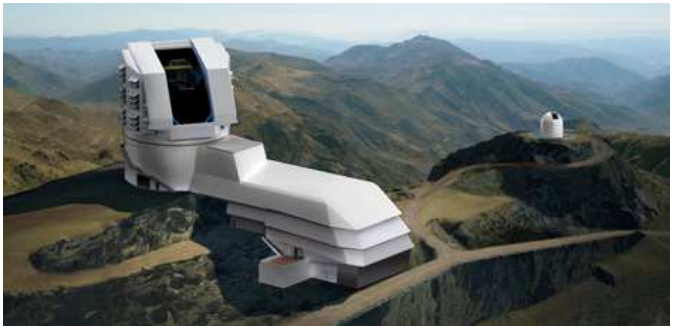

(b) LSST facility and auxiliary telescope.

Figure 2.1 – Artist views of the LSST telescope and facility at Cerro Pachón , Chile. The auxiliary telescope « Calypso » can be seen in the background (source `www.lsst.org`).

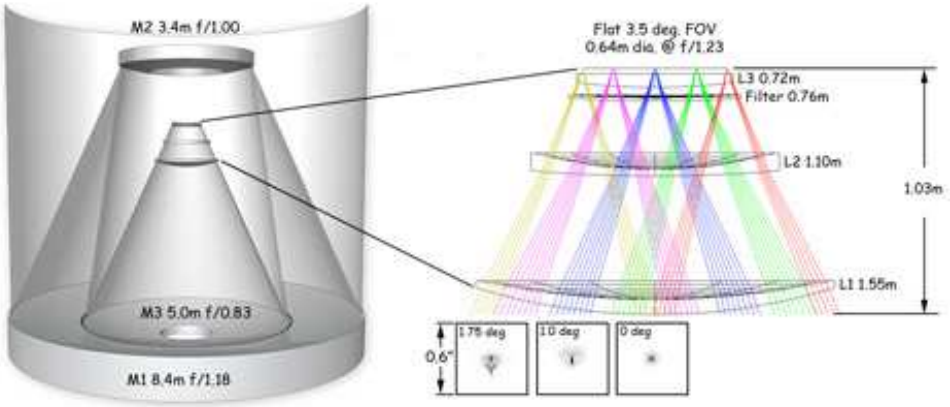

Figure 2.2 – LSST mirror characteristics (source `www.lsst.org`).

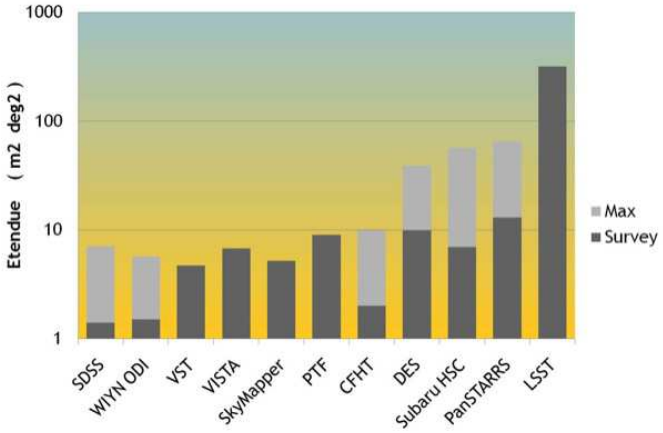

Figure 2.3 – Comparison of the étendue for several surveys (source `www.lsst.org`).

seen as the rate at which a survey is able to observe sources at a given depth. With an étendue of 319 $\mathrm{m}^2\,\mathrm{deg}^2$, LSST clearly oversteps all current surveys by at least one order of magnitude as shown on Figure 2.3.

LSST camera

The camera built for LSST is a 3.2-Gigapixel prime focus digital camera, the largest digital camera ever constructed (see Figure 2.4). The focal plane is flat, about 64 cm large, consisting of a mosaic of 16-Megapixel $> 75\,\mu$m-thick silicon detector, which allow the detection of near-infrared photons. It includes a shutter and a filter changing mechanism.

Optical filters

The survey will yield contiguous overlapping imaging of over half the sky in six broad optical bands *ugrizy*, whose raw bandpass is plotted on Figure 2.5 versus the wavelength, together with the instrument (or system) bandpass, which is the convolution of the filters bandpass with the quantum efficiency of the camera and the transmittance of the optics. As mentioned earlier, the thickness of the silicon detectors allows for near- infrared photons to be detected, which is of great advantage for e.g. the computation of the photometric redshifts.

These bandpasses are also affected by atmospheric transmittance (not shown here). On this Figure, the y filters adopts the fourth design, which ends up hitting the atmospheric water vapor absorption lines (contrary to the $y3$ filter which avoided them), which has quite an impact on the LSST photometric calibration (*cf.* Chapter 3)

The values listed on Table 2.1 are 5σ depth in AB magnitudes, and correspond to point sources and zenith observations (about 0.2 mag loss of depth is expected for realistic airmass distributions) and the visits are expressed per sky location, which account for a total of nearly 1000 visits over the 10 years.

Quantity	u	g	r	i	z	y
Single visit depth	23.9	25.0	24.7	24.0	23.3	22.1
Average number of visits (10y)	56	80	184	184	160	160
Final (coadded) depth	26.1	27.4	27.5	26.8	26.1	24.9

Table 2.1 – LSST baseline imaging parameters. The depth are given in AB magnitude.

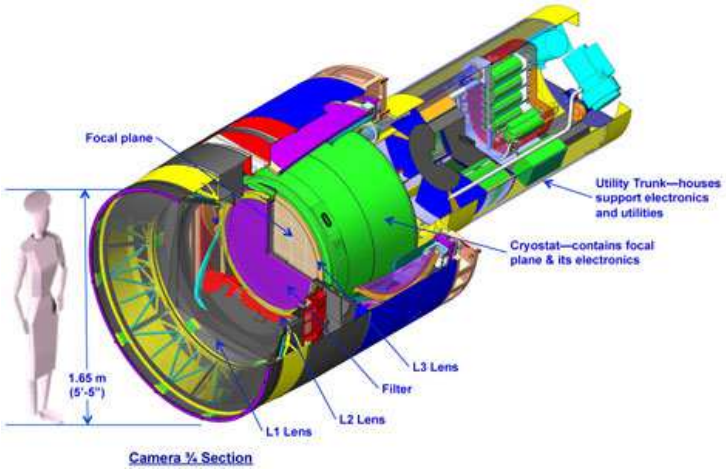

Figure 2.4 – LSST camera section (source `www.lsst.org`).

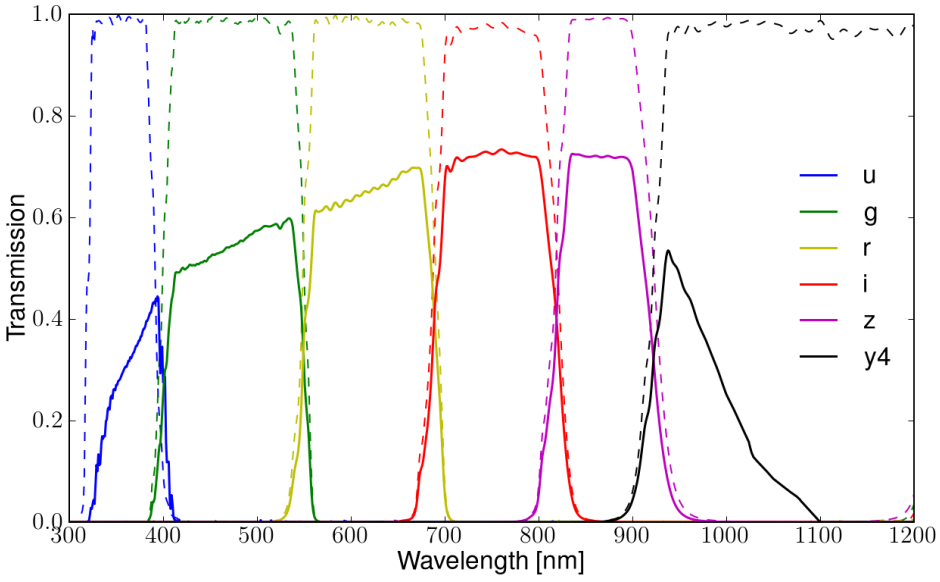

Figure 2.5 – LSST filter response as a function of wavelength. The dotted line show the raw filter transmission, while the solid line comprises the system response (mirrors + CCD quantum efficiency).

I.2 Science goals and requirements

The range of scientific investigations made possible by the LSST is extremely broad. Four main science themes have emerged from a report of the LSST Science Working Group:

1. Probing Dark Energy and Dark Matter
2. Taking an Inventory of the Solar System
3. Exploring the Transient Optical Sky
4. Mapping the Milky Way .

The LSST instrument shows an extreme adaptability to study a huge variety of objects, from stars to galaxy clusters, transients from asteroids to supernovæ, and scales from a few kiloparsecs (solar system) to cosmological scales, which we are mostly interested in. Each of these four themes itself encompasses a variety of analyses, with varying sensitivity to instrumental and system parameters, all done from the main survey mode.[1]

All these goals have set challenging requirements for the instrument and telescope, the most important concerning this thesis work being the photometric repeatability, which should achieve 5 mmag precision at the bright end, with zero-point stability across the sky of 10 mmag and band-to-band calibration errors no larger than 5 mmag. These requirements are driven by subjects like photometric redshift accuracy or the search for systematic effects in supernova light curves.

Two other requirements of interest for weak lensing studies are the coadded survey depth that should reach $r \sim 27.5$, with sufficient signal-to-noise ratio in other bands, and the distribution of visits on the sky that should reach at least $20\,000\,\mathrm{deg}^2$ to obtain the required number density of galaxies. A comparison of galaxy surveys doing weak lensing science is shown on Figure 2.6.

Last requirement mentioned here, the data processing, data products and data access that should efficiently respond to the huge load of information provided by the instrument. The working paradigm is that all scientific investigations will utilize a common database constructed from the main survey mode.

[1] 10 % of LSST observing time will be devoted to specifically selected fields, referred to as the « gold sample », in order to achieve a greater depth. This is called the deep drilling mode.

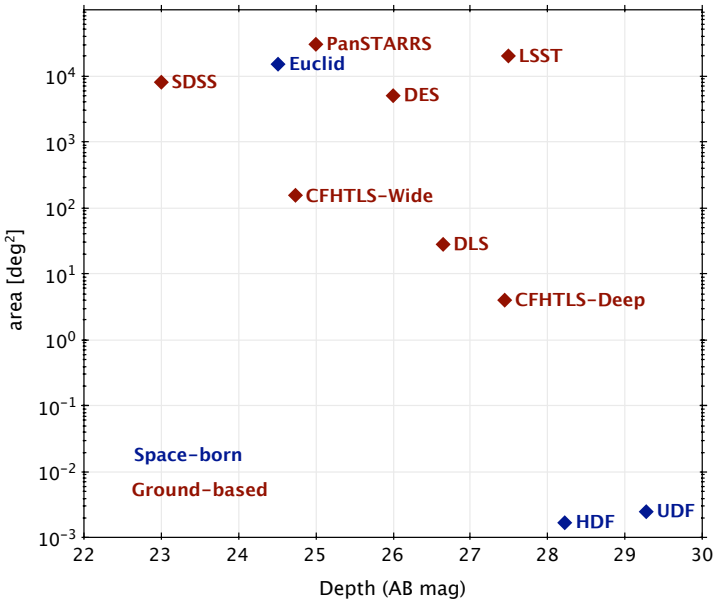

Figure 2.6 – Diagram of final survey area and depth of optical and near-infrared surveys mentioned in this thesis. The area axis is logarithmic.

I.3 Data products

Big data

The LSST camera will take a 15 second-exposure every 20 seconds for ten years, which accounts for over 200 000 pictures ($\simeq$ 1.3 Petabytes of raw data) a year undoubtedly more than what can be reviewed by humans. This is why the project puts a lot of efforts into the automated processes and in general data management. Managing and effectively data mining the enormous output of the telescope is expected to be the most technically difficult part of the project.

Initial computer requirements are estimated at 100 Teraflops of computing power (which is the equivalent of a 2011-like supercomputer), and 15 Petabytes of storage, rising as the project collects data. The reduced database will grow in size to about 30 Petabytes and 20 billion objects in ten years, and will include other metadata (parameter error estimates, system data, seeing summary, etc.).

Product types

As regards pure LSST data products, they are organized into two groups, mostly distinguished by the cadence with which they are generated.

Level 1 products are generated by a pipeline processing the stream of data from the camera system. These products are therefore being continuously generated and / or updated every observing night. This process is highly automated, and must proceed with absolutely

minimal human interaction. Level 1 data products are divided into *Images*, *Catalogs*, and *Alerts*. Periodically the accumulated nightly data products are processed and form the Level 2 products.

These Level 2 products, which include calibration images, co-added images, and the resulting catalogs, are generated on a much slower cadence, and their release will be driven by data quality assessments. Although many of the steps that generate Level 2 products will be automated, significant human interaction may be tolerated. The photometric calibration and specifically the *self*-calibration procedure, described in Chapter 3 will generate part of these products.

Level 2 products will be made publicly available through a yearly data release.

I.4 Project status (August 2013)

The LSST project is mostly supported by the National Science Foundation (NSF) and the US Department of Energy (DoE), as well as private fundings. On July 18, 2012, with approval of the National Science Board, the NSF announced its intention to advance the LSST to the final design stage. This action permits the NSF Director to include funds for LSST construction in a future budget request to US Congress. The project technology is ready for a construction start in fiscal year 2014 and awaits construction authorization.

II LSST-France

France, under the IN2P3[2] is currently involved in the LSST project with responsibilities concerning the camera development and the filter loader / carousel. IN2P3 is also part of the LSST Dark Energy Science Collaboration (DESC) regarding its science contribution to the forecast on dark energy probes and the improvement on photometric redshift techniques. Table 2.2 summarizes the participating French laboratories and their current related activities.

[2]Institut National de Physique Nucléaire et de Physique des Particules, French national institute for nuclear and particle physics

Laboratory	**Hardware**	**Science**
APC (Paris)	Camera Control System (+ filter changer module)	photometric calibration weak lensing magnification
CCIN2P3 (Lyon)	data center	
CPPM (Marseille)	filter auto-changer	joint constraints LSST + CMB synergy with Euclid
LAL (Orsay)	camera electronics	photometric redshifts
LMA (Lyon)	filter coating	
LPC (Clermont-Ferrand)	filter test unit PetaSky	supernovæ
LPNHE (Paris)	CCD camera (R&D + production) readout electronics filter carousel	supernovæ photometric redshifts
LPSC (Grenoble)	filter loader CCD test bench (CCOB)	photometric redshifts

Table 2.2 – LSST French participating laboratories and their current LSST-related activities (2013).

CHAPTER 3

Towards LSST photometry: calibrating atmospheric transmission effects

I Introduction

LSST novelty resides in the combination of impressive survey properties in terms of field-of view, area, depth or even cadence. The requirement to achieve a ground-based photometry to better than 1 % at such depths, even in non-optimal conditions, raises a challenge for the LSST calibration team, specifically when dealing with atmospheric variability. This goal has recently been achieved for optimally selected Sloan Digital Sky Survey data using the *Übercal* procedure (see Ivezic et al., 2007; Padmanabhan et al., 2008). But reaching the same uniformity for a wide-field camera in various atmospheric conditions still needs improvements in understanding and modeling the observation process.

In the past, precision photometry used to bypass these difficulties simply by limiting observations to narrow fields (and hence have a better control of signal distortions along the photon path in the instrument) and so-called « photometric nights ». These correspond to the nights when the distribution of atmospheric absorbers is smooth enough for their impact on photometry to be satisfactorily modeled by estimating a set of extinction coefficients, which variations along the night can be measured by dedicating part of the telescope time to monitoring a few reference stars. Also, the use of narrow-bandpass filters, which restricts the survey to very bright sources, helped minimize bandpass change effects due to the atmosphere transmission spectrum.

The ambition of large photometric surveys such as PanSTARRS (Kaiser et al., 2002), DES (Flaugher, 2005) or LSST invites us to define new calibration strategies. The LSST baseline strategy to achieve its goals is based on three main blocks,

- the instrument design and calibration,
- the auxiliary telescope and the plan to use an atmosphere transmittance models that breaks down the transmission spectrum into its well identified main physical components,
- the *self*-calibration.

Our contribution to the collaboration has consisted of providing a validation tool to test and optimize the calibration process under the whole variety of atmospheric conditions likely to prevail during the many years of LSST operations. This includes compiling existing data on the most critical atmospheric constituents and establish statistics on their time and space variability at Cerro Pachón , evaluating the photometric impact on calibration for flux and bandpasses, and producing an atmosphere simulator that reproduces the measured variations over long periods (up to 10 years), in order to validate the chosen calibration strategies.

I.1 Basic concepts

I.1.1 From fluxes to magnitudes

A ground-based photometric telescope like LSST records the flux F_b^{obs} received from sources in a given filter (or bandpass) b (*ugrizy* in the case of LSST). This process is described by the equation

$$F_b^{obs}(t) = \int_0^\infty F_\nu(\lambda, t)\, \phi_b^{obs}(\lambda, t)\, \mathrm{d}\lambda \,, \tag{3.1}$$

where $F_\nu(\lambda, t)$ is the true source spectral energy distribution (hereafter SED), which can be variable in some cases, weighted by the normalized system response function $\phi_b^{obs}(\lambda, t)$ that accounts for the atmosphere as well as the full system. The latter is defined as

$$\phi_b^{obs}(\lambda, t) \equiv \frac{T_b(\lambda, t)\, \lambda^{-1}}{\int_0^\infty T_b(\lambda, t)\, \lambda^{-1}\, \mathrm{d}\lambda} \,, \tag{3.2}$$

where $T_b(\lambda, t)$ is the system response at t and λ^{-1} accounts for the conversion of energy per unit frequency into the number of photons per unit wavelength. Astrophysicists use magnitudes instead of fluxes for convenience. We define the natural magnitude in bandpass b as

$$m_b^{nat} \equiv -2.5\, \log_{10}\left(\frac{F_b^{obs}}{F_{AB}}\right) \,, \tag{3.3}$$

where $F_{AB} = 3631\,\mathrm{Jy}$ is a standard flux defined in Oke & Gunn (1983).

Assuming a source has no spectral variation in time $F_\nu(\lambda, t) = F_\nu(\lambda)$, we need to be able to provide a standard flux F_b^{std} for that source. We therefore introduce the standardized bandpass response function $\phi_b^{std}(\lambda)$, that represents the typical hardware and atmospheric transmission curve, computed via a so-called *standardization procedure*.

$$F_b^{std} = \int_0^\infty F_\nu(\lambda)\, \phi_b^{std}(\lambda)\, \mathrm{d}\lambda \,, \tag{3.4}$$

and its associated standard magnitude

$$m_b^{std} \equiv -2.5\, \log_{10}\left(\frac{F_b^{std}}{F_{AB}}\right) \,. \tag{3.5}$$

I.1.2 The standardization procedure

Calibration is an iterative process comparing measured data with a set of standard sources to retrieve deviations from a zero-point in time, space and wavelength. As set in the requirements, the photometric calibration procedure must ensure the magnitude (or flux) deviations for a given

object do not exceed a certain value, under every condition of observation.

Measuring the accuracy of a flux measurement requires the knowledge of the initial source flux. In astronomy, we use celestial stellar sources with *hopefully* well-understood spectral energy distributions (SEDs), as calibration standards. There will be more than a hundred main-sequence stars with $17 < r < 20$ per LSST detector ($14' \times 14'$) to this end (Ivezic et al., 2008b). During the commissioning period, these calibrated sources will be visited often and the flux measurements taken during this period will be averaged out to create standardized measurements for each bandpass: ϕ_b^{std}.

These standard bandpass response functions will then be used to characterize the observed bandpass of every single observation. In terms of magnitudes, this can be written as

$$m_b^{nat} = -2.5 \log_{10} \left(\frac{F_b^{obs}}{F_b^{std}} \times \frac{F_b^{std}}{F_{AB}} \right) \tag{3.6}$$

$$= \Delta m_b^{obs} + m_b^{std} , \tag{3.7}$$

where the bandpass deviation is

$$\Delta m_b^{obs}(t) = -2.5 \log_{10} \left(\frac{F_b^{obs}(t)}{F_b^{std}} \right) \tag{3.8}$$

$$= -2.5 \log_{10} \left(\frac{\int_0^\infty F_\nu(\lambda)\, \phi_b^{obs}(\lambda, t)\, \mathrm{d}\lambda}{\int_0^\infty F_\nu(\lambda)\, \phi_b^{std}(\lambda)\, \mathrm{d}\lambda} \right) . \tag{3.9}$$

We should also mention two useful magnitudes for calibration

- m_b^{inst}, the instrumental magnitude. This number is directly related to the number of instrumental counts C_b^{obs} in a given exposure time, attributed to the object: $m_b^{inst} = -2.5 \log_{10} \left(C_b^{obs} \right)$,
- m_b^{corr}, the SED corrected instrumental magnitude.

These magnitudes are related to the previous mentioned through

$$m_b^{corr} = m_b^{inst} - \Delta m_b^{obs} \tag{3.10}$$

$$m_b^{std} = m_b^{corr} + Z_b^{obs} \tag{3.11}$$

where Z_b^{obs}, the zeropoint correction in bandpass b, contains gray-scale normalization effects (flat-field or cloud extinction).

I.1.3 The system response function, T_b

The system response function can be seen as the probability that a photon with a given wavelength λ, reaching the top of the atmosphere, will be recorded by the system in bandpass b. The instrumental response and the atmosphere transmittance are uncorrelated, since the reflect properties of completely independent systems. Hence these two main features can be treated separately

$$T_b(\lambda, t) = T^{atm}(\lambda, t) \times T_b^{instr}(\lambda, t) \ , \tag{3.12}$$

where T^{atm} is the dimensionless optical transmittance from the top of the atmosphere to the telescope pupil, and T_b^{inst} is the instrumental system response, also referred to as the instrumental throughput.

The decomposition into simple spectra in equation (3.12) is clearly insufficient to match the required standards of today's calibration precision. Particularly in a wide-field telescope like the LSST, the variations with time and position on the sky and on the detector of both transmission functions need to be tackled. The best way to do that is to use dedicated instrumentation to disentangle effects that have different dependencies. Those spectra become then measured quantities with added complexity: S_b^{instr} and S^{atm}.

Instrumental system response, S_b^{instr}

A wide field-of-view enables photons to come from multiple directions and hit the detector under a wide variety of angles. Second, a large collecting surface (or focal plane) means additional difficulties in getting uniformity across the full area. Therefore, the measured instrumental response is a function of time and source position on the detector

$$S_b^{instr}(x, y, t, \lambda) \ , \tag{3.13}$$

where x and y are the coordinates on the focal plane, t is the time and λ the wavelength. This throughput function includes the reflectivity of the mirrors, the transmission of refractive optics and filters, the quantum efficiency of the camera detectors and the gain and linearity of the read-out electronics.

The measurement of this function mixes sky flats taken from the twilight sky or stacks of images taken through the night, and dome flats acquired using a well-controlled diffuse light from artificial illumination. The outcome is the so-called « flat field », the true instrumental normalization as for science exposures.

Finally, the dust accumulating on the optics along the surveys duration has to be accounted

for in the total throughput. But the size of the particles and the fact they are out of focus makes their effect independent of wavelength or *gray*. Daily checks with a monochromatic source will be used to measure those changes in the system bandpass.

These instrumental effects are of small amplitude and can generally be corrected with a percent-like accuracy. This is not the case for the atmospheric transmittance which can vary way more rapidly in time and amplitude.

Atmospheric transmittance, S^{atm}

The atmospheric transmittance depends on the properties of the atmosphere at the time and in the direction of the pointing and thus can be expressed through the function

$$S^{atm}(alt, az, t, \lambda) \, , \tag{3.14}$$

where alt and az are, respectively, the altitude and azimuth of the pointing, t is the time and λ the wavelength. The measure of that transmittance will be described in details in the following subsection.

I.2 LSST baseline approach for the calibration of atmospheric effects

I.2.1 Calibration procedure

The overall photometric calibration procedure of LSST can be decomposed into three main steps. The first one is a nightly calibration that will try and estimate in real time the transmittance across the atmospheric layer in the telescope field at the ultimate precision, the resulting magnitudes will thus be obtained in a changing system. Then, a long-term process referred to as *self*-calibration which will homogenize all individual measurements in a single average system. Then a final color and flux calibration will bridge measurements in the average system to absolute physical units.

Real-time calibration

LSST will calibrate the data on a nightly basis. Real-time calibration based on the best available priors will thus be carried on to provide Level 1 Data Products (that come with a lower performance in precision and accuracy than released data). This will mainly be done using the auxiliary telescope and/or every other device able to, and will be discussed in the next subsection.

The *self*-calibration

The *self*-calibration is method based on the « Übercal » procedure developed for SDSS (Ivezic et al., 2007; Padmanabhan et al., 2008) whose purpose is to minimize the error dispersion in all observations and for all reference stars.

The idea is to gather a massive number of calibration stars, selected for their non-variability and as main-sequence stars, into a standard catalog. The main assumption under the star selection is that their SED can be inferred from multicolor photometry and that we can obtain their true magnitude by bootstrap from many difference observations. First, we use the standard bandpass response function $\phi_b^{std}(\lambda)$ computed during commissioning to produce a standardized magnitude m_b^{std} for all these calibration stars, denoted i. Second, we split the focal plane into small patches p, the size of a CCD detector. After a running period, each calibration star will have been observed many times in every patch, and the procedure can start.

The self-calibration procedure minimizes the difference between the standardized magnitude and the model magnitude

$$\chi_b^2(p) = \sum_{(i,j)} \left(\frac{m_{b,i,j}^{std} - m_{b,i,j}^{model}(p)}{\sigma_{b,i,j}^{std}} \right)^2 , \tag{3.15}$$

where the model magnitude is derived from the best-fit magnitude of the calibration star and a model describing how we expect the magnitude to vary from one observation to another. The simplest model consists of a normalization constant per patch, which is nothing but a zeropoint offset δZ_b.

$$m_{b,i,j}^{model}(p) = m_{b,i}^{best} + \delta Z_{b,j}(p) \tag{3.16}$$

While i denotes the stars, j stands for the exposures. There will be approximately a hundred million bright stars observed repeatedly during the survey operations. The relative errors $\delta Z_{b,j}(p)$ will then be used to correct the photometry for all other sources in patch p, on image j.

This is the calibration process that has to meet the survey requirements for photometric repeatability, uniformity and accuracy. But to start being efficient, the *self*-calibration procedure requires enough data, and will need a running period of the order of a year. LSST survey data will be made publicly accessible through periodic releases, for which the accumulated data of the last release will be entirely reprocessed by the self-calibration in addition to the new data acquired in between.

Absolute calibration of colors and fluxes

Once the color zero-point has been determined for each filter (after the *self*-calibration), we have to care about the calibration between colors. The idea is to bring the overall photometric calibration down to one single value, the value of the zero-point in one single filter. LSST reference filter is the r-band. Then we compute the zero-point difference with respect to that value,

$$Z_b = Z_r + \Delta_{b-r} \ , \tag{3.17}$$

where Z_b is the zeropoint of the standard bandpass b and Δ_{b-r} is the computed difference of zero-points between bandpasses b and r.

Then, when the bandpasses are inter-calibrated, with the absolute calibration down to the parameter Δ_r, one needs to relate this value to a physical quantity to achieve the absolute flux calibration.[1]

I.2.2 Spectral dependence

Based on the idea that at least on small scales and short time scales, the physical properties (molecular composition, granularity of particles, etc.) do not change, we admit that atmospheric transmission can be decomposed into the product of a wavelength independent part (also called « gray ») mainly caused by the cirrus clouds and a wavelength dependent one (here « non-gray ») made up of the absorption and diffusion lines of atmospheric components

$$S^{atm}(alt, az, t, \lambda) = S_g^{atm}(alt, az, t) \times S_{ng}^{atm}(alt, az, t, \lambda) \ . \tag{3.18}$$

The baseline assumption is that the gray contribution varies in short time and spatial scales (even shorter than the interval between two exposures) whereas the non-gray function varies quite slowly and on larger scales.

The gray extinction, S_g^{atm}

The gray extinction is measured directly on the LSST image by comparing the measured fluxes of reference stars over many observations. Because reference stars are scattered across each image, what we actually measure is a discretized map of the gray extinction. The density of reference stars then determines the angular scale of the smallest detectable features of gray extinction. One issue of great concern is to accurately model the cloud structure function to determine whether the discretized gray map is sampled enough to give a realistic extinction at

[1] Basically this means we have to relate Δ_r to the standard flux F_{AB} from equation (3.5). This process needs therefore to have identified a few celestial standards which has not been achieved yet.

any location on the image via interpolation. We have hints[2] that the cloud power spectrum gets weak on angular scales of less than $10'$.

The wavelength dependent transmission, S_{ng}^{atm}

LSST design plans to use a dedicated auxiliary telescope, located very close to the main one at Cerro Pachón , to make spectroscopic measurements of a small set of « probe » stars during the night and establish the spatial and temporal variations of the atmospheric extinction. These probe stars are selected to cover the overall survey area. It is not necessary to know the spectral energy distribution of those stars prior to the survey as it will be easily bootstrapped from many observation on differing nights. This is basically the same for the the instrumental response of the spectrograph on-board the auxiliary telescope. It will then use the latest atmospheric models (see Stubbs et al., 2007; Burke et al., 2010) and a radiative transfer code, MODTRAN 5, to accurately determine the contribution of the main atmospheric components in the spectra as a function of time and airmass. The slow varying assumption enters here and allows atmospheric transmission at a given pointing direction $S^{atm}(alt, az, t, \lambda)$ to be interpolated from the measured data.

I.2.3 Atmospheric model

The atmosphere is a complex gaseus medium with a lot of constituents which interact with the light, mainly via absorption or scattering. There are the molecules, which absorb some of the incoming radiation to operate a transition (rotational, vibrational, or an electronic transition), and can also scatter the light depending on their size along with other particulates. This processes induce an partial or sometimes total depletion of the electromagnetic radiation at specific wavelengths. The atmosphere opacity as a function of the wavelength is shown in Figure 3.1. This illustration gives some insight about the difficulty of detecting the electromagnetic radiation from the Earth's surface under a standard atmosphere. For that reason, the ground-based surveys aimed at detecting direct light from the cosmos are mostly in the visible or in the radio domain (or in very small windows e.g. in the infrared). Any other wavelength range is vain or needs to be detected undirectly after the radiation interaction with the atmosphere, like the showers of particles produced by high-energy cosmic rays.

In the visible domain, the molecular absorption is due to water vapor, ozone, and has a more negligible contribution from dioxygen and trace elements as shown in Figure 3.2. The respective contributions of the constituents are plotted separately in the wavelength range corresponding to that of LSST. Molecular absorption spectra are very stable and can be tuned with

[2]This is currently under investigation

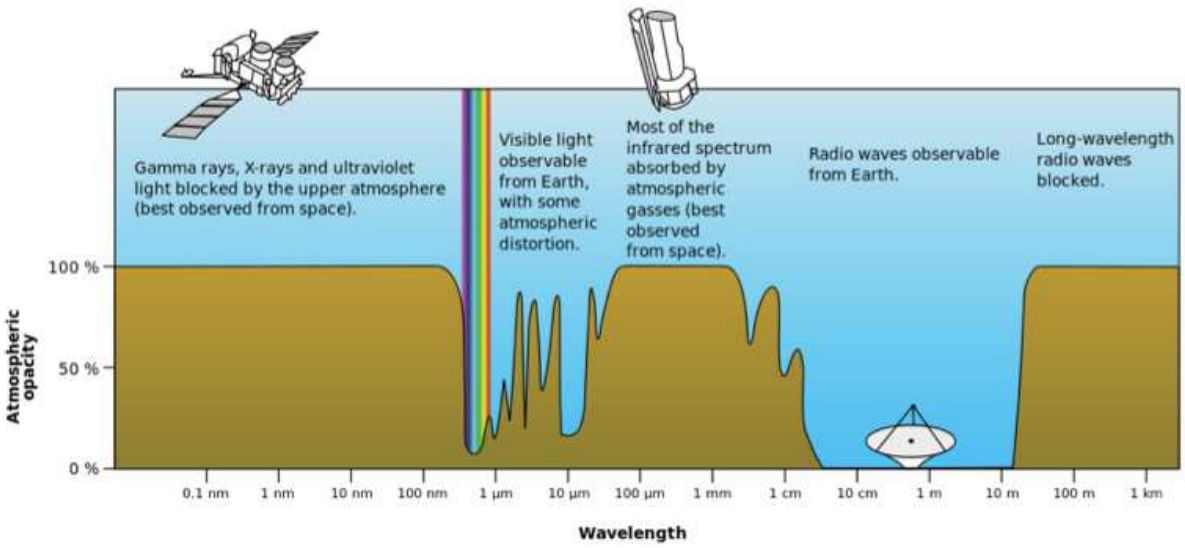

Figure 3.1 – Earth's atmosphere opacity as a function of the wavelength (credit NASA).

a simple amplitude factor given by the quantity of the constituent in the atmosphere in the line of sight.

Molecular oxygen, nitrogen and trace elements, represented in black, are fully mixed gases, and their total vertical column height is determined by the barometric pressure. Ozone, being situated in the stratosphere does not scale with barometric pressure but is known to be a slowly varying constituent, monitored on a daily basis by satellites. The spectral response of ozone has a simple shape (plotted in green) and depends on the height of the ozone column, which is measured in Dobson units. Concerning water vapor, as we deal in this context with an integrated process along the line of sight, we will describe it in terms of *precipitable water vapor* , which is the depth of water in the column of atmosphere if all the water in it were precipitated (in rain), and is measured in millimeters. Water vapor spectral shape (shown in blue) is rather complex, but accurately computed with MODTRAN, especially when dealing with vapor saturation.

Another light attenuation feature comes from the scattering of photons by atmospheric particles. We can already distinguish between the two types of scattering occurring:

– *Rayleigh scattering* when the particle size is much smaller than the radiation wavelength,

– *Mie scattering* for particles the size of the wavelength.

Rayleigh scattering, also known as molecular scattering, produces a strong light attenuation towards the UV spectrum. A standard spectral extinction curve is also displayed in red on Figure 3.2, under the label *mol. scattering*. Again the spectral shape is well-defined and

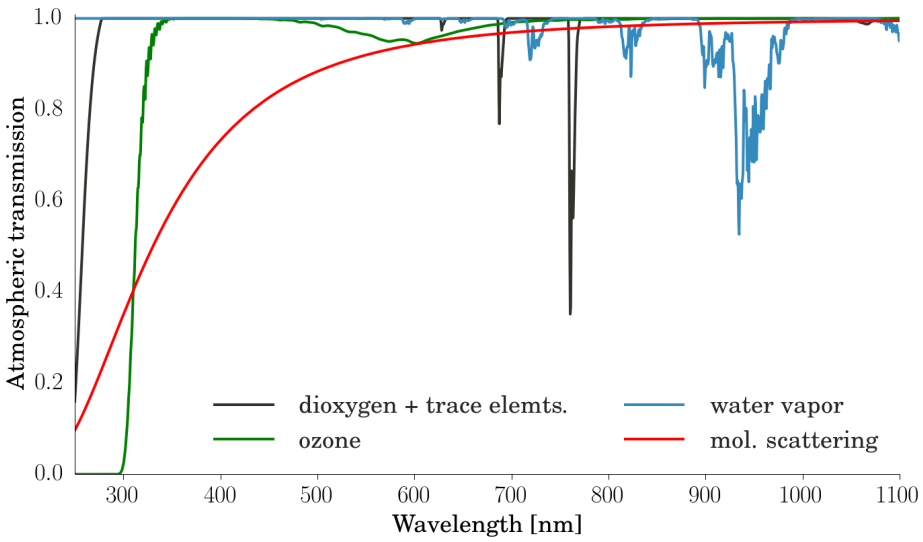

Figure 3.2 – Standard molecular absorption and scattering spectra, in the visible domain, computed using MODTRAN in the 1976 U.S. Standard option.

varies smoothly. It scales with the total molecular column thickness, which is proportional to the barometric pressure.

Mie scattering deals with macroscopic (micron-sized) particles more commonly referred to as aerosols. They gather constituents like dust (sand, volcanic), sea salt, smoke, small ice crystals, etc., that come in a variety of shapes and sizes, all of the order of the optical wavelength. That variety produces strong and not easily predictable spectral variations. Unlike molecules producing Rayleigh scattering which can always be found in the atmosphere, aerosols have a vagabond nature, being spread from specific spots all around the globe by winds. They are therefore erratic and must be precisely monitored because of their strong spectral dependence.

LSST baseline atmospheric model

The atmospheric model currently used by the LSST collaboration is described in Burke et al. (2010). This tranmission model assumes the atmospheric transmission spectrum has a well defined shape, which can be decomposed into the spectral transmission of its major components, and scaled with their absolute quantity, as described above. The full transmission spectra can

therefore be written as a product of all the contributions

$$\begin{aligned} S_{\rm fit}^{atm}(alt, az, t, \lambda) = T_{\rm gray}\ &\exp\left(-z(alt)\,\tau_{\rm aer}(alt, az, t, \lambda)\right) \\ &\times \left(1.0 - C_{\rm mol}\,({\rm BP}(t)/{\rm BP}_0)\,A_{\rm mols}(z(alt), \lambda)\right) \\ &\times \left(1.0 - \sqrt{C_{\rm mol}\,{\rm BP}(t)/{\rm BP}_0}\,A_{\rm mola}(z(alt), \lambda)\right) \\ &\times \left(1.0 - C_{\rm O_3}\,A_{\rm O_3}(z(alt), \lambda)\right) \\ &\times \left(1.0 - C_{\rm H_2O}(alt, az, t)\,A_{\rm H_2O}(z(alt), \lambda)\right). \end{aligned} \tag{3.19}$$

In the right order we have

- the gray extinction coefficient $T_{\rm gray}$,
- the airmass of the pointing z,
- the aerosol optical depth $\tau_{\rm aer}$,
- the barometric pressure BP and its local reference value ${\rm BP}_0$,
- the attenuation coefficients A_i (1.0 - transmission),
- the fitting coefficients C_i which basically scale as the constituent amount.

The subscript « mols » refers to the Rayleigh scattering while « mola » account for the molecular absorption lines of oxygen, nitrogen and other trace elements, which scale with barometric pressure, and whose quantity is represented by $C_{\rm mol}$.

With such a model and provided that these constituents do not vary extensively over the night, spectrophotometric observations of stellar references over the course of the night using an auxiliary telescope are used to fit the C_i coefficients. These coefficients are allowed to have a basic spatial dependence as for the water vapor one

$$C_{H_2O}(alt, az, t) = C_{H_2O}(t) + \frac{{\rm d}C_{H_2O}}{{\rm dEW}}\,\Delta{\rm EW} + \frac{{\rm d}C_{H_2O}}{{\rm dNS}}\,\Delta{\rm NS} \tag{3.20}$$

that has a normal variation in time $C_{H_2O}(t)$ and two spatial gradients in the north-south (NS $= \cos(alt)\cos(az)$) and east-west (EW $= \cos(alt)\sin(az)$) directions ; or for the aerosol optical depth

$$\tau_{aer}(alt, az, t, \lambda) = (\tau_0 + \tau_1\,{\rm EW} + \tau_2\,{\rm NS})\left(\frac{\lambda}{\lambda_0}\right)^{\alpha} \tag{3.21}$$

where the Ångström exponent α is a constant value at a given time but can slightly evolve over the course of the night.

This atmosphere component decomposition has been test by David Burke and associates against some spectrophotometric observations, obtained during a series of campaigns at CTIO (see Burke et al., 2010). These observations give good evidence that the combination of spectrophotometric observations of bright reference stars using a telescope the size of the planned auxiliary telescope with the use of the above described model, offers a monitoring of spectral atmospheric extinction which matches, in order of magnitude, most requirements for LSST photometry. This test is however limited to the diversity of atmospheric conditions encountered during the observing runs, most being under favorable atmospheric conditions.

It is the main motivation of the present analysis, first to gather every available piece of information relevant to atmospheric conditions likely to prevail at Cerro Pachón over the several years of a complete LSST campaign, second to build an atmosphere simulator able to mimic at all useful scales in time and space the detailed variations of transparency (including its spectral variability), then to use these simulated conditions to validate the calibration strategy, optimize its use and possibly propose improvements.

I.3 Simulating atmosphere extinction to test all weather calibration

For decades, astronomers have separated the nights in two very simple categories, photometric nights on the one hand, and non-photometric nights on the other hand. A night is considered photometric when the homogeneity of the atmospheric constituents allow for a linear reconstruction of atmospheric extinction with airmass using a few measurements over the night, which can then be extrapolated to a null airmass, otherwise called « above the atmosphere ». Therefore non-photometric nights are those which bear a rather non- homogeneous atmosphere. The photometric night ratio varies between sites and is sensitive to events like volcanic eruptions, but on average on is around 70 % of the time for good observation sites.

We entered recently in an era where astrophysics and cosmology meet to create and develop ground-based projects that cover over half of the observing sky while going to very faint magnitudes. The design in terms of cost for these projects therefore requires a high observing cadence combined to a large primary mirror. The LSST bears such a design, and has adopted a particular observing strategy, acquire data every single night for ten years, and scanning the entire survey area every three nights. This raises some basic difficulties for LSST photometric calibration,

- 30 % of the data will be acquired during non-photometric conditions,
- the observing direction and airmass will vary constantly during the night.

In addition, the design requirement on the precision of the photometry has been set to 1 %, which, as we previously mentioned, has only been achieved in specific conditions. To address that challenge, the photometric calibration team must propose a very efficient calibration strategy. The determination of the atmospheric transmittance for every night is key in this case.

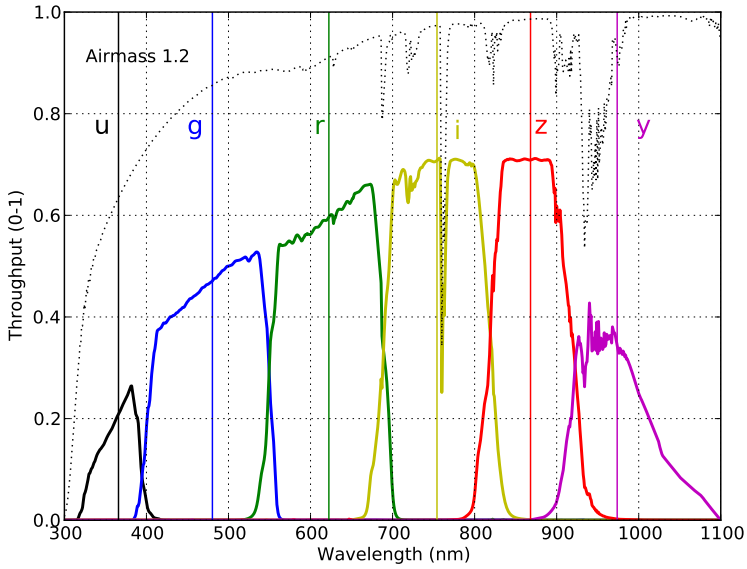

Figure 3.3 – LSST bandpasses with a standard atmosphere at airmass 1.2. The atmosphere transmission spectrum is shown in dotted line and each vertical line represents the median wavelength of the bandpass.

The current calibration strategy using an auxiliary spectrophotometric telescope, described in Section I.2.3, matches most of the LSST requirements but has only been tested on a limited number of nights, which cannot extensively sample the range of atmospheric conditions that occur in northern Chile in a 10-year period. Useful calibration simulations ought to include every effect likely to alter the precision of magnitudes ultimately tied to a uniform photometric system throughout the mission. This implies setting sufficient statistics of the critical time and amplitude scales of the variations of every atmospheric constituents in so far as they may impact the photometry, with special emphasis on those able to resist standard calibration procedures.

Furthermore, an atmosphere simulator, a realistic simulation of the atmospheric transmittance variability over long-periods of time based on the atmospheric components analysis will help determining the validity of the current atmospheric model[3] and will be useful to assess and possibly update the calibration strategy.

[3]coupled with an auxiliary telescope simulator, currently in an advanced stage of development

II Validating and optimizing calibration through atmospheric simulation

The novelty of the approach is such that the whole calibration scheme needs to be validated and optimized by extensive simulations, covering the whole diversity of atmospheric conditions prevailing at Cerro Pachón, in Chile.

For this purpose, we gathered realistic data to simulate space and time variation of the main contributors of the atmospheric extinction, exploring several sources of information (ground based, satellite, etc.) for each component. The general purpose being to

- establish robust statistics on atmospheric constituents able to significantly affect the photometry,
- investigate and point out possible improvements of the calibration tools that would bypass these effects when they cannot be treated using the baseline strategy,
- estimate from these statistics the relevant scales and variation periodicities and build a simulation whose goal is to evaluate the error propagation along the calibration pipeline.

II.1 Monitoring atmospheric components and impact on calibration

II.1.1 Ozone

Ozone (O_3) is a triatomic molecule far less stable than the common dioxygen molecule. It is produced in the upper atmosphere ($\sim 50\,\mathrm{km}$) via the photo-dissociation of the common molecular oxygen O_2 into oxygen atoms provoked by UV radiation or atmospheric electrical discharges. This process is followed by the combination of oxygen molecules and oxygen atoms to form O_3. A standard ozone spectral response computed using MODTRAN is shown in Figure 3.2. Atmospheric ozone concentrates in the stratosphere, forming the so-called *ozone layer* and acting as the principal UV-light shield for Earth. A small fraction of ozone also lies in the troposphere, closer to the ground as shown in the schematic atmospheric ozone profile on Figure 3.4. Figure 3.5a shows the worldwide ozone distribution on a typical daily northern winter situation. It gives a hint on the slow variability of ozone column in our latitude of interest. We will address in more details the ozone spatial variation in the specific region of Cerro Pachón in the Chilean desert (Figure 3.5b).

Temporal variability

The high altitude of the ozone layer is an advantage for space-born ozone mapping techniques,

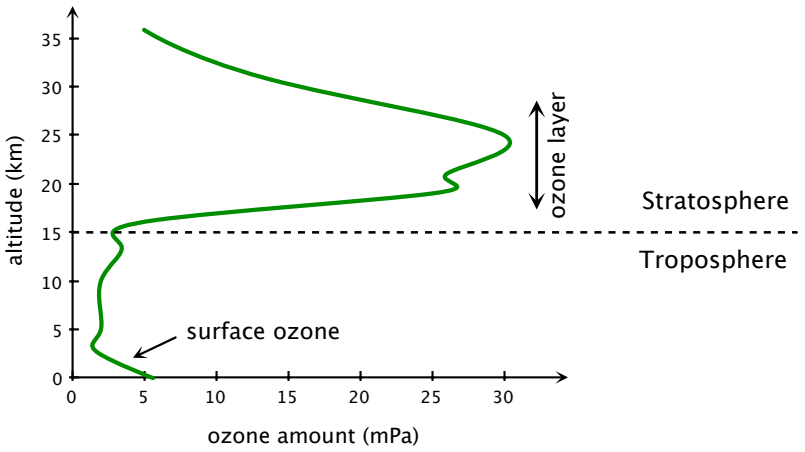

Figure 3.4 – Schematic view of ozone vertical profile.

preventing them from being affected by ground elevation. The Total Ozone Mapping Spectrometer[4] (TOMS) is an instrument installed onboard the NASA Earth Probe satellite (McPeters et al., 1998). TOMS monitored the total ozone column around the planet from 1996 to the end of 2005. It used backscatter ultraviolet light in six bands to compute the total amount of ozone in the column of air from the Earth's surface to the top of the atmosphere. The nine years of data covering the LSST site area are plotted on Figure 3.6a.

Despite a few gaps, TOMS data are dense enough to study day-to-day variations on the nine-year period of the experiment. The histogram of the daily variation for that period at Cerro Pachón is shown on Figure 3.6c. The median ozone density value is 275 DU, the standard deviation of the day-to-day variations is 12.64 DU, with 97 % of the measurements are below 20 DU and only two extreme values reaching 60 DU. From this, we conclude that using daily satellite measurements to correct observations for the ozone extinction would induce errors lower than 20 DU in the vast majority of cases (97 %), and up to a limit of 60 DU if a very few cases.

Spatial variability

TOMS data does not contain information about the spatial variations. However, more recently, stratospheric ozone has been mapped by the MODIS satellite[5]. MODIS, which stands for MOderate Resolution Imaging Spectroradiometer is an instrument onboard the NASA Terra and Aqua satellites. Its data is distributed free of charge through the NASA Level 1 and Atmosphere Archive and Distribution System (LAADS). It has a 5 km spatial ground resolution which is enough to interpolate between points and draw the 200 km × 200 km map of local atmospheric

[4] http://toms.gsfc.nasa.gov/
[5] `http://modis.gsfc.nasa.gov/`

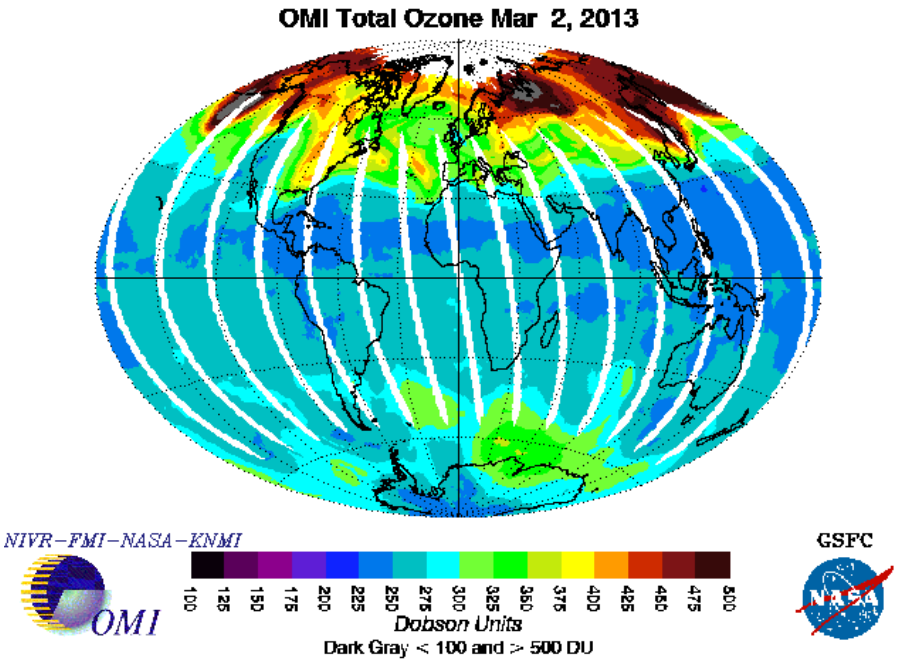

(a) Satellite based Earth coverage of ozone amplitude in a single day (credit NASA).

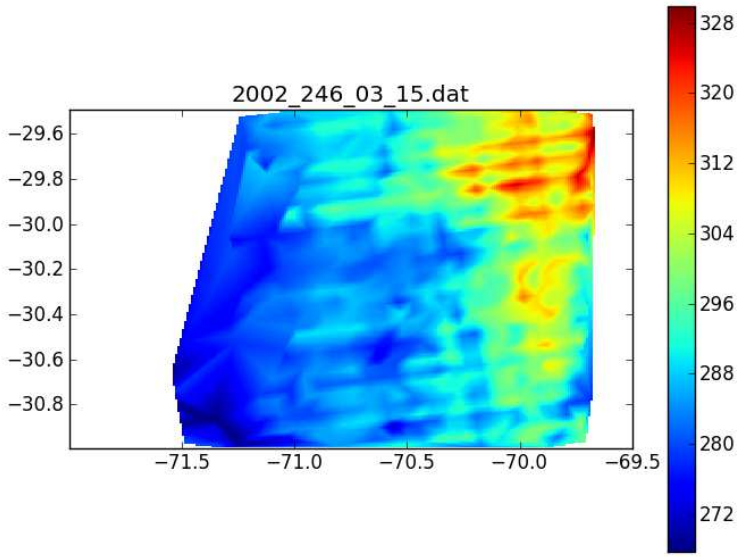

(b) Interpolated map of ozone amplitude extracted from MODIS data. The map is centered on Cerro Pachón , Chile. The scale is in Dobson units.

Figure 3.5 – Maps of ozone density around the globe and more specifically over LSST site.

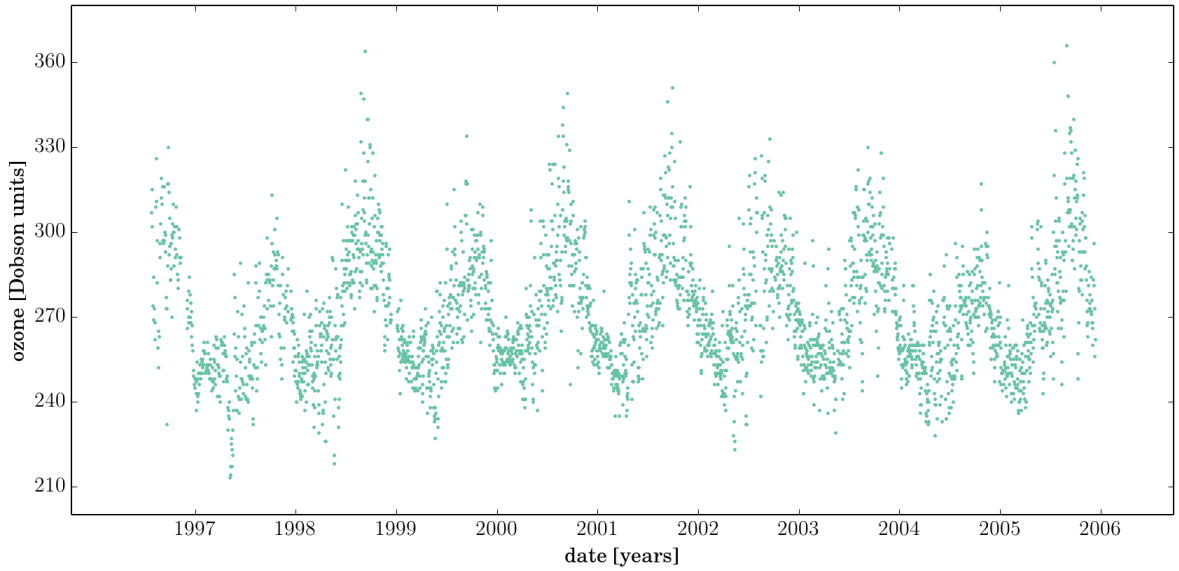

(a) Time-series of total ozone column.

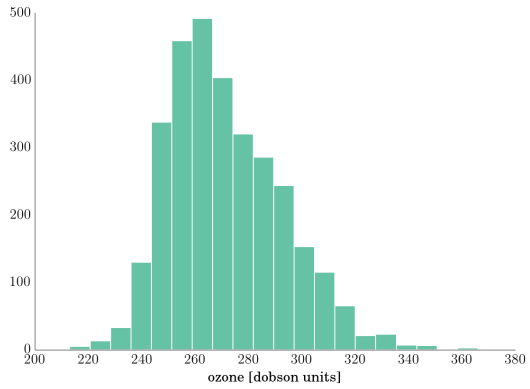

(b) Histogram of total ozone column.

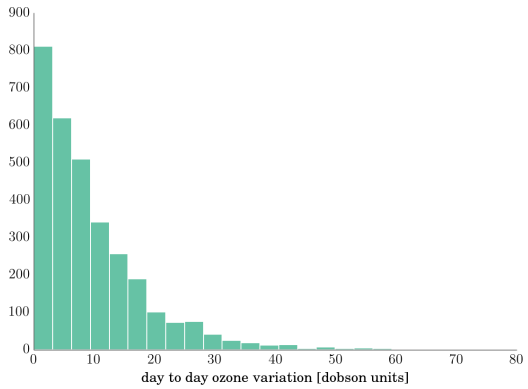

(c) Histogram of ozone column daily variations.

Figure 3.6 – Nine years of total ozone column measurements [1996–2005] over Cerro Pachón, from the space-born NASA Total Ozone Mapping Spectrometer (TOMS). Top panel shows the time-series, bottom left panel the corresponding histogram and bottom right panel the histogram of daily variations. The ozone column is expressed in Dobson Units..

properties centered on LSST.

An ozone map computed this way is shown on the bottom of Figure 3.5. As a matter of comparison on very large scales, the top figure shows an ozone map on globe. This latest figure there shows the ozone quantity quite constant on telescope latitudes. Now on the bottom close up to Cerro Pachón , the ozone deviations from the telescope location (central point) to any point under the telescope horizon (100 km) stay under 20 DU ($< 10\,\%$ variation). This is true for most of the maps that we studied, and consistent with the above-mentioned temporal

variations.

Source ID	**sp**	**g - i**	$\delta\mathbf{u}_{\mathrm{mmag}}$	$\delta\mathbf{g}_{\mathrm{mmag}}$	$\delta\mathbf{r}_{\mathrm{mmag}}$	$\delta\mathbf{i}_{\mathrm{mmag}}$	$\delta\mathbf{z}_{\mathrm{mmag}}$	$\delta\mathbf{y}_{\mathrm{mmag}}$
60 CYG	B1V	-1.47	1.5	1.8	6.0	0.9	0.2	0.0
HD 189689	B9V	-1.02	1.0	1.9	6.0	0.8	0.2	0.0
HD 191177	F4V	-0.31	0.8	2.2	5.8	0.8	0.1	0.0
HD 35296	F8V	0.03	0.9	2.3	5.8	0.8	0.1	0.0
HD 190470	K3V	0.63	0.8	2.6	5.7	0.8	0.1	0.0
HYAD 185		1.03	0.8	2.8	5.6	0.8	0.1	0.0
HD 132683	M0V	1.66	0.6	3.0	5.5	0.7	0.1	0.0

Table 3.1 – Impact of a 60 Dobson Units change in the LSST photometric bands. Each line represents the results for a calibration star with a different spectral energy distribution. The results are given in mmag.

Photometric impact of ozone errors

This ozone amount error can be converted into a natural magnitude error for various stellar sources. Source spectra are those of typical main sequence stars spanning a wide range of temperature. Stellar fluxes are taken from the observed spectrophotometric library of Gunn & Stryker (1983). Atmosphere spectra are computed using MODTRAN under standard conditions: mid-latitude, 2700 m ground altitude, moderate aerosols. A series of MODTRAN atmospheres differing only by the amount of ozone were produced. The stellar fluxes are split on 5212 *iso*-frequency bins, then multiplied by the atmosphere transmission and the various LSST filter system responses. The results are summarized in Table 3.1.

The natural magnitude errors computed in this work show non negligible values (6 mmag in the r-band) compared to the error budget of the calibration (< 10 mmag). However we must keep in mind these correspond to the worst case scenarios on the nine-year duration of the TOMS mission. Considering the standard deviation value instead of the maximum observed deviation, these magnitude errors are lowered by a factor of five, which is way more acceptable.

One can also consider the effect of the bandpass shape distortion, that is the magnitude error arising from the deviation from a standardized bandpass (here with a column of 170 DU) induced by ozone spectral features as a function of the ozone quantity. Such deviation computed using spectral distributions from three typical stars, is shown in Figure 3.7 for the first three bandpasses, the other three bands not being affected by ozone.

That analysis confirms that u, r and g-bands (cf. Figure 3.3) are the most affected by ozone, as we could have expected from the ozone spectral absorption curve seen on Figure 3.2.

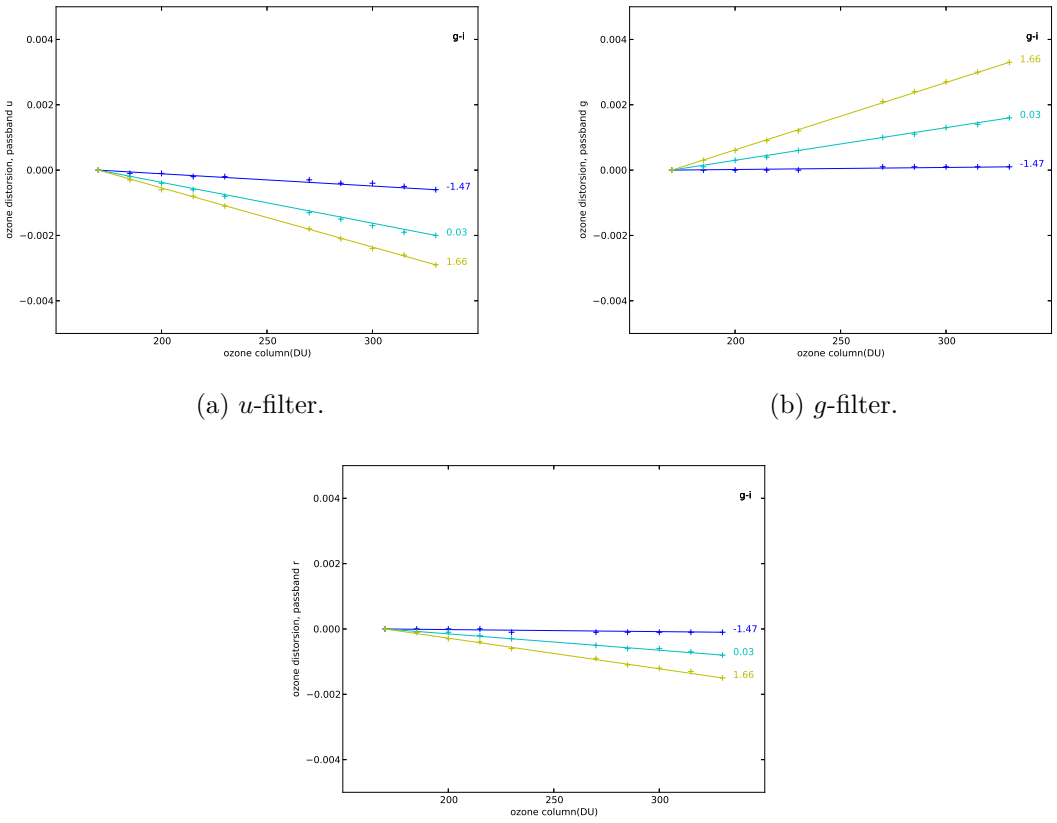

(a) u-filter.

(b) g-filter.

(c) r-filter.

Figure 3.7 – Errors in LSST magnitudes induced by a bandpass change (standard bandpass computed with 170 DU) as a function of ozone quantity. This result is computed in the most affected three bands. The different colors represent different stellar fluxes.

While the magnitude errors are non negligible for a rapid change in the total ozone column, time-series measurements rather point towards a smoothly varying ozone quantity from one day to another. The ozone constituent therefore seems « under control ». The last thing to verify is whether the ozone spatial repartition is homogeneous or not, which could affect the direction of observation.

Conclusion

The error made on the natural magnitude can be significant if the ozone quantity is not determined with precision. However, ozone being a high altitude atmospheric constituent, its temporal and spatial variability at the latitude of interest are slow enough to be well constrained using daily satellite monitoring and might even be better than the the corrections from spectroscopy alone. With that in mind, the error residuals coming from the bandpass shape distortion will also be negligible.

II.1.2 Water vapor

Water is one of the most common chemical on the planet. Water molecules mostly located in the lower part of the atmosphere – the troposphere – absorb the electromagnetic waves mostly in the microwave and radio domain, but also has very specific features in the visible spectrum. A standard atmospheric absorption curve for molecular water is shown on Figure 3.2. The intensity of absorption scales with the quantity of water up to a saturation point. The high spatial and temporal variability of water vapor is therefore a threat to precision photometry is not properly monitored.

Atmospheric water vapor monitoring can be achieved via satellite instruments, using the ground reflectivity to derive the water vapor column, and also with ground-based instruments such as a radiometer which measures the amount of water vapor in the line-of-sight using micrometer wavelengths, or a GPS station using wavelength dependent phase delay between GPS satellites. While space-born monitoring is ideal for the quick spatial coverage, it only provides a few measurements a day. Since water vapor is known to vary on short time-scales of the order of minutes, ground-based instrumentation can be used to probe the quick temporal variations. Concerning Cerro Pachón , we found no currently available ground-based data on water vapor, which placed our default choice to satellite. To confirm the high temporal variability of water vapor, the last paragraph before the conclusion of this section presents GPS data from a dry region of the United-States.

MODIS data

The longest and most recent dataset that regularly span the Chilean desert is again the MODIS instrument, which acquires up to two precipitable water vapor measurements a day since 2004. In order to create a water vapor time-series, we then have selected in each MODIS Chilean coverage the closest point to the LSST location. The histogram of computed values is presented on Figure 3.8, together with the histogram of the day-to-day variations. First thing to notice is that the region is very dry with a peak around 1 mm. The second thing is the day-to-day variation, which is low in absolute value, but become quite high considering the local values. This serves as a hint on the high variability on water vapor. However that data is too sparse in time to conclude anything, which calls for other sources of information on water vapor, in similar dry areas.

The major difference with ozone is that most of the precipitable water vapor content in the atmosphere stays very close to the ground. The instrument on-board a satellite measures the total water vapor column, integrated from the ground. However in such hilly regions as

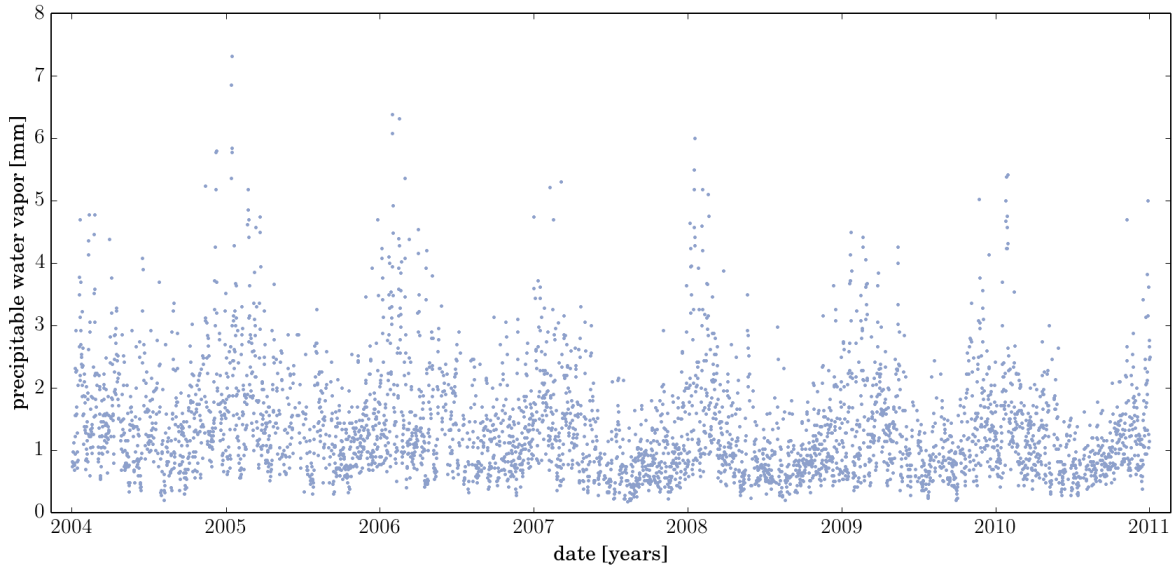

(a) Time-series of precipitable water vapor.

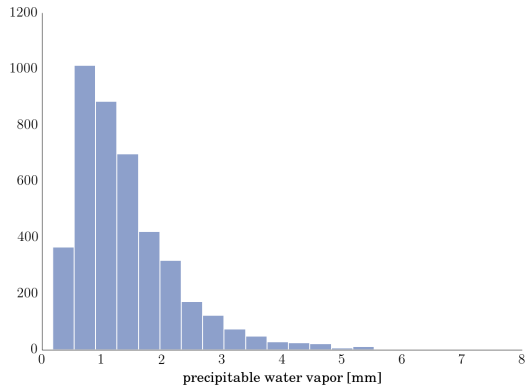

(b) Histogram of precipitable water vapor.

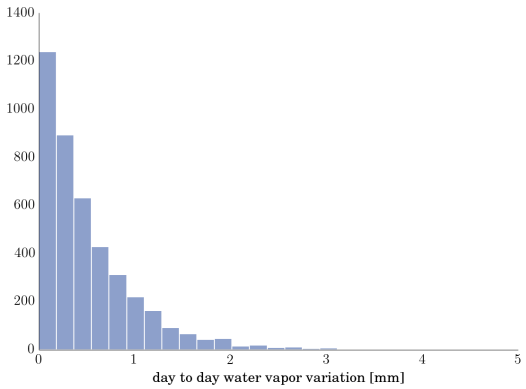

(c) Histogram of water vapor daily variations.

Figure 3.8 – Seven years of precipitable water vapor satellite measurements [2004–2011] from the MODIS instrument, selected over Cerro Pachón. Top panel shows the time-series, bottom left panel the corresponding histogram and bottom right panel the histogram of daily variations. The values are corrected for the elevation.

Chile, the ground elevation seen from a satellite is constantly changing, which means the water vapor measurements have to be corrected for the elevation (or rather the mean local elevation for MODIS, since the instrument has a 5 km ground resolution).

Line-of-sight reconstruction

Figure 3.9 shows an interpolated map of raw values of total precipitable water vapor columns from MODIS, superimposed with the terrain map of the region. We can see a clear water vapor gradient in the map. It is due to the local ground altitude gradient (from the Pacific Ocean to

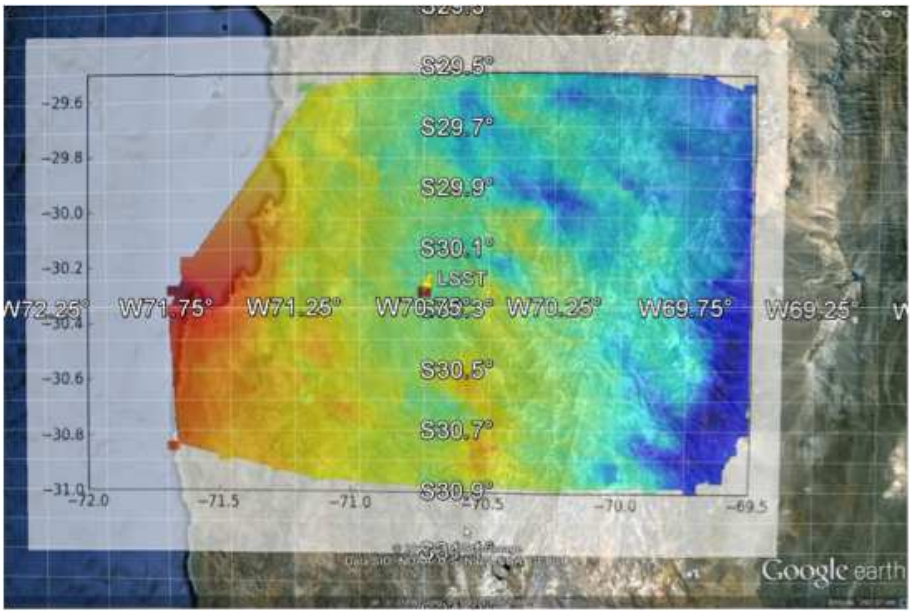

Figure 3.9 – Map of interpolated MODIS precipitable water vapor raw values, superimposed on a geographical map of region surrounding LSST site. The water vapor column values seem tightly correlated with the terrain altitude, indicating most of the atmospheric the water vapor lies in the lower atmospheric layer.

the Andes) not taken into account, which adds geographical variations to the precipitable water vapor measurements, while we want them at constant altitude.

For the mapping purpose, we define local coordinates, according to Figure 3.10. The origin O is centered on the telescope. The x-axis is pointed to the north and the y-axis to the west. while the z-axis indicates zenith. The observing direction is parameterized by the zenith angle ζ, the azimuth θ from x-axis, and the line-of-sight coordinate r, with its ground projection q. x and y ground coordinates are related to the geographic coordinates λ (longitude) and φ (latitude) by

$$\left| \begin{array}{l} x = r \sin\zeta \cos\theta = \kappa\,(\varphi - \varphi_0) \\ y = r \sin\zeta \sin\theta = -\kappa\,(\lambda - \lambda_0)\cos\varphi \\ z = r \cos\zeta \end{array} \right. \tag{3.22}$$

where $\kappa = 111.265\,\mathrm{km}$ is the distance corresponding to 1° of meridian circle.

MODIS Level 2 products, used in this analysis, give access to the longitude, latitude and ground elevation, in addition to the water vapor column. These informations allow us to construct for each acquisition a three-dimensional water vapor map

$$\sigma_{\mathrm{int}}(x, y, z) = \sigma_0(x, y)\, f(z)\,, \tag{3.23}$$

where $\sigma_{\rm int}$ denotes the depth of the integrated absorbing layer, σ_0 the volume density integrated over the vertical column, and $f(z)$ the vertical profile of precipitable water vapor in the region. The water vapor volume density ρ can then be expressed as

$$\rho(x,y,z) = \frac{\mathrm{d}}{\mathrm{d}z}\left[\sigma_{\rm int}(x,y,z)\right] = \sigma_0(x,y)\,\frac{\mathrm{d}f}{\mathrm{d}z}(z)\,. \tag{3.24}$$

Using the coordinate change (3.22), we can now express the water vapor column along the slant path for any observing direction (ζ,θ), integrating this volume density along r,

$$\sigma_{\rm int}(\zeta,\theta) = \int_0^\infty \mathrm{d}r\,\sigma_0(r\sin\zeta\cos\theta, r\sin\zeta\sin\theta)\,\frac{\mathrm{d}f}{\mathrm{d}z}(r\cos\zeta)\,. \tag{3.25}$$

Vertical profile

In order to reconstruct the vertical profile $f(t)$ at Cerro Pachón in each map, we use the diversity of MODIS measurements in the region. We plot the water vapor column versus the ground elevation and adjust a polynomial curve

$$f(z) = a_0 + a_1\,z + a_2\,z^2 + a_3\,z^3$$

to the data points. Since the vertical profile varies with the season, we applied the method selecting the data first to obtain fitting coefficients for each season (*cf.*Table 3.2, actually we consider fall = autumn). In this analysis we excluded data at low altitude not to be biased by measures above the Pacific ocean.

A given MODIS visit provides a set of discretized points on the map (x_i, y_i, z_i) along with a precipitable water vapor value σ_i. We use the determined vertical profile to correct these

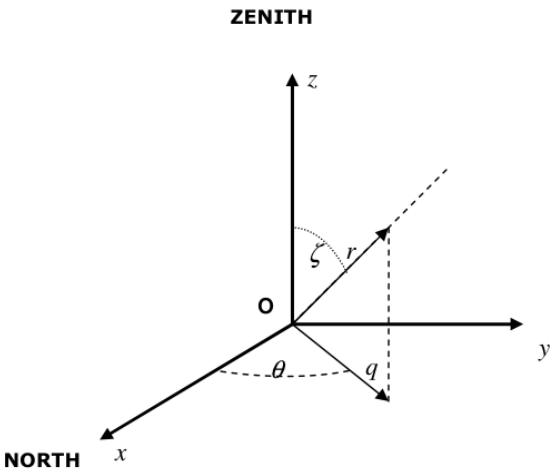

Figure 3.10 – Local coordinate basis.

Season	α_0	α_1	α_2	α_3	**stdev**
Summer	1.107	−0.576	0.020	−0.002	0.041
Fall	0.439	−0.494	0.002	−0.002	0.025
Winter	−0.196	−0.352	−0.041	0.001	0.025

Table 3.2 – Fitting coefficients for the water vapor vertical profile.

points to create an horizontal map at a given altitude z_0,

$$\sigma_i(x_i, y_j)|_{z_0} = \sigma_i \frac{f(z_0)}{f(z_i)} \tag{3.26}$$

Horizontal gradient features

We produced these horizontal maps of water vapor columns above the telescope altitude (2700 m) in a 100 km × 100 km area around the LSST site. On each map we estimate the slope and azimuth of the maximum precipitable water vapor gradients. This was achieved for one winter (dry) and one summer (wet) season, the results are presented on Figure 3.11.

The mechanism that enhances water vapor gradients appears quite plainly on these figures: masses of wet air migrate roughly along the West East axis enhancing the horizontal gradient. Gradients as high as 0.1 mm/km are not infrequent on such events (irrespective of the season). For each one of these observations we compute the total precipitable water vapor along slant observation paths at various zenith angles while fixing the azimuth so that equation (3.25) becomes,

$$\sigma(\zeta) = \int_0^\infty \mathrm{d}r \, (\sigma_0 + \alpha_x \, r \sin\zeta) \, \alpha_z \, e^{-\alpha_z \, r \cos\zeta} \,, \tag{3.27}$$

which integrates into

$$\sigma(\zeta) = \frac{1}{\cos\zeta} \left(\sigma_0 + \frac{\alpha_x}{\alpha_z} \, \tan\zeta \right) . \tag{3.28}$$

The second term of equation (3.28) is exactly the error we would make in an observation directed towards the maximum gradient by assuming that the water vapor column is in the whole area identical to that at its central point.

The amplitude of this effect is displayed in Figure 3.12. It shows that even at air masses not exceeding 2, the error made by using local axisymmetrical interpolations instead of measures along one specific direction may frequently be as large as 0.5 mm. It would be twice as much if the value measured in one direction is used in the opposite azimuth. Errors in the photometry may be as large as 10 mmag in the most sensitive filters. Furthermore these errors being both seasonal and affecting always the same azimuths may induce unfair systematics.

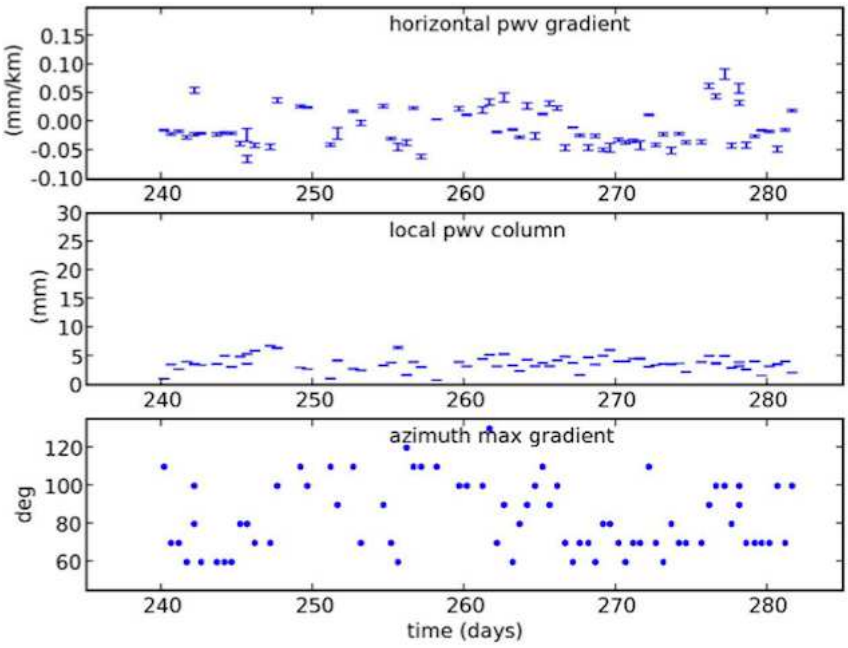

(a) Winter 2002.

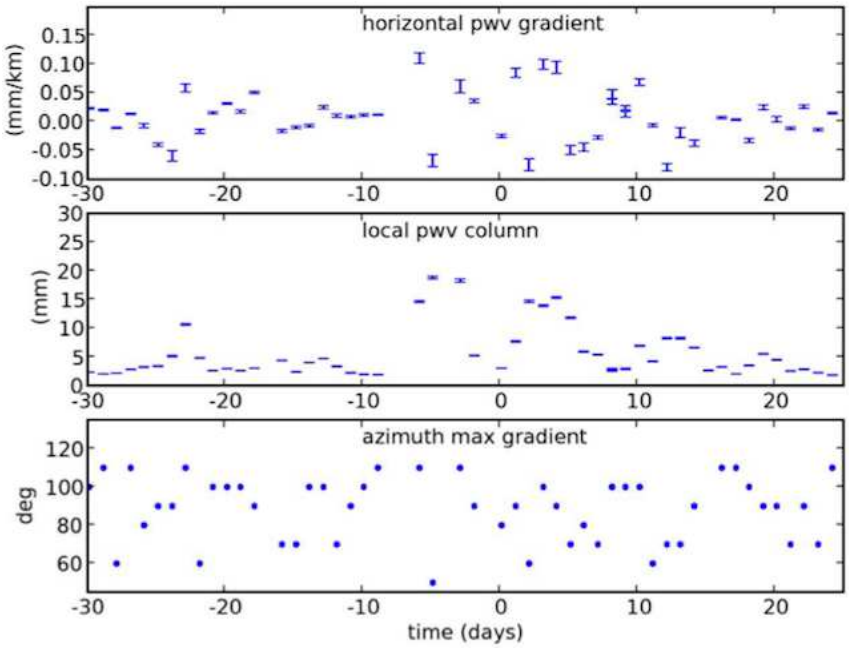

(b) Summer 2011-2012.

Figure 3.11 – Evolution of precipitable water vapor at Cerro Pachòn at two opposite seasons. Top plot is the horizontal precipitable water vapor gradient, middle plot shows the amplitude of the precipitable water vapor column above the telescope and bottom plot tells you about the direction of the biggest water vapor gradient. Abscissa shows days since 1st January 2012.

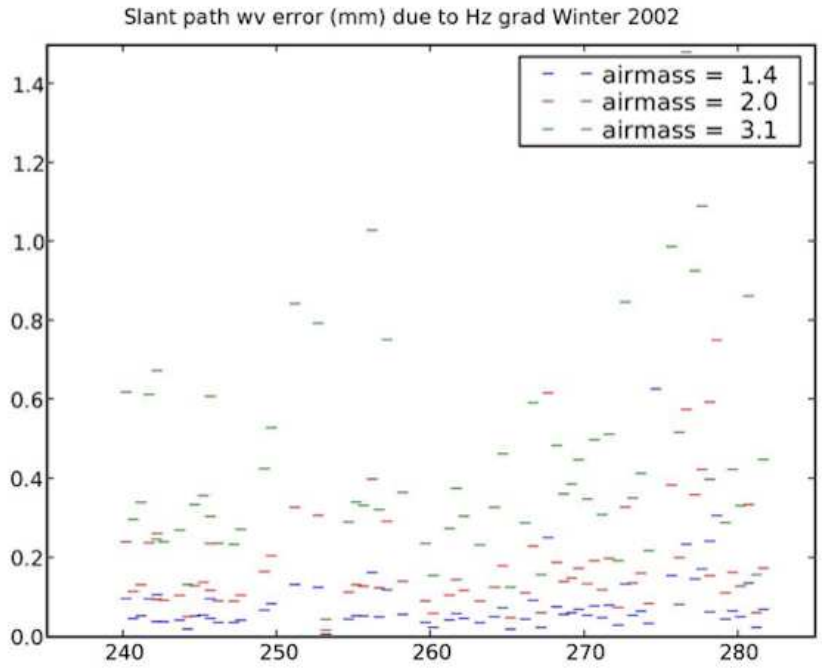

(a) Winter 2002.

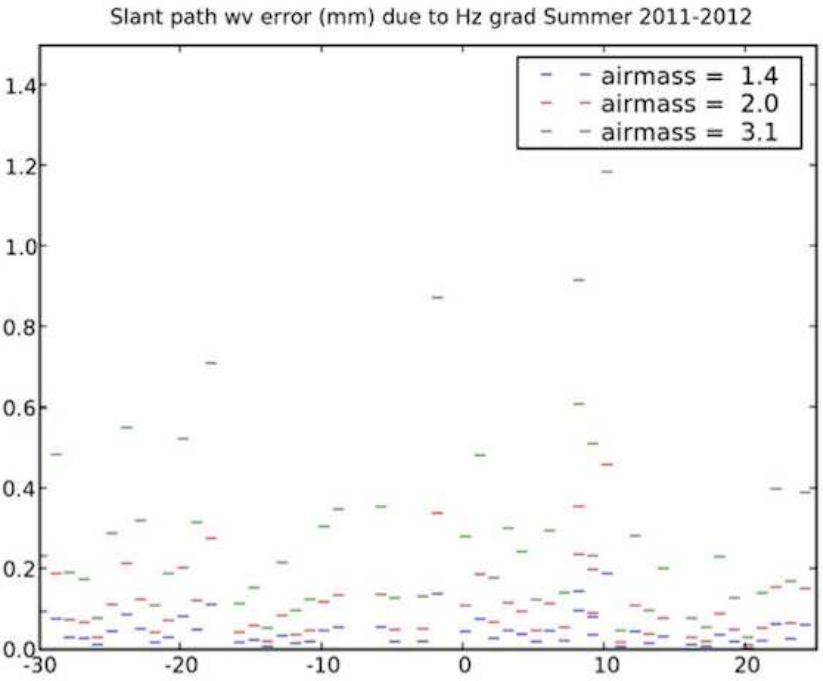

(b) Summer 2011-2012.

Figure 3.12 – Deviation of total water vapor column along slant path if local model ignores gradient at Cerro Pachón at two opposite seasons. The deviations are plotted for three values of air mass covering LSST range. Abscissa shows days since 1st January 2012.

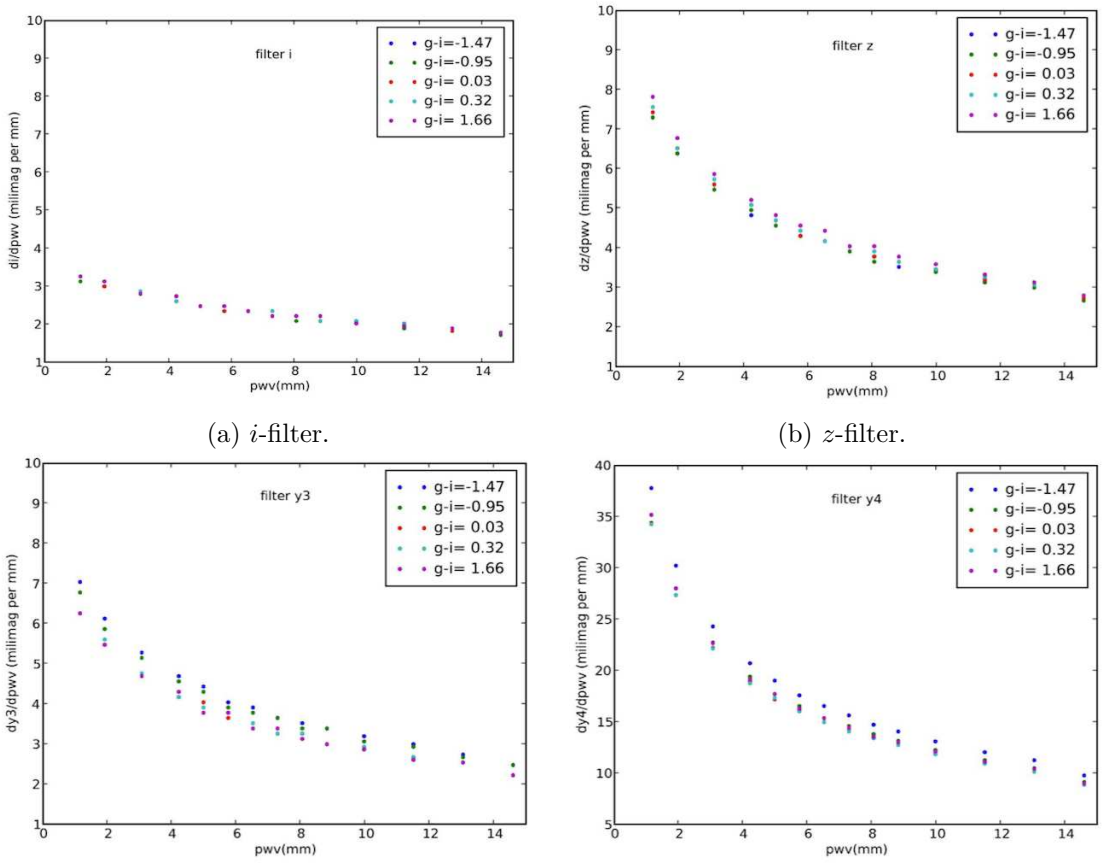

(a) i-filter. (b) z-filter.

(c) $y3$-filter. (d) $y4$-filter.

Figure 3.13 – Errors in LSST magnitudes induced by a 1 mm error in the estimation of precipitable water vapor in the most affected three bands. The different colors represent different stellar fluxes. The y-filter not being yet selected, this study enlightens the differences between y3 and y4.

Impact on photometry

To evaluate the photometric error induced by insufficient knowledge of the total precipitable water vapor along the line of sight of an observation, we use the same stellar fluxes and integration methodology as described in the ozone analysis. The deviation of the response in AB magnitude induced by a 1 mm change in the amount of precipitable water vapor has been computed as a function of the total precipitable water vapor on the line of sight for a same series of stars and plotted on Figure 3.13.

Results on Figures 3.13 read quite easily: assuming that water vapor can be sensed by external means down to 1 mm accuracy, the residual magnitude error will be less than 10 mmag in worst cases (filter y under extreme dry conditions). Only the y4 option does create problems unless this channel is used conversely for self calibration purposes but this would be at the expense of extra burden in the treatment of degeneracies.

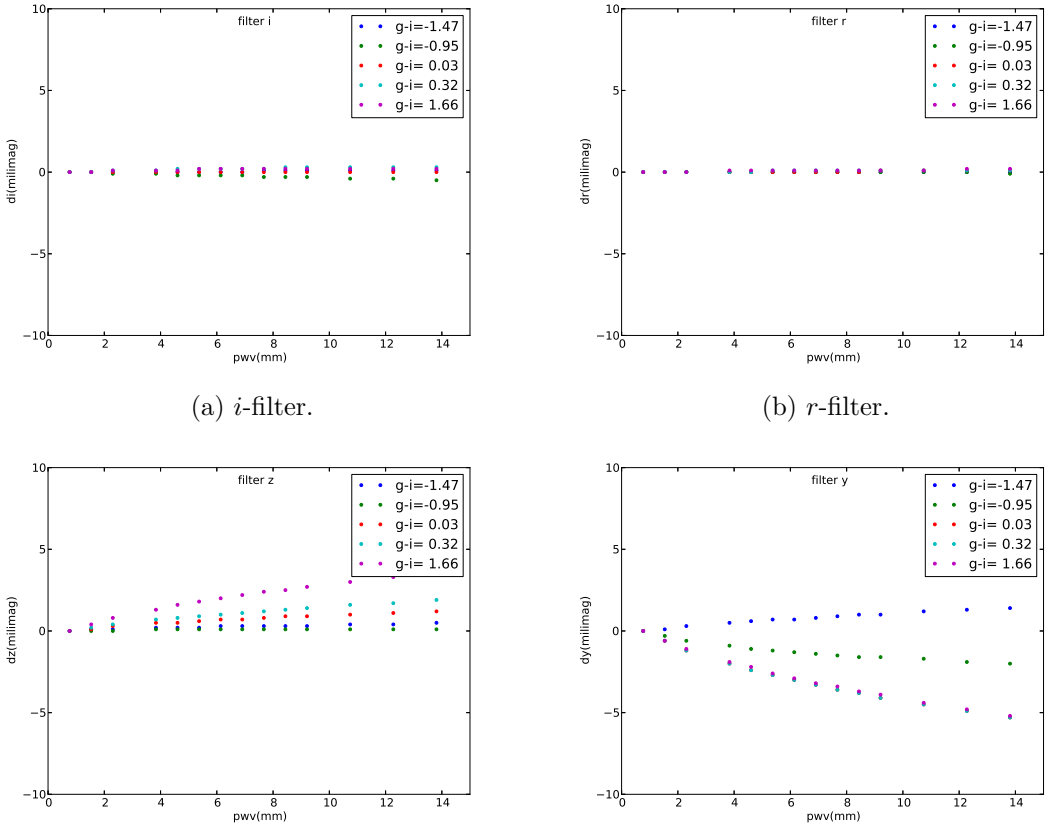

(a) i-filter.

(b) r-filter.

(c) z-filter.

(d) y-filter.

Figure 3.14 – Errors in LSST magnitudes due to a change in the bandpass shape as a function of the error on the precipitable water vapor amount. The five colors represent different stellar fluxes. Here the y-filter is y3.

This impact on the photometry can also be evaluated by means of error in the atmospheric bandpass shape, Δm^{obs} defined in equation (3.9). This is done using the same stellar spectra as before, comparing an atmosphere changing by its amount of precipitable water vapor with a standard bandpass computed with 1 mm of water vapor.

Due to the rapidly varying nature of water vapor in time and space, these magnitude deviations are of great concern, if not properly accounted for. The well-defined shape of water-vapor absorption might help the auxiliary telescope when fitting for a water vapor quantity, but the duration of the spectrophotometric observations will be longer than the characteristic time span of water vapor change. Therefore it seems necessary for the photometric calibration to call upon external instruments in order to secure the water vapor component.

GPS observations

Atmospheric water vapor introduces a wavelength dependent phase delay in the propagation of

Stations	**Distance** [10^3 m]	**Elevation diff.** [m]
P041-SA60	7.6	118
P041-DSRC	7.4	90
SA60-DSRC	1.9	208

Table 3.3 – Information about the SuomiNet GPS stations in Colorado, USA.

an electromagnetic wave. This is a nuisance to high precision GPS localization, but properly calibrated, can be used to sense the precipitable water vapor along the slant path between GPS emitter satellites and GPS receivers. The foundations of this method are extensively described e.g. in Solheim (1993). Detailed estimation and experimental validation of the best performances achievable are given by Ware et al. (1997).

The SuomiNet collaboration (see e.g. Ware et al., 2000) implements and operates a world wide network with a dense coverage of the US territory and a scarce on in the south hemisphere. These GPS stations are mostly based in local airports with quite a various range in elevation. Everyone can access SuomiNet data freely through their website[6]. On Figure 3.15, one can see water vapor data extracted from SuomiNet stations in Colorado, USA. We selected these particular stations because of dryness, the elevation (which is reasonably high for the US territory and close to that of LSST) and also because they are neighbors (see Table 3.3).

The error bars on the precipitable water vapor measurements, not displayed on both plots on Figure 3.15, are on the order of 1 mm (*cf.* Ware et al. (2000)). We see a very good agreement between the measurements on the different stations during the winter and the summer. GPS measurements probe with a good efficiency the temporal variation with – at least – a measure every hour, day and night. These plots enhance the fact that water vapor is highly non stable in time. During summer, Figure 3.15b shows the total column quadruple within a single day. Not taken properly into account, these effects could lead to a dramatic error on the photometric calibration. Both figures are also an indirect attempt to probe the spatial variation of water vapor. Based on plots, which are only a few days long, we see an obvious spatial correlation that extends at least to a few kilometers.

Conclusions

Water vapor is a highly variable component at small temporal and spatial scales. However, the shape of its spectral absorption curve is known to a high precision and only depends on the precipitable water vapor along the line-of-sight. This could be measured with good accuracy using a dedicated micro-wave radiometer co-pointed with the telescope. This solution has been

[6] `http://www.suominet.ucar.edu/`

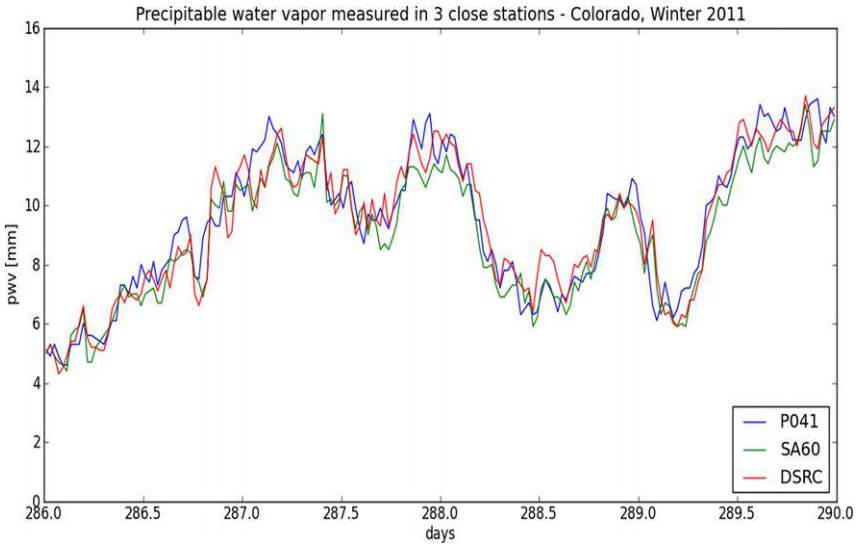

(a) Winter 2011.

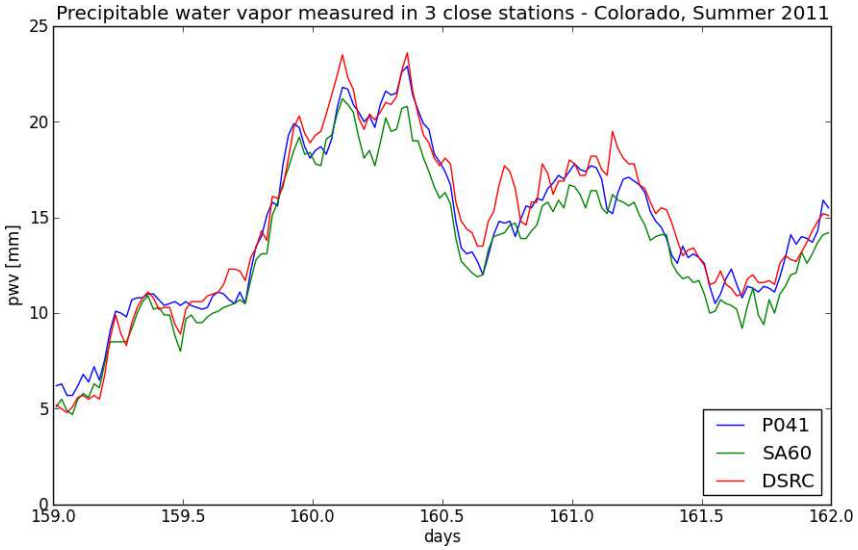

(b) Summer 2011-2012.

Figure 3.15 – Comparison of precipitable water vapor amplitudes acquired by three neighboring GPS stations in Colorado, USA, belonging to the SuomiNet network.

adopted e.g. by the ALMA interferometer to correct the co-phasing of separate dishes for local deviations of water vapor columns (see e.g. Wiedner et al., 2001). This would also safely solve the problem of the wet air masses drifting in the field-of-view and inducing errors in the photometry as large as 7 mmag in the most sensitive filters ; as well as limit the residual errors from the bandpass shape distortion, especially in the most affected z and y bands.

After sharing this study in the collaboration, and due to the low cost of such an instrument, the photometric calibration team has pushed the radiometer idea forward and included it into the current Level 2 Calibration Plan. In the meantime, a GPS station has been installed close to the auxiliary telescope. It will provide information on the local properties with a good time resolution to better constrain our simulation models.

II.1.3 Aerosols

An aerosol refers to micron-sized solid particles or liquid droplets, suspended in a gas. In the atmosphere, many types of aerosols, like sea salt, volcanic dust, sand, water droplets or ice crystals, are gathered in different proportions, sizes and shapes. The theoretical model for the electromagnetic scattering produced by these particulates is called Mie scattering, whose spectral response has a simple exponential shape in the visible domain. However the variety of aerosol particulates induce a spectral dependence in the spectra which makes it difficult to create templates. This is one of the main reason why aerosols are such an issue for photometric calibration. Under the basic assumption the atmospheric aerosol population is dominated by particulates of a certain size L. This case is referred to as monomodal aerosol distribution and characterized by its Ångström exponent α,

$$\tau(\lambda) \propto \left(\frac{\lambda}{\lambda_0}\right)^{\alpha}, \tag{3.29}$$

where λ_0 refers to the characteristic size of this distribution. Spectroscopic or multi-wavelength observations show the Ångström exponent varies with wavelength, reflecting the fact that aerosol grain size distribution is by no means monomodal. For the needs of long-term multisite aerosol observation campaigns, atmosphere specialists have developed an expended model with a bimodal distribution (O'Neill et al., 2001, 2003), with two populations of characteristic sizes L_1 and L_2 ($L_1 < L_2$), respectively, *fine grain* and *coarse grain* populations, which can be extracted from the aerosol distribution. An example of these two populations is shown in Figure 3.16.The ratio between the fine grain population and the full population is referred to as *fine mode fraction.*

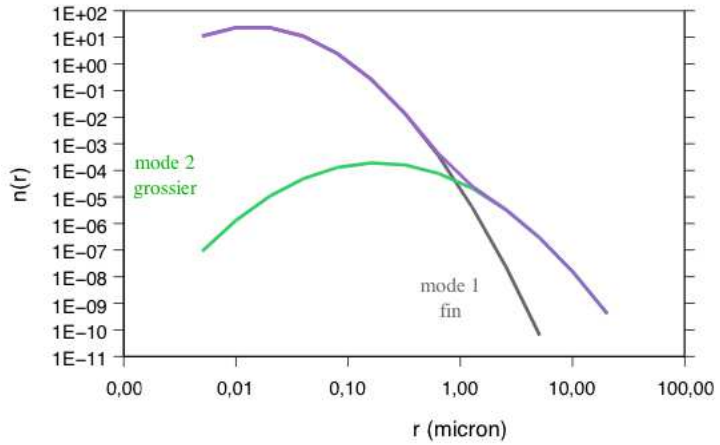

Figure 3.16 – Example of bimodal size distribution of aerosols.

The AERONET network

A wealth of highly documented and calibrated data about the aerosols is currently held by the AERONET collaboration[7]. This collaboration has defined a unified data acquisition (and data processing) protocol based on a multi-channel sun-pointed photometer. The photometer measures the sun radiance in several narrow bands which allow the reconstruction of the optical depth of aerosols in these bands, followed by a combination of these optical depths channels to derive many other informative parameters using a highly homogenized protocol (Holben et al., 1998).

The station located at Mauna Loa, Hawaii, which serves as a worldwide AERONET calibration station, has been running for two decades. It provides a long time baseline and therefore a statistically robust source for aerosols variations analysis. The Mauna Loa dataset used in this analysis is a subset of thirteen years of sub-daily monitoring from 1997 to 2009 (*cf.* Figure 3.17a). Another station, located in the astronomical complex El Leoncito (CASLEO) in Argentina, is very close to Cerro Pachón (220 km in a beeline) and approximately at the same altitude as LSST[8]. It started taking data on January 2011 and the dataset used comprises 475 days of processed measurements. Among the AERONET products, we use the aerosol optical depths τ_λ at 380 nm, 440 nm, 500 nm, 675 nm and 870 nm, the airmass information $z(alt)$, the Ångström exponent α and the fine mode fraction. The time-series of each optical depth channel as well as the fine mode fraction for both stations are plotted on Figure 3.17. We expect, due to the proximity of CASLEO station to Cerro Pachón that the experience similar aerosol regimes. Therefore, while Mauna Loa data are used as the reference for aerosol long-term variability in

[7] `http://aeronet.gsfc.nasa.gov/`
[8] however both sites are separated by the Andes summits

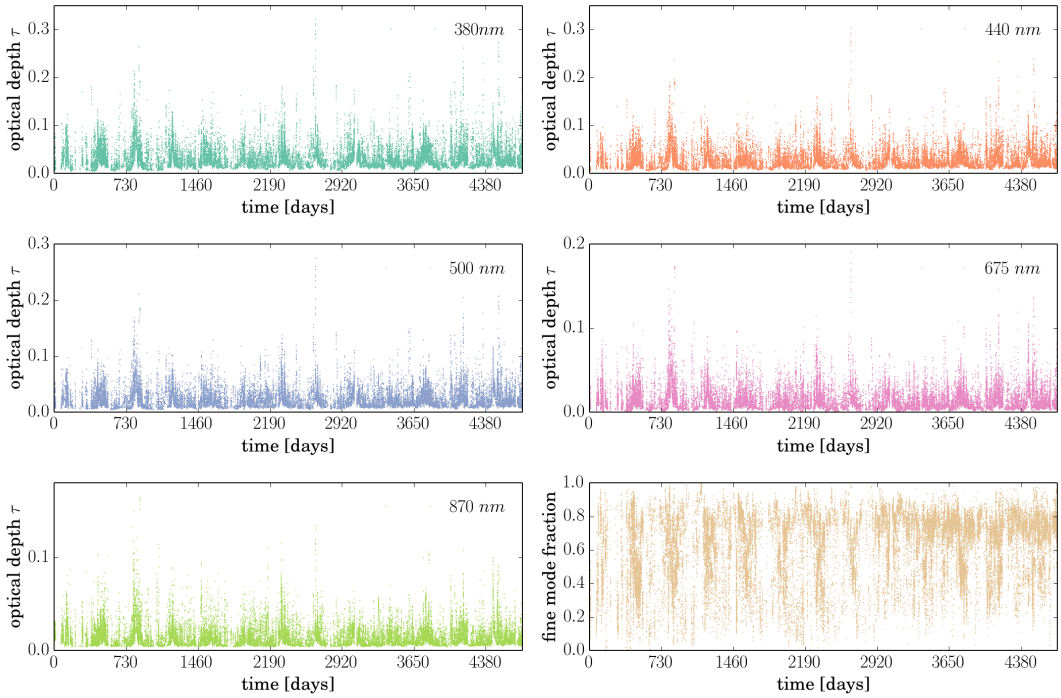

(a) Mauna Loa dataset (Hawaii).

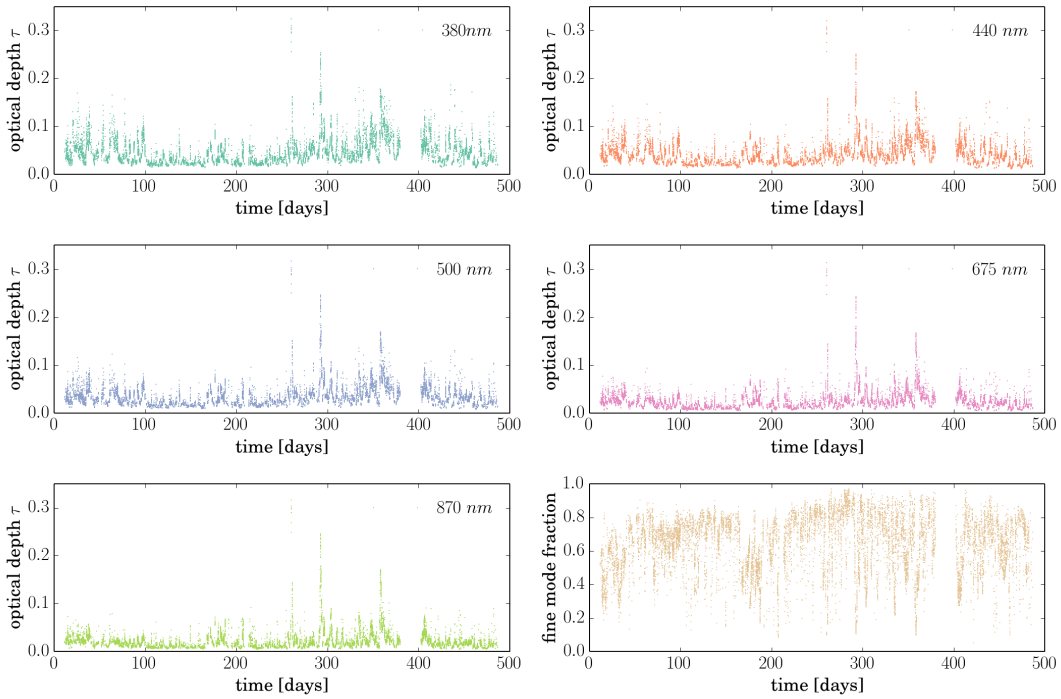

(b) CASLEO dataset (Argentina).

Figure 3.17 – Aerosol optical depth and fine mode fraction time-series from AERONET network stations.

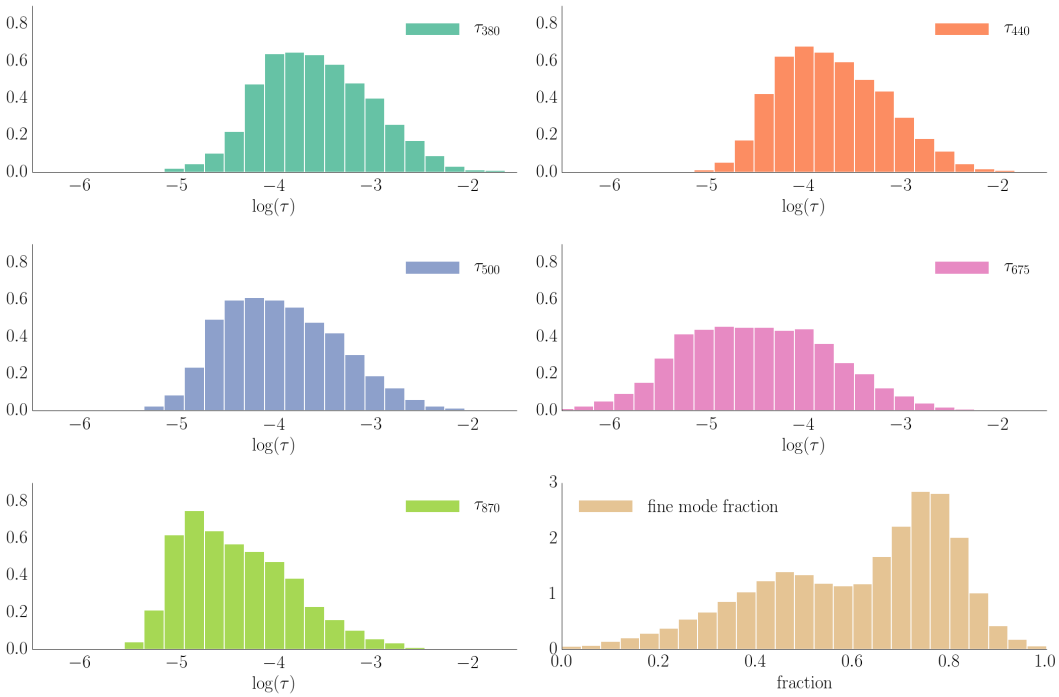

(a) Mauna Loa dataset (Hawaii).

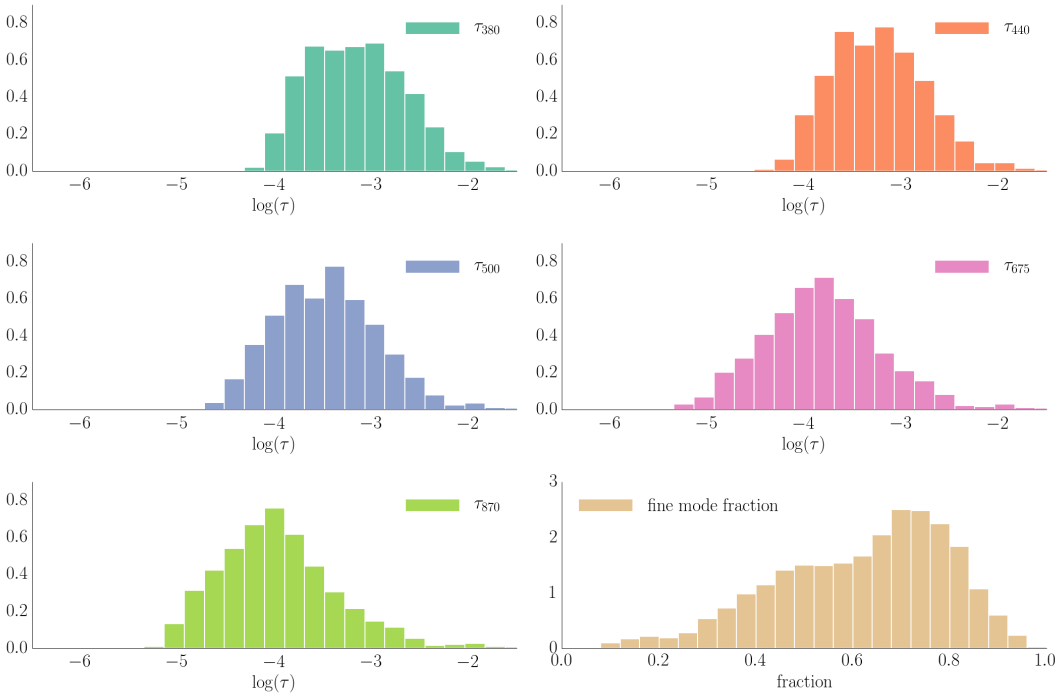

(b) CASLEO dataset (Argentina).

Figure 3.18 – Histograms of optical depth data from the AERONET network (in log).

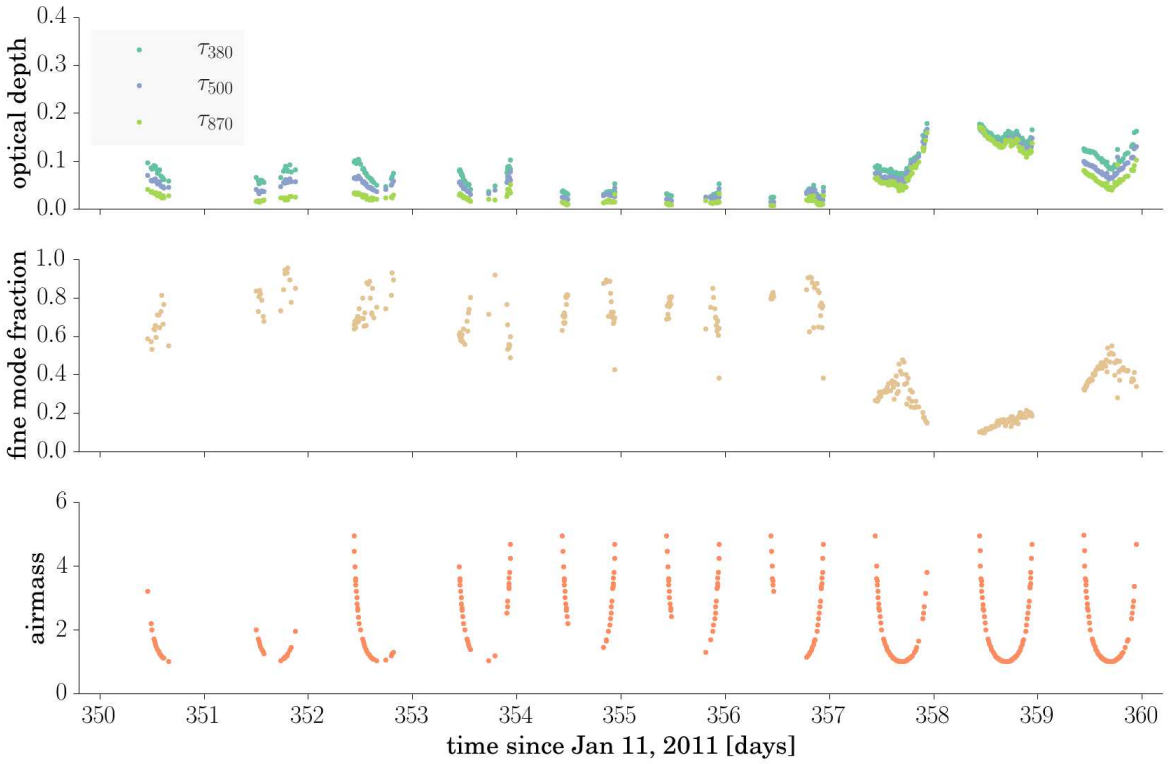

Figure 3.19 – Ten-day subset of aerosol data from CASLEO, showing strong variations. Top panel displays the aerosol optical depth in three channels, 380, 500 and 870 nm ; middle panel the fine mode fraction, and bottom panel the airmass of acquisition pointing.

space and time, in the scope of building a realistic long-term simulation, CASLEO data are used for scaling purposes and to derive the impact on photometry.

The normalized histograms corresponding to the time-series shown on Figure 3.17 are plotted on Figure 3.18. Since optical depth data range from zero to some small value, for visibility the histograms display the decimal logarithm of the optical depth. A quick comparison between both locations yields a difference in shape. Putting aside the Mauna Loa 675 nm channel which behaves oddly compared to the other channels, Mauna Loa data seems a bit more scattered and less peaky than CASLEO data, and shifted towards lower amplitudes. This difference is summarized in the empirical scaling relation,

$$\boldsymbol{\tau}_{\mathrm{CASLEO}} = \boldsymbol{\tau}_{\mathrm{HAWAII}} \times 1.45 + 0.004\,, \tag{3.30}$$

generalized for all the channels, which will be used for the atmospheric simulator.

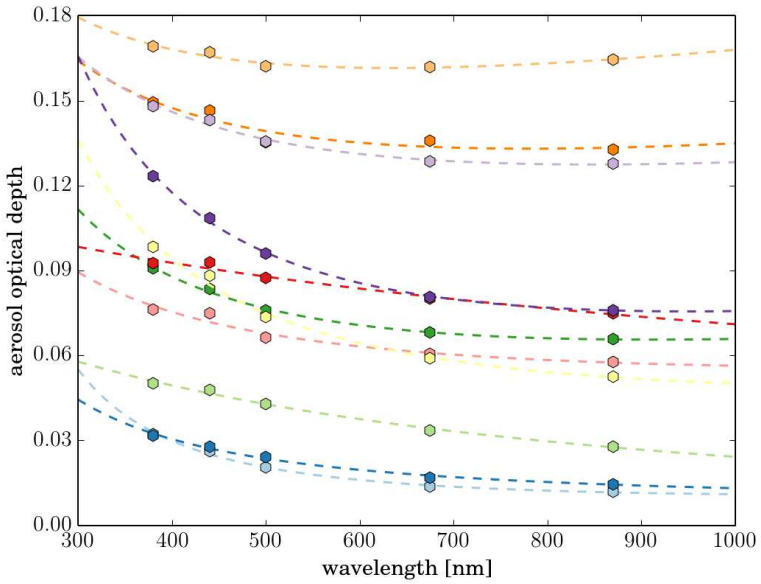

Figure 3.20 – Aerosol optical depth spectrum reconstructed via a second-degree polynomial fit in logarithmic space, for 12 measurements during the ten-day subset of CASLEO data.

Spectral variation interpretation

Figure 3.19 shows the time evolution of two indicators: the 675 nm optical depth as an indicator of the total optical depth density along the line of sight and the fine mode fraction (FMF) which is an indication of the spectral variation. Both are plotted over five days around a CASLEO aerosol data peak, which can be observed around day 358 on Figure 3.17b. To facilitate the interpretation, we give also the airmass of each observation. The behavior of the FMF is quite illustrative: between days 357 and 358, the FMF decreases abruptly, indicating the surge of a strong population of coarse grain aerosols which are the main cause of the raise of the total optical depth. During day 357, the FMF grows linearly while the sun is rising and decreases linearly when the sun sets. This suggests that the vertical profile of the fine mode component has a scale height much larger than the coarse mode, so that the contribution of the coarse mode is minimum at zenith. On day 358, while it is clear that the coarse mode is receding, there is no midday FMF peak, meaning that the coarse mode decline is so fast that it cannot be compensated by the line of sight going away from zenith.

This spectral variation is illustrated on Figure 3.20 where the optical depth in the five AERONET channels is plotted (using bullets) against the wavelength for a few measurements spread over the five-day subset of Figure 3.19. Dashed lines represent logarithmic second-degree

polynomial fits,

$$\log \tau(\lambda) = \alpha_0 \log^2 \lambda + \alpha_1 \log \lambda + \alpha_2 \,, \tag{3.31}$$

over the five data points, expanded to the LSST spectral range. While the fit seems accurate, the slope of the fitting curves dramatically changes with wavelength, especially close to the UV domain ($< 400\,\mathrm{nm}$), which confirms that the spectrum of aerosols cannot be represented correctly by a single Angstrom exponent independent of the wavelength.

Impact on the performances of LSST photometric calibration

Such a spectral variation if not properly taken into account would be the main source of error concerning aerosols. Its impact can be measured by looking at the bandpass shape distortion obtained with a standard atmosphere without aerosols combined with the aerosol transmission from the curves fitted ion the data and a standard atmosphere with low aerosols. The result is computed on Figure 3.21 for all the data points of Figure 3.19 and for two standard stellar sources with very different spectral energy distribution. Aerosol spectral variation being higher in the UV-domain, the residual error on the magnitude of a source with low energy toward the UV (e.g. a red star) will be more affected as depicted on Figure 3.21b. The amplitude of the deviation reaches 17 mmag in the u-band on day 359. While this is an extreme case, the deviation on the remaining days range between 2 and 10 mmag, which is still very concerning. Now comparing Figures 3.19 and 3.21, we observe quite no correlation between the optical depth variation and the error on the magnitude. The reason is the spectral variation is mainly due to the mixing of the fine grain and coarse grain populations, and cannot be tied to a single optical depth value.

Figure 3.22 displays the histograms of these magnitude errors, this time computed on the full CASLEO data, and for the two stellar standard sources. While the blue dwarf magnitude errors stay within the LSST error budget, the one from the red dwarf extend well past it.

Conclusion

Even under low or moderate aerosol conditions, we expect a distortion of the effective bandpass at least in u and g-bands, inducing a deviation from the standard bandpass in a way that is strongly dependent on the source spectral energy distribution. This results in magnitude errors exceeding 10 mmag in u-band and 5 mmag in g-band. Calibrating the photometry assuming a monomodal aerosol distribution and a constant Ångström exponent aerosol model will lead to huge systematic errors, unless it uses external instruments to measure in real-time the optical depth in several wavelengths. This could be achieved for example, with a multi-wavelength

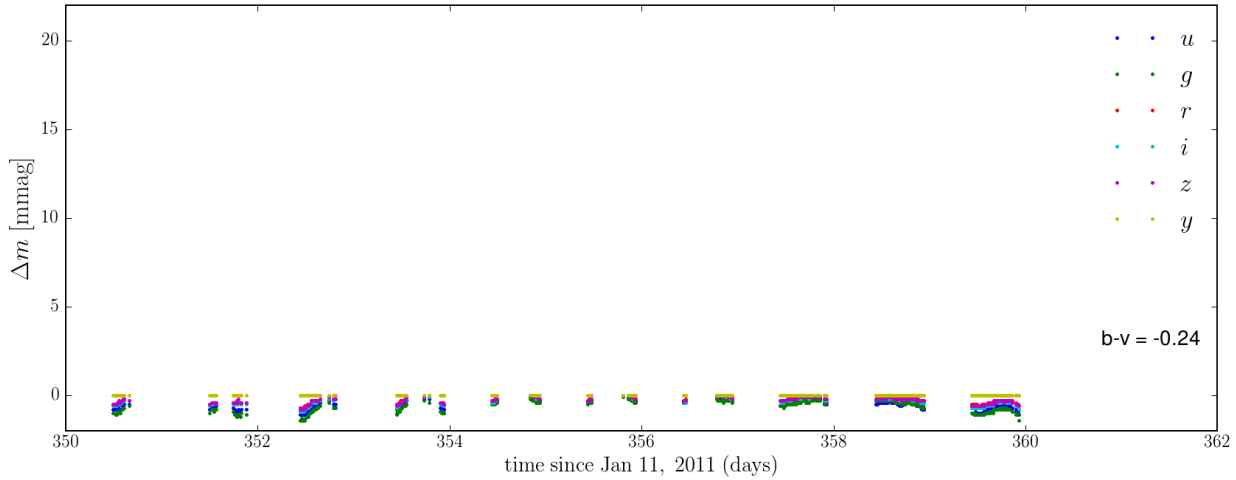

(a) Standard blue dwarf.

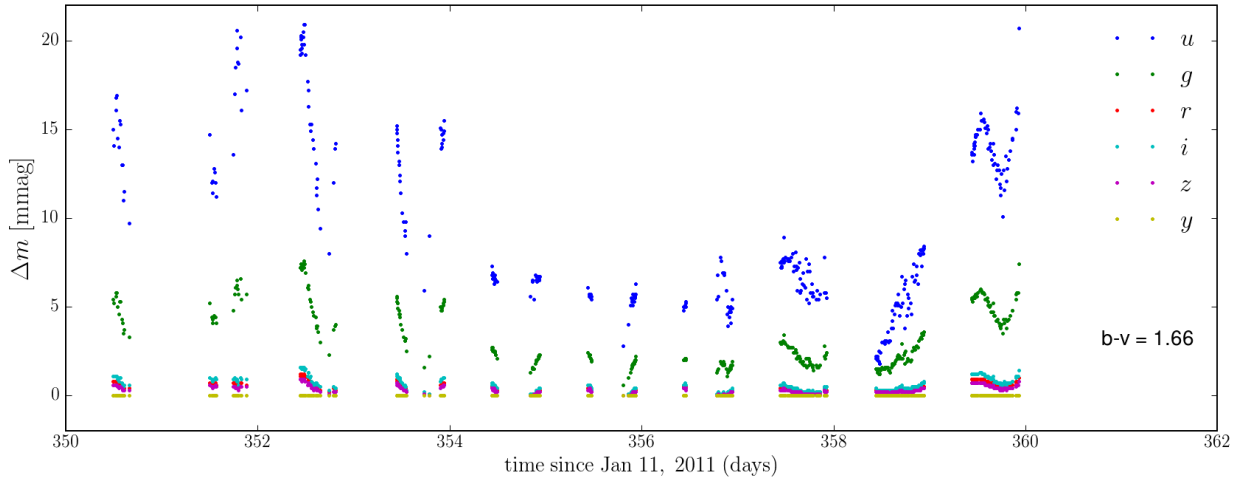

(b) Standard red dwarf.

Figure 3.21 – Magnitude error residuals due to aerosols (when considering a standard atmosphere) for five days with particularly strong aerosols presence of CASLEO data and for two different stellar sources.

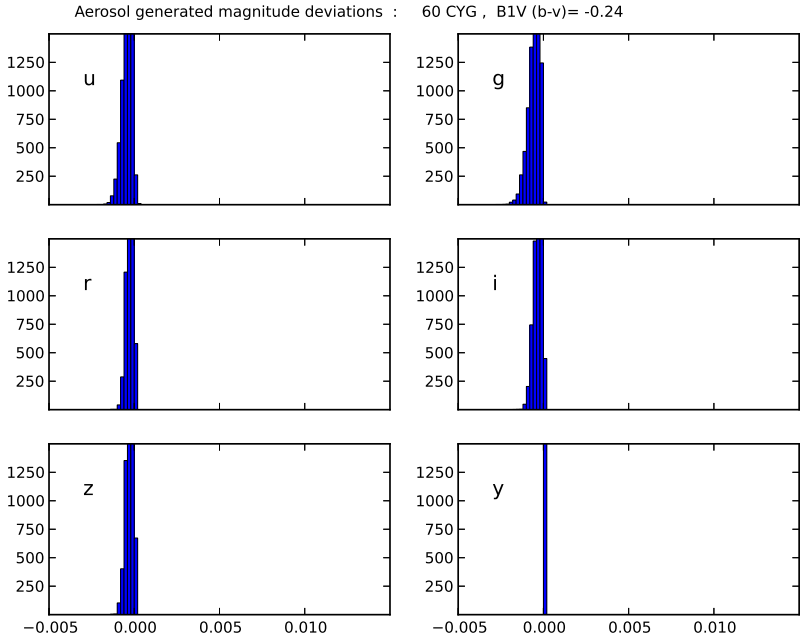

(a) Standard blue dwarf.

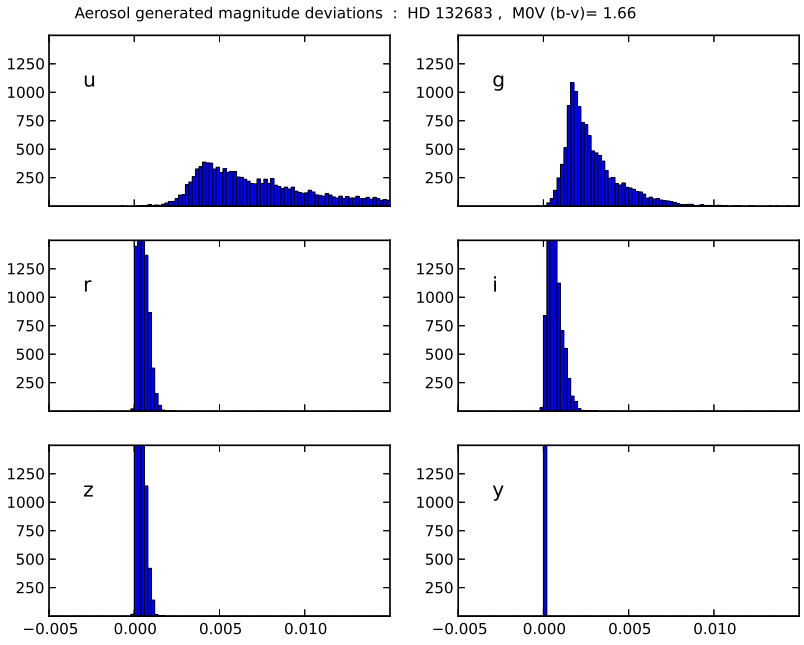

(b) Standard red dwarf.

Figure 3.22 – Histograms of magnitude error residuals due to aerosols (compared to a standard atmosphere) for the complete CASLEO dataset and for two different stellar sources.

narrow-band imager, as shown in Li et al. (2012).

This suggests that the atmospheric model presented in Burke et al. (2010) and developed in Section I.2.3 may fail providing appropriate estimates of the atmospheric extinction in the LSST field under severe non photometric conditions created by the combination of complex aerosols layers at various altitudes.It therefore emphasizes the necessity of a realistic atmospheric simulation that reproduces these effects at an appropriate rate and duration, in order to evaluate the effective impact on the photometry, monitor the systematic effects, and validate alternative calibration strategies.

II.2 The atmosphere simulator

The atmosphere simulator required to validate and optimize the LSST photometric calibration procedure is expected to provide extinction spectra for the atmospheric layers in front of the telescope.

Considering the temporal and spatial variations of the main atmospheric components studied in the last section, the goal of this simulator is to reproduce these variations in amplitude and frequency, in a simulated time- series that extends over the period of LSST data acquisition ($\sim$ 10 years). First, we carefully select relevant data for each of the main constituent we want to simulate (ozone, water vapor and aerosols).

Then, we extract the long-term seasonal variations by creating a one-year-long time-series made of the averaged data values folded up on a year. To prepare for the Fourier analysis, we create an equispaced dataset in time using the initial time-series, and we use the averaged series to fill in the missing values. In order to study the excursions of the data around the mean, we subtract the seasonal variation from the equispaced time-series.

Last, we analyze the excursions via the Fourier transform, creating a power spectrum of the variation frequencies, that we use to draw random time-series with identical statistical properties as the initial ones. These time-series are then translated into spectral information, using MODTRAN for ozone and water vapor and a second degree polynomial fit using the five optical depth channels for the aerosols.

II.2.1 Data selection

The step of the simulation that drives data selection is the Fourier analysis used to retrieve the frequency and amplitude of the components excursions around the mean value, which in the case of discrete data points should be referred to as discrete Fourier transform (DFT). This

procedure requires the data to be equally spaced in time. [9] Every constituent being treated separately in the simulation, this does however not require homogeneity between the datasets.

The time repartition of data $d(t)$ might vary a lot between datasets. While satellite data is quite scheduled, with one or two data points a day, ground- based acquisition time is quite unpredictable, although generally more frequent. In terms of significance for the analysis of short-term variations, the more values a day, the better. But in all time-series there remains days without any values. Taking into account the need for equispaced data, we therefore looked statistically for a compromise between the number of values per day and the number of missing values in that case, in the perspective that we should fill these values at some point.

That considered, we selected for the analysis TOMS data[10] for the ozone, which on average is rich of one value per day ; MODIS data[11] for water vapor, which has up to two data points per day ; and AERONET data at Mauna Loa, Hawaii[12] for the aerosols, which has sporadic data (as much as fifty values a day and then none for a few days) but on average at least on vector per day (optical depth in five wavelength channels). These datasets extend on a long continuous period and have been acquired in the last two decades which make them statistically robust and representative of the current atmospheric conditions. Aerosol data used for the simulation is not probing the constituent over Cerro Pachón and we decided to scale it up using the properties of the data for AERONET station at CASLEO Observatory in Argentina, following equation (3.30).

Building the equispaced time-series

The average values/vectors per day in the original time-series sets the number of values per day in a new empty equispaced array. Next step is to set these values using the unevenly sampled data, the case of missing values being treated during the time-series analysis. For satellite data, its intrinsic regularity eases the task. For each day, there is either one ozone value or none, so the array is given that value or left with a blank. The water vapor time-series is a bit richer with either one, two data points per day, or none. Again the array is given the values or left with a blank. In the case of a single value, MODIS acquisition time indicates it is during day or night, which helps choosing the abscissa on the new array. Finally, since we determined we need a value per day for the aerosols, the selection of that value when there is more than one can be either random, or chosen to be the mean or median value. After conducting some tests, we settled

[9] There is a comparable method for the analysis of non-equispaced discrete data points, known as non-discrete Fourier transform (NDFT) but it involves a better understanding of the data itself to draw conclusions and use it for random simulations.

[10] satellite, [mid-1996–end of 2006]

[11] satellite, [2004–2011]

[12] ground-based, [1997–2009]

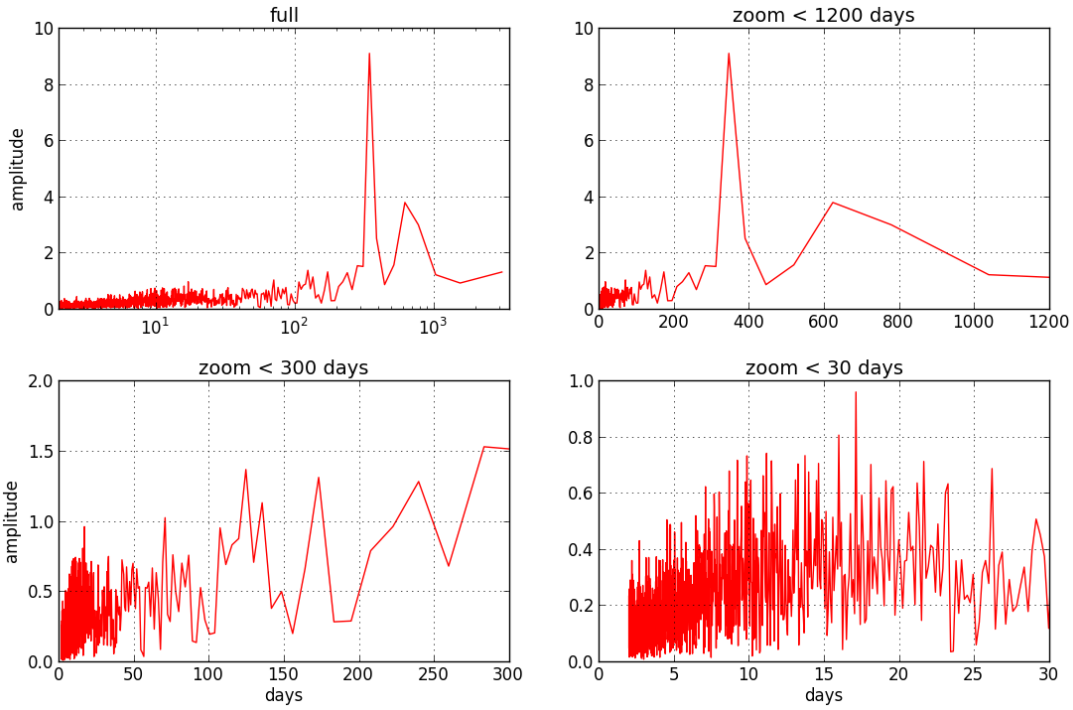

Figure 3.23 – Temporal spectrum of the TOMS ozone time-series of nine years obtained via a discrete Fourier transform. The upper left panel shows the full spectrum in a log axis. The remaining panels show portions of that spectrum in a linear axis, as mentioned in their respective titles, under 1200 days, under 300 days, under 30 days. The amplitude of the spectrum basically corresponds to the occurrence of the periodicity in axis.

on the random picked value in that day, otherwise the biggest excursions tend to be smoothed out. Also, AERONET instruments are sun-photometers which follow the sun throughout the day and probe a continuously changing airmass. The goal is to compute the spectra at very low airmass. Again, there is a right balance between well restricting the values and keeping enough data. We choose to eliminate values with an airmass lower than 3.

From this point, the original data is discarded and replaced with the equispaced time-series $d_{ES}(t)$ for the analysis.[13]

II.2.2 Seasonal variations and trend analysis of time-series

Time-series shown in Figures 3.6, 3.11 and 3.17a all present obvious periodicity at the scale of a year, known as seasonal variation. That 365 day periodicity is well detected using a Fourier transform on the data. On Figure 3.23 is shown the spectrum resulting from a discrete Fourier

[13]Precipitable water vapor quantity and aerosol optical depths vary, unlike ozone quantity, between none and some small value. Such an analysis is therefore performed in log space for simplicity and to retrieve sinusoidal fluctuations.

transform of ozone data. The amplitude of such a spectrum captures how frequent a certain periodicity will emerge from the time-series. In the first and second panel, a distinct peak comes out of the spectrum at a periodicity of about 350 days (with a non negligible uncertainty). This is coherent with a periodic variation of a year, as previously observed. However, such a analysis need some refinement to be able to constrain the periodicity of the very noisy short-term variations seen in the fourth panel, since we have missing values.

Following the ozone analysis of Jones et al. (2009), we would like to model these long-term periodicities $d_{\mathrm{long}}(t)$ with time, as

$$d_{\mathrm{long}}(t) = A + B\,t + C(t) + N(t)\,, \tag{3.32}$$

where A is a constant offset, B is a linear trend (approximation), C is the periodic fluctuation (seasonal cycle + solar cycles + quasi-biennial oscillations (QBO)) and N is the error term.

In order to obtain such a curve for each constituent, we create a new time-array with the same number of data points per day, but only one year long. On each data point, all the values of the time-series for that particular day are overlapped. Then, the mean value and the standard deviation for the constituent are computed for each day of the year (half-day for water vapor). This way, since the missing values are (in general) well spread over time, we can still have a statistically robust estimation of the average value over the full year.

While making this averaged data curves, adjacent data points are treated independently, which is obviously wrong. This is why we obtain a non smoothed curve. A general yearly behavior, which bears some continuity between points is instead wanted. To recover that continuity aspect, a moving average is applied on the data to create a seasonal curve. This curve is shown on Figure 3.24, top panel, superimposed on the original data. The standard deviation around that average value is displayed in shaded light blue (1 and 2-σ) to confirm this embraces quite all data points. To compute such a smooth seasonal variation, we applied a sixty- day window. This is the model for the long-term variation of the constituent. It contains the offset, the seasonal variation (+ others) and the difference between the first and the last point accounts for the trend. In this simple model, the noise was washed out using the moving averaging.

Before moving on to the next step on determining the short-term fluctuations, the missing values need to be filled in.

Filling the missing values

The Discrete Fourier transform is very sensitive to missing values and can produce very unexpected outputs. This is why we want to complete the daily time-series we have created. For

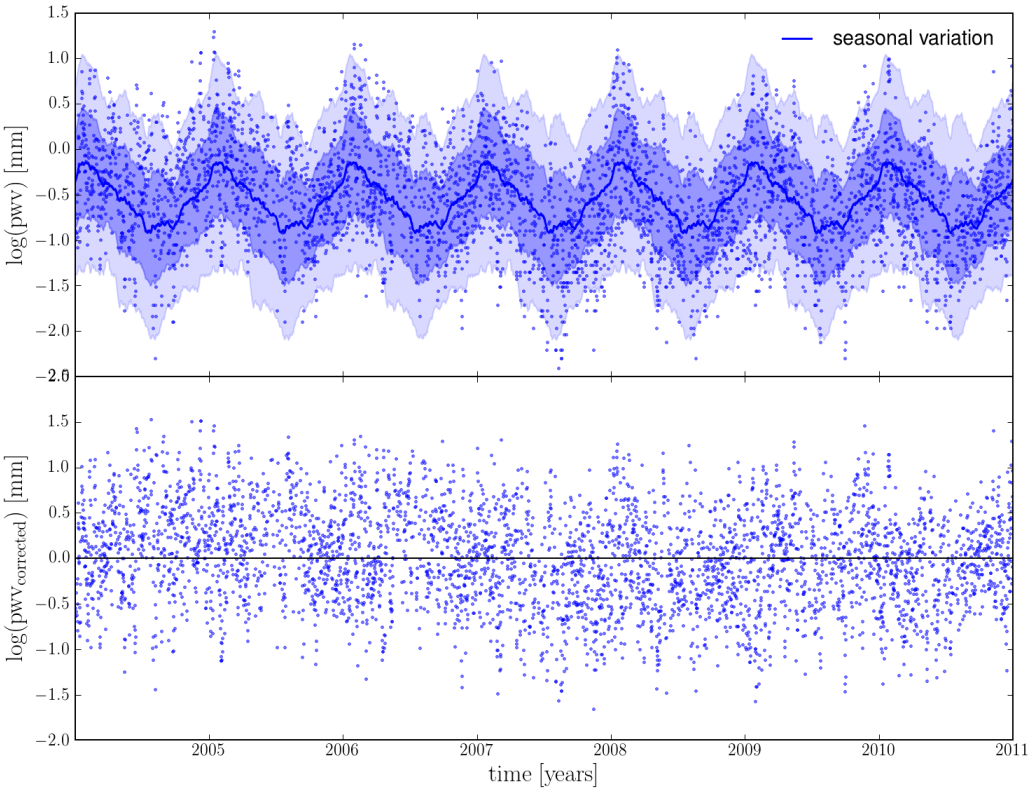

Figure 3.24 – Seasonal variation determination and correction on the precipitable water vapor time-series. Top panel shows the original data from MODIS (blue dots), the computed seasonal average (blue line) and the 1 and 2-σ deviation around the average. Bottom panel represents the original data corrected for the seasonal variation.

each missing value, we pick up its abscissa within the current year, then we draw a Gaussian random value using the computed average value and standard deviation of the constituent for that abscissa. Good statistics is important at this point since it will output more accurate values. Once the time-series is complete, before moving on with the Fourier transform, we proceed by striping the data off the smooth long-term fluctuation, in order to obtain the deviation from that curve.

$$f(t) = d_{ES}(t) - d_{\mathrm{long}}(t)\,. \tag{3.33}$$

The resulting time-series in the case of precipitable water vapor is shown on the bottom panel of Figure 3.24.

II.2.3 From Fourier analysis of short term variations to simulation

For simulation purposes, it is more important to know how frequent an excursion with a given amplitude occurs during the time-series, rather than knowing it happened at a specific time. This is the reason for taking the excursion time-series into Fourier space, to sample the signal with coefficients associated with frequencies, and therefore retrieve all its periodicities and amplitudes at once. The Fast Fourier Transform (FFT) algorithm is used to compute the discrete Fourier transform (Cooley & Tukey, 1965; Press, 2007). The general case can be described as follows. It starts by applying the FFT to the excursion data $f(t)$,

$$\tilde{f}(\omega) = \mathrm{FFT}\left[f(t)\right] , \tag{3.34}$$

to get the data in terms of frequencies $\tilde{f}(\omega)$ (or power spectrum). One has to be careful about using the real Fourier transform (RFFT), that can be used for purely real input, as it does not compute the negative frequency terms (complex conjugates of the positive ones) redundant in this case, and can thus lead to mistakes. The information in Fourier space is complex so that it keeps information on the phase (which allows to reconstruct initial data via an inverse Fourier transform). Instead, we would like to produce a new time-series with identical characteristics from the initial one. This is possible in the Fourier space using Gaussian randomization of the amplitudes of the frequency modes as well as shuffling the phase. We end up with a randomized signal in the frequency domain $\tilde{f}_{\mathrm{rand}}(\omega)$ that can be inverse Fourier transform to obtain a randomized time-series $f_{\mathrm{rand}}(t)$ of excursions.

$$f_{\mathrm{rand}}(t) = \mathrm{FFT}^{-1}\left[\tilde{f}_{\mathrm{rand}}(\omega)\right] \tag{3.35}$$

A code example of the process is given here for illustration. It uses the Python language.

```
"""Starting with a time-series data (array) the following lines
produce a randomize time-series with the same characteristics"""
import numpy
# Fourier transform of the data
freq = numpy.fft.fft(data)
# Randomization of amplitudes..
r_amp = numpy.random.normal(0, numpy.abs(freq))
#.. and phase
r_phi = numpy.random.uniform(0, 2 * numpy.pi, int(len(data)))
r_phase = numpy.cos(phi) + 1j*numpy.sin(r_phi)
# New frequency series
```

```
r_freq = r_amp * r_phase
# Inverse Fourier transform to get the new time-series
r_data = numpy.fft.ifft(r_freq)
```

The last step is to add the long-term periodicity to recover a usable component quantity time-series,

$$d_{\rm rand}(t) = d_{\rm long}(t) + f_{\rm rand}(t) \tag{3.36}$$

Ozone and water vapor have atmospheric transmission curves that have a well defined shape and can scale in amplitude using this single parameter time-series.

The specific case of aerosols

Since Mie scattering has no well defined spectral shape, we use measurements of extinction at several wavelengths and interpolate between them in order to recover the shape of the transmission curve in the visible domain. The analysis/simulation process thus differs slightly. Aerosol data extracted from AERONET is made of five optical depth time-series $\tau_{\lambda_X}(t)$ where λ_X corresponds to the specific wavelengths of the AERONET instruments 380 nm, 440 nm, 500 nm, 675 nm and 870 nm. The signal from these narrow bands being acquired simultaneous in five different channels, the data points are obviously correlated. That correlation must be taken into account in order to realistically reproduce their behavior. We thus study the five wavelength dependent time-series in parallel, using the two-dimensional vector

$$\boldsymbol{\tau}(\lambda, t) = \begin{pmatrix} \tau_{380}(t) \\ \tau_{440}(t) \\ \tau_{500}(t) \\ \tau_{675}(t) \\ \tau_{870}(t) \end{pmatrix} . \tag{3.37}$$

The Fourier transform is applied to get the corresponding five frequency data sets in a new vector $\tilde{\boldsymbol{\tau}}$,

$$\tilde{\boldsymbol{\tau}}(\lambda, \omega) = \mathrm{FFT}\left[\boldsymbol{\tau}(\lambda, t)\right] = \begin{pmatrix} \mathrm{FFT}\left[\tau_{380}(t)\right] \\ \mathrm{FFT}\left[\tau_{440}(t)\right] \\ \mathrm{FFT}\left[\tau_{500}(t)\right] \\ \mathrm{FFT}\left[\tau_{675}(t)\right] \\ \mathrm{FFT}\left[\tau_{870}(t)\right] \end{pmatrix} = \begin{pmatrix} \tilde{\tau}_{380}(\omega) \\ \tilde{\tau}_{440}(\omega) \\ \tilde{\tau}_{500}(\omega) \\ \tilde{\tau}_{675}(\omega) \\ \tilde{\tau}_{870}(\omega) \end{pmatrix} . \tag{3.38}$$

We then form the covariance matrix between wavelength $\mathbf{C}_{\lambda\lambda'}$ by correlating two vectors.

In Fourier space, we deal with complex numbers so the cross-product is Hermitian. The covariance results in the difference between the cross-product averaged over the frequencies and the cross-product of the averaged vectors

$$\mathbf{C}_{\lambda\lambda'} = \langle \tilde{\boldsymbol{\tau}}(\lambda)\, \tilde{\boldsymbol{\tau}}^{\dagger}(\lambda') \rangle_{\omega} = \overline{\tilde{\boldsymbol{\tau}}_{\lambda} \,.\, \tilde{\boldsymbol{\tau}}^{\dagger}_{\lambda'}} - \overline{\tilde{\boldsymbol{\tau}}_{\lambda}} \,.\, \overline{\tilde{\boldsymbol{\tau}}^{\dagger}_{\lambda'}} \,. \tag{3.39}$$

Doing so, we assume the correlation is only between the wavelengths and not the frequencies.[14] Initial data not being complex, the covariance matrix is symmetric and therefore can be diagonalized,

$$\mathbf{D}_{\lambda\lambda'} = \mathbf{T}^{-1} \,.\, \mathbf{C}_{\lambda\lambda'} \,.\, \mathbf{T} \,, \tag{3.40}$$

where $\mathbf{D}_{\lambda\lambda'}$ is the diagonal matrix containing the five eigenvalues of this new basis, and $\mathbf{T}$ is the eigenvector associated. Both of these objects are used to randomly recreate data keep the correlation between the wavelengths.

When drawing the random amplitudes, instead of using the absolute value of the Fourier transform as the standard deviation of the Gaussian distribution, the eigenvalues given by the diagonal of $\mathbf{D}_{\lambda\lambda'}$ are now used. Amplitudes for each channel are drawn given their corresponding eigenvalue, and for all the frequencies. A new vector $\tilde{\boldsymbol{\tau}}'_{\mathrm{new}}(\lambda, \omega)$ is obtained. Then, using the eigenvector $\mathbf{T}$ as projector the amplitudes are brought back to the original basis,

$$\tilde{\boldsymbol{\tau}}_{\mathrm{rand}}(\lambda, \omega) = \mathbf{T} \,.\, \tilde{\boldsymbol{\tau}}'_{\mathrm{new}}(\lambda, \omega) \tag{3.41}$$

The final step is identical to the analysis of ozone and water vapor, the random frequency vectors are inverse Fourier transformed to obtain the random-but-correlated optical depth excursion time-series vector,

$$\boldsymbol{\tau}_{\mathrm{rand}}(\lambda, t) = \mathrm{FFT}^{-1} \left[\tilde{\boldsymbol{\tau}}_{\mathrm{rand}}(\lambda, \omega) \right] \,, \tag{3.42}$$

which are finalized by adding the long-term periodicity. These random-simulated time-series can easily be reproduced using a random seed.

A proof of concept in shown on Figures 3.25 and 3.26 where one can see the simulation of 675 nm optical depth time serie compared to the data, and the histograms of nine simulated series of data are plotted against the original one. The data are log scaled in the histograms to account for extremely faint values. One can remark in the time series that the data show higher excursions than the simulation. The reason of that small bias is due to the assumption during the simulation procedure, that the logarithmic distribution of optical depth values around the

[14] This assumption is a simple Gaussian approximation, it has not been tested.

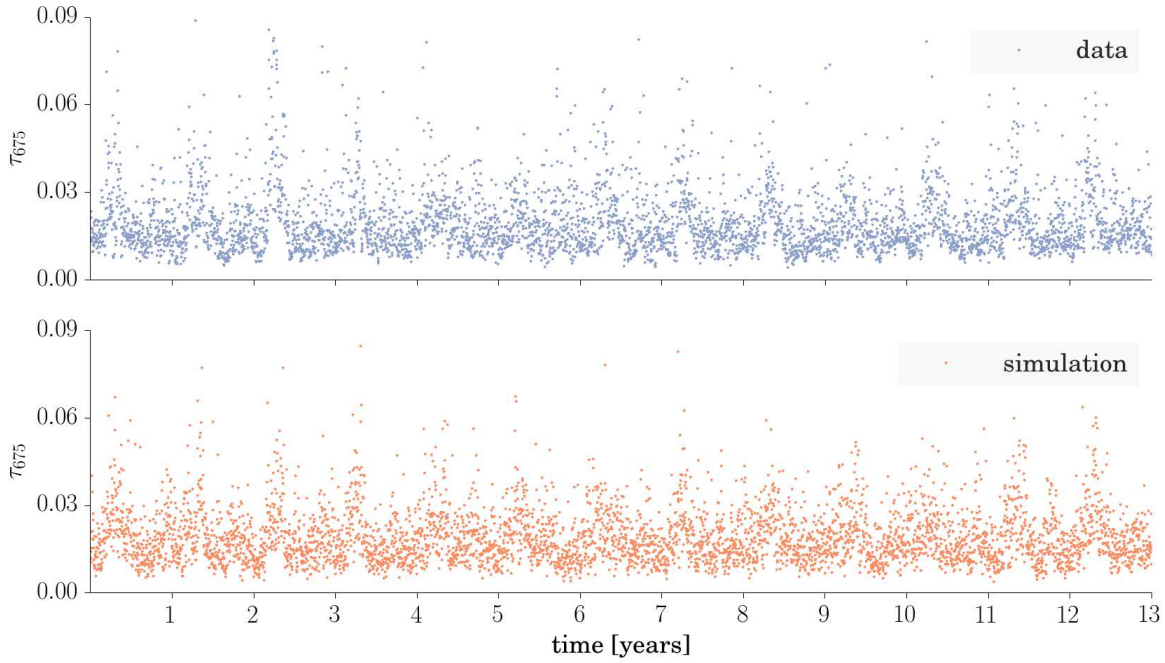

Figure 3.25 – Comparison between original and simulated time series of aerosol 675 nm optical depth and nine simulated histograms with different seeds.

seasonal variation, follows a normal distribution ; which is not totally the case in the data, as shown in Figure 3.26 on the right handside of each histogram realisation.

A second proof of concept, this time for the simulated correlation between the aerosol optical depth values at different wavelengths, is shown on Figure 3.27, where the time series and histograms displayed represent the values of the logarithmic polynomial fit (see equation (3.31)) coefficients for the data and a simulation. Again, that Figure shows a good agreement between the data and the simulation, even if the data histograms are slightly more peaky that the simulation one.

The procedure hereby presented has been included into a more general algorithm called the *atmosphere simulator*.

II.2.4 The simulator

The atmospheric simulator is the generic name for the algorithm we have developed, written in Python (collaboration coding language), that outputs the transmission spectrum of photons (without the gray extinction) from the top of the atmosphere to the telescope, given a time and a pointing direction. This algorithm can be split into three main components,

– an atmosphere constituents generator,

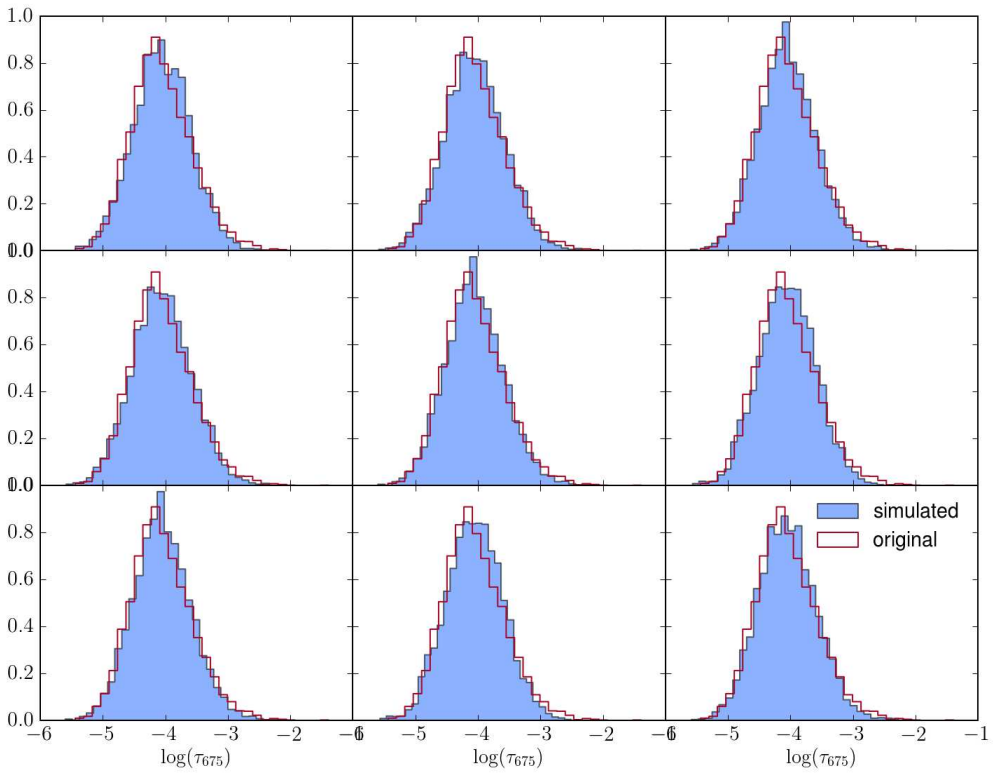

Figure 3.26 – Comparison between original (Mauna Loa) histogram of aerosol 675 nm optical depth excursions around the seasonal variation (brick red line) and nine simulated histograms with different seeds.

– a MODTRAN interface,

– an overall interface that handles long sequences of pointings.

Atmosphere generator

The atmosphere constituents generator is the code component that is related to the weather and physical conditions tied to the LSST location, at Cerro Pachón in Chile. Its goal is first to produce realistic long-term variations of the atmospheric constituents relevant to compute the atmospheric transmission, and then to provide a dictionary with MODTRAN input parameters corresponding to the date of the given pointing or pointing series.

MODTRAN interface

MODerate spectral resolution atmospheric TRANsmittance algorithm and computer model (MODTRAN) is a radiation transfer algorithm that is used to model the spectral absorption,

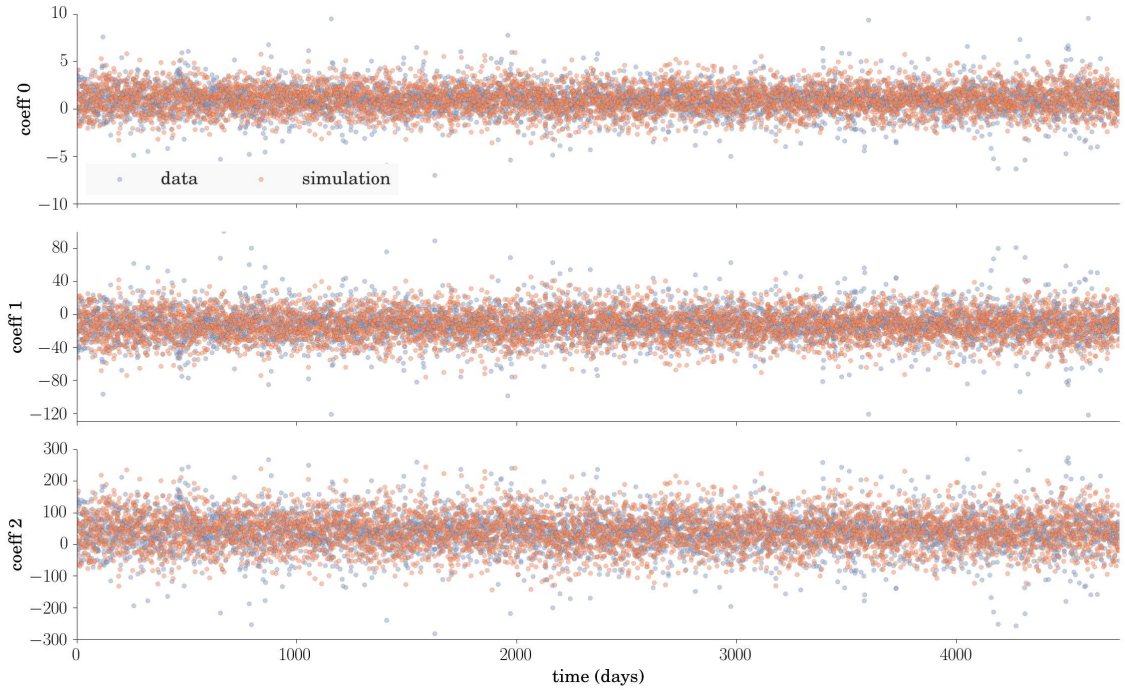

(a) Time series of the data and simulation fit coefficients.

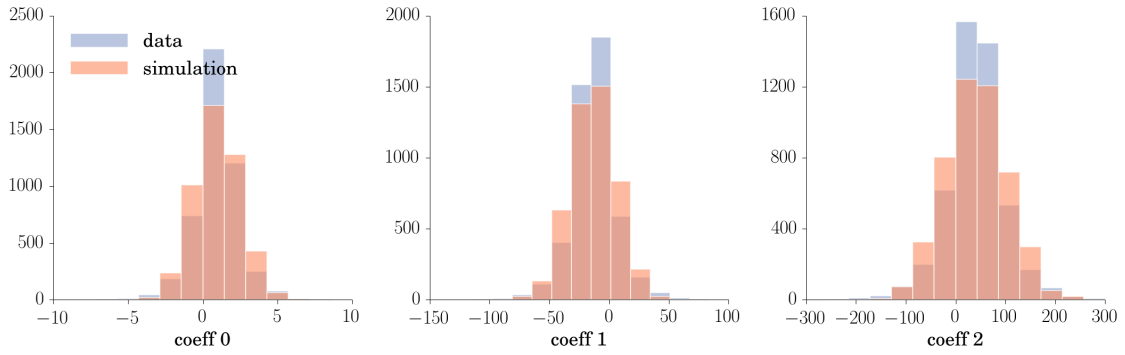

(b) Histograms of the data and simulation fit coefficients.

Figure 3.27 – Time series and histograms of the aerosol optical depth logarithmic polynomial fit coefficients (Eq. (3.31)), computed for the original data (Mauna Loa) and one simulated realisation..

transmission, emission and scattering characteristics of the atmosphere. A brief description of its inputs/outputs is given in Appendix II.2.

The seasonal models of MODTRAN are used to set amplitude of the Rayleigh scattering and molecular absorption from dioxygen, nitrogen and trace elements that scale with barometric pressure.

Atmosphere sequence: the upper layer

The atmosphere sequence module is thought to be the interface between the user and the atmosphere generator. The user provides a list of pointings in the form of dictionaries. In return, he is given, for each pointing, an array corresponding to the atmospheric transmittance per wavelength.[15] The minimum input required for a pointing is

- an identification number ('ID'),
- a date in modified Julian calendar ('MJD')[16],
- a right ascension ('RA'),
- a declination ('DEC').

The algorithm then goes through a number of steps that can be summarized as,

1. generate long-term time-series of atmospheric components
2. retrieve the values of this parameters and compute the zenith angle and azimuth for the given dates
3. run MODTRAN with the relevant information (ozone, water vapor, season, zenith angle, etc.)
4. compute the aerosol spectrum separately and correct for airmass
5. combine with MODTRAN output and save final spectra in output file (text format) along with corresponding wavelengths

When calling the method, the user can also provide a random seed, which can be interpreted as a simulation identification. The atmosphere generator called with the same seed will always return the same atmospheric time-series and thus the same atmospheric transmission for a given pointing.

[15] The wavelength bins are those of MODTRAN

[16] the dates in a given list should not be scattered over a range superior to nine years

The algorithm has been designed to operate in two different kinds of inputs, either with a list of pointing dictionaries stored in a file, or with input directly from user, so-called « on the fly ».

III Conclusions

The narrow band photometry techniques as well as the assumptions about the regularly distributed and slowly varying absorbing layers in the atmosphere have to be completely reconsidered in the framework of LSST. Its wide field-of-view, rapid cadence and broad filters make it particularly vulnerable to all kinds of atmospheric spectral distortions. The major constituents responsible for these distortions have been identified as ozone, water vapor and aerosols ; the first two through molecular absorption, the last one through Mie scattering. Their respective contributions are independent, so each of these constituents can be studied separately.

We showed that ozone can have a non negligible effect on the photometry not knowing its absolute quantity. At such latitudes as Cerro Pachón , the ozone layer, which is at high altitude, is very stable in space and time, and is constantly monitored via satellite, at least once a day. This ensures ozone will not be a problematic constituent for LSST.

On the opposite, water vapor is known to vary quickly in time and space, which it does over Cerro Pachón . The location of the site, between the Pacific ocean and the Andes, is subject to a strong water vapor gradient which can lead to errors up to 1 mm of precipitable water vapor , just on the pointing direction. A way to stay safe concerning the water vapor is to use a micro-wave radiometer, co-pointed with the main telescope, that will retrieve the total column of precipitable water vapor along the line- of-sight.

Concerning the aerosols, we found strong variations of the aerosol spectrum along the line-of-sight over time scales of a few hours, in relation with the development during some periods of a coarse grain aerosol layer near the ground. In addition, this coarse grain layer may have a vertical profile quite different from the fine grain distribution and this profile may change rapidly with time. As a consequence the spectrum is highly airmass sensitive and this sensitivity is also time dependent. Depending on the type of reference star used for calibration, this could lead to huge residual errors on the magnitudes of u and g-bands.

The threat to the LSST photometric calibration posed by the high spectral variation of these constituents, in particular the aerosols, has not been taken into account in the baseline atmospheric model described in Burke et al. (2010). LSST therefore needs a calibration tool that produces realistic situations and atmospheric conditions in order to test and validate the

whole calibration pipeline, or seek for alternative calibration strategies.

In this context, we propose an atmospheric simulator, based on abundant statistics of each of the above mentioned constituents, and producing a realistic atmospheric transmission spectrum at a given time and pointing direction. The simulator uses MODTRAN to retrieve the molecular absorption spectra given the constituents amplitude but computes the aerosol extinction spectrum on its own, using a polynomial fit on the five simulated optical depth at 380 nm, 440 nm, 500 nm, 675 nm and 870 nm.

However, the limitation of such aerosol simulation arises with the lack of AERONET nighly data.[17] The only available data on the variation of the fine and coarse grain populations is restricted to the day, and more particularly the direction of the sun. The sunlight might therefore have a influence on the grain fluctuations which may not happen during the night.

The auxiliary telescope simulator, whose goal is to test the observing strategies of the LSST auxiliary spectrophotometric telescope, might soon be able to tell whether the current atmospheric model with aerosols can be reconstructed or not.

[17] which cannot be provided by a sun-photometer

CHAPTER 4

Cosmic lensing as a cosmological probe

I Gravitational Lensing

Gravitational lensing is the deflection of light bundles when they propagate through a gravitational field. This effect, although suspected long before Einstein's theoretical work, appeared at the beginning of the twentieth century as a direct consequence of Einstein's General Relativity. This theory implies that light propagates along the shortest path between two events, called geodesics. While in the vacuum, the geodesics are straight lines, in the presence of a gravitational potential, these geodesics are slightly bent, and for a photon propagating along them, the deflections are sum up.

The Universe being essentially empty now, most photon trajectories only feel faint gravitational potentials, which results in tiny deflections, even on cosmological scales. However, these trajectories sometimes happen to pass by a massive structure (star, galaxy, galaxy cluster) creating a strong gravitational potential and are therefore deflected much more. Between the mass of the structure and the distance between it and the light path, one can imagine there are lots of different regimes of perturbation, from a the one that can only be detected on average to the clearly visible deflection features, the latter being less likely to occur.

The observation of a strong lensing system with a giant arc was reported by Soucail et al. (1987) and Soucail et al. (1988) on the galaxy cluster Abell 370. The original image was taken at the Canada France Hawaii Telescope (CFHT) and is shown on the left of Figure 4.1. The same lensing system was again studied with higher precision a decade later thanks to the image quality of space telescope such as Hubble (image on the right side of Figure 4.1). This figure illustrates well the tight relation between fundamental science progress and technological improvement. In particular, gravitational lensing have been a flourishing science field in the past fifteen years thanks to the constant development of advanced technologies.

I will start by presenting the general theory of gravitational light deflection, before switching to the weak gravitational regime. Then, I will present the uncertainties associated with shear measurement, before introducing the weak lensing magnification.

I.1 Lensing basics

Gravitational lensing is the science of mapping the propagation of light throughout the cosmos, and more particularly towards Earth. For the cases in this chapter, we assume the geometry of the Universe is well described by the FLRW metric (1.13), and inhomogeneities in the metric leading to gravitational effects will be treated as local perturbations. We start with a simple case of a photon propagating from a source to an observer and flying by a massive object of mass M, referred to as the lens. Under the mentioned assumptions, the photon journey can be

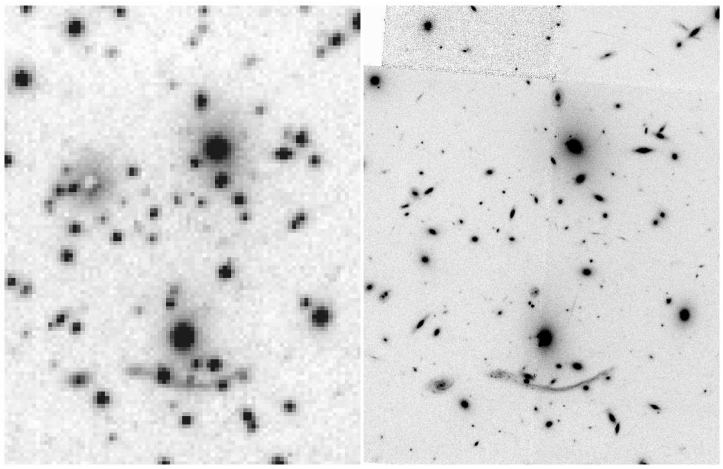

Figure 4.1 – Observations of the same galaxy cluster Abell 370, taken on the left by the Canada France Hawaii Telescope (CFHT) in 1985, and on the right by the Hubble Space Telescope (HST) in 1995.

divided into three main steps. First, the propagation occurs in a flat unperturbed spacetime ; second, it is deviated by the gravitational potential Φ of the lens ; and last, the trajectory from the lens to the observer in a flat unperturbed spacetime, again. This approximation is valid only if the potential is small, i.e. $|\Phi|/c \ll 1$. The goal of this section is to derived the deflection angle of the light occurring during the second step of this journey and study the relation between the position the light source with the one of its perceived image.

In the presence of a Newtonian gravitational potential Φ, the perturbed FLRW metric can be expressed as

$$\mathrm{d}s^2 = \left(1 - \frac{2\Phi}{c^2}\right) c^2 \mathrm{d}t^2 - a^2(t) \left(1 + \frac{2\Phi}{c^2}\right) \left[\frac{\mathrm{d}r^2}{1 - c^2 k\, r^2} + r^2 \left(\mathrm{d}\theta^2 + \sin^2\theta\, \mathrm{d}\phi^2\right)\right] .$$

From the light perspective, entering the lens area, the flat space-time is perturbed by the gravitational potential of the lens resulting in slightly curved geodesics and the photon path is thus bend. An analogy with optics can be made, here, seeing the region around the potential as having a continuously changing refractive index, slighty superior to one. While the empty Universe can be described as a vacuum with a refractive index of 1, nearby the lens the refractive index changes to

$$n = 1 - \frac{2\Phi}{c^2} = 1 + \frac{2|\Phi|}{c^2}$$

which is superior to unity because the gravitational potential is negative. As for geometrical optics, when the refractive index changes along the light propagation, the photon path exiting the lens system has deviated from the incoming photon path by a certain angle, which is referred

to as the deflection angle.

I.1.1 Deflection angle

The deflection angle can easily be measured by integrating over the path λ the tiny deflections coming from the gradient of the refractive index perpendicular to the trajectory,

$$\begin{aligned}\hat{\boldsymbol{\alpha}} &= -\int \boldsymbol{\nabla}_\perp n \,\mathrm{d}\lambda \\ &= \frac{2}{c^2}\int \boldsymbol{\nabla}_\perp \Phi \,\mathrm{d}\lambda\,,\end{aligned} \tag{4.1}$$

where the negative factor accounts for the incoming ray (Bonometto et al., 2010). Due to the small perturbation in the cases of our concern[1], the deflection angle remains small. The *Born approximation*, whose cosmological version states that in the presence of a small deflection angle $\hat{\boldsymbol{\alpha}}$, the integral along the true light path λ can be replaced by an integral along the unperturbed (straight) light path, denoted by z in the following.

A common example is to take the Newtonian gravitational potential of a point-like lens of mass M

$$\Phi(r) = -\frac{GM}{r} = -\frac{GM}{\sqrt{\xi^2+z^2}}\,,$$

where ξ is the impact parameter of the light path assumed to be larger that the Schwartzschild radius of the lens, and z the position along the unperturbed path. Its perpendicular gradient reads

$$\nabla_\perp \Phi = -GM\,\frac{\partial}{\partial \xi}\left(\frac{1}{\sqrt{\xi^2+z^2}}\right) = \frac{GM\xi}{(\xi^2+z^2)^{3/2}}\,,$$

and is then integrated along the unperturbed path to find the deflection angle

$$\hat{\alpha} = \frac{2}{c^2}\int \frac{GM\xi}{(\xi^2+z^2)^{3/2}}\,\mathrm{d}z = \frac{2\,GM}{c^2\xi}\int \frac{\mathrm{d}z'}{(1+z'^2)^{3/2}} = \frac{4\,GM}{c^2\xi}\,. \tag{4.2}$$

It is worth noting that the Schwartzschild radius of an astrophysical object of mass M being $R_\mathrm{S} = 2\,GM/c^2$ this object bends a light ray passing at a distance ξ from its center with an angle $\hat{\alpha} = 2R_\mathrm{S}/\xi$. For the solar mass, the Schwartzschild radius is about 1.5 km. Hence, the light from background sources observed during an eclipse at the outer edge of the Sun is deflected with an angle

$$\hat{\alpha}_\mathrm{sun} = 2R_\mathrm{S}/r_\mathrm{sun} \simeq 2\times 1.5/7.10^5 \simeq 0.9 \text{ arcsec}\,.$$

[1]The case of gravitational lensing by black holes will not be treated here.

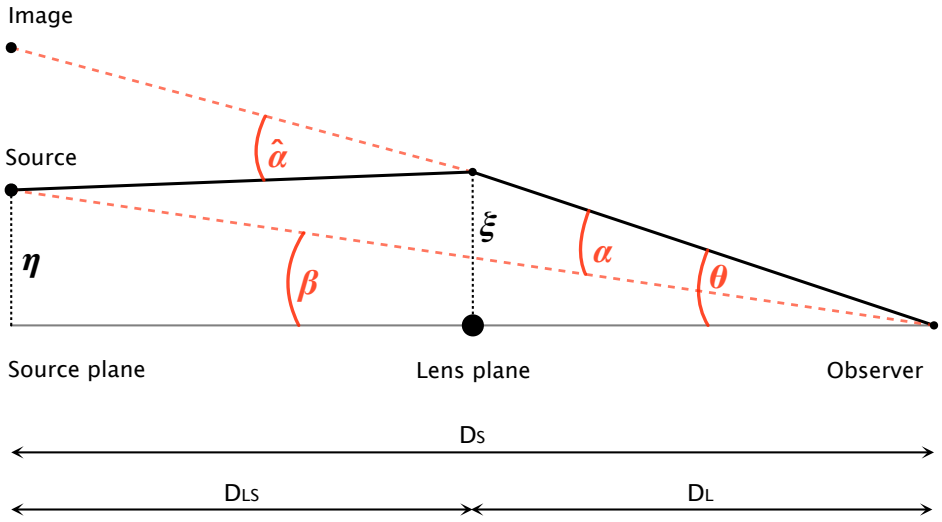

Figure 4.2 – Schematic view of a typical gravitational lens system.

I.1.2 The lens equation

We shall now follow the light path from the observer back to the source. On Figure 4.2 one can see a sketch of the studied system, composed by a point-like observer, a lens and the corresponding lens plane, and a source, sitting in the source plane. We define the distances D_l, D_s and D_ls, respectively from the observer to the lens, from the observer to the source plane, and from the lens to the source plane. Introducing $\boldsymbol{\eta}$ the two-dimensional position of the source in the source plane, and making use of the smallness of angles $\tan\hat{\alpha} \approx \hat{\alpha} \approx \sin\hat{\alpha}$, we can write the geometrical relation,

$$\boldsymbol{\eta} = \frac{D_\mathrm{s}}{D_\mathrm{l}}\,\boldsymbol{\xi} - D_\mathrm{ls}\,\hat{\boldsymbol{\alpha}}(\boldsymbol{\xi})\,. \tag{4.3}$$

Now introducing new angular coordinates $\boldsymbol{\beta}$ and $\boldsymbol{\theta}$ defined as $\boldsymbol{\eta} = D_\mathrm{s}\,\boldsymbol{\beta}$ and $\boldsymbol{\xi} = D_\mathrm{l}\,\boldsymbol{\theta}$, equation (4.3) can be rewritten as

$$D_\mathrm{s}\,\boldsymbol{\beta} = D_\mathrm{s}\,\boldsymbol{\theta} - D_\mathrm{ls}\,\hat{\boldsymbol{\alpha}}(D_\mathrm{l}\,\boldsymbol{\theta})\,.$$

Going a step further and canceling the source distance and introducing the *reduced deflection angle* (the angle between the true and image positions of the source)

$$\boldsymbol{\alpha} = \frac{D_\mathrm{ls}}{D_\mathrm{s}}\,\hat{\boldsymbol{\alpha}}\,, \tag{4.4}$$

one finds the *lens equation*

$$\boldsymbol{\beta} = \boldsymbol{\theta} - \boldsymbol{\alpha}(\boldsymbol{\theta})\,. \tag{4.5}$$

This equation allows to retrieve the true source position from the lensed image position, provided information on the lens.

Point mass example

In the previous example of the point mass lens, using equation (4.2) with the newly defined coordinates and the lens equation yields

$$\beta = \theta - \frac{4GM}{c^2 D_\mathrm{l}\,\theta}\frac{D_\mathrm{ls}}{D_\mathrm{s}} \tag{4.6}$$

$$= \theta - \frac{\theta_0^2}{\theta}\,, \tag{4.7}$$

with

$$\theta_0^2 = \frac{4GM}{c^2}\frac{D_\mathrm{ls}}{D_\mathrm{l} D_\mathrm{s}}\,.$$

θ_0 is usually referred to as the *Einstein radius* or the radius of an annular image surrounding a point mass source M if the source and the lens are both aligned. Equation (4.7) can be rewritten as a traditional quadratic equation in θ

$$\theta^2 - \beta\theta - \theta_0^2 = 0\,,$$

which admits two distinct solutions

$$\theta_\pm = \frac{1}{2}\left[\beta \pm \sqrt{\beta^2 + 4\theta_0^2}\right]\,.$$

This tells us that in such system configuration, gravitational lensing will produce two images of the source. Their distance with respect to the center of the lens is given by those two theta angles. For the study of more realistic systems please refer to e.g. Bartelmann & Schneider (2001) or a recent review Bartelmann (2010).

I.1.3 The effective lensing potential

From Equations (4.1) and (4.4) we can write

$$\boldsymbol{\alpha} = \frac{2}{c^2}\frac{D_\mathrm{ls}}{D_\mathrm{s}}\int \boldsymbol{\nabla}_\perp \Phi \,\mathrm{d}\lambda\,. \tag{4.8}$$

Using the thin lens approximation (Blandford & Kochanek, 1987), we can swap the integral and the gradient

$$\boldsymbol{\alpha} = \frac{2}{c^2}\frac{D_\mathrm{ls}}{D_\mathrm{s}}\,\boldsymbol{\nabla}_\perp \int \Phi \,\mathrm{d}\lambda\,;$$

and with the obvious relation between gradients when using the angular coordinates

$$\boldsymbol{\nabla}_\perp = \frac{1}{D_\mathrm{l}}\,\boldsymbol{\nabla}_{\boldsymbol{\theta}}\,,$$

we end up with the formula

$$\boldsymbol{\alpha} = \boldsymbol{\nabla}_{\boldsymbol{\theta}}\left[\frac{2}{c^2}\frac{D_\mathrm{ls}}{D_\mathrm{l}D_\mathrm{s}}\int \Phi\,\mathrm{d}\lambda\right].$$

We can now define the lensing potential

$$\psi(\boldsymbol{\theta}) \equiv \frac{2}{c^2}\frac{D_\mathrm{ls}}{D_\mathrm{l}D_\mathrm{s}}\int \Phi(D_\mathrm{l}\boldsymbol{\theta},\lambda)\,\mathrm{d}\lambda\,, \tag{4.9}$$

which is the weighted projection of the Newtonian potential, so that the reduced deflection angle is its gradient

$$\boldsymbol{\alpha} = \boldsymbol{\nabla}_{\boldsymbol{\theta}}\psi\,. \tag{4.10}$$

I.1.4 Surface-mass density

The divergence of the reduced deflection angle is the Laplacian of the lensing potential

$$\boldsymbol{\nabla}.\,\boldsymbol{\alpha} = \boldsymbol{\nabla}^2\psi = \frac{2}{c^2}\frac{D_\mathrm{l}D_\mathrm{ls}}{D_\mathrm{s}}\int \boldsymbol{\nabla}_\perp^2\,\Phi\,\mathrm{d}\lambda\,. \tag{4.11}$$

In Equation (4.11), following the previous definitions, only the perpendicular component Laplacian of the Newtonian potential is integrated. The integration of the parallel component of the Laplacian

$$\begin{aligned}\int \frac{\partial^2\Phi}{\partial\lambda^2}\,\mathrm{d}\lambda &= \left.\frac{\partial\Phi}{\partial\lambda}\right|_{\text{boundaries}}\\ &= \quad 0 \qquad \text{far from the lens}\end{aligned}$$

vanishes as long as the boundaries are chosen far for the potential (the lens) which is always true in cosmological cases for isolated lensing mass distributions. The parallel term can thus be added to the Laplacian to get the full three-dimensional Laplacian

$$\boldsymbol{\nabla}^2\psi = \frac{2}{c^2}\frac{D_\mathrm{l}D_\mathrm{ls}}{D_\mathrm{s}}\int\left(\boldsymbol{\nabla}_\perp^2 + \frac{\partial^2}{\partial\lambda^2}\right)\Phi\,\mathrm{d}\lambda \tag{4.12a}$$

$$= \frac{2}{c^2}\frac{D_\mathrm{l}D_\mathrm{ls}}{D_\mathrm{s}}\int \boldsymbol{\nabla}_r^2\Phi\,\mathrm{d}\lambda\,. \tag{4.12b}$$

Poisson's equation relate the Laplacian of the potential to the mass density ρ of the lens,

$$\boldsymbol{\nabla}_r^2 \Phi = 4\pi G \rho \,, \tag{4.13}$$

and inserting (4.13) into (4.12) yields

$$\boldsymbol{\nabla}^2 \psi = \frac{8\pi G}{c^2} \frac{D_\mathrm{l} D_\mathrm{ls}}{D_\mathrm{s}} \, \Sigma(\boldsymbol{\theta}) \,, \tag{4.14}$$

where we introduce the projected surface-mass density of the gravitational lens,

$$\Sigma(\boldsymbol{\theta}) = \int \rho(D_\mathrm{l}\boldsymbol{\theta}, \lambda) \, \mathrm{d}\lambda \,. \tag{4.15}$$

The Laplacian of the lensing potential being dimensionless, the expression in front of Σ in equation (4.14) has the dimension of an inverse surface-mass density. We therefore define the critical surface-mass density

$$\Sigma_\mathrm{cr} = \frac{c^2}{4\pi G} \frac{D_\mathrm{s}}{D_\mathrm{l} D_\mathrm{ls}} \,, \tag{4.16}$$

so that the lensing potential now obeys the Poisson equation

$$\boldsymbol{\nabla}^2 \psi(\boldsymbol{\theta}) = 2 \, \kappa(\boldsymbol{\theta}) \,, \tag{4.17}$$

where

$$\kappa(\boldsymbol{\theta}) = \frac{\Sigma(\boldsymbol{\theta})}{\Sigma_\mathrm{cr}} \tag{4.18}$$

is called convergence and will be defined in more details in the following subsection. The convergence can be used to encapsulate the properties of a system [observer/lens plane/source plane], and solve equation (4.17) in two dimensions, yielding the lensing potential

$$\psi(\boldsymbol{\theta}) = \frac{1}{\pi} \int \kappa(\boldsymbol{\theta}') \ln |\boldsymbol{\theta} - \boldsymbol{\theta}'| \, \mathrm{d}^2\boldsymbol{\theta}' \,. \tag{4.19}$$

Inserting (4.19) into the formula (4.10) yields a new expression for the reduced deflection angle

$$\boldsymbol{\alpha}(\boldsymbol{\theta}) = \frac{1}{\pi} \int \frac{\kappa(\boldsymbol{\theta}')(\boldsymbol{\theta} - \boldsymbol{\theta}')}{|\boldsymbol{\theta} - \boldsymbol{\theta}'|^2} \, \mathrm{d}^2\boldsymbol{\theta}' \,.$$

I.1.5 Light distortion and magnification

A point-like source at $\boldsymbol{\beta}$ can produce multiple images located at the angular positions $\boldsymbol{\theta}$ solutions of the lens equation (4.5) (*cf.* section I.1.2). For extended sources, the shape of the images will

vary from the shape of the source because light bundles are deflected differentially. Therefore, the shape of the image must be determined in principal by solving the lens equation for all points within the extended source. Liouville theorem implies that lensing conserves the surface brightness in absence of emission of absorption of photons. Thus, if $I^s(\boldsymbol{\beta})$ is the surface brightness distribution in the source plane, the observed surface brightness distribution in the lens plane is

$$I(\boldsymbol{\theta}) = I^s[\boldsymbol{\beta}(\boldsymbol{\theta})]\,. \tag{4.20}$$

If a source is much smaller than the angular size at which the lens properties change, the lens mapping can be locally linearized. The distortion of images is then described by a Jacobi matrix. The one that yields the inverse mapping (the true shape of the source given the shape of its image) is called the *amplification matrix* $\mathcal{A}$ and has the components

$$\mathcal{A}_{ij} = \frac{\partial \beta_i}{\partial \theta_j} = \delta_{ij} - \frac{\partial^2 \psi}{\partial \theta_j \partial \theta_i} = \delta_{ij} - \psi_{ij}\,, \tag{4.21}$$

where δ_{ij} is the Kronecker symbol and for simplicity we defined

$$\psi_{ij} \equiv \frac{\partial^2 \psi}{\partial \theta_j \partial \theta_i}\,.$$

A Jacobian matrix can generally be decomposed into a kernel (a matrix whose trace is zero and referred to as tracefree), and a projection matrix. The tracefree part preserves the volume in general, and here particularly, the area of the surface of background objects. This is a local distortion matrix. The part left is a scalar projection yielding a local isotropical enlargement or shrinkage of the objects. Taking the trace of the amplification matrix,

$$\mathrm{Tr}(\mathcal{A}) = 2 - \boldsymbol{\nabla}^2 \psi = 2\,(1 - \kappa)\,, \tag{4.22}$$

and inserting (4.17) into (4.22), the tracefree part of the matrix reads as

$$\mathcal{A} - \frac{1}{2}\,\mathrm{Tr}(\mathcal{A})\,\mathcal{I} \equiv -\begin{pmatrix} \gamma_1 & \gamma_2 \\ \gamma_2 & -\gamma_1 \end{pmatrix}\,, \tag{4.23}$$

where $\mathcal{I}$ is the two-dimensional unit matrix and introducing the shear γ and its components

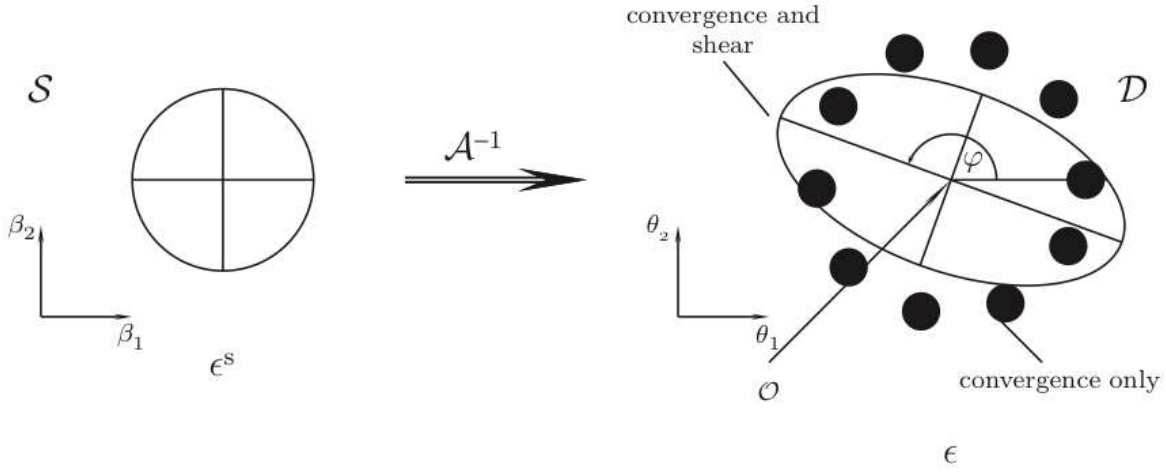

Figure 4.3 – Schematic view of the lensing distortions (right) applied to a circular source (left). The shear and convergence effects are decoupled to show their respective contribution (credit M. Bradac).

components $\gamma \equiv \gamma_1 + \imath\,\gamma_2 = |\gamma|\, e^{2\imath\,\varphi}$, related to the potential by

$$\gamma_1 = \frac{1}{2}\,(\psi_{11} - \psi_{22}) \tag{4.24a}$$

$$\gamma_2 = \psi_{12}\,. \tag{4.24b}$$

The amplification matrix can thus be written using (4.22) and (4.23)as

$$\mathcal{A} = \begin{pmatrix} 1-\kappa-\gamma_1 & -\gamma_2 \\ -\gamma_2 & 1-\kappa+\gamma_1 \end{pmatrix}, \tag{4.25}$$

and generally admits two eigenvalues

$$\lambda_\pm = 1 - \kappa \pm \gamma\,, \tag{4.26}$$

and a determinant

$$\det(\mathcal{A}) = \lambda_+\,\lambda_- = (1-\kappa)^2 - \gamma^2\,. \tag{4.27}$$

If $\boldsymbol{\theta}_0$ is a point within an image, corresponding to the point $\boldsymbol{\beta}_0 = \boldsymbol{\beta}(\boldsymbol{\theta}_0)$, the lens equation can be linearized locally around that point,

$$\boldsymbol{\beta} - \boldsymbol{\beta}_0 = \mathcal{A}(\boldsymbol{\theta}_0).(\boldsymbol{\theta} - \boldsymbol{\theta}_0)\,,$$

so that Liouville theorem (4.20) becomes,

$$I(\boldsymbol{\theta}) = I^s[\boldsymbol{\beta}_0 + \mathcal{A}(\boldsymbol{\theta}_0).(\boldsymbol{\theta} - \boldsymbol{\theta}_0)]\,. \tag{4.28}$$

According to equation (4.28), the image of a circularly symmetric sources is an ellipse. The ratios of the semi-axes of such an ellipse to the radius of the source are given by the inverse of the eigenvalues of $\mathcal{A}$ (4.26) and the ratio of the solid angles subtended by an image and the unlensed source is the inverse of the determinant of $\mathcal{A}$ (4.27). The latter is called the magnification factor μ and its expression for a rather small source is given by

$$\mu = \det(\mathcal{A}^{-1}) = \frac{1}{\det(\mathcal{A})} = \frac{1}{(1-\kappa)^2 - \gamma^2}\,. \tag{4.29}$$

Due to all the considerations above, the images of a small source at position $\boldsymbol{\beta}$ are magnified by $|\mu(\boldsymbol{\theta}_i)|$, and the total magnification of the source is given by the sum of the magnifications over all its images

$$\mu(\boldsymbol{\beta}) = \sum_i |\mu(\boldsymbol{\theta}_i)|\,.$$

However, multiple images arise only in certain configurations, where the convergence is greater that unity which means according to (4.18) that the locally the surface mass density is superior to the critical mass density. In such cases, the phenomenon is referred to as *strong* gravitational lensing and can lead to huge distortion features such as giant arcs or Einstein rings. We will leave the strong lensing subject to the literature and instead look more carefully at the opposite case, where the convergence and shear are smaller than unity, called *weak gravitational lensing.*

I.2 Weak lensing regime

So far in this chapter, we have treated gravitational lensing as a physical effect occurring on an isolated system. But since the gravitational field in the Universe is a continuum, every path than photons can take will be subject to a deflection. Since the Universe is quite empty now, strong gravitational system are few. However, most the observed cosmos is subject to tiny deflections that cannot be observed from one image to another, but only on a statistical sense by averaging the images over a certain area (Blanchard & Schneider, 1987). This is called the weak gravitational lensing regime and is characterized by an amplification matrix close to unity.

As any statistical effect, a major source of measurement uncertainty is the low number of observables, here the sources. In order to measure the lensing effect, the spatial average has to be made on a scale within which the the gravitational potential does not change significantly.

Weak lensing surveys are therefore very sensitive to the number density of usable sources for measurement. This is the main reason why it took a decade for weak lensing observations (starting with Tyson et al., 1990) to be cross the threshold of statistical detection (Wittman et al., 2000; Van Waerbeke et al., 2000; Bacon et al., 2001; Rhodes et al., 2001), time for new instruments and techniques to be developed.

One of the major source of noise is the variation of the point spread function (PSF), creating a spurious deformation across the field-of-view. This subject will be treated in more details on page 121.

Before looking at the difficulties of such measurements, we shall briefly describe the theory of shear measurements and its current applications in an ideal case. For the remainder of this chapter, we now only consider cases within the weak lensing regime, that is κ, $|\gamma| \ll 1$.

I.2.1 Shear measurement theory

Galaxies on the sky face our direction with every possible inclination, which make their intrinsic apparent shape somewhat elliptical. Lensing preserves this elliptical shape while adding its own distortion known as shear γ to that ellipticity. The first step for measuring the shear is to measure the shape of galaxies. Considering an isolated galaxy with a brightness distribution $I(\boldsymbol{\theta})$, one can define the first brightness moment of this distribution,

$$\bar{\boldsymbol{\theta}} \equiv \frac{\int \mathrm{d}^2\theta\, I(\boldsymbol{\theta})\, q_I[I(\boldsymbol{\theta})]\, \boldsymbol{\theta}}{\int \mathrm{d}^2\theta\, I(\boldsymbol{\theta})\, q_I[I(\boldsymbol{\theta})]}\,,$$

where $q_I(I)$ is a suitable weight function (e.g. Heaviside step function) that helps distinguishing the source boundaries from the background sky. $\bar{\boldsymbol{\theta}}$ marks the center of the image. Then one can define the symmetric tensor of second brightness moments,

$$Q_{ij} = \frac{\int \mathrm{d}^2\theta\, I(\boldsymbol{\theta})\, q_I[I(\boldsymbol{\theta})]\, (\theta_i - \bar{\theta}_i)\, (\theta_j - \bar{\theta}_j)}{\int \mathrm{d}^2\theta\, I(\boldsymbol{\theta})\, q_I[I(\boldsymbol{\theta})]}\,; \quad i,j \in \{1,2\}$$

The trace of Q describes the size of the image, whereas the traceless part contains the ellipticity information. The three independent components of this tensor are then used to define the complex ellipticity of the image,

$$\epsilon \equiv \frac{Q_{11} - Q_{22} + 2\imath\, Q_{12}}{Q_{11} + Q_{22} + 2\,\sqrt{\det(Q)}}\,.$$

The phase of ϵ indicates the orientation of the ellipse with respect to the θ_1-axis. If the elliptical image were to have a major axis a and minor axis b, then one would find $|\epsilon| = (1-b/a)/(1+b/a)$.

Both Q and ϵ are lensed observables. The measured tensor of second brightness moments can be linked to the unlensed one Q^s via the amplification matrix $\mathcal{A}$,

$$Q^s = \mathcal{A}\, Q\, \mathcal{A}^T \,.$$

Since we are interested in the measurement of the tidal distortion due to shear and not the isotropic enlargement, it is useful to separate both lensing contributions in the amplification matrix and redefine it as

$$\mathcal{A}(\boldsymbol{\theta}) = (1-\kappa) \begin{pmatrix} 1-g_1 & -g_2 \\ -g_2 & 1+g_1 \end{pmatrix} , \tag{4.30}$$

where g is called the *reduced shear*

$$g \equiv \frac{\gamma}{1-\kappa} = \frac{|\gamma|}{1-\kappa}\, e^{2\imath\,\varphi} \,. \tag{4.31}$$

Using this new observable, Seitz & Schneider (1997) showed the observed ellipticity could be related to the unlensed one via the expression

$$\epsilon = \frac{\epsilon^s + g}{1 + \epsilon^s g^*} \approx \epsilon^s + g \approx \epsilon^s + \gamma \,, \tag{4.32}$$

which turns out to be a very simple sum of the intrinsic ellipticity plus the shear term in the weak regime. However the intrinsic ellipticity is not accessible via observations. In order to measure the shear, the assumption that galaxies are randomly distributed in the Universe has to be made, which translates to

$$\langle \epsilon^s \rangle = 0 \,, \tag{4.33}$$

provided the average is made a large enough number of galaxies. Hence measuring the average ellipticity of galaxies in a given region yields a measure of the local shear

$$\langle \epsilon \rangle \approx g \approx \gamma \,. \tag{4.34}$$

This key result of the shear theory proves that each image ellipticity provides a noisy but unbiased estimate of the local shear. The noise associated to that measurement is determined by the intrinsic ellipticity dispersion of galaxies

$$\sigma_\epsilon = \sqrt{\langle \epsilon^s\, \epsilon^{s*} \rangle} \,, \tag{4.35}$$

in the sense that, when averaging over N galaxies subject to the same shear, the 1-σ deviation of their mean ellipticity from the true shear is

$$\sigma = \frac{\sigma_\epsilon}{\sqrt{N}} \,. \tag{4.36}$$

This shear signal can be exploited to create mass maps of small systems, using the relation between the shear and the convergence, derived from equations (4.19) and (4.24)

$$\gamma(\boldsymbol{\theta}) = \frac{1}{\pi} \int \mathrm{d}^2\theta' \mathcal{D}(\boldsymbol{\theta} - \boldsymbol{\theta}')\, \kappa(\boldsymbol{\theta}') \quad \text{with} \quad \mathcal{D}(\boldsymbol{\theta}) = \frac{\theta_2^2 - \theta_1^2 - 2\imath\, \theta_1\theta_2}{|\boldsymbol{\theta}|^4} \,.$$

It can also be used to map out the matter in the Universe on cosmological scales. This requires a bit more equations.

I.2.2 Cosmic shear: weak lensing on cosmological scales

For cosmological light deflection, we are interested in the deflection angle of a beam with respect to another beam. The detailed computation of this differential deflection can be found in Bartelmann & Schneider (2001). The is to compute the deflection angle and the lensing quantities as a function of the density contrast, the redshift and the cosmological parameters.

The deflection angle first computed for a simple system in equation (4.8), can be rewritten in the cosmological perspective using cosmological distances defined on Section III, page 17,

$$\boldsymbol{\alpha}(\boldsymbol{\theta}, \chi) = \frac{2}{c^2} \int_0^\chi \mathrm{d}\chi' \frac{f_k(\chi - \chi')}{f_k(\chi)} \boldsymbol{\nabla}_\perp \Phi\left(f_k(\chi')\boldsymbol{\theta}, \chi\right) \,. \tag{4.37}$$

Using equations (4.11) and (4.17), we can write the cumulative effective convergence along the line-of-sight

$$\begin{aligned} \kappa_{\mathrm{eff}}(\boldsymbol{\theta}, \chi) &= \frac{1}{2} \boldsymbol{\nabla}_{\boldsymbol{\theta}} . \boldsymbol{\alpha}(\boldsymbol{\theta}, \chi) \\ &= \frac{1}{c^2} \int_0^\chi \mathrm{d}\chi' \frac{f_k(\chi - \chi')\, f_k(\chi')}{f_k(\chi)} \boldsymbol{\nabla}_\perp^2 \Phi\left(f_k(\chi')\boldsymbol{\theta}, \chi\right) \,. \end{aligned} \tag{4.38}$$

Following the same assumptions as in equations (4.12), the perpendicular derivative can be replaced by the three-dimensional Laplacian. The 3-D Laplacian of the potential, whose expression is given by equation (4.13), need to be expressed in the cosmological context, that is using comoving coordinates $\boldsymbol{\nabla}_x = a\, \boldsymbol{\nabla}_r$, the matter density of the Universe $\rho = \rho_{\mathrm{m}} a^{-3} = (3\Omega_{\mathrm{m}} H_0^2)/(8\pi G a^3)$

and the density contrast in the line-of-sight $\delta(\boldsymbol{x}, \chi)$,

$$\begin{aligned}\boldsymbol{\nabla}_x^2 \Phi &= 4\pi G a^2 \rho\, \delta \\ &= 4\pi G a^2 \times \frac{3\,\Omega_\mathrm{m} H_0^2}{8\pi G a^3}\,\delta \\ &= \frac{3\,\Omega_\mathrm{m} H_0^2}{2}\,\frac{\delta}{a}\,.\end{aligned}$$

The effective convergence (4.38) therefore becomes

$$\kappa_\mathrm{eff}(\boldsymbol{\theta}, \chi) = \frac{3\,\Omega_\mathrm{m} H_0^2}{2\,c^2} \int_0^\chi \mathrm{d}\chi'\, \frac{f_k(\chi - \chi')\, f_k(\chi')}{f_k(\chi)}\, \frac{\delta(f_k(\chi')\boldsymbol{\theta}, \chi')}{a(\chi')}\,. \tag{4.39}$$

This expression can now be generalized for a redshift distribution $p(z)$ of the sources. They are no longer at a distance χ but spread between us and the comoving horizon distance χ_H. We introduce the weighted projection of the effective convergence

$$\kappa(\boldsymbol{\theta}) = \int_0^{\chi_\mathrm{H}} \mathrm{d}\chi\, p(\chi)\, \kappa_\mathrm{eff}(\boldsymbol{\theta}, \chi)\,, \tag{4.40}$$

where $p(\chi)\,\mathrm{d}\chi = p(z)\,\mathrm{d}z$. A commonly found expression of (4.40) is

$$\kappa(\boldsymbol{\theta}) = \frac{3\,\Omega_\mathrm{m} H_0^2}{2\,c^2} \int_0^{\chi_\mathrm{H}} \mathrm{d}\chi\, \frac{g(\chi)\, f_k(\chi)}{a(\chi)}\, \delta(f_k(\chi)\,\boldsymbol{\theta}, \chi)\,, \tag{4.41}$$

where

$$g(\chi) = \int_\chi^{\chi_H} \mathrm{d}\chi'\, p_g(\chi')\, \frac{f_k(\chi' - \chi)}{f_k(\chi')}\,, \tag{4.42}$$

is referred to as the *lensing efficiency*. The latter represents the cosmological counterpart of optics efficiency when trying to find the position of the lens that maximized the magnification of the object. Figure 4.4 shows some contours representing the best lens position for a range of redshift of the source.

Without going much further into details (more detailed explanations can be found e.g. in Bartelmann, 2010), the Fourier transform of the convergence field κ,

$$\tilde{\kappa}(\boldsymbol{\ell}) = \int \mathrm{d}^2\theta\, e^{\imath\, \boldsymbol{\ell}.\boldsymbol{\theta}} \kappa(\boldsymbol{\theta})\,, \tag{4.43}$$

is tightly coupled to that of the shear:

$$\tilde{\gamma}(\boldsymbol{\ell}) = e^{2\imath\,\beta} \tilde{\kappa}(\boldsymbol{\ell}) \tag{4.44}$$

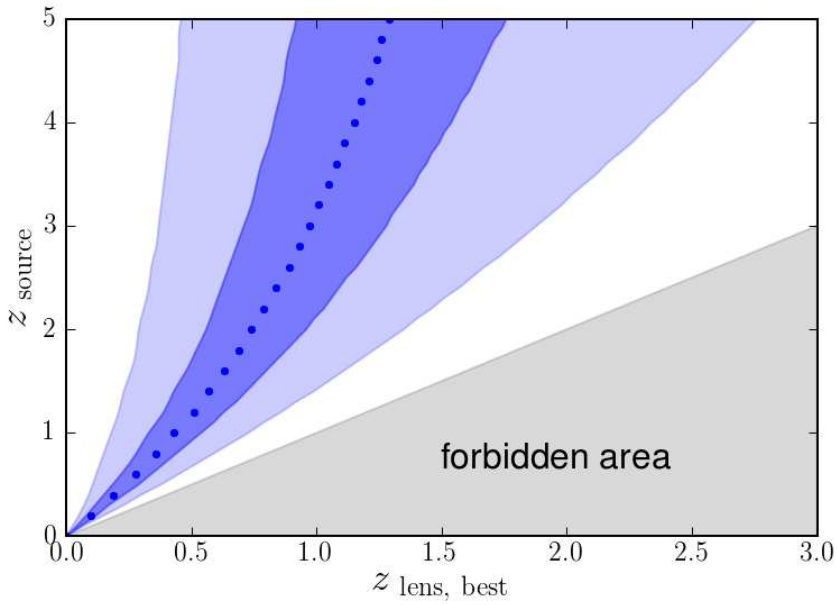

Figure 4.4 – Lensing efficiency contours plotted for lens-source redshift configurations. Dark blue and light blue represent, respectively, 95% and 68% of the maximum efficiency, plotted in dotted blue.

where β is the polar angle of the wave-vector $\boldsymbol{\ell}$. This relation implies that their two-point correlation functions are identical

$$\langle \tilde{\gamma}(\boldsymbol{\ell})\, \tilde{\gamma}^*(\boldsymbol{\ell}') \rangle = \langle \tilde{\kappa}(\boldsymbol{\ell})\, \tilde{\kappa}^*(\boldsymbol{\ell}') \rangle = (2\pi)^2 \delta_{\rm D}(\boldsymbol{\ell} - \boldsymbol{\ell}')\, P_\kappa(\ell) \tag{4.45}$$

and related to the shear power spectrum P_κ. The shear / convergence power spectrum is thus obtained via shear measurements, thus tightly related to shape measurements (*cf.* equation (4.34)). After establishing the ideal case, let us now look at the shear measurement uncertainty that can pollute the spectrum estimation.

II Weak lensing: from shear to magnification

Weak lensing science is accomplished using galaxy surveys, which refer in this context to catalogs of any type of distant astrophysical sources: red/blue/sub-millimeter galaxies, etc. For each source in such catalogs, the minimum required information is the redshift, the coordinates in the sky and the measured ellipticity specifically for weak lensing shear measurements.

Shear measurements in a wide-survey consist of creating sky patches to make local spatial averages of the measured ellipticity. The randomness of the unlensed source ellipticity ensures

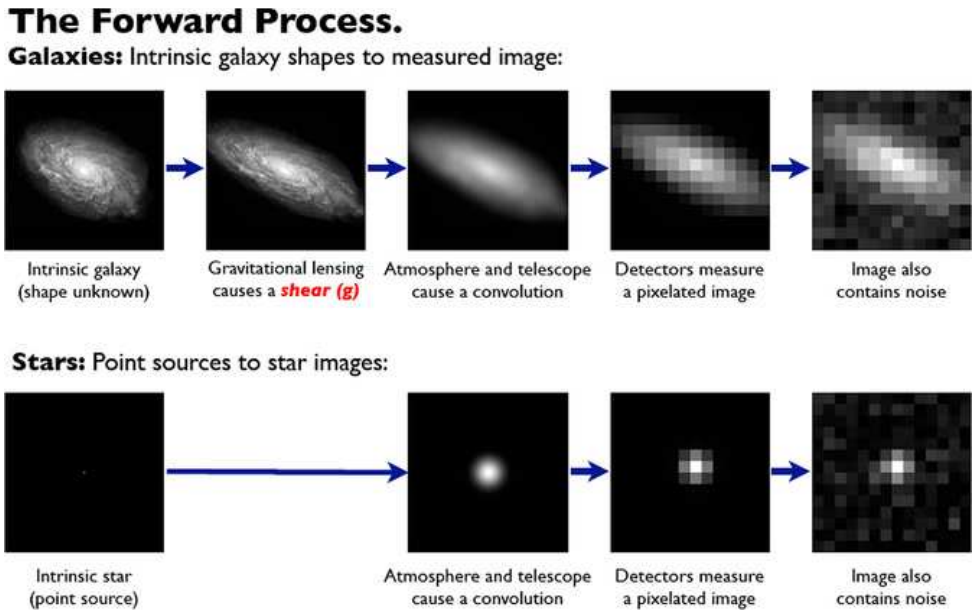

Figure 4.5 – Process of image degradation from the true image of a source, to the raw image obtained in the instrument (source Bridle et al. (2009)).

that the spatial average of intrinsic ellipticities on the sky should be zero (*cf.* equation (4.33)), approximation that should hold on small individual patches as long as the number of sources in the patch is significant (> 10), and thus provide a measurement of the local shear γ (4.34). However, the ellipticity measurement process itself is a rather complicated task, associated with instrumental as well as some intrinsic uncertainty.

II.1 Shape measurement errors

II.1.1 Instrumental issues

When observing the sky, either from the ground or from space, the images are altered by a few instrumental features. Among them, the three most relevant for shape measurement are

- the point-spread function (or PSF),
- the pixelization,
- the noise .

These are well illustrate by Figure 4.5.

The PSF is the instrument response to a point-like source. It is affected by instrumental (detector) response as well as atmospheric turbulence for ground- based surveys, that creates a blurring pattern on the image leading in our case to an biased ellipticity. Whereas with small

fields-of-view experiments, one can approximate a single PSF for the image, in the case of very large cameras, the PSF needs to be modeled in real-time, simultaneously across the focal plane.

Pixelization is another recurring issue. For most digital cameras, the pixels have a squared shape so the measured flux from a source is the sum of the intensity in the enlighted pixels. Detecting a source only requires that photons hit a single pixel, but measuring a shape requires more than one pixel. This is pure sampling consideration (see the Nyquist sampling theorem). The more pixels per object, the better the sampling and thus the cleaner the shape.

Eventually, images contain photon noise. The low number of photons hitting the detector follows a Poisson distribution which tends to light up some dark (background) pixels. Hence there is a need for *background removal* to make faint objects appear on the image. Removing too much background leads too a lost in flux.

II.1.2 Intrinsic alignments contamination

The simple picture of shear assumes that galaxy shapes are random and average down as $1/\sqrt{N}$. Unfortunately some galaxies exhibit correlations of their intrinsic shapes that contaminate the lensing effect. The intrinsic shapes can also be correlated with the density field, which causes an additional type of systematic error. These effects are called intrinsic alignments and are of two kinds, referred to as GI and II terms, plotted on Figure 4.6.

The first, easy to understand, is when two galaxies belong and are affected by a common dark matter gravitational potential, which imposes tidal forces that tend to align the galaxies. This II term therefore creates a correlation between both ellipticities, at first supposed to be independent. This is represented by Figure 4.6a.

The second effect appears when the gravitational potential that contributes to the lensing signal of a distant source (in red on Figure 4.6b) also tidally aligns a close by galaxy. It creates a correlation between spatially uncorrelated galaxies

These effects are being modeled and in the future it may be possible to eliminate it by using its different redshift dependence with tomography. Although they will always be contaminated by instrinsic alignments, the improvement of instruments have lead to the development of new techniques to improve the accuracy of shape measurements.

II.2 Weak lensing shear: improving measurement accuracy

II.2.1 Shear measurement challenges

The techniques dedicated to processing a raw image, deconvolving the PSF, dealing with noise and pixelization and outputting a catalog of galaxy ellipticities have greatly improved over the

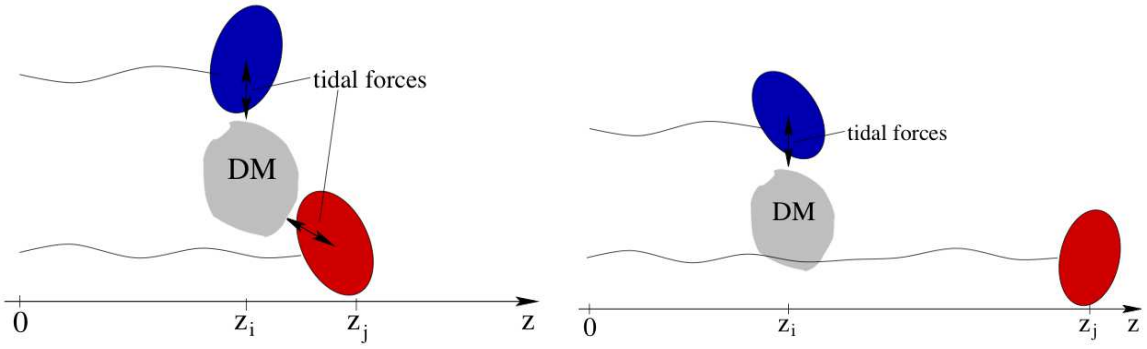

(a) II term. (b) GI term.

Figure 4.6 – Schematic view of the intrinsic alignment effects in the line-of-sight (source B. Joachimi).

last decade. That constant improvement is quite unique in fundamental physics as it has been driven by challenges thrown out to the scientific community. It started with the STEP programs described in Heymans et al. (2006) and Massey et al. (2007) ; followed by the GREAT challenges (Bridle et al., 2009; Kitching et al., 2011; Mandelbaum et al., 2013, ongoing). These wide open image analysis contests gathered people (mathematicians, engineers) with no previous knowledge of astronomy, to tackle a problem bringing their pure unbiased knowledge. This way, new ideas emerge over the years and some techniques are perfected.

II.2.2 Higher order moments

In order to quantify how convergence and shear change across an image, one can use lensing fields which are third-order derivatives of the lensing potential ψ, called flexion. First combining the two components of the gradient $\boldsymbol{\nabla}_\theta$ into two operators

$$\partial = \frac{\partial}{\partial\theta_1} + \imath\,\frac{\partial}{\partial\theta_2} \quad \text{and} \quad \partial^* = \frac{\partial}{\partial\theta_1} - \imath\,\frac{\partial}{\partial\theta_2}\,, \tag{4.46}$$

the convergence and the shear can be expressed, using (4.17) and (4.24), as

$$\kappa = \frac{1}{2}\,\partial^*\partial\psi\,, \quad \gamma = \frac{1}{2}\,\partial\partial\psi\,. \tag{4.47}$$

One can therefore introduce the F flexion

$$F = \partial\kappa = \frac{1}{2}\,\partial\partial^*\partial\psi = \frac{1}{2}\,(\psi_{111} + \psi_{122}) + \frac{\imath}{2}\,(\psi_{112} + \psi_{222})\,,$$

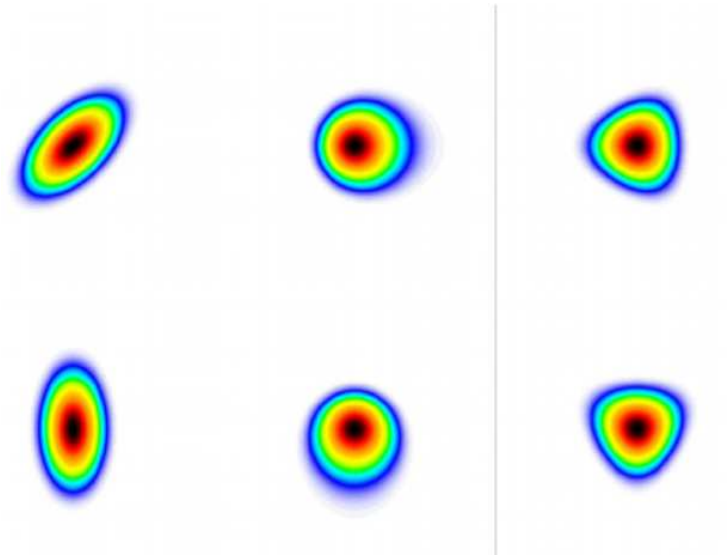

Figure 4.7 – Representation of the second (shear) and third (flexion) moments of the ellipticity of a source image (source M. Bartelmann).

and the G flexion

$$G = \partial\gamma = \frac{1}{2}\,\partial\partial\partial\psi = \frac{1}{2}\,(\psi_{111} - 3\,\psi_{122}) + \frac{i}{2}\,(3\,\psi_{112} - \psi_{222})\,,$$

whose associated distortions are schematically represented on Figure 4.7, along with the shear. They give more flexibility to describe the symmetries of the lensing field.

II.3 Weak lensing magnification: a discrete outsider

Using the same data as for shear measurements, and replacing the shape information of the source by its magnitude, one has access to another gravitational lensing effect, called magnification. Selecting using the redshift a foreground and a background source populations, well separated, one can look at the projected correlation between the position of the foreground sources and the one of the background sources. Without gravitational lensing, there should be no correlations between both populations. Turning on gravitational effects, the mass of the foreground galaxies will modify the light path of background sources close to their surface and will thus enlarge the solid-angle of the background. This has two main effects, sketched on Figure 4.8,

1. decrease the density of background objects in the projected vicinity of foreground ones by isotropically « pushing them away » ⇒ dilution,

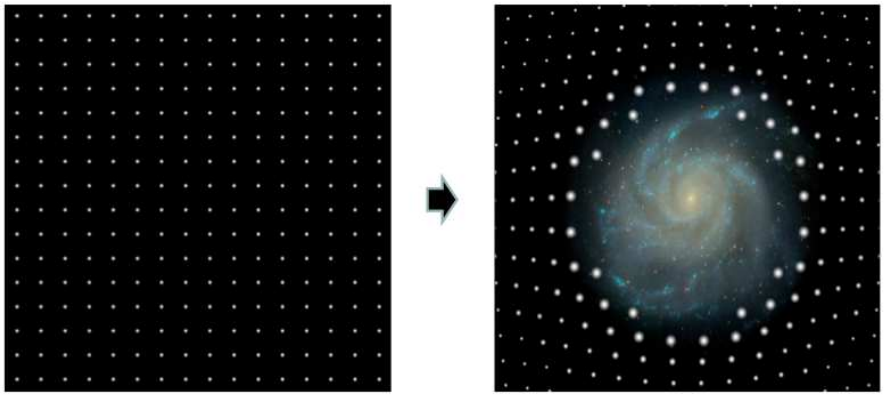

Figure 4.8 – Effect of magnification on a field of circular sources. Left: unlensed, right: lensed (source Y. Mellier).

2. enlarge the background sources size, hence increase their flux[2] and therefore faint sources invisible without lensing become visible ⇒ magnification.

Counting background sources in angular bins for every foreground object (pair count) gives a direct measurement of the two-point angular correlation that is cosmic magnification. The rate of appearance of new background objects is given by the slope of the number count of the selected population. A careful selection of that population allows for either a positive or a negative correlation (*cf.* Section I).

II.3.1 Signal-to-noise

For more than a decade, the higher sensitivity of shear upon magnification convinced numerous scientists that magnification was not worth the effort measuring, shape measurement being much more efficient at constraining the cosmology. These ideas were essentially conveyed by the signal-to-noise ratio formulæ for both observables.

The signal-to-noise ratio of shear, simply taking the shape noise into account (4.36), is given as

$$\left(\frac{\mathrm{S}}{\mathrm{N}}\right)_{\mathrm{shear}} = \frac{|\gamma|}{\sigma_\epsilon}\sqrt{N}\,, \tag{4.48}$$

where σ_ϵ is the typical intrinsic ellipticity dispersion of galaxies and N is the number of objects the shear measurement is averaged on.

In comparison, the signal-to-noise ratio from magnification number counts derived in the

[2]Liouville theorem states that lensing conserves the surface brightness of objects (see equation (4.20))

Bartelmann & Schneider (2001) (and justified in Chapter 5) reads

$$\left(\frac{\mathrm{S}}{\mathrm{N}}\right)_{\mathrm{counts}} = 2\,\kappa\,|\alpha - 1|\,\sqrt{N}\,, \tag{4.49}$$

where α is the logarithmic slope of the background galaxies number count.

A quick comparison of both SNRs with typical numbers, that is $\sigma_\epsilon \simeq 0.25$ and $\alpha \simeq 1.5$ (and $|\kappa| \simeq |\gamma|$), yields

$$\left(\frac{\mathrm{S}}{\mathrm{N}}\right)_{\mathrm{shear}} \sim 3 - 5\,\left(\frac{\mathrm{S}}{\mathrm{N}}\right)_{\mathrm{counts}}\,. \tag{4.50}$$

That statement is somewhat true, but only to the extent we are able to actually resolve the sources.

For a given survey area, the number density of objects grows as the survey depth increases. A higher number density enhances the signal differently for shear and magnification. While shear needs the sources to be resolved for measuring the ellipticity, magnification only requires counts, which means that at a given faint magnitude or high redshift, the usable number density of sources will be higher for magnification than shear. A greater depth also means a higher completeness which is key when performing magnitude cuts on the source plane to get positive and negative cross-correlations (*cf.* Chapter 5, Section I.1.1).

This difference is made larger by atmospheric distortion effects on the point spread function of ground-based imagery. In that sense, LSST will provide a wealth of sources rejected for shear measurement but perfect for magnification cross-correlation whereas Euclid and its exceptional image quality will have in comparison a usable number density of sources for shear closer to that of magnification.

The point being that shear and magnification actually are very complementary measurements. A good proof is the mass sheet degeneracy problem.

II.3.2 Mass sheet degeneracy

The mass-sheet degeneracy is an issue raised by gravitational lensing when trying to find a model for the lens mass distribution of an observed lensing system (multiple images, shape distortion, etc.). Since weak lensing shear allows for mass reconstruction, this topic is of primordial importance. The weak lensing case of the mass-sheet degeneracy has been first addressed by Schneider & Seitz (1995).

Let $\kappa(\boldsymbol{\theta})$ be a mass distribution providing a good fit to the observables, all the models

with a mass distribution following

$$\kappa_\lambda(\boldsymbol{\theta}) = (1-\lambda) + \lambda\,\kappa(\boldsymbol{\theta}) \tag{4.51}$$

will also end up being good fit to the data. The first term corresponds to the addition of a homogeneous mass density to the distribution, whereas the second describes a rescaling of the initial fitting model.

The reduced deflection angle corresponding to κ_λ is

$$\alpha_\lambda(\boldsymbol{\theta}) = (1-\lambda)\,\theta + \lambda\,\alpha(\boldsymbol{\theta})\,, \tag{4.52}$$

leading to a lensing potential of the form

$$\psi_\lambda(\boldsymbol{\theta}) = \frac{1-\lambda}{2}\,|\theta|^2 + \lambda\,\psi(\boldsymbol{\theta})\,, \tag{4.53}$$

which also satisfies the Poisson equation (4.17), $\nabla^2\psi_\lambda = 2\,\kappa_\lambda$. Combining these expressions, one ends up with the lens equation for the transformed mass distribution κ_λ that reads

$$\frac{\boldsymbol{\beta}}{\lambda} = \boldsymbol{\theta} - \boldsymbol{\alpha}(\boldsymbol{\theta})\,, \tag{4.54}$$

which resembles the original mass distribution accept the source angular coordinate is multiplied by a factor $1/\lambda$. Since the source is never directly observed, this rescaling cannot be probed. The same reasoning applies for the reduced shear g to show it remains unchanged under such a transformation $g_\lambda(\boldsymbol{\theta}) = g(\boldsymbol{\theta})$, which means the axis ratios of the elliptical images are unaffected. The mass-sheet degeneracy therefore causes different mass profiles to have very similar reduced shear profiles. However, since the amplification matrix and magnification behave as

$$\mathcal{A}_\lambda = \lambda\,\mathcal{A} \quad \text{and} \quad \mu_\lambda = \frac{\mu}{\lambda^2} \tag{4.55}$$

the absolute measurement of such observables could break the degeneracy.

To summarize, if nothing sets an absolute scale for the source size or luminosity or an absolute mass scale for the lens, one cannot distinguish between models κ_λ or κ. The second term of equation (4.55) shows that number density magnification could help solve that degeneracy and thus constrain the mass.

I shall now present the theoretical concepts and measurements methods of cosmic magnification.

CHAPTER 5

Cosmic Number Magnification

The new generation of deep and wide field optical instruments is scheduled to start around 2020. We can mention the LSST (see Chapter 2) or the European Space Agency satellite Euclid[1] which will achieve an all-sky survey with unprecedented depth. Partially developed with the aim of studying gravitational effects like strong lensing of cosmic shear, these instruments will produce catalogs of billions of astrophysical objects.

Among the cosmological probes, such data enables us to look at the repartition of matter in the Universe, and more specifically the angular distribution of objects. Using that probe and these catalogs, one can in particular compute the two-point correlation function between foreground and background sources (as shown in Menard & Bartelmann, 2002), to study an effect called *cosmic number magnification*.

I Motivations and concepts

I.1 Magnification bias

I.1.1 Slope of the number counts

Because of its specific exposure time, an imager is intrinsically limited in depth, and is thus generally referred to as *flux / magnitude-limited*. It is interesting to compute for such experiment the expected density of objects at a magnitude cut. Using the probability distribution of the objects, as well as their flux dependence and the field of view, it is easy to do so for a given redshift. But while this is true for undisturbed light paths, lensing effects will slightly modify the computation.

Magnification is characterized by the flux gain of the lensed sources. That gain is described by the so-called magnification factor μ so that for an isolated source with initial flux f_0, the observed lensed flux is $\mathrm{f}_{\mathrm{obs}} = \mu\,\mathrm{f}_0$. At the same time, the effective solid angle on the lensed sky is also distorted by a factor μ, $\Delta\Omega_{\mathrm{obs}} = \mu\,\Delta\Omega_0$. Both effects lead to an observed (lensed) number density of objects in the sky at a redshift z and a limiting flux f,

$$n_{\mathrm{obs}}\left(>\mathrm{f}, z\right) = \frac{1}{\mu(z)}\, n_0\left(>\frac{\mathrm{f}}{\mu(z)}, z\right)\,, \tag{5.1}$$

where n_0 denotes the unlensed number density.

Assuming the change in the density of sources per unit flux at a given redshift is a power law $n_0\left(\mathrm{f}, z\right) \propto \mathrm{f}^{-s}$ and trading flux with magnitude $m = -2.5\log\mathrm{f}$, (5.1) becomes

$$n_{\mathrm{obs}}(<m) = \mu^{2.5\,s(m)-1}\, n_0(<m)\,, \tag{5.2}$$

[1] `http://www.euclid-ec.org/`

for a sources placed at infinity and where $s(m)$ is the logarithmic slope of the source number counts at magnitude m

$$s(m) = 2.5 \frac{\mathrm{d} \log n_0(m)}{\mathrm{d}m} \,. \tag{5.3}$$

For convenience purposes, we will refer in the following to the slope of the number counts as being $\alpha(m) = 2.5\, s(m)$ so that the magnification bias writes in a simple way

$$\frac{n_{\rm obs}(< m)}{n_0(< m)} = \mu^{\alpha(m)-1} \,. \tag{5.4}$$

Figure 5.1 shows the resulting number of source (in log) as a function of magnitude before and

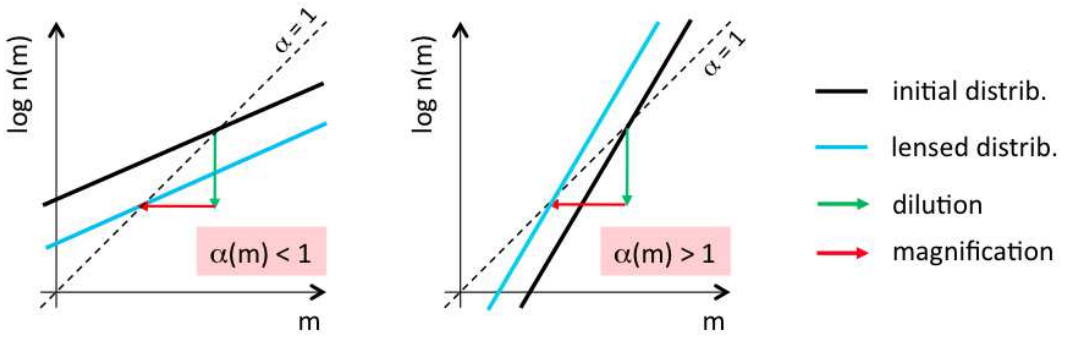

Figure 5.1 – Evolution of the numbers counts of a population under gravitational lensing as a function of the initial slope. The arrows represent gravitational lensing magnification effects, in green the sky enlargement (or dilution) and in red the flux gain. Both are of equal amplitude μ.

after magnification acts. On the left, the slope of the number counts α is less than one, which leads to a decrease in the actual observed number density, and on the right panel the opposite effect, when α is greater than one. These effects being of small amplitude, the observed number densities are simply fluctuations around the averaged one n_0.

I.1.2 Selection of background source population

The source number counts is a physical property of the source population. It evolves with epochs and needs to be computed for targeted population. The fainter the objects, the more they are, but the evolution of the slope α with the magnitude is not linear. However, within a small range of magnitude, the slope of the number counts can be approximated by the average value within that range. For a given population, we can create magnitude bins, within which the number counts slope will be considered linear. Therefore, the magnification bias depends on the magnitude cuts we impose on the data and can take many different values for a single

population. The cases can be summarized again:

- $\alpha > 1$, the number density increases and new sources are promoted into the image ;
- $\alpha = 1$, there is no lensing effect, the number density is the averaged one ;
- $\alpha < 1$, the number density decreases and we thus lose sources compared to average .

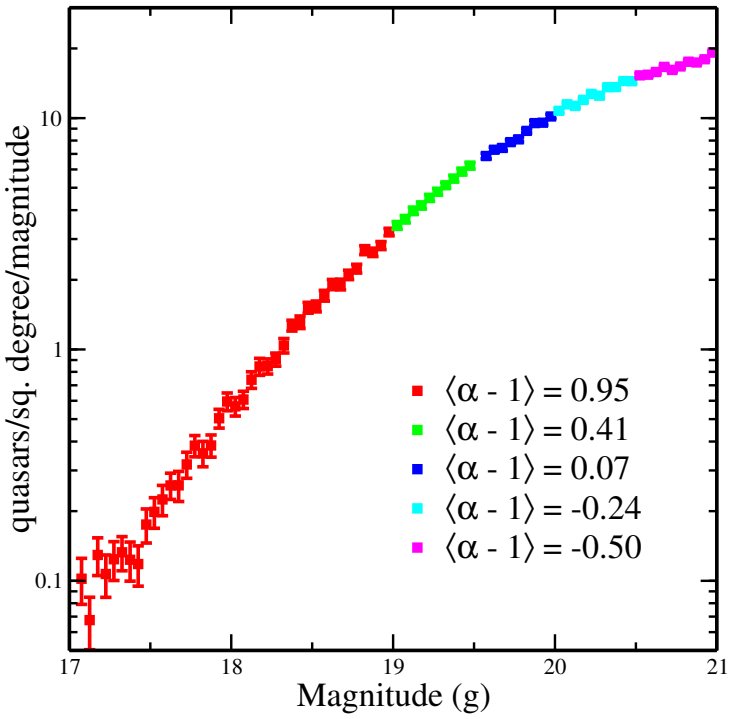

Figure 5.2 – Distribution of quasar counts with respect to the magnitude in g-band. The five colors indicate the selected magnitude bins and the respective slope are labeled on the plot (source Scranton et al., 2005).

Figure 5.2 shows the magnitude bins chosen within the quasar catalog for the first detection of cosmic magnification cross correlation in 2005. The mean measured slope of each bin is indicated on the figure. We see that the three cases above are probed within the same magnitude distribution.

I.1.3 Looking for completeness

The slopes of the source counts are measured on the data and can suffer from biasing effects. In particular, one should mention the completeness of the survey with respect to the magnitude,

for a given population. The shape of count is usually well defined by cosmological models but the faint end of the curve is coupled with a higher uncertainty due to the incompleteness. This propagates the error to the determination of α and therefore affects the magnification measurement.

I.2 Cosmic magnification measurements

I.2.1 From local to global effects

The strong gravitational effects that we did not extensively mention are very specific as they require a massive « lens » and (a) background source(s) to be quite perfectly aligned. They are thus isolated event, treated with a global model, but tuned with the local properties of the matter field. Weak lensing effects, which are characterized by a weak gravitational potential, can also be computed locally on the outskirts of these massive lens systems, to create shear maps and derive the mass of these astrophysical objects. But because the matter field is a continuous field on the sphere and that lensing effects are integrated along the line-of-sight, weak lensing observables could, in principle, be computed at any point on the sphere and specifically weighted in order to constrain the cosmology.

These new aspects of gravitational lensing have encountered a massive rise in detections over the last decade, and are generally split into two categories, CMB lensing and cosmic shear. On the one hand, CMB lensing aims at reconstructing, on the sphere, the full integrated gravitational potential between a redshift of $z = 1100$ (CMB emission by recombination) and now ($z = 0$), in order to correct for those effect that bias the measurements of CMB polarization signal by mixing the modes (Zaldarriaga & Seljak, 1998). That integrated lensing potential contains lots of information on the cosmology and helps constraining the cosmological parameters (Planck Collaboration, 2013b,c). On the other hand, the shear signal computed on large areas on the sky and combined between different pointing directions is known as cosmic shear. Like CMB lensing, cosmic shear provides information on the cosmological models, especially when using the tomography technique (cf. section II.2.5) that slices the Universe into shells and looks at the composition inside each shell.

Cosmic magnification is the matching effect of cosmic shear as it probes the same field(s), but using a different set of observables.

I.2.2 The angular correlation function

In the case of a cosmological observable, the direction of pointing is not relevant anymore and we need a parameter that captures the essence of the signal. Since we have catalogs of objects, we have a discretized representation of the matter field through point-like gravitational potentials. The relevant parameter is thus the distance to the center of the potential (the lens) denoted in the following by $\theta = |\boldsymbol{\theta}|$, the norm of the direction vector $\boldsymbol{\theta}$. The observable is a cross-correlation between the lens and the background. The densities are calculated in ring-like bins as shown in Figure 5.3.

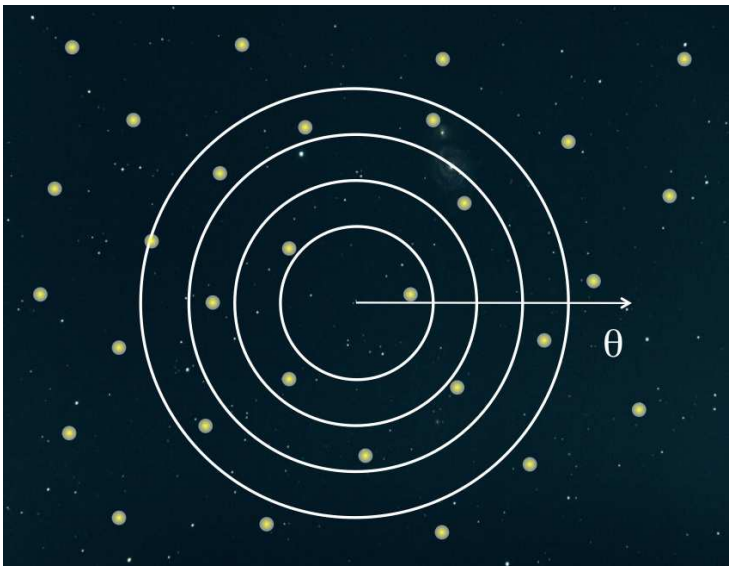

Figure 5.3 – Angular bins centered on foreground galaxies, to count the represented background source density (sources represented by yellow dots).

The magnification bias described in the previous subsection can be considered as a local effect, since it depends on the background population, but can also easily be imagined on a cosmological scale. Due to flux conservation, the positive and negative changes to the number density of background objects must, on average, cancel out on the sphere. But, not the absolute value of the magnification. Therefore, we can capture the lensing signal due to magnification by comparing the number density of the background population objects relative to the distance θ to the center of the foreground objects (initiated by Tyson, 1986).

The constructed observable is the angular cross-correlation function w,

$$w_{\times}^{ij}(\theta) = \frac{\langle [n_i(\boldsymbol{\phi}) - \bar{n}_i]\,[n_j(\boldsymbol{\theta}+\boldsymbol{\phi}) - \bar{n}_j]\rangle}{\bar{n}_i\,\bar{n}_j}\,, \tag{5.5}$$

where i and j stand for the shell (or tomographic bin) number, and the average extends over all

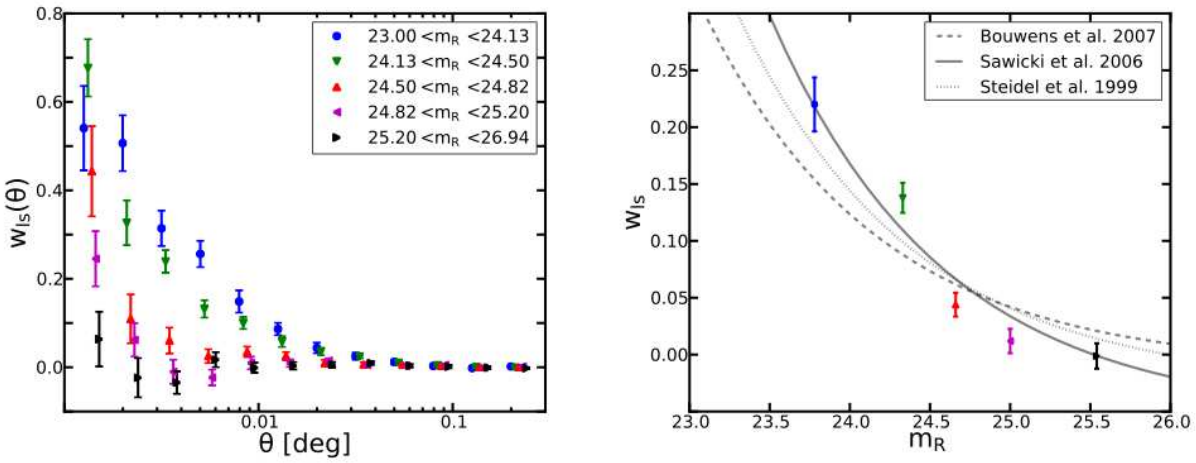

Figure 5.4 – Angular cross-correlation functions between foreground galaxies and background LBGs. *Left panel* represents the cross-correlation as a function of angular radius (θ) and LBG magnitude bins (color). *Right panel* shows the same correlation function computed in a single angular bin $0.001 < \theta < 0.01$ as a function of LBG magnitude (source Morrison et al., 2012).

positions $\boldsymbol{\phi}$ and all directions $\boldsymbol{\theta}$. The cross-correlation (5.5) can be understood as a pair count between two populations as a function of angular bin.

I.2.3 Previous measurements

This effect has been considered in the eighties between foreground galaxies and bright background quasars (Canizares, 1981; Vietri & Ostriker, 1983; Schneider, 1986, 1987, 1989; Peacock, 1986). However, the achievable depth of the surveys at that time was low, so was the bright quasar number and the statistical noise therefore dominated the signal. After some claims of detection, for which the uncertainty seemed to be underestimated, the cosmic magnification signal was finally detected up to 8-σ by Scranton et al. (2005) with the Sloan Digital Sky Survey (SDSS). The foreground population was made of 13 million galaxies and the background was composed of $\sim 200,000$ quasars on a field of $4000\,\mathrm{deg}^2$.

In 2009, Hildebrandt et al. (2009) achieved another magnification measurement and introduced the Lyman-break galaxies (LBGs) as a new possibility for background sources, due to their high redshift ($z \sim 2-5$). Then some other possible correlations followed like Ménard et al. (2010) with galaxy-dust correlation, sub- millimeter galaxies in Wang et al. (2011); Hildebrandt et al. (2013) or high-redshift clusters in Hildebrandt et al. (2011). The first measurement to date to use lensing tomography has been achieved by Morrison et al. (2012) with the Deep Lens Survey. They used 9,000 galaxies and 12,000 LBGs distributed over the $4\,\mathrm{deg}^2$ of the DLS field.

The measured angular correlation function is shown in Figure 5.4.

I.3 A niche for upcoming deep and wide surveys

The main features of current cosmic magnification measurements can be summarized in three items

- the biggest probed field covers a tenth of the total surface of the sky,
- only a single measurement uses tomography (Morrison et al., 2012),
- the measurements before 2010 were still limited by statistical uncertainties.

Barely a decade ago, the Dark Energy Task Force (Albrecht et al., 2006), a committee in charge of advising the NASA, the NSF and the U.S. Department of Energy on the future of dark energy science, elected a few cosmological probes that were the most promising to provide the next level constraints on the dark energy parameters. They settled on baryon acoustic oscillations (BAO), supernovæ (SN), galaxy cluster science (CL) and weak lensing (WL). The main reason these probes have a high constraining power on dark energy and its evolution is because they trace the repartition of matter on several length scales and at different epochs. An observable that highly depends on the the cosmological parameters are the cosmological distances (cf. Section III). Baryon acoustic oscillations and considered as a standard ruler in cosmology in the sense that it has imprinted at the moment of recombination a pattern of comoving size 150 h^{-1}Mpc in the cosmos, which has evolved since but is detectable at several epochs. Supernovæ Ia are designated as standard candles as their explosion process is fairly well modeled and thus bring information on the radial distance between them and us (several Mpc). Galaxy clusters are among the biggest gravitationally bound structures in the Universe and the study of their radial mass profile provides information on the a scale lower than a Mpc. Finally, weak lensing carries information of the mass repartition on a large scale range (from Mpc to 500 Mpc) but in projection as well as redshift or temporal information via tomography.

Concerning the weak lensing probe, the current decade has seen the development of advanced projects like the Dark Energy Survey (DES), PanSTARRS or SuMIRe, that are ground-based telescopes designed for studying cosmic shear. Their individual improvement compared to the previous decade is either about the observed volume, the maximum depth of the survey or the total scanned area. As we start building the software pipeline for the data analysis of the next generation projects, expected around 2020, like the European satellite Euclid or the American telescope LSST, we can wonder if cosmic magnification might enhance the expected constraints on the cosmological parameters and whether it needs specific design requirements. The best

argument behind that analysis is the current limitation of cosmic magnification signal by the statistical noise (or *shot noise*). These new wide and deep projects will collect information on billions of astrophysical objects and enable the measurement of magnification on high redshifts where the effective density of objects available for shear measurement drops significantly.

In order to quantify the constraining power of a given project on the evolution of dark energy, Albrecht et al. (2006) defined the *figure of merit* or FoM, which is the area of the 95% confidence contours on the (w_0, w_1) parameter plane. The starting point of this project has been the desire to derive the figure of merit of cosmic magnification alone as well as the combination of probes, likely to be observed in the framework of LSST and Euclid. We present in the following our study of cosmic magnification, that consists of the expected sources of systematic errors, numerical simulations and the final results and a discussion.

II Magnification signal via cross-correlation

II.1 Theory

The observable of interest in this study is primarily the angular correlation function we defined in equation (5.5). To better understand its behavior, we will now express it in terms of other observable quantities and cosmological parameters. In the following, we make no assumptions on the curvature of the Universe and thus use the general expression for the proper distance, defined in equation (1.45) on page 19 and expressed as a function of the comoving distance χ.

II.1.1 Number density contrast

In Chapter 4, page 115, we defined a general expression for the magnification (4.29). In the weak lensing regime, one should consider κ, γ_1 and $\gamma_2 \ll 1$. In this scope, we can expand the magnification expression to first order in κ[2],

$$\mu = \frac{1}{(1-\kappa)^2 - \gamma^2} \simeq \frac{1}{(1-\kappa)^2} \simeq 1 + 2\,\kappa\,. \tag{5.6}$$

We define the number density contrast δn within an angular scale $\boldsymbol{\theta}$

$$\delta n(< m, \boldsymbol{\theta}) = \frac{n_{\rm obs}(< m, \boldsymbol{\theta}) - n_0(< m, \boldsymbol{\theta})}{n_0(< m, \boldsymbol{\theta})} = \frac{n_{\rm obs}}{n_0}(< m, \boldsymbol{\theta}) - 1\,. \tag{5.7}$$

[2]It is worth noting at this point that a measure of the local magnification bias in a region of weak deformation is a direct measure of the convergence and can be used to derive an estimate of the local surface mass density. This is particularly helpful to break degeneracies coming from shape measurements, know as the mass-sheet degeneracy (see subsection II.3.2)

Using the expression for the magnification bias (5.4) while dropping the magnitude consideration for now and the magnification expansion (5.6), we end up with an expression relating the number density contrast to the magnification,

$$\delta n_m(\boldsymbol{\theta}) = \mu(\boldsymbol{\theta})^{\alpha(m)-1} - 1 \tag{5.8}$$

$$\simeq (1 + 2\,\kappa(\boldsymbol{\theta}))^{\alpha(m)-1} - 1 \tag{5.9}$$

$$\simeq 2\,(\alpha - 1)\,\kappa(\boldsymbol{\theta})\,, \tag{5.10}$$

where the expansion from (5.9) to (5.10) also assumes $\kappa(\boldsymbol{\theta}) \ll 1$. The reason we appended a subscript m to the δn is because magnification is not the only source of number density contrast. If we consider instead of two separate populations, the angular correlation on the same population, we probe what is called the intrinsic clustering, in addition to the lensing effects that are roughly two orders of magnitude lower. We designate those effects with δn_g. However, when probing the intrinsic clustering of a population, we are affected by stochastic effects due to the finite number of objects in the selected population. These effects are generally referred to as shot noise or Poisson noise, and denoted by $\delta n_{sn} \propto 1/\sqrt{\bar{n}}$. Therefore, the total expression for the number density contrast is,

$$\delta n(\boldsymbol{\theta}) = \delta n_g(\boldsymbol{\theta}) + \delta n_m(\boldsymbol{\theta}) + \delta n_{sn}(\boldsymbol{\theta})\,. \tag{5.11}$$

II.1.2 Weighted sky projections

A number density is a number of object per unit area on the sky in this context, which is a two-dimensional representation of the matter field, with no direct information on the depth. A number density is therefore a projection of the three-dimensional density contrast along the line-of-sight from here to the comoving horizon, weighted by the distribution of the population. In the case of intrinsic clustering, this can be written

$$\delta n_g(\boldsymbol{\theta}) = b \int_0^{\chi_\mathrm{H}} \mathrm{d}\chi\, p_g(\chi)\, \delta(f_k(\chi)\,\boldsymbol{\theta}, \chi)\,, \tag{5.12}$$

where $p_g(\chi)$ is the normalized comoving distance probability distribution of the population such that

$$\int_0^{\chi_\mathrm{H}} \mathrm{d}\chi'\, p_g(\chi') = 1\,,$$

and $\delta_g(\chi\,\boldsymbol{\theta}, \chi)$ is the galaxy density contrast at redshift $z(\chi)$, taken on a length scale $\chi\,\boldsymbol{\theta}$. The prefactor b is the galaxy bias, which links the galaxy density contrast δ_g to the matter density

contrast δ (*cf.* equation (1.60)).

Concerning the magnification number density contrast, it is related through equation (5.10) to the convergence field κ. The convergence is also a line-of-sight weighted projection of the matter density field, whose expression was calculated on equation (4.40) and can be rewritten

$$\kappa(\boldsymbol{\theta}) = \int_0^{\chi_{\rm H}} \mathrm{d}\chi \, p_m(\chi) \, \delta(f_k(\chi)\,\boldsymbol{\theta}, \chi) \,, \tag{5.13}$$

with a weighting function $p_m(\chi)$ whose expression is

$$p_m(\chi) = \frac{3}{2} \frac{H_0^2}{c^2} \, \Omega_m \, \frac{f_k(\chi)}{a(\chi)} \int_\chi^{\chi_H} \mathrm{d}\chi' \, p_g(\chi') \, \frac{f_k(\chi' - \chi)}{f_k(\chi')} \,. \tag{5.14}$$

which is more complex than just a probability distribution as it is related to the lensing kernel.

II.1.3 Angular cross-correlation function

With an expression for the number density contrast for a given population, the angular cross-correlation function between two number density contrasts denoted i and j can be written according to equation (5.5),

$$w^{(ij)}(\theta) = \langle \delta n^i(\boldsymbol{\phi}) \, \delta n^j(\boldsymbol{\theta} + \boldsymbol{\phi}) \rangle \,. \tag{5.15}$$

Using the decomposition of the number density contrast into several components in equation (5.11), the angular cross-correlation function can then be expanded as,

$$w^{(ij)}(\theta) = w_{gg}^{(ij)}(\theta) + w_{gm}^{(ij)}(\theta) + w_{mg}^{(ij)}(\theta) + w_{mm}^{(ij)}(\theta) + \delta_K^{ij} \, w_{sn}^{(ij)}(\theta) \,, \tag{5.16}$$

where δ_K stands for the Kronecker function and where

$$w_{xy}^{(ij)}(\theta) = \langle \delta n_x^{(i)}(\boldsymbol{\phi}) \, \delta n_y^{(j)}(\boldsymbol{\theta} + \boldsymbol{\phi}) \rangle \quad \text{with} \quad x, y = \{g, m\} \,, \tag{5.17}$$

except for the stochastic noise term. As we mentioned in Section II.1.2, both the magnification and clustering number density contrasts are projections of the matter density field. Therefore, we define $\boldsymbol{\theta}' = \boldsymbol{\theta} + \boldsymbol{\phi}$, and use equations (5.12) and (5.13) to write,

$$w_{xy}^{(ij)}(\theta) \propto \left\langle \int_0^{\chi_{\rm H}} \mathrm{d}\chi \, p_x^{(i)}(\chi) \, \delta(\chi\,\boldsymbol{\theta}, \chi) \int_0^{\chi_{\rm H}} \mathrm{d}\chi' \, p_y^{(j)}(\chi') \, \delta(f_k(\chi')\,\boldsymbol{\theta}', \chi') \right\rangle \tag{5.18}$$

$$\propto \int_0^{\chi_{\rm H}} \mathrm{d}\chi \, p_x^{(i)}(\chi) \int_0^{\chi_{\rm H}} \mathrm{d}\chi' \, p_y^{(j)}(\chi') \, \langle \delta(f_k(\chi)\,\boldsymbol{\theta}, \chi) \, \delta(f_k(\chi')\,\boldsymbol{\theta}', \chi') \rangle \,, \tag{5.19}$$

where the cross-correlation function in equation (5.19) is the same as in equation (1.59), that is the two-point correlation function of matter, that we can express in Fourier space via the matter power spectrum P_δ using equation (1.63).

After some steps and the Limber approximation explained in Appendix 2 page 175, we come up with the expression

$$w_{xy}^{(ij)}(\theta) \propto \int \mathrm{d}\chi\, p_x^{(i)}(\chi)\, p_y^{(j)}(\chi) \int \frac{\mathrm{d}^2 k_\perp}{(2\pi)^2}\, e^{-\imath\, f_k(\chi)\, \boldsymbol{k}_\perp \cdot \boldsymbol{\theta}}\, P_\delta(|\boldsymbol{k}_\perp|, \chi) \tag{5.20}$$

$$\propto \int \mathrm{d}\chi\, p_x^{(i)}(\chi)\, p_y^{(j)}(\chi) \int \frac{k \mathrm{d}k}{2\pi}\, P_\delta(k, \chi)\, \mathrm{J}_0(f_k(\chi)\, \theta k) \tag{5.21}$$

where $\boldsymbol{k}_\perp$ represent the wave-vectors in the plane of the sky and J_0 is the zeroth-order Bessel function.

II.1.4 Cross-correlation power spectra

While the angular cross-correlation function is usually the measured observable, it is convenient for simulations to have an observable in Fourier space that characterizes the cross-correlation. The Fourier transform of a correlation function is a power spectrum, we write that transformation as,

$$P_{xy}^{(ij)}(\ell) = \int \mathrm{d}^2\theta\, w_{xy}^{(ij)}(\theta)\, e^{\imath\, \boldsymbol{\ell} \cdot \boldsymbol{\theta}} \tag{5.22}$$

$$\propto \int \mathrm{d}\chi\, p_x^{(i)}(\chi)\, p_y^{(j)}(\chi) \int \frac{\mathrm{d}^2 k_\perp}{(2\pi)^2}\, e^{-\imath\, f_k(\chi)\, \boldsymbol{k}_\perp \cdot \boldsymbol{\theta}}\, P_\delta(|\boldsymbol{k}_\perp|, \chi)\, (2\pi)^2\, \delta_D(\boldsymbol{\ell} - f_k(\chi)\, \boldsymbol{k}_\perp) \tag{5.23}$$

$$\propto \int \mathrm{d}\chi\, \frac{p_x^{(i)}(\chi)\, p_y^{(j)}(\chi)}{\chi^2}\, P_\delta\left(\frac{\ell}{f_k(\chi)}, \chi\right). \tag{5.24}$$

where once again we use Limber's approximation and the expression derived in (5.20). Following (5.11) and (5.16), we therefore introduce our set of cross-correlation power spectra,

$$P_{gg}^{(ij)}(\ell) = b^2 \int \mathrm{d}\chi\, \frac{p_g^{(i)}(\chi)\, p_g^{(j)}(\chi)}{\chi^2}\, P_\delta\left(\frac{\ell}{f_k(\chi)}, \chi\right) \tag{5.25a}$$

$$P_{gm}^{(ij)}(\ell) = 2\,(\alpha^{(j)} - 1)\, b \int \mathrm{d}\chi\, \frac{p_g^{(i)}(\chi)\, p_m^{(j)}(\chi)}{\chi^2}\, P_\delta\left(\frac{\ell}{f_k(\chi)}, \chi\right) \tag{5.25b}$$

$$P_{mg}^{(ij)}(\ell) = P_{gm}^{(ji)}(\ell) \tag{5.25c}$$

$$P_{mm}^{(ij)}(\ell) = 4\,(\alpha^{(i)} - 1)(\alpha^{(j)} - 1) \int \mathrm{d}\chi\, \frac{p_m^{(i)}(\chi)\, p_m^{(j)}(\chi)}{\chi^2}\, P_\delta\left(\frac{\ell}{f_k(\chi)}, \chi\right) \tag{5.25d}$$

$$P_{sn}^{(ij)}(\ell) = \delta_K^{ij}\, \frac{1}{\langle n \rangle^{(i)}}\,. \tag{5.25e}$$

With these definitions, we now have an expression for the power spectrum associated with the total angular cross-correlation function $w_{\times}^{(ij)}$,

$$P_{\times}^{(ij)}(\ell) = P_{gg}^{(ij)}(\ell) + P_{mg}^{(ij)}(\ell) + P_{gm}^{(ij)}(\ell) + P_{mm}^{(ij)}(\ell) + P_{\rm sn}^{(ij)} \,. \tag{5.26}$$

As we see from equation (5.26), the magnification cross- correlation signal (5.25b) is measured among other signals. The relative strength of these signals, depending on the choice of population and the wave-number value is important to derive the signal-to-noise ratio of cosmic magnification.

II.1.5 Bias modelling

The three main contributions (5.25) to the number density cross- power spectrum, the intrinsic clustering gg and the cross-terms gm and mg, are dependent on the galaxy bias. Unfortunately, the galaxy bias is considered as a nuisance parameters since it is very difficult to probe and its evolution is currently highly undetermined.

The galaxy bias could in principle be both redshift and scale dependent, $b(k, z)$, like the matter power spectrum. In this case, it would enter the integral on the line-of-sight in equations (5.25). However, in this preliminary work, we only consider the simple case where the bias can take a different value for each redshift bin $b^{(i)}$, but where their fiducial values are set to unity. This will allow the bias to be fitted by the data in the forecasting analysis.

II.2 Redshift distributions

In order to separate the sources in the line-of-sight, one has to measure their redshift. Redshifts can be obtained via spectroscopy, since it basically is the measure of the shift of the source spectrum from one at rest. Emission and absorption lines of elements produce easily recognizable features that allow for a very accurate determination. However, obtaining enough photons of a distant source to reconstruct its spectrum is highly time-consuming. Another technique can be used to determine the redshift of multiple faint objects at once, but at a cost of accuracy.

II.2.1 Photometric redshifts

In broad-band photometric surveys such as the current and upcoming wide-field surveys the redshift of every sources on an image cannot be measured absolutely, but is determined using data collected in all the bandpasses of the instrument. The integrated flux of a source in each bandpass yields the source magnitudes (see equation (3.3)), which are then processed via a

minimization procedure using integrated spectral templates of many populations of sources at different redshifts, to produce an estimation of the source redshift. The redshift measurement is not exact but rather associated with a certain probability due to degeneracies between the spectral responses. The resulting probability distribution for each object is called the photometric redshift or *photo-z*.

In Chapter 3, we discussed the impact of atmospheric constituents measurement errors on the overall atmospheric transmission as well as the residual impact from photometric calibration on magnitudes. These residuals will affect the determination process of photometric redshifts. This effect can be evaluated, in order to derive the impact on the science goals (*cf.* Chapter 6, Section II).

For now, we assume a perfect knowledge of redshifts and address the line-of- sight effects.

II.2.2 The relative impact of weighting functions

The magnification cross-correlation signal P_{gm} is the one we would like to maximize the contribution with respect to the full cross-correlation signal $P_{\times}$. To understand the respective behavior of the power spectra contributing to $P_{\times}$, we set the bias and the logarithmic slope of number counts to *ad hoc* but reasonable values: $b = 1$ and $\alpha = 1.5$ so that we have our spectra (5.25a) to (5.25d) differing only by their weighting functions $p_x(\chi)$, $x = \{g, m\}$.

For illustration, we plot on Figure 5.5 these weighting functions with redshift rather that comoving distance using the equality $p_g(\chi)\,\mathrm{d}\chi = p_g(z)\,\mathrm{d}z$, for two population distributions centered respectively on $z = 0.4$ and $z = 0.8$. distinct on Figure 5.5a and overlapping on Figure 5.5b. The bottom panels represent the integration window functions obtained via the combination of these weighting functions, which are a direct estimator of the amplitude of the corresponding power spectra. We remark that contrary to the galaxy distribution function p_g, the lensing distribution function is very broad and extends to a redshift of zero. The reason is that also the matter between us and the source contributes to the lensing effect while galaxies at a certain redshift have no causal connexion with galaxies at a distant redshift. Still with top an middle panels, another interesting feature from the lensing distribution is that fact that is does not seems to change much as the galaxy distribution broadens, which tells us that the lensing distribution is dependent on the median redshift of the distribution, rather than its width.

Concerning bottom panel, which is plotted in log, the difference between both configurations is striking. In first case with non overlapping galaxy distributions, the amplitude of the magnitude cross-correlation tops three orders of magnitude higher than other contributions.

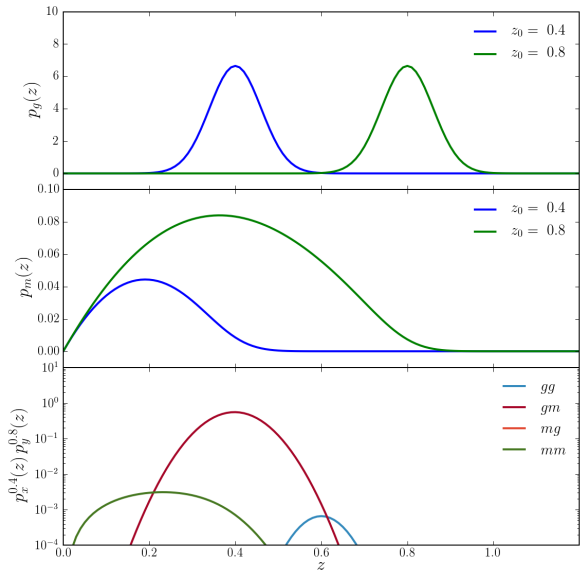

(a) Distinct populations.

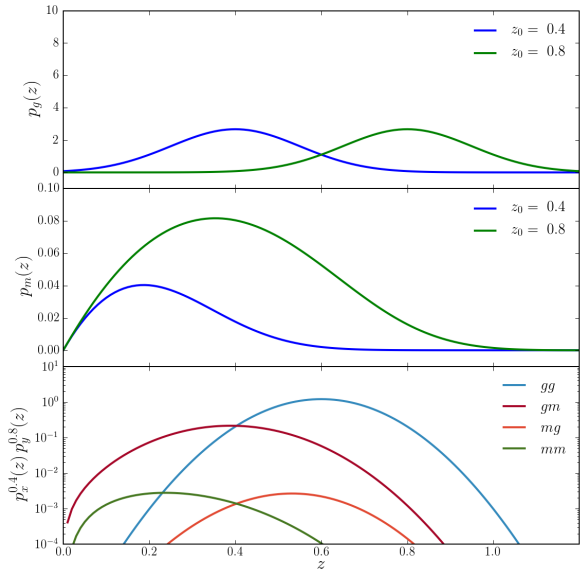

(b) Overlapping populations.

Figure 5.5 – Probability distribution functions of populations at $z = 0.4$ and $z = 0.8$ with respect to redshift. *Top panel*: galaxy distribution (weighting) function. *Middle panel*: lensing weighting function. *Bottom panel*: window functions for the computation of the cross-correlation power spectra, combining two distributions from the upper panels..

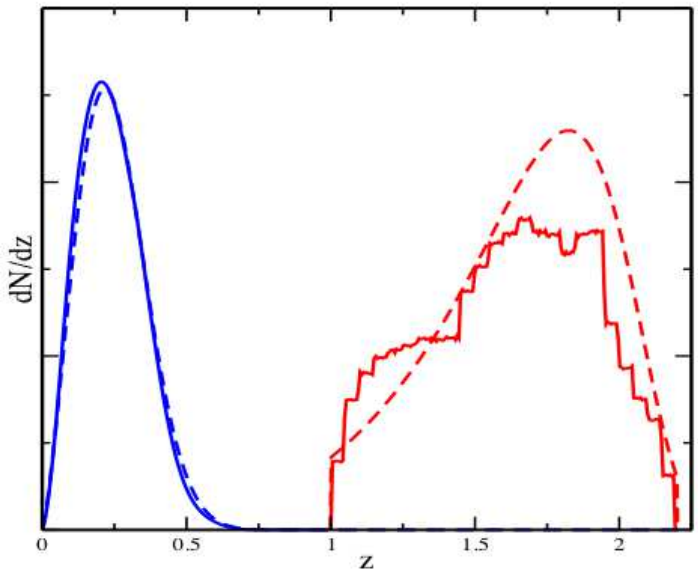

Figure 5.6 – Galaxy and quasar redshift distributions with special cuts, used to compute the first magnification cross-correlation measurement. (source Scranton et al., 2005).

This means basically that the full cross-correlation signal $P_\times$ with such a configuration simplifies to the magnification cross-correlation signal P_{gm}. However, if the populations happen to overlap, even over a small redshift range, the clustering signal is so strong that it takes over most of the signal, therefore diluting the lensing signal.

To retrieve the lensing signal, it is thus key when cross-correlating two distributions to ensure that they do no overlap. This task is particularly hard when dealing with photometric redshifts as there are always features in the templates that create degeneracies, leading to failures in the redshift determination.

II.2.3 A basic approach

To make sure the distributions are not overlapping, the easiest way is to select different populations and perform redshift cuts on the data. That was the method chosen by Scranton et al. (2005) for the first measurement of cosmic magnification. They selected foreground SDSS galaxies as the lens, and background quasars as the source, cutting the latter distribution at a redshift of $z = 1$, as shown on Figure 5.6.

The data used for this first detection was extracted from the third data release of SDSS covering 3800 deg (Abazajian et al., 2005), in which the galaxy sample used a the lens was selected in the magnitude range $17 < r < 21$, which yielded a galaxy number density of 1 per

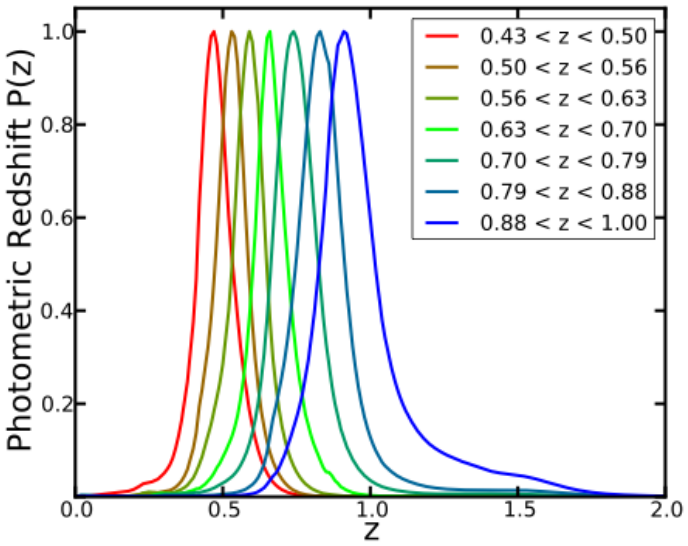

Figure 5.7 – Redshift distribution of the seven photometric bins used as a lens in the measurement of cosmic magnification (source Morrison et al., 2012).

arcmin^2 (13.5 million objects). Such a low number density is incompatible with redshift cuts to keep a high enough signal, which is why they used the galaxy distribution as a whole. In such conditions, the dominant uncertainty on the magnification measurement is the Poisson noise (*cf.* Section III.1)).

II.2.4 Towards tomographic studies

A decade ago, Hu (1999, 2002); Jain & Taylor (2003), introduced the concepts of lensing tomography, that is the separation of a given population in several redshift bins, thus to retrieve information on the cosmology at different epochs in order the better constrain the evolution of the cosmological parameters and models. While it appears as a straightforward continuation, tomography is a big step forward to climb. First it needs very accurate photometric redshifts to divide your survey while keeping control of the contamination for the overlap between faint ends of the the distributions. Second, the bins being smaller than the initial distribution, one needs to ensure that there is enough statistics in each bin to have a good signal-to-noise ratio.

Post-SDSS surveys, like the Canada France Hawaii Telescope Lensing Survey (CFHTLS) and the Deep Lens Survey (DLS) mostly dedicated to lensing measurements have chosen to focus on small fields to gain a greater depth, thus a greater number density of sources for weak lensing measurements and be able to divide their population into bins (Benjamin et al., 2013). In such conditions, Morrison et al. (2012) achieved the first magnification measurement using

tomography with DLS. They separated their lens population in seven photometric redshift bins (*cf.* Figure 5.7) and cross-correlation them with distant luminous blue galaxies (LBGs) at a redshift $z > 2$.

II.2.5 Tomographic simulations for future surveys

An extremely deep and wide LSST-like survey, which goal is to reach a magnitude $i_{AB} = 27.5$, will gather an exceptional catalog of sources. In particular, its main galaxy distribution will extend to very high redshifts. This is an ideal instrument for weak lensing and specifically tomographic magnification studies. Using appropriate cuts, one could use the distribution and cross-correlate it with other populations (e.g. quasars, LBGs, sub-millimeter galaxies (SMGs), etc.). Instead, we decided to investigate that lensing power of that distribution on its own, cross-correlating the tomographic bins with each other.

For these forecasts, we focused on LSST but the same method applies for Euclid or other surveys. Starting from the prediction of the redshift distribution of galaxies for LSST (LSST Science Collaboration, 2009, p. 73) given by

$$p(z) = \frac{1}{2\,z_0}\left(\frac{z}{z_0}\right)^2 \exp\left[-\frac{z}{z_0}\right] \tag{5.27}$$

where z_0 is obtained using a linear relationship with the limiting i magnitude fitted on DEEP2 data

$$z_0 = 0.0417\; i - 0.744\,. \tag{5.28}$$

The limiting goal magnitude of LSST is $r < 27.5$ and $i < 27$, this latest value is therefore chosen for the calculation of z_0. This yields a simulated redshift distribution of galaxies with median redshift $z_m = 1.0$ and average number density of galaxies $\bar{n} = 45$ arcmin^{-2} shown as the envelope on Figure 5.8a. As a matter of comparison, the expected Euclid redshift distribution is shown on Figure 5.8b. It has a median redshift of $z_m = 0.9$, an average number density of galaxies $\bar{n} = 35$ arcmin^{-2} and follows the Smail et al. (1994) distribution for magnitude-limited survey

$$p(z) = z^\alpha \exp\left[-\left(\frac{z}{z_0}\right)^\beta\right] \quad \text{with} \quad \begin{matrix}\alpha = 2 \\ \beta = 1.5\end{matrix} \tag{5.29}$$

where $z_0 = z_m/\sqrt{2\pi}$.

Figure 5.8 shows a ten tomographic bins selection for each survey. The bins have been calculated so that they have the save number of galaxies. However, due to the photometric redshift uncertainty taken into account in this figure, the bins overlap. This adds some complexity

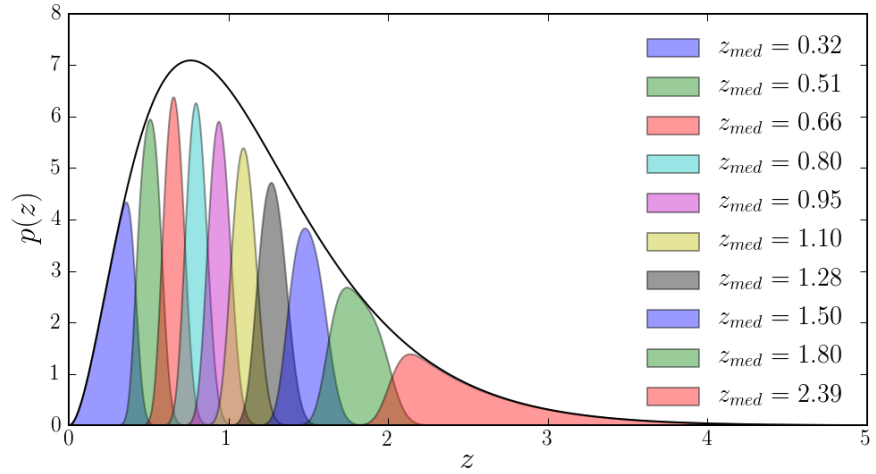

(a) LSST distribution.

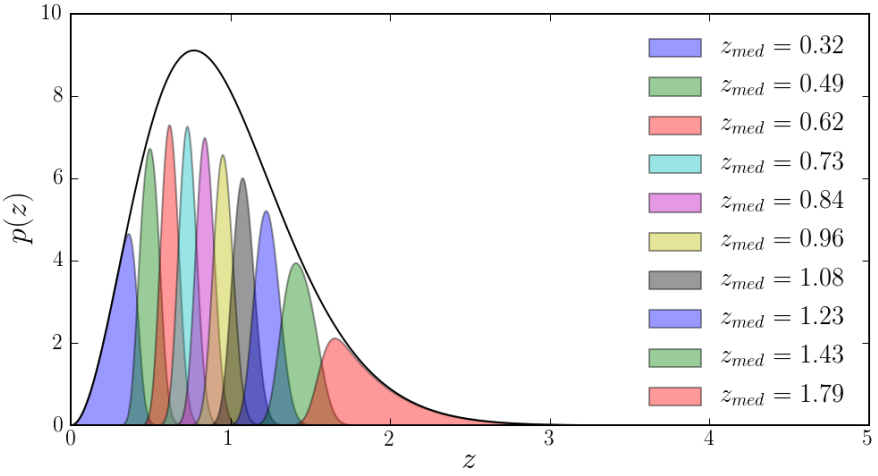

(b) Euclid distribution.

Figure 5.8 – Redshift probability distribution function of galaxies for two surveys. Each distribution is split in ten tomographic bins of equal area, weighted by the photometric redshift uncertainty. The median redshift is labeled for each bin..

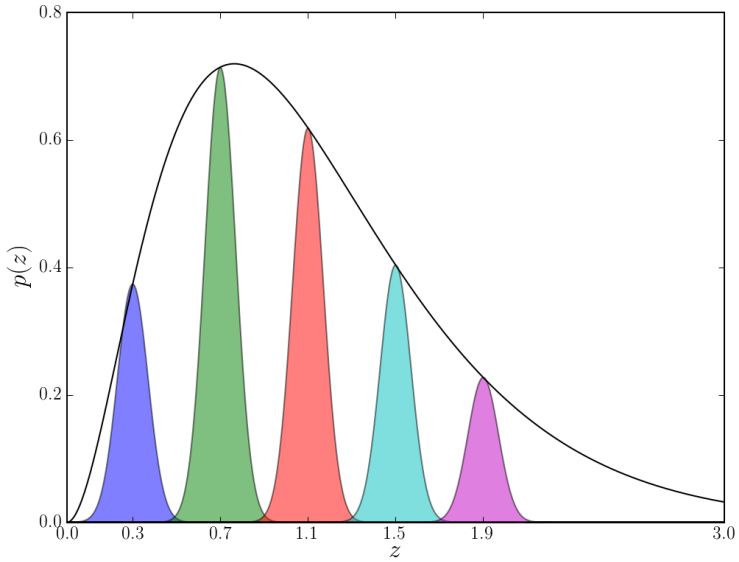

Figure 5.9 – Tomographic bins inside the full LSST galaxy distribution chosen with a magnitude limit of $i < 27.5$.

and will thus be dealt later (see Section II.2 page 165). We will thus start with a much simpler case of five non overlapping bins chosen in the LSST distribution and shown on Figure 5.9.

II.3 Simulation algorithm

II.3.1 Overview

During this thesis work, I developed an algorithm in Python that computes numerically the calculations needed to obtain the cross-correlation power spectra, as well as their derivatives with respect the cosmological parameters, in order to study the cosmic magnification and determine its constraining power on the cosmological parameters for a particular survey. The code takes as input

- a set of cosmological parameters $\{h, \Omega_\mathrm{m}, \Omega_b, \Omega_\Lambda, w_0, w_a, \sigma_8, n_s, b_i\}$,
- a survey, with includes essential parameters like the survey area A, the average number density of galaxies $\bar{n}_g$, the limiting magnitude and the photometric redshift error $\sigma_z(z)$,

and the other relevant cosmological parameters not mentioned here are set to Planck fiducial model (Planck Collaboration, 2013b).

The algorithm aims at computing the number density cross-correlation power spectrum (5.26) via the analytical formulæ (5.25a) to (5.25d). However, the complexity of structure

formation mechanisms prevents us from obtaining an analytical expression for the matter power spectrum, as explained in Section IV.2.3.

II.3.2 Fitting formula for the matter power spectrum

In the absence of an analytical expression, one has to find a fitting model that either describe physical transitions with accuracy (transfer function) or renders the small scale clustering (non linearities).

A fitting formula for the cold dark matter linear power spectrum transfer function at late times was proposed by Bardeen et al. (1986), and revised a decade later by Eisenstein & Hu (1998) to include more accurate contributions of the baryonic matter, especially the baryon acoustic oscillation features imprinted on the power spectrum. This is the current reference for calculation of the transfer function.

These fitting formulæ being already implemented in various cosmological codes, I integrated one in my algorithm, through a wrapper, to account for the specific computation of the matter power spectrum. I chose the C-code *NICAEA* (NumerIcal Cosmology And lEnsing cAlculations) written by Martin Kilbinger which is fast and easily tunable.[3] For the analysis, the matter power spectrum is computed with the analytical fitting formula for the transfer function from Eisenstein & Hu (1998), with the BAO wiggles. The non-linear power spectrum is computed using *halofit* model from Smith et al. (2003) revised by Takahashi et al. (2012) to better fit the wCDM models.

Examples of NICAEA matter power spectra are plotted on Figure 5.10. Each panel shows the matter power spectrum scale dependence on a single cosmological parameter, respectively the dark energy equation-of- state parameter w_{DE}, the dark energy ratio Ω_Λ (for a flat cosmology $\Omega_\Lambda + \Omega_\mathrm{m} = 1$), baryon amount Ω_b and the Hubble parameter h.

II.3.3 Numerical derivatives of magnification power spectra

The parameter forecast using the Fisher matrix formalism (see Section III) requires the computation of the derivatives of the observables with respect to the parameters to be constrained (*cf.* Section III.2). In this work, the observable is the number density cross-correlation power spectrum $P_\times(\ell)$, which needs to be derived with respect to a set of cosmological parameters. Since most of the selected cosmological parameters affect the shape of the matter power spectrum, the derivatives $\dfrac{\partial P_\times(\ell)}{\partial p}$ have to be computed numerically.

[3] `http://www2.iap.fr/users/kilbinge/nicaea/`

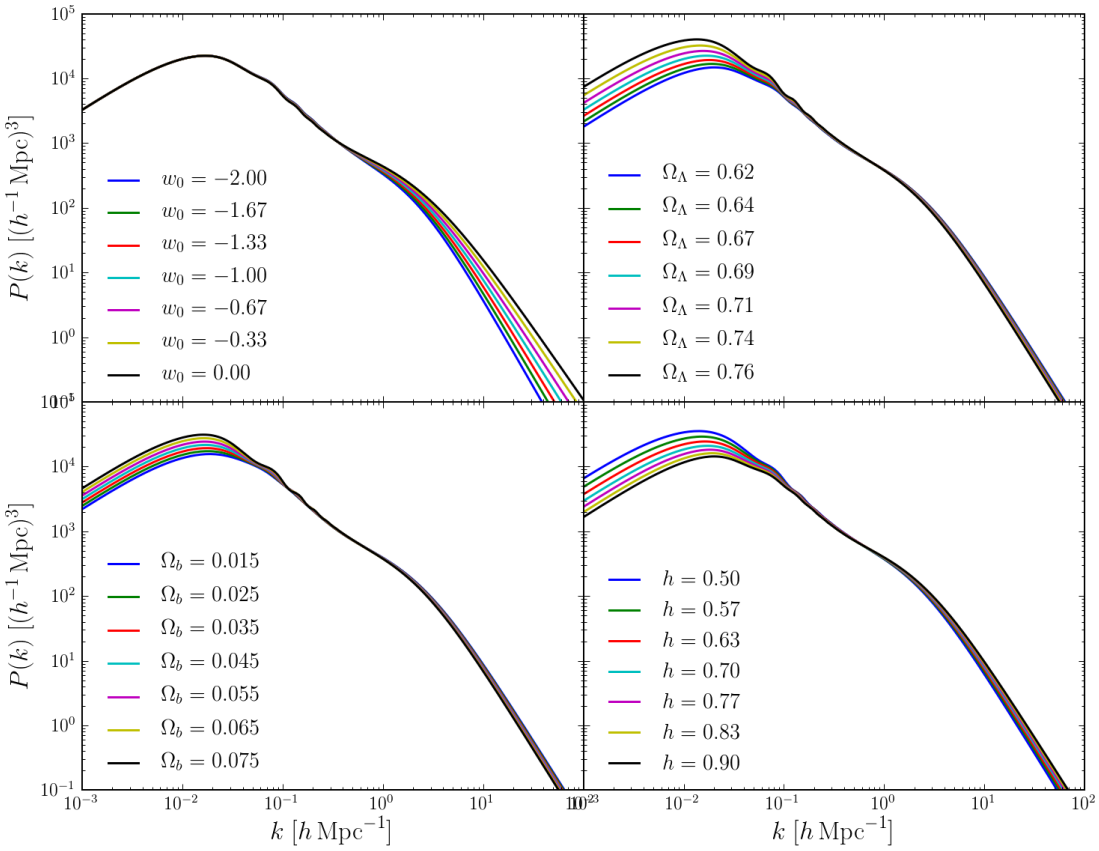

Figure 5.10 – Matter power spectra computed with NICAEA while varying one cosmological parameter at a time. Top left panel shows the w_{DE} dependence, top right the dark energy content for a flat cosmology, bottom left the baryon content and bottom right the Hubble parameter.

For each parameter p, we create a range of N_{val} values between $p_{fid} - \Delta p$ and $p_{fid} + \Delta p$. We then compute the power spectrum $P_\times(\ell)$ for each of these values, fit an interpolated spline between the spectra for each ℓ value, and take the derivative of the spline at the fiducial value p_{fid}. As numerical derivatives are generally very unstable computations, we took special care in the convergence of these computations. The code runs with $N_{val} = 10$ for all parameters, but Δp has been tuned empirically for each parameter to ensure it converges for all wavemode ℓ values. It is of order 10^{-4}.

III Parameter forecasting method

III.1 The number density covariance matrix

The covariance matrix for an observable (the number density cross power spectra here) describes the measurement accuracy of that observable, in the context of a given survey. It depends on

survey design parameters such as the scanned area, which accounts for the shot noise and cosmic variance, and the maximum depth of the co-added images, which will define the redshift distribution of the sources as well as their number density.

As we pointed out in Section II.3.2, the number density cross- correlation power spectra are strongly connected to the matter power spectrum, and therefore to the non linear evolution at small scales. Since those scales (< 1 Mpc) are relevant and carry a lot of information in regarding the lensing signal, the computation of a precise covariance matrix would require numerical simulations. Sato et al. (2009); Sato & Nishimichi (2013) showed that the shear-shear covariance matrix obtained from ray-tracing simulations could be approached with a formula including non Gaussian contributions from the mass density fluctuations, following the halo model formalism. The impact of a non-Gaussian errors could be added in a future work, together with halomodel corrections shown in Kayo et al. (2013), but throughout this thesis work, we only use Gaussian errors, and thus assume the ℓ-modes are independent.

A general expression for the Gaussian covariance matrix of a power spectrum P is

$$\mathrm{Cov}\left[P^{(ij)}(\ell), P^{(kl)}(\ell')\right] = \frac{1}{N_{\mathrm{pairs}}(\ell)}\left[P^{(ik)}(\ell)\,P^{(jl)}(\ell') + P^{(il)}(\ell)\,P^{(jk)}(\ell')\right].\delta_K^{\ell,\ell'}\,, \tag{5.30}$$

where N_{pairs} is the number of independent pairs of modes available for a given survey.

III.1.1 Number of independent ℓ-modes and their range

Under a flat-sky approximation, the number density power spectrum is constructed from the two-dimensional Fourier transform of the measured number density field available over a given survey region. The Fourier decomposition has to be done for modes $\boldsymbol{\ell}$ taken from a finite survey region, thus in a limited number. Therefore, the Fourier decomposition is by nature discrete, and the fundamental mode is limited by the size of surveyed area, $\ell_f = 2\pi/\Theta_s$, where the survey area is given by $\Omega_s = \Theta_s^2$. [4]

The number of independent mode pairs $\boldsymbol{\ell}$ and $\boldsymbol{\ell}'$ with length ℓ_i is evaluated as a sum in the range $\ell_i - \Delta\ell_i/2 \leq |\boldsymbol{\ell}| \leq \ell_i + \Delta\ell_i/2$, but discriminated by the fundamental Fourier mode ℓ_f. $\Delta\ell_i$ is the bin width used in the analysis. This number is thus approximately given by

$$N_{\mathrm{pairs}}(\ell_i) \simeq \frac{A_{\mathrm{sh}}(\ell_i)}{(2\pi/\Theta_s)^2}\,, \tag{5.31}$$

[4] We assume a square survey geometry for simplicity, which is not irrelevant since most information of the lensing power spectrum comes from small angular scales and are not affect by the geometry as long as the survey area is sufficiently large.

where $A_{\rm sh}(\ell_i)$ is the area of the two-dimensional shell around the bin ℓ_i

$$A_{\rm sh}(\ell_i) = \pi(\ell_i + \Delta\ell_i)^2 - \pi\ell_i^2 = \pi(2\,\ell_i\,\Delta\ell_i\, + \pi\,\Delta\ell_i^2) \approx 2\pi\,\ell_i\,\Delta\ell_i\,. \tag{5.32}$$

Introducing the observed sky fraction $f_{\rm sky} = \Omega_s/4\pi$, the expression for the number of independent pairs (5.31) can be rewritten as

$$N_{\rm pairs}(\ell) \simeq 2\,\ell\,\Delta\ell\,f_{\rm sky}\,. \tag{5.33}$$

The covariance matrix for the number density power spectrum therefore reads

$$\mathrm{Cov}\left[P_\times^{(ij)}(\ell), P_\times^{(i'j')}(\ell')\right] = \frac{1}{2\,\ell\Delta\ell\,f_{sky}}\,\left[P_\times^{(ii')}(\ell)\,P_\times^{(jj')}(\ell) + P_\times^{(ij')}(\ell)\,P_\times^{(ji')}(\ell)\right] \tag{5.34}$$

$$= \mathcal{C}_{(ij)(i'j')}(\ell) \tag{5.35}$$

Throughout this work, we employ a fixed logarithmic bin width $\Delta\log_{10}\ell = 0.1$ and use 30 bins in the range $10 \leq \ell \leq 3000$. While the lower bound $\ell_{\rm min} = 10$ is fixed using Limber approximation arguments, the upper range mode $\ell_{\rm max}$ is somewhat flexible. The high ℓ modes corresponding to small angular scales, they carry a lot of lensing signal. However, they entered the non-linear domain of the matter power spectrum, and based on the results from Sato et al. (2009) which show that the *halofit* model (Smith et al., 2003, used in this analysis) under-predicts the lensing power for $\ell > 3000$, we decided to limit our range to that value.

In order highlight the correlation between data vectors in the covariance matrix, one generally plots the reduced covariance matrix $\mathcal{R}$ defined as

$$\mathcal{R}_{ij} = \frac{\mathcal{C}_{ij}}{\sqrt{\mathcal{C}_{ii}\,\mathcal{C}_{jj}}}\,. \tag{5.36}$$

The correlation matrix for the number density cross power spectra is displayed on Figure 5.11 for two wavemodes. One clearly picks up a stronger correlation (lighter color) between pairs that share one bin, either the source, or the lens. This is consistent with the above mentioned theory.

III.1.2 Source of errors in the covariance

This work aims at studying the magnification cross-correlation P_{gm} signal inside the main galaxy distribution of a survey. The magnification signal is a contribution to the more general number density cross-correlation $P_\times$, which dominates the signal in the special case where the redshift

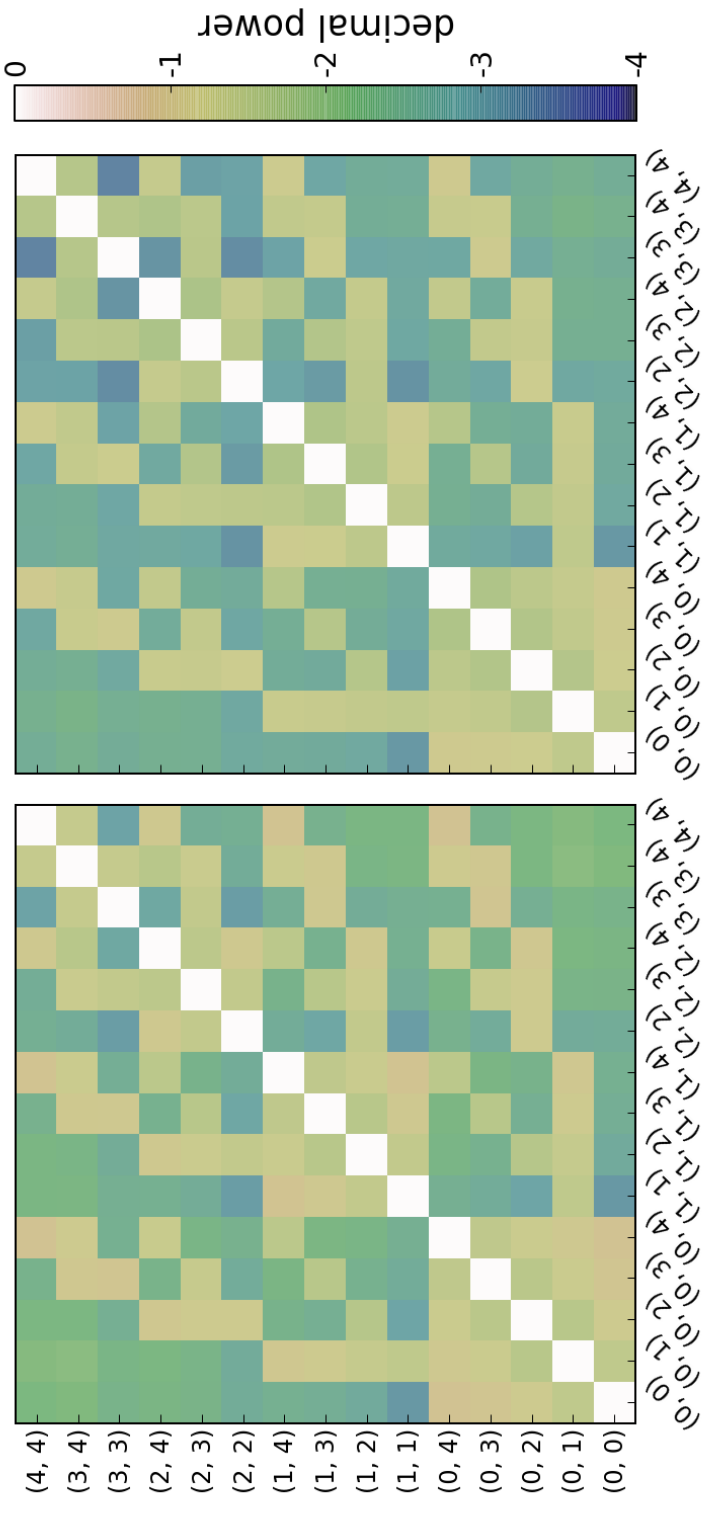

Figure 5.11 – Number density power spectra correlation matrix, plotted on the left for $\ell = 100$ and on the right for $\ell = 1000$.

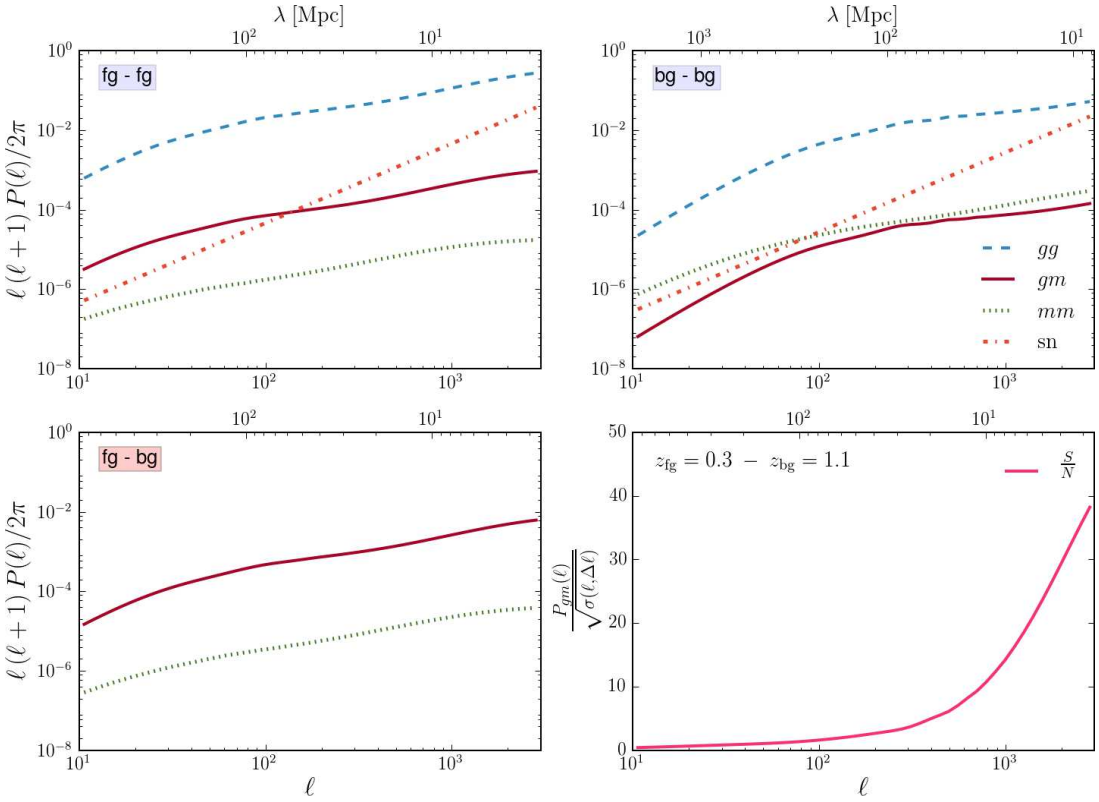

Figure 5.12 – Spectra contributing to the covariance matrix for two redshifts bins, respectively at $z = 0.3$ and $z = 1.1$ taken in the LSST distribution (Figure 5.9). The three bin combinations are displayed along with the signal-to-noise as a function of the wavemode.

populations do not overlap. For this reason, we consider a particular redshift distribution, obtained by splitting the main survey galaxy distribution into non overlapping redshift bins, as shown in Figure 5.9. It enables us to compute all possible cross-correlations between bins while making sure the signal is not being « polluted » by any other contribution (except maybe second-order lensing terms up to a few percents).

On Figure 5.12 is plotted the individual power spectra contributing to the number density cross power spectrum $P_\times$ (*cf.* equation (5.26)) for the three bin combinations available using the first and second bins of Figure 5.9. The first bin with mean redshift $z = 0.3$ is denoted as the foreground « fg » and the second at $z = 1.1$ is the background « bg ». We clearly see on bottom left panel the dominant contribution being the galaxy-magnification term, as a result of the binning choice.

As shown by the covariance matrix expression (5.34), the signal coming from the pure cross-correlation between two distant bins is affected by the contribution of the intrinsic clustering of each bin. Indeed, choosing a foreground $i' = i$ and a background $j' = j$ with $i \neq j$

yield the covariance

$$\mathcal{C}_{(ij)(ij)}(\ell) = \frac{1}{2\,\ell\Delta\ell\,f_{sky}}\left[P_{\times}^{(ii)}(\ell)\,P_{\times}^{(jj)}(\ell) + P_{\times}^{(ij)}(\ell)^2\right]. \tag{5.37}$$

The covariance matrix (5.37) for two bins is thus proportional to the product of the auto-correlation spectrum of each bin plus twice the cross-correlation one. On Figure 5.12, top panels show the spectra contributing to the auto-correlation term and the bottom left panel shows the one contributing to the cross-correlation. The resulting spectrum in each of these panels is not displayed but is the sum of all the plotted lines. From the numbers, it is obvious the signal from the autocorrelation terms $P_{\times}^{(ii)}$ and $P_{\times}^{(jj)}$ are up to two orders of magnitude stronger than the cross-correlation one $P_{\times}^{(ij)}$, and thus dominate the covariance matrix.

Looking more closely at this dominant autocorrelation term (one of the top panels), the figure clearly shows that for a LSST-like survey, the shot noise (dotted-dashed orange line) is not the dominant contribution anymore, at all scales. In other words, the wealth of new sources brought by these very deep surveys dramatically lowers the statistical noise, so that the now dominant noise contribution is now of a physical origin. The diminution of the shot noise was expected. However, the intrinsic clustering domination is a different issue. While the most part of the intrinsic clustering power spectrum (5.25a) can be modeled, it is dependent on the galaxy bias b, which is highly undetermined. We will see in Section IV.1 how we might turn this in our advantage by using the cross-correlation to retrieve information about the galaxy bias.

III.2 Fisher information matrix

The cosmological parameter forecast is conducted using the Fisher matrix formalism. An introduction on the subject and the justification for the following fomulæ can be found in Appendix II.2, page 177. A Fisher analysis is used to assess the ability of a given imaging survey to constrain the model parameters θ given an observable. In this case, the observable is the number density power spectrum computed using tomographic information from all the available combinations of the redshift bins and the mode bins and the model parameters are the cosmological parameters. More precisely, the constraints are computed for a parameter subset including the nuisance bias parameters given as

$$\Theta = \{h, \Omega_{\rm m}, \Omega_\Lambda, \Omega_b, \sigma_8, n_s, w_0, w_a, b_i\} \tag{5.38}$$

whose fiducial values are given in Table 1.1 except for the b_i, the galaxy bias in bin i, whose fiducial values are all set to unity.

Assuming the covariance matrix $\boldsymbol{\mathcal{C}}$ does not depend on the cosmological parameter, the Fisher information matrix for the number density power spectrum is :

$$F_{\alpha\beta} \equiv \sum_{\ell} \frac{\partial \mathbf{P}(\ell)}{\partial \theta_\alpha} \boldsymbol{\mathcal{C}}^{-1}(\ell) \frac{\partial \mathbf{P}(\ell)}{\partial \theta_\beta} \tag{5.39}$$

where the data vector $\mathbf{P}$ contains the number density power spectra computed for certain redshift bin combinations within the n_b bins of the chosen distribution. We distinguish between two cases:

$$\mathbf{P}(\ell) = \left\{ P_\times^{(ij)}(\ell) \right\} \text{ with } i,j \in \{1,\dots,n_b\} \text{ and } \begin{cases} i = j & \text{for the auto-correlation} \\ i \neq j & \text{for the pure cross-correlation} \end{cases} . \tag{5.40}$$

While the auto-correlation term determines the intrinsic clustering power, the cross-correlation will yield a pure magnification cross-correlation signal, which is best in order to be fairly compared to shear power.

Figure of Merit

In order to quantify the improvement brought by future surveys on the evolution of dark energy equation of state parameters, it is common to use the figure of merit (FoM) defined by the Dark Energy Task Force (Albrecht et al., 2006) as the area of the 95% confidence limit contours in the (w_0, w_a) plane. These will be used together with the constraints to give a possible comparison with other probes for the same survey.

IV Cosmological implications

IV.1 Cosmological parameter forecasting results

Our results (Figure 5.13) confirm the recent results of Duncan et al. (2013) on the limited contribution of cosmic magnification to the cosmic lensing power, compared to shear and clustering. The intrinsic noise of cosmic magnification, once the statistical barrier (shot-noise) passed, is dominated by the intrinsic clustering signal – around two orders of magnitude stronger – which limits its constraining power on the cosmological parameters. For the shear, this intrinsic noise is dominated by the intrinsic alignments (which though not well understood, have a shallower effect on the covariance), shot noise and the signal itself.

Since cosmic magnification does not require a specific type of observables like the shape, it can still be computed with any kind of all-sky survey designed e.g. for shear. However, unlike shear, the number density of usable sources is higher and stays significant up to a higher redshift.

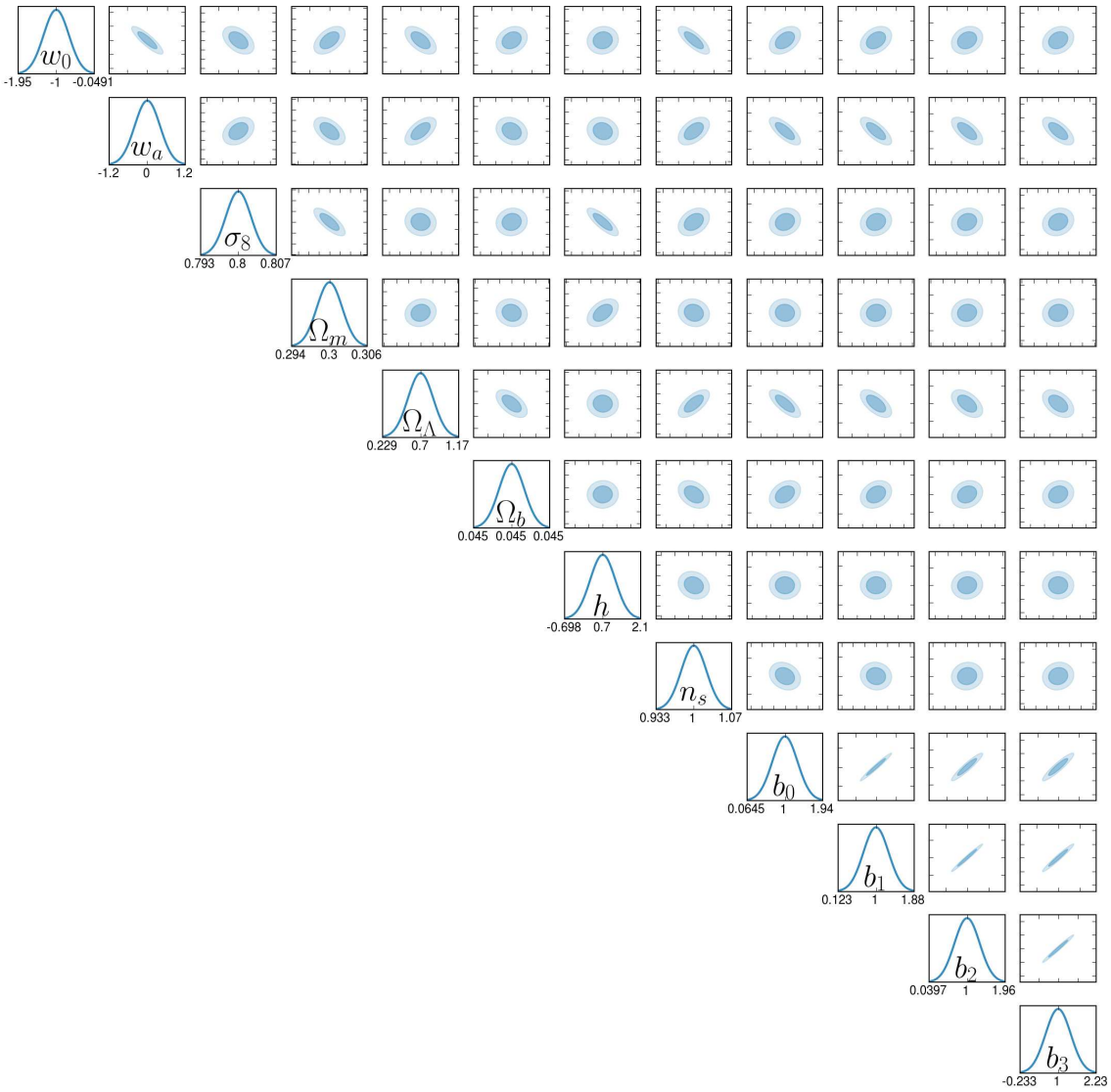

Figure 5.13 – Confidence contours on cosmological parameters using magnification cross-correlation alone.

Even with a low signal-to-noise ratio, the magnification is unique in that sense.

IV.1.1 Combining the probes

We now consider a subset of cosmological parameters from the initial (5.38)

$$\Theta_{\rm bis} = \{w_0, w_a, \sigma_8, b_i\} \ , \tag{5.41}$$

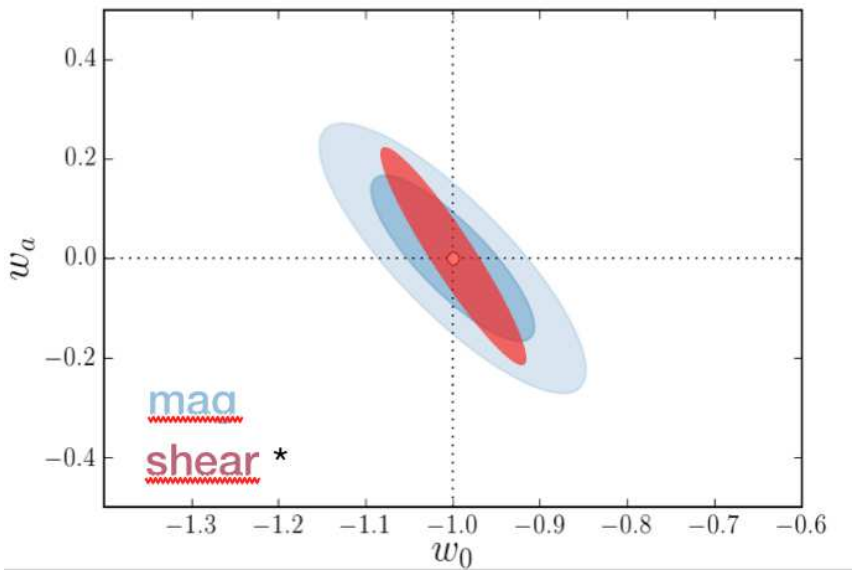

Figure 5.14 – Confidence contours on the dark energy equation-of-state parameters from magnification cross correlation alone at 68% and 95% CL (blue) and the 95% CL shear contours (red) with no systematic errors. The matter power spectrum normalization σ_8 and the galaxy bias of all bins have been marginalized on. The shear forecasts have been extracted from LSST Science Collaboration (2009).

assuming the others are fixed by other probes like the CMB and BAOs (Planck Collaboration, 2013b).

Most of the information on the dark equation-of-state parameters is embedded in the growth factor (*cf.* Section IV.4.1 page 30) driving the evolution of matter perturbations after the start of the dark energy domination era ($z \sim 1$). Tomography is thus a key probe in order to follow the evolution of the matter power spectrum at different redshifts.

With this subset, the contours on the dark energy equation-of-state parameters have clearly improved, (Figure 5.14 vs. Figure 5.13) even when marginalized over the bias and σ_8. The shear constraints extracted from LSST Science Collaboration (2009) are shown for comparison. For this plot, the dark energy figure of merit of magnification is 66 compared to that of shear which is 250. One has to keep in mind these results are ideal cases, not affected by systematics which would clearly reduce the constraints.

Bias determination

On the one hand, a measure of the matter power spectrum (scaling as σ_8^2) at a given redshift, is given by the measure of the intrinsic clustering signal of a galaxy population at that redshift. However, as points out equation (5.25a), the strong dependence of intrinsic clustering on galaxy bias ($\propto b^2$), whose own evolution is highly uncertain, prevent it from being accurate.

On the other hand, cosmic magnification cross-correlation between multiple redshift bins using tomography therefore yields multiple (noisy) measurements of the matter power spectrum, but this time with a linear dependence on the galaxy bias of the foreground population (*cf.* equation (5.25b)).

A combination of intrinsic clustering and magnification should thus be able to determine the bias, the linear and quadratic dependences breaking the degeneracy. Once the bias determined, σ_8 can be measured precisely and the growth factor with it, hence improving the constraints on w_0 and w_a.

IV.2 Conclusion

In this work, we have studied the potential of cosmic number magnification to constrain the cosmological parameters and especially the evolution of dark energy, in the context of large and deep imaging surveys. We found that the usable number density of objects for this probe will be high enough for the statistical errors to become a subdominant term in the covariance. We showed, however, that the covariance is now dominated by the intrinsic clustering signal of each cross-correlated bins, creating a barrier that cannot be lowered. As a comparison, the shear experiences the same kind of issue, but the variance is dominated by intrinsic alignments, the signal itself, and the shot noise ; which are of a lower amplitude than intrinsic clustering. For this reason, in an ideal case with no systematic errors, the shear constraints will be better than the magnification ones.

Nevertheless, cosmic number magnification has advantages that makes its measurement useful. First, it comes for free in an imaging survey, provided the photometry is accurate enough. Second, shape measurement are beset by numerous observational difficulties, while photometry presents a simpler measurement procedure ; therefore, the number density of usable sources for magnification is much higher than that of shear, since shear PSF measurements require a usable source to be detected in every exposure, which have a lower depth than the co-added images of the final survey. Third, for the same reason, magnification can probe higher redshift bins than shear, and can easily be correlated with catalogs from various surveys. Last, the direct measure of the convergence gives magnification the ability to break the mass-sheet degeneracy that affects mass determination from shear measurements.

Although not as powerful as shear, cosmic number magnification is worth measuring in a large imaging survey, and will serve the cosmology best combining its results with similar probes and controlling systematics.

CHAPTER 6

Conclusions

I Conclusion

In this thesis we addressed two topics related to large imaging surveys. We studied the temporal and spatial variation of atmospheric constituents above Cerro Pachón in Chile, and their direct impact on the photometric calibration of the Large Synoptic Survey Telescope. An atmospheric simulator was developed to realistically reproduce these variations on a long time-scale, which can be used to test the LSST photometric calibration pipeline. We also investigated a gravitational lensing effect, known as magnification, in the framework of a wide and deep survey, to establish how such a probe could improve current constraints on cosmological parameters and especially the dark energy equation of state w.

LSST is a project of a ground-based wide and deep photometric survey, covering 20 000 deg^2 in the southern hemisphere. As a synoptic telescope, it will scan the full survey area in three nights, using its six photometric broad bands *ugrizy* ; and will observe continuously for 10 years, starting in 2022. LSST science goals ranging from astrophysical to cosmological scales, they have set stringent constraints on the telescope requirements. The one of interest in this thesis, is the challenging photometric repeatability of 10 mmag across the sky, with a band-to-band calibration no larger than 5 mmag. Considering the design characteristics of LSST – wide survey, wide field-of-view, fast cadence, broad optical filters and suboptimal observing conditions – one of the major threat to the achievement of such a requirement is the atmosphere variability, and more precisely the modulated absorption of its main constituents, ozone, water vapor and aerosols.

We gathered data on these very constituents to characterize their intrinsic variability above the telescope site, to find that the high altitude of ozone makes it a relatively stable constituent with slow daily variations. The water vapor, on the contrary, evolves in the lower atmosphere and is subject to rapid variations of significant amplitude in time and space, probably boosted by a pressure gradient between the Pacific ocean and the Andes mountains. Then we discovered a strong spectral dependence of the Mie scattering (usually assumed to be constant) induced by the separate evolution of aerosols populations with different grain sizes, resulting in unpredictable and rapidly varying extinction spectra. We therefore highlighted the possible failure of the LSST baseline atmospheric model to accurately reconstruct the full atmospheric transmittance over the course of the night, simply using the spectrophotometric observation from an auxiliary telescope, under severe non photometric conditions.

We also evaluated the impact of the variation of these constituents on the photometry, calculating, on the one hand, the natural magnitude errors and on the other hand, the magnitude deviation due to the modification of the bandpass shape, resulting from an error on the

measurement of the absolute quantity of the given constituent in the line-of-sight. While the first one can be statistically corrected for, the bandpass shape error produces a calibration residual error that cuts into the requirement error budget. We found that, contrary to water vapor and aerosols, a daily satellite monitoring of ozone is enough to prevent that constituent from producing significant errors. We proposed the use of a microwave radiometer co-pointed with the telescope to limit the impact of water vapor uncertainty, and a multi-wavelength narrow-band imager to monitor the aerosol optical depth at several wavelength.

In order to propagate atmospheric induced errors, test new alternative calibration strategies and eventually validate LSST photometric calibration pipeline, we developed a simulation algorithm to realistically reproduce long-term variations of the above-mentioned constituents and produce « on-demand » atmospheric transmission spectra given a pointing direction.

The computed magnitude residual errors are crucial since they directly impact science objectives. This is the case, e.g., for photometric redshift accuracy, which depends on the band-to-band calibration to limit the template degeneracies, or for science probes that uses magnitudes as part of their signal, like weak lensing magnification. Magnification, which is a gravitational lensing effect, arises from the isotropic enlargement of background sources which results, in the observer point-of-view, in a magnitude change, due to surface brightness conservation. For magnitude-limited imagers, a magnitude change means a higher / lower number of sources in the lensed part of the image. It therefore creates a correlation between background sources and the foreground ones that compose the lens.

In the context of large imaging surveys, this correlation, called *cosmic magnification*, can then be used to probe the energy content of the Universe, between the observer and the background sources. The more accurate the redshifts are, the best the source distribution can be separated along the line-of-sight, thus yielding more information on the cosmological parameters via cosmological distances. These measurements are affected with an uncertainty, that translated into an error on the determination of the cosmological parameters.

We employed the Fisher matrix formalism to derive the error forecast on these parameters, especially on the equation-of-state parameter w and its redshift dependent parameterization, via the figure of merit (FoM). We found that the shot noise, which used to dominate the covariance of cosmic magnification measurements, is no longer the dominant error term. However, we discovered another critical noise contribution, which is the intrinsic clustering signal of both populations. This term, which can also be referred to as the cosmic variance, reduces the constraining power of cosmic magnification alone, compared to the cosmic shear measurements,

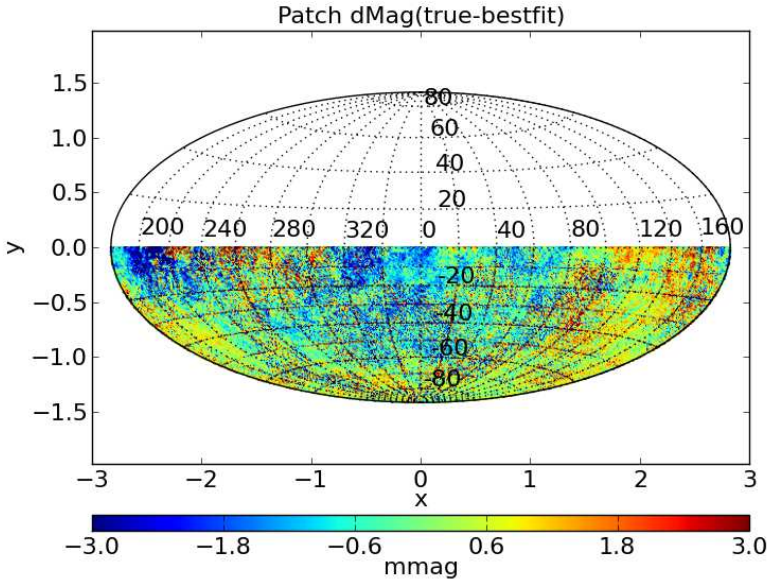

Figure 6.1 – Simulated map of the *self*-calibration residual errors (credit P.Yoachim).

which are affected by a different noise (i.e. intrinsic alignments, shot noise and the signal itself).

Nevertheless, cosmic magnification, which only needs magnitudes and photometric redshifts, can still be used as a complementary probe with e.g. cosmic shear or BAOs to break degeneracies and thus improve the constraints on dark energy equation-of-state parameters. It is thus worth measuring.

II Perspectives

II.1 Impact of calibration residual errors on cosmic magnification

After having measured the absolute impact of atmospheric constituents on the photometry and create an algorithm to realistically reproduce the long term variation of these very constituents, the step that naturally follows is to propagate the realistic atmosphere-related errors through the photometric calibration pipeline. Combining the atmosphere simulator and a pointing strategy, one can derive the magnitude errors in a given direction and a given patch on the sky. Then the *self*-calibration procedure (see Section I.2.1 page 56) minimizes the magnitude differences with respect to standardized ones.

For the simulation, the output of the *self*-calibration can then be compared to the input magnitudes to yield a map of the residual errors like the one on Figure 6.1. From these maps, one can construct a power spectrum of the residual errors on the survey area, which can then be compared with the power spectrum of the signal to be measured, e.g. the cosmic magnification

cross power spectrum.

If the science signal is considered as a priority, the spectrum of residual errors could be used to verify that the requirements on the photometric calibration are set high enough to ensure a low noise, or set stronger ones.

II.2 Testing the impact of photometric redshifts on cosmic magnification constraints

Errors on the measurement of photometric redshifts can have vicious effects on the measurement of the magnification signal. In particular, if objects mistakenly selected as the background population, belong to the same population as the foreground ones, the cross-correlation will yield a strong signal interpreted as a magnification, while it is actually pure clustering.

The error is expressed as a variance on the distribution, that depends on the redshift,

$$\sigma_z(z) = \bar{\sigma}_z\,(1+z)\,. \tag{6.1}$$

To take these errors into account, we use a simple model assuming for each galaxy a Gaussian error distribution around the actual redshift of the galaxy z_g and a possible bias in the mean of the distribution z_{bias} (which we assume equal to zero in this study),

$$p(z|z_g,\sigma_z) = \frac{1}{\sqrt{2\pi}\,\sigma_z(z_g)}\,\exp\left[-\frac{(z-z_g+z_{bias})^2}{2\,\sigma_z^2(z_g)}\right]. \tag{6.2}$$

The error distribution is then used to weight every galaxy (or tiny redshift slice) of the survey. Starting with spectroscopic / ideal tomographic bins as seen on Figure 6.2a, each bin is then treated so that within its redshift range, the normalized survey distribution is weighted for each redshift by the integral of the redshift error distribution. This way, the bin area is conserved but spread over a larger redshift range displayed on Figures 6.2b and 6.2c.

The impact of the photometric redshift errors on the magnification measurements appears in the comparison of the distributions of Figure 6.2. In the ideal case, there is absolutely no overlap between the N bins, which allows for $N(N-1)/2$ cross-correlations free of clustering signal. In the realistic and optimistic scenario with a mean redshift error variance of 0.02, the error has created an overlap between adjacent bins. Starting from the first bin, the cross-correlation needs to be done by skipping the next bin. This yields a total of $(N-1)(N-2)/2 = N(N-1)/2-(N-1)$ clean magnification cross-correlations, which is already less than the ideal case. Finally, in the worst case scenario (for LSST) of a redshift error variance of 0.05, the overlap between bins for a distribution with $N=10$ bins extends to the third party which

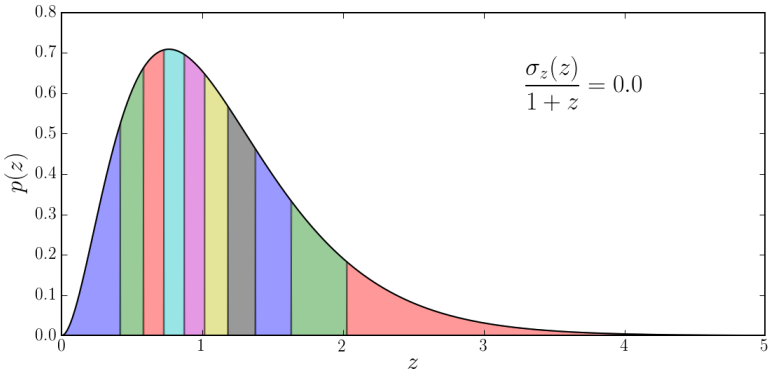

(a) Ideal tomographic redshift distribution.

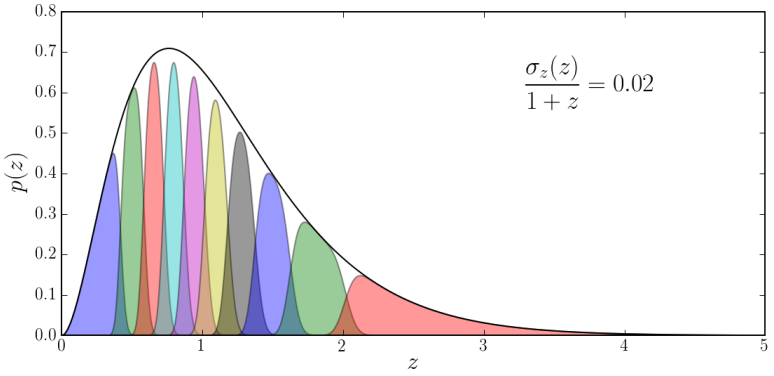

(b) Tomographic distribution with optimistic photometric redshift errors.

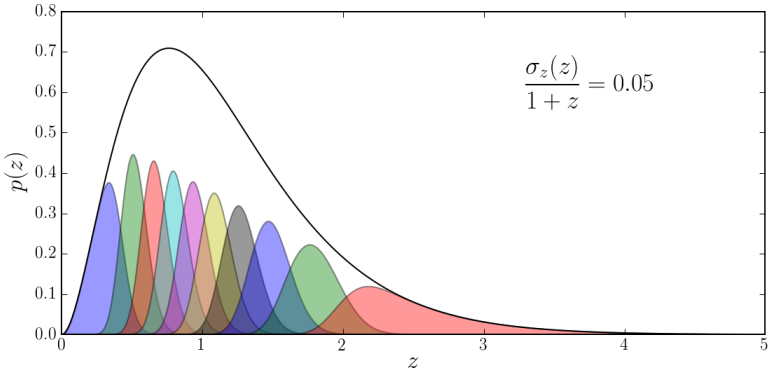

(c) Tomographic distribution with pessimistic photometric redshift errors.

Figure 6.2 – Redshift probability distribution function of galaxies for LSST split in 10 bins and represented in an ideal case on top panel, and more realistic cases below. Middle panel shows the LSST requirement error and the goal error on bottom panel.

result in a high loss of cross- correlations with a good signal-to-noise for magnification.

MODTRAN

MODTRAN, which stands for MODerate spectral resolution atmospheric TRANsmittance algorithm and computer model, is a radiative transfer algorithm used to model the spectral absorption, transmission, emission and scattering characteristics of the atmosphere, whose last version is MODTRAN5[1] (Berk et al., 2006). It has been developed by the US Air Force Research Laboratories in collaboration with Spectral Sciences, Inc and capitalizes the knowledge accumulated over decades by atmosphere physicists and specialists of remote sensing.

This code includes all major constituents of the atmosphere under their various physical phases, parameterizes their abundance, computes the thermodynamic equilibrium of the resulting atmosphere layer, the refraction path of light along upwards or downwards, and eventually, the radiative transfer budget along this path at UV, optical and radio wavelengths. The radiative transfer includes smooth scattering processes by large and intermediate size particles, and molecular processes generating complex band spectra. The spectral range extends from the UV into the far-infrared ($0\,\mathrm{cm}^{-1}$ to $5000\,\mathrm{cm}^{-1}$), providing resolution as fine as $0.2\,\mathrm{cm}^{-1}$.

The following sections are a synthetic description of MODTRAN inputs and outputs, greatly inspired from a LSST calibration internal reference document written by Michel Crézé.

MODTRAN inputs

MODTRAN needs input parameters to describe essentially the state of the atmosphere and the observing process of each specific experience or observation. Due to its old architecture, the input parameters will be passed by a `.tp5` file formated following a fixed fortran format which

[1] `http://www.modtran5.com/`

mimics old punched cards. The full path to that file must be specified as a single string in the root name file `modroot.in` located in MODTRAN executable directory.

Atmosphere inputs

Atmosphere inputs: atmosphere constituents, temperature and pressure profiles, aerosols and cloud characteristics, plus a number of options that determine the modeling approach. The fixed characteristics are settled in `Cardtemplate.dat`. The variable ones are the result of an atmospheric scenario produced by the atmospheric simulator.

Seasonal thermodynamic model

The MODTRAN parameter model governs a series of options relevant to season and latitude that impacts essentially the gross features of the seasonal effects including the pressure temperature equilibrium. Via pressure, the total amount of oxygen and nitrogen above the observer is obviously affected. Via temperature there are side effects on the water vapor: basically winter air contains less water this can be modulated via the H2O handle (below) but if the water amount is forced into the computation above the saturation point, then MODTRAN drops the extra water which is not turned into clouds of aerosols (or rain). Clouds and aerosols are modulated independently. There are also typical seasonal values for Ozone. Currently only three standard mid latitude models are used, namely: mid-latitude summer, mid-latitude winter and US76 (in the MODTRAN nomenclature).

Here is a non exhaustive list of the tunable parameters and their meaning.

Molecules generating the main absorption lines

- **H2O** water vapor can be modulated with respect to via a specific handle,
- **O3** ozone can be modulated arbitrarily with respect to the typical season value,
- **CO2** can be modulated too, but it does not play a major role in our case, having its main effects in the infrared outside the wavelength range of interest,
- **O2** molecular oxygen produces important absorption line features, but being a dominant constituent in the equilibrium it cannot be modulated by a separate handle.

Aerosol drivers

- **IHAZE** on/off aerosol switch,
- **ISEAS** season aerosol switch,

- **IVULC** volcanic aerosol type,
- **IVSA** on/off switch for the activation of a specific algorithm for computing the vertical structure of the low aerosol layers in relation with the measure of the atmosphere transparency observed on ground,
- **VIS** ground meteorological range (km). It is the most flexible handle to play with to drive aerosol variations,
- **ZAER11** bottom first aerosol layer,
- **ZAER12** top first aerosol layer,
- **ZAER21** bottom second aerosol layer,
- **ZAER22** top second aerosol layer,
- **SCALE1** and **SCALE2** scales of aerosol layers

Cloud drivers

- **ICLD** cloud type can introduce a layer of absorbing clouds.

There are a number of cloud types in MODTRAN, however those relevant to astronomical observations are thin layers of cirrus. A separate tool, not in the scope of the present document is currently being developed to simulate small scale random cloud structures generating gray extinction.

Observing process inputs

Observing process characteristics are either permanent when related to the telescope and the required spectral resolution, non permanent characteristics are field and time dependent. The permanent features are telescope altitude longitude and latitude, ground altitude and the adopted spectral range and spectral resolution. They are frozen in the `Cardtemplate.dat` file and passed to MODTRAN by the `ModtranCards.py` module.

Telescope specifications

- Geo-coordinates of the telescope (*cf.* Chapter 2),
- Telescope altitude: 2200 m,
- Ground altitude: 1500 m.

This last parameter plays a role in the computation of the aerosol layers, the adopted value is arbitrary, it was chosen in order to produce the required flexibility in the control of aerosol extinction.

Spectral resolution specifications

The MODTRAN spectra are computed in 5212 iso-frequency (or energy) bins starting at frequency $9040\,\mathrm{cm}^{-1}$ (1106.1947 nm) ending at frequency $35\,095\,\mathrm{cm}^{-1}$ (284.940 87 nm).

Field specifications

Target sky coordinates and observing time are extracted from simulated catalogs and converted to zenith angle and azimuth at the level of the MakeSequence.py module in order to

- transfer to MODTRAN the zenith angle needed for its refraction and radiation transfer computations,
- use the azimuth to alter the VIS driver of aerosol intensity. So as to generate azimuth dependent variations of the aerosol layer.

Formating inputs to MODTRAN

Eventually, the parameter set gathered by the code given a pointing direction is converted to MODTRAN card sequence by the `ModtranCards.py` module. This module uses two rigidly locked files

- `Cardtemplate.dat` which is a standard set of MODTRAN Cards. All the card sets produced by the simulation are build by altering the template set according to the parameter specifications produced by the sequence file.
- `Formparm.dat` which specifies the card number of each parameter in the card set its position on the card and the fortran format to write it.

`ModtranCards.py` eventually produces a `.tp5` file file containing as many card sets as you need each set leading to a transparency spectrum.

MODTRAN outputs

Standard MODTRAN outputs

MODTRAN returns automatically 6 standard files containing long tables with all details describing the atmosphere characteristics and the absorption spectrum. The most important are

`.tp6`, `.tp7` and `.plt`.

- `.tp6` apart from returning an echo of all the input parameters, gives the vertical structure of the column for each molecular and aerosol component The integrated quantity of each component along the line-of-sight plus the spectrum of the main components. It is of great help to understand the physics.
- `.tp7` gives the detailed absorption of each component including those of many minor molecules it is extremely voluminous. And only moderately useful for our purpose.
- `.plt` gives the transmission spectrum, i.e. the fraction of energy transmitted at each wavelength.

Conversion from physical units to MODTRAN units

Water vapor and ozone factors fed to MODTRAN through the `.tp5` file are not the raw values expressed in physical units. These factors are scaled following a relation that depends on the seasonal model used. These scaling relations are given below.

Water vapor

First of all, the water vapor column should be expressed in atm.cm. The conversion with the widely used g.cm^{-2} is

$$1 \text{ g.cm}^{-2} = 1\,244 \text{ atm.cm}\,.$$

Then the column is normalized to 449 atm.cm, multiplied by a seasonal scaling factor S_{H2O}(see Table 1) and finally by the pointing airmass z

$$\text{H2O}_{\text{MODTRAN}} = \frac{\text{H2O}_{\text{meas}}}{449} \times S_{\text{H2O}}(season) \times z(alt)\,.$$

Seasonal model	2–Summer	3–Winter	6–US76
S_{H2O} [449 atm.cm]	2.5396	0.8534	1.4164
S_{O3} [275 DU]	0.8292	0.7299	0.8005

Table 1 – Seasonal scaling factor for MODTRAN ozone and water vapor parameters.

Ozone

Ozone column is generally expressed in Dobson units DU or g.m^{-2} and must be converted to Dobson units for the scaling

$$1 \text{ g.m}^{-2} = 46.69 \text{ DU} .$$

The vertical column must then be normalized to 275 DU, multiplied by the corresponding seasonal coefficient S_{O3}(see Table 1) and the airmass of the pointing z

$$\mathrm{O3}_{\mathrm{MODTRAN}} = \frac{\mathrm{O3}_{\mathrm{meas}}}{275} \times S_{\mathrm{O3}}(season) \times z(alt) .$$

Limber's approximations

In order to compute the two-point correlation function of the matter density contrast arising in the angular correlation function expression,

$$w_{xy}^{(ij)}(\theta) \propto \int_0^{\chi_{\mathrm{H}}} \mathrm{d}\chi \, p_x^{(i)}(\chi) \int_0^{\chi_{\mathrm{H}}} \mathrm{d}\chi' \, p_y^{(j)}(\chi') \, \langle \delta(\chi \, \boldsymbol{\theta}, \chi) \, \delta(\chi' \, \boldsymbol{\theta}', \chi') \rangle \ ,$$

we use its Fourier space decomposition,

$$\begin{aligned} \langle \delta(\chi \, \boldsymbol{\phi}, \chi) \, \delta(\chi' \, \boldsymbol{\theta}', \chi') \rangle = \int \frac{\mathrm{d}^3 k}{(2\pi)^3} \int \frac{\mathrm{d}^3 k'}{(2\pi)^3} \, e^{-\imath \, [f_k(\chi) \, \boldsymbol{k}_\perp \cdot \boldsymbol{\phi} + \chi \, k_\parallel]} \, e^{\imath \, [f_k(\chi') \, \boldsymbol{k}'_\perp \cdot \boldsymbol{\theta}' + \chi' \, k'_3]} \\ \times \left\langle \hat{\delta}(\boldsymbol{k}, \chi) \, \hat{\delta}(\boldsymbol{k}', \chi') \right\rangle \ , \end{aligned} \tag{.3}$$

where $\boldsymbol{k}_\perp$ expressed the transverse wave-vectors, $k_\parallel$ is the line of sight wave-vector, and χ represents the line-of-sight comoving distance while $f_k(\chi)$ stands for the transverse comoving distance (see equation (1.45)). By definition, the two-point correlation function of the Fourier transform of the matter density contrast is related to the three-dimensional matter power spectrum P_δ via $\left\langle \hat{\delta}(\boldsymbol{k}, \chi) \, \hat{\delta}(\boldsymbol{k}', \chi') \right\rangle \equiv (2\pi)^3 \, \delta_{\mathrm{D}}^{(3)}(\boldsymbol{k} - \boldsymbol{k}') \, P_\delta(\|\boldsymbol{k}\|, \chi)$, which introduces the three-dimensional Dirac delta function $\delta_{\mathrm{D}}^{(3)}$. Inserting this expression into (.3) yields the expression

$$\begin{aligned} \langle \delta(\chi \, \boldsymbol{\phi}, \chi) \, \delta(\chi' \, \boldsymbol{\theta}', \chi') \rangle = \int \frac{\mathrm{d}^3 k}{(2\pi)^3} \, e^{-\imath \, [f_k(\chi) \, \boldsymbol{k}_\perp \cdot \boldsymbol{\phi} + \chi \, k_\parallel]} \, P_\delta(\|\boldsymbol{k}\|, \chi) \\ \times \int \mathrm{d}^3 k' \, \delta_{\mathrm{D}}^{(3)}(\boldsymbol{k} - \boldsymbol{k}') \, e^{\imath \, [f_k(\chi') \, \boldsymbol{k}'_\perp \cdot \boldsymbol{\theta}' + \chi' \, k'_3]} \, . \end{aligned} \tag{.4}$$

At this point, we can introduce Limber's approximations, well described in Bartelmann & Schneider (2001). We start by assuming there is no power in the density fluctuations above a coherent scale L_{coh}. This means the two-point correlation function of the density contrast

$\langle \delta(\chi\,\boldsymbol{\phi},\chi)\,\delta(\chi'\,\boldsymbol{\theta'},\chi')\rangle$ vanishes for $|\chi'-\chi| \gtrsim L_{coh}$. However, L_{coh} is small enough so that the density contrast does not evolve significantly under such a scale. The weight functions $p_x(\chi)$ are therefore assumed not to vary over scales $|\chi'-\chi| \lesssim L_{coh}$ which leads to both Limber's approximations

$$\begin{cases} f_k(\chi') \simeq f_k(\chi) \\ p_x(\chi') = p_x(\chi) \end{cases} \tag{.5}$$

The first approximation allows us to carry out the $\boldsymbol{k'}$ integration on equation (.4) in order to express the angular cross-correlation function as,

$$\begin{aligned} w_{xy}^{(ij)}(\theta) \propto & \int_0^{\chi_{\rm H}} \mathrm{d}\chi\, p_x^{(i)}(\chi) \int_0^{\chi_{\rm H}} \mathrm{d}\chi'\, p_y^{(j)}(\chi') \\ & \times \int \frac{\mathrm{d}^3k}{(2\pi)^3}\, e^{-\imath\,[f_k(\chi)\,\boldsymbol{k}_\perp\cdot(\boldsymbol{\phi}-\boldsymbol{\theta'})+(\chi-\chi')\,k_\parallel]}\, P_\delta(\|\boldsymbol{k}\|,\chi)\,, \end{aligned} \tag{.6}$$

while applying the second approximation and using the vector relation $\boldsymbol{\theta'} = \boldsymbol{\theta} + \boldsymbol{\phi}$ leads to

$$\begin{aligned} w_{xy}^{(ij)}(\theta) \propto & \int_0^{\chi_{\rm H}} \mathrm{d}\chi\, p_x^{(i)}(\chi)\, p_y^{(j)}(\chi) \int \frac{\mathrm{d}^3k}{(2\pi)^3}\, e^{-\imath\,[f_k(\chi)\,\boldsymbol{k}_\perp\cdot(\boldsymbol{\theta})+\chi\,k_\parallel]}\, P_\delta(|\boldsymbol{k}|,\chi)\,, \\ & \times \int_0^{\chi_{\rm H}} \mathrm{d}\chi'\, e^{\imath\,\chi'\,k_\parallel} \end{aligned} \tag{.7}$$

The last step of this calculation uses the Fourier transform and inverse transform relations

$$\int_0^{\chi_{\rm H}} \mathrm{d}\chi'\, e^{\imath\,\chi'\,k_\parallel} = 2\pi\,\delta_{\rm D}(k_\parallel) \tag{.8}$$

$$\int \mathrm{d}k_\parallel\, e^{-\imath\,\chi\,k_\parallel}\,\delta_{\rm D}(k_\parallel) = 1 \tag{.9}$$

to obtain the Dirac delta function and perform a partial integration on $k_\parallel$ to come up with the simpler result

$$w_{xy}^{(ij)}(\theta) \propto \int \frac{\mathrm{d}^2k_\perp}{(2\pi)^2}\, e^{-\imath\,\chi\,\boldsymbol{k}_\perp\cdot\boldsymbol{\theta}}\, P_\delta(\|\boldsymbol{k}_\perp\|,\chi) \tag{.10}$$

Fisher matrix formalism

Following the notations of Tegmark et al. (1997), we introduce the likelihood $L(\boldsymbol{x}|\boldsymbol{\Theta})$, a fundamental statistical quantity for parameter estimation, which returns the probability of obtaining a N-dimensional data vector $\boldsymbol{x}$, given a vector of M model parameters $\boldsymbol{\Theta} = (\theta_1, \theta_2, \ldots, \theta_n)$. The refer to the fiducial parameters as $\boldsymbol{\Theta}_0$ while $\boldsymbol{\Theta}$ refers to the parameter estimate. Assuming Gaussianity, $\boldsymbol{x}$ is a random variable, and so is $\boldsymbol{\Theta}$ since it is a function of $\boldsymbol{x}$. We also assume that $\boldsymbol{\Theta}$ is an unbiased estimator

$$\langle \boldsymbol{\Theta} \rangle = \boldsymbol{\Theta}_0 \,. \tag{.11}$$

In this case, the likelihood reads

$$L(\boldsymbol{x}|\boldsymbol{\Theta}) = \frac{1}{(2\pi)^{\frac{N}{2}} \sqrt{\det(C(\boldsymbol{\Theta}))}} \exp\left[-\frac{1}{2} \left(\boldsymbol{x} - \bar{\boldsymbol{x}}(\boldsymbol{\Theta})\right)^T C(\boldsymbol{\Theta})^{-1} \left(\boldsymbol{x} - \bar{\boldsymbol{x}}(\boldsymbol{\Theta})\right)\right] \tag{.12}$$

where $\bar{\boldsymbol{x}}$ is the prediction of the model and C is the covariance matrix of the data $\boldsymbol{x}$. The best fit to the data is then given by the set of parameters that maximizes the likelihood. The likelihood is therefore useful to infer the parameter constraints given observations. However, when forecasting the performance of cosmological probes for future experiments, likelihood-based methods like the Markov Chain Monte-Carlo (MCMC) algorithm are computationally heavy.

One option is to use the Fisher information matrix, defined as the second derivative of the log-likelihood with respect to the parameters $\boldsymbol{\Theta}$, evaluated at the fiducial values $\boldsymbol{\Theta}_0$

$$F_{ij} \equiv \left\langle \frac{\partial^2 \mathcal{L}}{\partial \theta_i \partial \theta_j} \right\rangle \Bigg|_{\boldsymbol{\Theta}_0} \tag{.13}$$

where $\mathcal{L}(\boldsymbol{x}|\boldsymbol{\Theta}) \equiv -\log L(\boldsymbol{x}|\boldsymbol{\Theta})$ is the log-likelihood. The Fisher matrix predicts how well an experiment will be able to constrain the model parameters, without even simulating the experiment in any detail. It can be used to forecast the results of different experiments given a model, keeping in mind that the Fisher matrix result is the best that can be achieved.

Plugging (.12) into (.13), one obtains for the Fisher matrix a general expression that reads

$$F_{ij} = \frac{1}{2} \operatorname{Tr} \left[C^{-1} \frac{\partial C}{\partial \theta_i} C^{-1} \frac{\partial C}{\partial \theta_j} + C^{-1} \left(\frac{\partial \bar{\boldsymbol{x}}}{\partial \theta_i} \frac{\partial \bar{\boldsymbol{x}}^T}{\partial \theta_j} + \frac{\partial \bar{\boldsymbol{x}}}{\partial \theta_j} \frac{\partial \bar{\boldsymbol{x}}^T}{\partial \theta_i} \right) \right] . \tag{.14}$$

The first member of the trace in (.14) refers to the covariance matrix dependence to the model parameters. Ignoring that contribution (which is the case in this thesis work), one finds a simpler expression

$$F_{ij} = \sum_{\alpha,\beta} \frac{\partial \bar{x}_\alpha}{\partial \theta_i} \left(C^{-1}\right)_{\alpha\beta} \frac{\partial \bar{x}_\beta}{\partial \theta_j} , \tag{.15}$$

where the sum runs over all the vector components denoted by α and β.

The uncertainty on the model parameters can then be obtained easily from the Fisher matrix. The Cramér-Rao theorem states that any unbiased estimator for the parameters (assumed here) will deliver a 1-σ confidence uncertainty on the parameters that is

$$\Delta\theta_i \geq \left(\sqrt{F_{ii}} \right)^{-1} . \tag{.16}$$

This is the minimum error attainable on θ_i, if the other parameters are known and fixed. However, if the other parameters are estimated from the data as well, the minimum standard deviation rises to

$$\Delta\theta_i \geq \sqrt{\left(F^{-1}\right)_{ii}} \tag{.17}$$

This value is usually referred to as the *marginalized error* on θ_i. It provides the best-case scenario for the experiment to constrain all the model parameters at once, given a set of observations.

Regarding the numerical computation of Fisher matrices, the tricky part is usually the mandatory computation of numerical derivatives, which can easily be unstable. Good advice is given in Albrecht et al. (2009) on the step used for derivation as well as better marginalization procedure for the parameters. And the conversion details from the parameter covariance matrix to the ellipses are explained in Coe (2009).

Bibliography

Abazajian, K., Adelman-McCarthy, J.K., Agüeros, M.A., Allam, S.S., Anderson, K.S., Anderson, S.F., Annis, J., Bahcall, N.A., Baldry, I.K., Bastian, S., et al., The third data release of the Sloan Digital Sky Survey, *The Astronomical Journal*, 2005, vol. 129, no. 3, p. 1755

Albrecht, A., Bernstein, G., Cahn, R., Freedman, W., Hewitt, J., Hu, W., Huth, J., Kamionkowski, M., Kolb, E., Knox, L., et al., Report of the dark energy task force, *arXiv astro-ph/0609591*, 2006

Albrecht, A., Amendola, L., Bernstein, G., Clowe, D., Eisenstein, D., Guzzo, L., Hirata, C., Huterer, D., Kirshner, R., Kolb, E., et al., Findings of the joint dark energy mission figure of merit science working group, *arXiv preprint arXiv:0901.0721*, 2009

Alimi, J.M., Bouillot, V., Rasera, Y., Reverdy, V., Corasaniti, P.S., Balmes, I., Requena, S., Delaruelle, X., Richet, J.N., DEUS Full Observable ΛCDM Universe Simulation: the numerical challenge, *arXiv preprint arXiv:1206.2838*, 2012

Allen, S.W., Evrard, A.E., Mantz, A.B., Cosmological parameters from observations of galaxy clusters, *arXiv preprint arXiv:1103.4829*, 2011

Allen, S., Rapetti, D., Schmidt, R., Ebeling, H., Morris, R., Fabian, A., Improved constraints on dark energy from chandra x-ray observations of the largest relaxed galaxy clusters, *Monthly Notices of the Royal Astronomical Society*, 2008, vol. 383, no. 3, pp. 879–896

Alpher, R.A., Bethe, H., Gamow, G., The origin of chemical elements, *Phys. Rev*, 1948, vol. 73, p. 7

Alpher, R.A., Herman, R.C., On the relative abundance of the elements, *Physical Review*, 1948, vol. 74, no. 12, p. 1737

Angloher, G., Bauer, M., Bavykina, I., Bento, A., Bucci, C., Ciemniak, C., Deuter, G., von Feilitzsch, F., Hauff, D., Huff, P., et al., Results from 730 kg days of the CRESST-II Dark Matter Search, *The European Physical Journal C*, 2012, vol. 72, no. 4, pp. 1–22

Aprile, E., Alfonsi, M., Arisaka, K., Arneodo, F., Balan, C., Baudis, L., Bauermeister, B., Behrens, A., Beltrame, P., Bokeloh, K., et al., Dark matter results from 225 live days of XENON100 data, *Physical review letters*, 2012, vol. 109, no. 18, p. 181 301

Armengaud, E., Augier, C., Benoît, A., Bergé, L., Blümer, J., Broniatowski, A., Brudanin, V., Censier, B., Chardin, G., Chapellier, M., et al., Final results of the EDELWEISS-II WIMP search using a 4-kg array of cryogenic germanium detectors with interleaved electrodes, *Physics Letters B*, 2011, vol. 702, no. 5, pp. 329–335

Bacon, D.J., Refregier, A., Clowe, D., Ellis, R.S., Numerical simulations of weak lensing measurements, *Monthly Notices of the Royal Astronomical Society*, 2001, vol. 325, no. 3, pp. 1065–1074

Bardeen, J.M., Bond, J., Kaiser, N., Szalay, A., The statistics of peaks of gaussian random fields, *The Astrophysical Journal*, 1986, vol. 304, pp. 15–61

Bartelmann, M., Gravitational lensing, *Classical and Quantum Gravity*, 2010, vol. 27, no. 23, p. 233 001

Bartelmann, M., Schneider, P., Weak gravitational lensing, *Physics Reports*, 2001, vol. 340, no. 4, pp. 291–472

Benjamin, J., Van Waerbeke, L., Heymans, C., Kilbinger, M., Erben, T., Hildebrandt, H., Hoekstra, H., Kitching, T.D., Mellier, Y., Miller, L., et al., Cfhtlens tomographic weak lensing: quantifying accurate redshift distributions, *Monthly Notices of the Royal Astronomical Society*, 2013, vol. 431, no. 2, pp. 1547–1564

Bennett, C.L., Bay, M., Halpern, M., Hinshaw, G., Jackson, C., Jarosik, N., Kogut, A., Limon, M., Meyer, S., Page, L., et al., The Microwave Anisotropy Probe Mission, *The Astrophysical Journal*, 2003, vol. 583, no. 1, p. 1

Bennett, C., Larson, D., Weiland, J., Jarosik, N., Hinshaw, G., Odegard, N., Smith, K., Hill, R., Gold, B., Halpern, M., et al., Nine-Year Wilkinson Microwave Anisotropy Probe (WMAP) Observations: Final Maps and Results, *arXiv preprint arXiv:1212.5225*, 2012

Benson, B., de Haan, T., Dudley, J., Reichardt, C., Aird, K., Andersson, K., Armstrong, R., Ashby, M., Bautz, M., Bayliss, M., et al., Cosmological constraints from sunyaev-zel'dovich-selected clusters with x-ray observations in the first 178 deg2 of the south pole telescope survey, *The Astrophysical Journal*, 2013, vol. 763, no. 2, p. 147

Berk, A., Anderson, G., Acharya, P., Bernstein, L., Muratov, L., Lee, J., Fox, M., Adler-Golden, S., Chetwynd Jr, J., Hoke, M., et al., Modtran 5- 2006 update, in *Proc. SPIE*, vol. 6233, 2006 pp. 508–515

Bernabei, R., Belli, P., Cappella, F., Cerulli, R., Dai, C., d'Angelo, A., He, H., Incicchitti, A., Kuang, H., Ma, X., et al., New results from DAMA/LIBRA, *The European Physical Journal C*, 2010, vol. 67, no. 1-2, pp. 39–49

Blanchard, A., Schneider, J., Gravitational lensing effect on the fluctuations of the cosmic background radiation, *Astronomy and Astrophysics*, 1987, vol. 184, pp. 1–6

Blandford, R.D., Kochanek, C.S., Gravitational imaging by isolated elliptical potential wells. i-cross sections. ii-probability distributions, *The Astrophysical Journal*, 1987, vol. 321, pp. 658–675

Blumenthal, G.R., Faber, S., Primack, J.R., Rees, M.J., Formation of galaxies and large-scale structure with cold dark matter, *Nature*, 1984, vol. 311

Bondi, H., Gold, T., The steady-state theory of the expanding universe, *Monthly Notices of the Royal Astronomical Society*, 1948, vol. 108, p. 252

Bonometto, S., Gorini, V., Moschella, U., *Modern cosmology*, CRC Press, 2010

Bridle, S., Shawe-Taylor, J., Amara, A., Applegate, D., Balan, S.T., Berge, J., Bernstein, G., Dahle, H., Erben, T., Gill, M., et al., Handbook for the GREAT08 Challenge: An image analysis competition for cosmological lensing, *The Annals of Applied Statistics*, 2009, pp. 6–37

Burke, D.L., Axelrod, T., Blondin, S., Claver, C., Ivezić, Ž., Jones, L., Saha, A., Smith, A., Smith, R.C., Stubbs, C.W., Precision determination of atmospheric extinction at optical and near-infrared wavelengths, *The Astrophysical Journal*, 2010, vol. 720, no. 1, p. 811

Canizares, C.R., Gravitational focusing and the association of distant quasars with foreground galaxies, 1981

CDMS Collaboration, Agnese, R., Ahmed, Z., Anderson, A., Arrenberg, S., Balakishiyeva, D., Thakur, R.B., Bauer, D., Billard, J., Borgland, A., et al., Dark Matter Search Results Using the Silicon Detectors of CDMS II, *arXiv preprint arXiv:1304.4279*, 2013

Chevallier, M., Polarski, D., Accelerating universes with scaling dark matter, *International Journal of Modern Physics D*, 2001, vol. 10, no. 02, pp. 213–223

Clowe, D., Randall, S., Markevitch, M., Catching a bullet: direct evidence for the existence of dark matter, *Nuclear Physics B-Proceedings Supplements*, 2007, vol. 173, pp. 28–31

Coe, D., Fisher Matrices and Confidence Ellipses: A Quick-Start Guide and Software, 2009, arXiv:0906.4123v1

Cole, S., Percival, W.J., Peacock, J.A., Norberg, P., Baugh, C.M., Frenk, C.S., Baldry, I., Bland-Hawthorn, J., Bridges, T., Cannon, R., Colless, M., Collins, C., Couch, W., Cross, N.J.G., Dalton, G., Eke, V.R., De Propris, R., Driver, S.P., Efstathiou, G., Ellis, R.S., Glazebrook, K., Jackson, C., Jenkins, A., Lahav, O., Lewis, I., Lumsden, S., Maddox, S., Madgwick, D., Peterson, B.A., Sutherland, W., Taylor, K., 2dFGRS Team, T., The 2dF Galaxy Redshift Survey: power-spectrum analysis of the final data set and cosmological implications, *Monthly Notices of the Royal Astronomical Society*, 2005, vol. 362, no. 2, pp. 505–534

Cooley, J.W., Tukey, J.W., An algorithm for the machine calculation of complex Fourier series, *Mathematics of computation*, 1965, vol. 19, no. 90, pp. 297–301

Cowsik, R., McClelland, J., Gravity of neutrinos of nonzero mass in astrophysics, *The Astrophysical Journal*, 1973, vol. 180, pp. 7–10

Das, S., Louis, T., Nolta, M.R., Addison, G.E., Battistelli, E.S., Bond, J.R., Calabrese, E., Devlin, D.C.M.J., Dicker, S., Dunkley, J., et al., The atacama cosmology telescope: temperature and gravitational lensing power spectrum measurements from three seasons of data, *arXiv preprint arXiv:1301.1037*, 2013

Davis, M., Efstathiou, G., Frenk, C.S., White, S.D., The evolution of large-scale structure in a universe dominated by cold dark matter, *The Astrophysical Journal*, 1985, vol. 292, pp. 371–394

Dodelson, S., *Modern cosmology*, Academic press, 2003

Duncan, C., Joachimi, B., Heavens, A., Heymans, C., Hildebrandt, H., On the complementarity of galaxy clustering with cosmic shear and flux magnification, *arXiv preprint arXiv:1306.6870*, 2013

Einstein, A., The Foundation of the General Theory of Relativity, *Annalen Phys*, 1916, vol. 49, pp. 769–822

Einstein, A., Kosmologische betrachtungen zur allgemeinen relativitätstheorie, *Sitzungsberichte der Königlich Preußischen Akademie der Wissenschaften (Berlin), Seite 142-152.*, 1917, vol. 1, pp. 142–152

Eisenstein, D.J., Hu, W., Baryonic features in the matter transfer function, *The Astrophysical Journal*, 1998, vol. 496, no. 2, p. 605

Eisenstein, D.J., Zehavi, I., Hogg, D.W., Scoccimarro, R., Blanton, M.R., Nichol, R.C., Scranton, R., Seo, H.J., Tegmark, M., Zheng, Z., et al., Detection of the baryon acoustic peak in the large-scale correlation function of sdss luminous red galaxies, *The Astrophysical Journal*, 2005, vol. 633, no. 2, p. 560

Etherington, I., On the definition of distance in general relativity, *The London, Edinburgh, and Dublin Philosophical Magazine and Journal of Science*, 1933, vol. 15, no. 100, pp. 761–773

Faber, S., Jackson, R.E., Velocity dispersions and mass-to-light ratios for elliptical galaxies, *The Astrophysical Journal*, 1976, vol. 204, pp. 668–683

Fixsen, D., The temperature of the Cosmic Microwave Background, *The Astrophysical Journal*, 2009, vol. 707, no. 2, p. 916

Flaugher, B., The Dark Energy Survey, *International Journal of Modern Physics A*, 2005, vol. 20, no. 14, pp. 3121–3123

Friedmann, A., On the Curvature of Space, *Zeitschrift für Physik*, 1922, vol. 10, pp. 377–386

Friedmann, A., Über die Möglichkeit einer Welt mit konstanter negativer Krümmung des Raumes, *Zeitschrift für Physik A Hadrons and Nuclei*, 1924, vol. 21, no. 1, pp. 326–332

Gamow, G., The origin of elements and the separation of galaxies, *Physical Review*, 1948a, vol. 74, pp. 505–506

Gamow, G., The Evolution of the Universe, *Nature*, 1948b, vol. 162, pp. 680–682

Gershtein, S., Zeldovich, Y.B., Rest mass of muonic neutrino and cosmology, *JETP Letters*, 1966, vol. 4, no. 120-122, p. 1

Group, S.S.W., et al., The square kilometre array design reference mission: Ska phase 1, *SKA project document*, 2011

Gunn, J.E., Stryker, L., Stellar spectrophotometric atlas, wavelengths from 3130 to 10800 å, *The Astrophysical Journal Supplement Series*, 1983, vol. 52, pp. 121–153

Hamilton, A., Kumar, P., Lu, E., Matthews, A., Reconstructing the primordial spectrum of fluctuations of the universe from the observed nonlinear clustering of galaxies, *The Astrophysical Journal*, 1991, vol. 374, pp. L1–L4

Hektor, A., Raidal, M., Tempel, E., Evidence for Indirect Detection of Dark Matter from Galaxy Clusters in Fermi γ-Ray Data, *The Astrophysical Journal Letters*, 2013, vol. 762, no. 2, p. L22

Heymans, C., Van Waerbeke, L., Bacon, D., Berge, J., Bernstein, G., Bertin, E., Bridle, S., Brown, M.L., Clowe, D., Dahle, H., et al., The Shear Testing Programme–I. Weak lensing analysis of simulated ground-based observations, *Monthly Notices of the Royal Astronomical Society*, 2006, vol. 368, no. 3, pp. 1323–1339

Hildebrandt, H., Van Waerbeke, L., Erben, T., CARS: The CFHTLS-Archive-Research Survey, *Astronomy and Astrophysics*, 2009, vol. 507, no. 2, pp. 683–691

Hildebrandt, H., van Waerbeke, L., Scott, D., Béthermin, M., Bock, J., Clements, D., Conley, A., Cooray, A., Dunlop, J., Eales, S., et al., Inferring the mass of submillimetre galaxies by exploiting their gravitational magnification of background galaxies, *Monthly Notices of the Royal Astronomical Society*, 2013, vol. 429, no. 4, pp. 3230–3237

Hildebrandt, H., Muzzin, A., Erben, T., Hoekstra, H., Kuijken, K., Surace, J., van Waerbeke, L., Wilson, G., Yee, H.K., Lensing Magnification: A novel method to weigh high-redshift clusters and its application to SpARCS, *The Astrophysical Journal Letters*, 2011, vol. 733, no. 2, p. L30

Hogg, D.W., Distance measures in cosmology, *arXiv preprint astro-ph/9905116*, 1999

Holben, B., Eck, T., Slutsker, I., Tanre, D., Buis, J., Setzer, A., Vermote, E., Reagan, J., Kaufman, Y., Nakajima, T., et al., AERONET - A federated instrument network and data archive for aerosol characterization, *Remote sensing of environment*, 1998, vol. 66, no. 1, pp. 1–16

Hoyle, F., Steady-State Theory, *Modern Cosmology in Retrospect*, 1990, p. 221

Hu, W., Power spectrum tomography with weak lensing, *The Astrophysical Journal Letters*, 1999, vol. 522, no. 1, p. L21

Hu, W., Dark energy and matter evolution from lensing tomography, *Physical Review D*, 2002, vol. 66, no. 8, p. 083 515

Hubble, E., A relation between distance and radial velocity among extra-galactic nebulae, *Proceedings of the National Academy of Sciences*, 1929, vol. 15, no. 3, pp. 168–173

Ivezic, Z., Axelrod, T., Brandt, W., Burke, D., Claver, C., Connolly, A., Cook, K., Gee, P., Gilmore, D., Jacoby, S., et al., Large Synoptic Survey Telescope: From science drivers to reference design, *Serbian Astronomical Journal*, 2008a, vol. 176, pp. 1–13

Ivezic, Z., Monet, D., Bond, N., Juric, M., Sesar, B., Munn, J., Lupton, R., Gunn, J., Knapp, G., Tyson, A., et al., Astrometry with digital sky surveys: from SDSS to LSST, *Proceedings of the International Astronomical Union*, 2007, vol. 248, p. 537

Ivezic, Z., Tyson, J., Acosta, E., Allsman, R., Anderson, S., Andrew, J., Angel, R., Axelrod, T., Barr, J., Becker, A., et al., LSST: from science drivers to reference design and anticipated data products, *arXiv:0805.2366*, 2008b

Ivezic, Z., et al., The LSST Science Requirements Document, 2010

Jain, B., Taylor, A., Cross-correlation tomography: measuring dark energy evolution with weak lensing, *Physical Review Letters*, 2003, vol. 91, no. 14, p. 141 302

Jones, A., Urban, J., Murtagh, D.P., Eriksson, P., Brohede, S., Haley, C., Degenstein, D., Bourassa, A., Von Savigny, C., Sonkaev, T., et al., Evolution of stratospheric ozone and water vapour time series studied with satellite measurements, *Atmospheric Chemistry and Physics*, 2009, vol. 9, pp. 6055–6075

Kaiser, N., On the spatial correlations of Abell clusters, *The Astrophysical Journal*, 1984, vol. 284, pp. L9–L12

Kaiser, N., Aussela, H., Burkeb, B., Boesgaarda, H., Chambersa, K., Chunc, M., Heasleya, J., Hodappc, K., Huntd, B., Jewitta, R.J.D., et al., Pan-STARRS large synoptic survey telescope array, in *Proc. of SPIE Vol*, vol. 4836, 2002 p. 155

Kaiser, N., Squires, G., Mapping the dark matter with weak gravitational lensing, *Astrophysical Journal*, 1993, vol. 404, no. 2, pp. 441–450

Kassim, N., Lazio, T., Ray, P., Crane, P., Hicks, B., Stewart, K., Cohen, A., Lane, W., The low-frequency array (lofar): opening a new window on the universe, *Planetary and Space Science*, 2004, vol. 52, no. 15, pp. 1343–1349

Kayo, I., Takada, M., Jain, B., Information content of weak lensing power spectrum and bispectrum: including the non-gaussian error covariance matrix, *Monthly Notices of the Royal Astronomical Society*, 2013, vol. 429, no. 1, pp. 344–371

Kitching, T., Amara, A., Gill, M., Harmeling, S., Heymans, C., Massey, R., Rowe, B., Schrabback, T., Voigt, L., Balan, S., et al., Gravitational Lensing Accuracy Testing 2010 (GREAT10) Challenge Handbook, *The Annals of Applied Statistics*, 2011, vol. 5, no. 3, pp. 2231–2263

Kowalski, M., Rubin, D., Aldering, G., Agostinho, R., Amadon, A., Amanullah, R., Balland, C., Barbary, K., Blanc, G., Challis, P., et al., Improved cosmological constraints from new, old, and combined supernova data sets, *The Astrophysical Journal*, 2008, vol. 686, no. 2, p. 749

Lemaître, G., Un univers homogène de masse constante et de rayon croissant rendant compte de la vitesse radiale des nébuleuses extra-galactiques, *Annales de la Societe Scietifique de Bruxelles*, 1927, vol. 47, pp. 49–59

Lemaître, G., The Beginning of the World from the Point of View of Quantum Theory, *Nature*, 1931, vol. 127, p. 706

Li, T., DePoy, D., Kessler, R., Burke, D., Marshall, J., Wise, J., Rheault, J.P., Carona, D., Boada, S., Prochaska, T., et al., atmcam: a simple atmospheric transmission monitoring camera for sub 1% photometric precision, in *SPIE Astronomical Telescopes+ Instrumentation*, International Society for Optics and Photonics, 2012 pp. 84 462L–84 462L

LSST Science Collaboration, LSST Science Book, version 2.0, *arXiv:0912.0201*, 2009

Mandelbaum, R., Rowe, B., Collaboration, G., GREAT3: The Third Gravitational Lensing Accuracy Testing Challenge, in *American Astronomical Society Meeting Abstracts*, vol. 221, 2013

Marchini, A., Melchiorri, A., Salvatelli, V., Pagano, L., Constraints on modified gravity from the atacama cosmology telescope and the south pole telescope, *Physical Review D*, 2013, vol. 87, no. 8, p. 083 527

Massey, R., Heymans, C., Bergé, J., Bernstein, G., Bridle, S., Clowe, D., Dahle, H., Ellis, R., Erben, T., Hetterscheidt, M., et al., The Shear Testing Programme 2: Factors affecting high-precision weak-lensing analyses, *Monthly Notices of the Royal Astronomical Society*, 2007, vol. 376, no. 1, pp. 13–38

Mather, J.C., Cheng, E., Cottingham, D., Eplee Jr, R., Fixsen, D., Hewagama, T., Isaacman, R., Jensen, K., Meyer, S., Noerdlinger, P., et al., Measurement of the cosmic microwave background spectrum by the COBE FIRAS instrument, *The Astrophysical Journal*, 1994, vol. 420, pp. 439–444

McPeters, R.D., Bhartia, P., Krueger, A.J., Herman, J.R., Wellemeyer, C.G., Seftor, C.J., Jaross, G., Torres, O., Moy, L., Labow, G., et al., Earth Probe Total Ozone Mapping Spectrometer (TOMS): data products user's guide, 1998

Menard, B., Bartelmann, M., Cosmological information from quasar-galaxy correlations induced by weak lensing, *Astronomy and Astrophysics*, 2002, vol. 386, no. 3, pp. 784–795

Ménard, B., Scranton, R., Fukugita, M., Richards, G., Measuring the galaxy–mass and galaxy–dust correlations through magnification and reddening, *Monthly Notices of the Royal Astronomical Society*, 2010, vol. 405, no. 2, pp. 1025–1039

Mohr, P.J., Taylor, B.N., Newell, D.B., Codata recommended values of the fundamental physical constants: 2010a), *Journal of Physical and Chemical Reference Data*, 2012, vol. 41, no. 4, p. 043 109

Morrison, C.B., Scranton, R., Ménard, B., Schmidt, S.J., Tyson, J., Ryan, R., Choi, A., Wittman, D., Tomographic magnification of Lyman-break galaxies in the Deep Lens Survey, *Monthly Notices of the Royal Astronomical Society*, 2012, vol. 426, no. 3, pp. 2489–2499

Oke, J., Gunn, J., Secondary standard stars for absolute spectrophotometry, *The Astrophysical Journal*, 1983, vol. 266, pp. 713–717

O'Neill, N., Dubovik, O., Eck, T., Modified Angstrom exponent for the characterization of sub-micrometer aerosols, *Applied Optics*, 2001, vol. 40, no. 15, pp. 2368–2375

O'Neill, N., Eck, T., Smirnov, A., Holben, B., Thulasiraman, S., Spectral discrimination of coarse and fine mode optical depth, *Journal of Geophysical Research: Atmospheres*, 2003, vol. 108, no. D17

Oort, J., Note on the distribution of luminosities of K and M giants, *Bulletin of the Astronomical Institutes of the Netherlands*, 1932, vol. 6, p. 289

Padmanabhan, N., Schlegel, D.J., Finkbeiner, D.P., Barentine, J., Blanton, M.R., Brewington, H.J., Gunn, J.E., Harvanek, M., Hogg, D.W., Ivezić, Ž., et al., An improved photometric calibration of the Sloan Digital Sky Survey imaging data, *The Astrophysical Journal*, 2008, vol. 674, no. 2, p. 1217

Peacock, J., Flux conservation and random gravitational lensing, *Monthly Notices of the Royal Astronomical Society*, 1986, vol. 223, pp. 113–128

Peacock, J., Dodds, S., Non-linear evolution of cosmological power spectra, *Monthly Notices of the Royal Astronomical Society*, 1996, vol. 280, no. 3, pp. L19–L26

Peacock, J., Smith, R., Halo occupation numbers and galaxy bias, *Monthly Notices of the Royal Astronomical Society*, 2000, vol. 318, no. 4, pp. 1144–1156

Peebles, P.J.E., *Principles of physical cosmology*, Princeton University Press, 1993

Peebles, P., Large-scale background temperature and mass fluctuations due to scale-invariant primeval perturbations, *The Astrophysical Journal Letters*, 1982, vol. 263

Penzias, A.A., Wilson, R.W., A Measurement of Excess Antenna Temperature at 4080 Mc/s., *The Astrophysical Journal*, 1965, vol. 142, pp. 419–421

Perlmutter, S., Aldering, G., Goldhaber, G., Knop, R., Nugent, P., Castro, P., Deustua, S., Fabbro, S., Goobar, A., Groom, D., et al., Measurements of λ from 42 high-redshift supernovae, *The Astrophysical Journal*, 1999, vol. 517, no. 2, p. 565

Planck Collaboration, Planck 2013 results. I. Overview of products and scientific results, *arXiv preprint arXiv:1303.5062*, 2013a

Planck Collaboration, Planck 2013 results. XVI. Cosmological parameters, *arXiv preprint arXiv:1303.5076*, 2013b

Planck Collaboration, Planck 2013 results. XVII. Gravitational lensing by large-scale structure, *arXiv preprint arXiv:1303.5077*, 2013c

Polarski, D., Dark energy, in *AIP Conference Proceedings*, vol. 1514, 2013 p. 111

Press, W.H., *Numerical recipes 3rd edition: The art of scientific computing*, Cambridge university press, 2007

Refregier, A., Amara, A., Kitching, T., Rassat, A., Scaramella, R., Weller, J., et al., Euclid imaging consortium science book, *arXiv preprint arXiv:1001.0061*, 2010

Reichardt, C.L., de Putter, R., Zahn, O., Hou, Z., New limits on early dark energy from the south pole telescope, *The Astrophysical Journal Letters*, 2012, vol. 749, no. 1, p. L9

Rhodes, J., Refregier, A., Groth, E.J., Detection of Cosmic Shear with the Hubble Space Telescope Survey Strip, *The Astrophysical Journal Letters*, 2001, vol. 552, no. 2, p. L85

Rich, J., *Fundamentals of cosmology*, Springer Verlag, 2001

Riess, A.G., Filippenko, A.V., Challis, P., Clocchiatti, A., Diercks, A., Garnavich, P.M., Gilliland, R.L., Hogan, C.J., Jha, S., Kirshner, R.P., et al., Observational evidence from supernovae for an accelerating universe and a cosmological constant, *The Astronomical Journal*, 1998, vol. 116, no. 3, p. 1009

Robertson, H.P., Kinematics and world-structure I., *The Astrophysical Journal*, 1935, vol. 82, p. 284

Robertson, H.P., Kinematics and World-Structure III., *The Astrophysical Journal*, 1936a, vol. 83, p. 257

Robertson, H.P., Kinematics and World-Structure II., *The Astrophysical Journal*, 1936b, vol. 83, p. 187

Rozo, E., Wechsler, R.H., Rykoff, E.S., Annis, J.T., Becker, M.R., Evrard, A.E., Frieman, J.A., Hansen, S.M., Hao, J., Johnston, D.E., et al., Cosmological Constraints from the Sloan Digital Sky Survey maxBCG Cluster Catalog, *The Astrophysical Journal*, 2010, vol. 708, no. 1, p. 645

Rubin, V.C., Ford Jr, W.K., Rotation of the Andromeda Nebula from a spectroscopic survey of emission regions, *The Astrophysical Journal*, 1970, vol. 159, p. 379

Rubin, V.C., Ford Jr, W.K., Thonnard, N., Rotational properties of 21 SC galaxies with a large range of luminosities and radii, from NGC 4605/R= 4kpc/to UGC 2885/R= 122 kpc, *The Astrophysical Journal*, 1980, vol. 238, pp. 471–487

Saab, T., An introduction to dark matter direct detection searches & techniques, *arXiv preprint arXiv:1203.2566*, 2012

Sato, M., Hamana, T., Takahashi, R., Takada, M., Yoshida, N., Matsubara, T., Sugiyama, N., Simulations of wide-field weak lensing surveys. i. basic statistics and non-gaussian effects, *The Astrophysical Journal*, 2009, vol. 701, no. 2, p. 945

Sato, M., Nishimichi, T., Impact of the non-gaussian covariance of the weak lensing power spectrum and bispectrum on cosmological parameter estimation, *arXiv preprint arXiv:1301.3588*, 2013

Schneider, P., Apparent number density enhancement of quasars near foreground galaxies due to gravitational lensing. i-amplification cross sections. ii-the amplification probability density distribution and results, *Astronomy and astrophysics*, 1987, vol. 179, pp. 71–92

Schneider, P., Statistical gravitational lensing and quasar-galaxy associations, *The Astrophysical Journal*, 1986, vol. 300, pp. L31–L34

Schneider, P., The number excess of galaxies around high redshift quasars, *Astronomy and Astrophysics*, 1989, vol. 221, pp. 221–229

Schneider, P., Seitz, C., Steps towards Nonlinear Cluster Inversion Through Gravitational Distortions. I. Basic Considerations and Circular Clusters, *Astronomy and Astrophysics*, 1995, vol. 294, no. 411

Scranton, R., Ménard, B., Richards, G.T., Nichol, R.C., Myers, A.D., Jain, B., Gray, A., Bartelmann, M., Brunner, R.J., Connolly, A.J., et al., Detection of cosmic magnification with the Sloan Digital Sky Survey, *The Astrophysical Journal*, 2005, vol. 633, no. 2, p. 589

Seitz, C., Schneider, P., Steps towards Nonlinear Cluster Inversion Through Gravitational Distortions. III. Including a redshift distribution of the sources, *Astronomy and Astrophysics*, 1997, vol. 318, no. 617

Seljak, U., Analytic model for galaxy and dark matter clustering, *Monthly Notices of the Royal Astronomical Society*, 2000, vol. 318, no. 1, pp. 203–213

Sievers, J.L., Hlozek, R.A., Nolta, M.R., Acquaviva, V., Addison, G.E., Ade, P.A., Aguirre, P., Amiri, M., Appel, J.W., Barrientos, L.F., et al., The atacama cosmology telescope: Cosmological parameters from three seasons of data, *arXiv preprint arXiv:1301.0824*, 2013

Slosar, A., Iršič, V., Kirkby, D., Bailey, S., Delubac, T., Rich, J., Aubourg, É., Bautista, J.E., Bhardwaj, V., Blomqvist, M., et al., Measurement of baryon acoustic oscillations in the lyman-α forest fluctuations in boss data release 9, *Journal of Cosmology and Astroparticle Physics*, 2013, vol. 2013, no. 04, p. 026

Smail, I., Ellis, R.S., Fitchett, M.J., Gravitational lensing of distant field galaxies by rich clusters: I.–faint galaxy redshift distributions, *arXiv preprint astro-ph/9402048*, 1994

Smith, R.E., Peacock, J., Jenkins, A., White, S., Frenk, C., Pearce, F., Thomas, P., Efstathiou, G., Couchman, H., Stable clustering, the halo model and non-linear cosmological power spectra, *Monthly Notices of the Royal Astronomical Society*, 2003, vol. 341, no. 4, pp. 1311–1332

Smoot, G.F., Bennett, C., Kogut, A., Wright, E., Aymon, J., Boggess, N., Cheng, E., De Amici, G., Gulkis, S., Hauser, M., et al., Structure in the COBE differential microwave radiometer first-year maps, *The Astrophysical Journal*, 1992, vol. 396, pp. L1–L5

Solheim, F., *Use of pointed water vapor radiometer observations to improve vertical GPS surveying accuracy*, Ph.D. thesis, University of Colorado, 1993

Soucail, G., Mellier, Y., Fort, B., Mathez, G., Cailloux, M., Discovery of the first gravitational einstein ring-the luminous arc in abell 370, *The Messenger*, 1987, vol. 50, p. 5

Soucail, G., Mellier, Y., Fort, B., Mathez, G., Cailloux, M., The giant arc in a 370-spectroscopic evidence for gravitational lensing from a source at z= 0.724, *Astronomy and Astrophysics*, 1988, vol. 191, pp. L19–L21

Springel, V., White, S.D., Jenkins, A., Frenk, C.S., Yoshida, N., Gao, L., Navarro, J., Thacker, R., Croton, D., Helly, J., et al., Simulations of the formation, evolution and clustering of galaxies and quasars, *Nature*, 2005, vol. 435, no. 7042, pp. 629–636

Steigman, G., Primordial Nucleosynthesis in the Precision Cosmology Era, *Annual Review of Nuclear and Particle Science*, 2007, vol. 57, pp. 463–491, 0712.1100

Stubbs, C.W., High, F.W., George, M.R., DeRose, K.L., Blondin, S., Tonry, J.L., Chambers, K.C., Granett, B.R., Burke, D.L., Smith, R.C., Toward More Precise Survey Photometry for PanSTARRS and LSST: Measuring Directly the Optical Transmission Spectrum of the Atmosphere, *Publications of the Astronomical Society of the Pacific*, 2007, vol. 119, no. 860, pp. 1163–1178

Takahashi, R., Sato, M., Nishimichi, T., Taruya, A., Oguri, M., Revising the halofit model for the nonlinear matter power spectrum, *The Astrophysical Journal*, 2012, vol. 761, no. 2, p. 152

Tegmark, M., Taylor, A.N., Heavens, A.F., Karhunen-loeve eigenvalue problems in cosmology: how should we tackle large data sets?, *The Astrophysical Journal*, 1997, vol. 480, no. 1, p. 22

Tempel, E., Hektor, A., Raidal, M., Fermi 130 GeV gamma-ray excess and dark matter annihilation in sub-haloes and in the Galactic centre, *Journal of Cosmology and Astroparticle Physics*, 2012, vol. 2012, no. 09, p. 032

Tyson, J., Galaxy clustering in QSO fields at Z= 1-1.5-Evidence for galaxy luminosity evolution, *The Astronomical Journal*, 1986, vol. 92, pp. 691–699

Tyson, J., Wenk, R., Valdes, F., Detection of systematic gravitational lens galaxy image alignments-mapping dark matter in galaxy clusters, *The Astrophysical Journal*, 1990, vol. 349, pp. L1–L4

Van Engelen, A., Keisler, R., Zahn, O., Aird, K., Benson, B., Bleem, L., Carlstrom, J., Chang, C., Cho, H., Crawford, T., et al., A measurement of gravitational lensing of the microwave background using south pole telescope data, *The Astrophysical Journal*, 2012, vol. 756, no. 2, p. 142

Van Waerbeke, L., Mellier, Y., Erben, T., Cuillandre, J., Bernardeau, F., Maoli, R., Bertin, E., Cracken, H.M., Fevre, O.L., Fort, B., et al., Detection of correlated galaxy ellipticities on CFHT data: first evidence for gravitational lensing by large-scale structures, *Astronomy and Astrophysics*, 2000, vol. 358, pp. 30–44

Vietri, M., Ostriker, J., The statistics of gravitational lenses–apparent changes in the luminosity function of distant sources due to passage of light through a single galaxy, *The Astrophysical Journal*, 1983, vol. 267, pp. 488–510

Vikhlinin, A., Kravtsov, A., Burenin, R., Ebeling, H., Forman, W., Hornstrup, A., Jones, C., Murray, S., Nagai, D., Quintana, H., et al., Chandra cluster cosmology project iii: cosmological parameter constraints, *The Astrophysical Journal*, 2009, vol. 692, no. 2, p. 1060

Walker, A., The Boltzmann equations in general relativity, *Proc. Edinb. Math. Soc*, 1936, vol. 4, pp. 238–253

Wang, L., Cooray, A., Farrah, D., Amblard, A., Auld, R., Bock, J., Brisbin, D., Burgarella, D., Chanial, P., Clements, D., et al., HerMES: detection of cosmic magnifica-

tion of submillimetre galaxies using angular cross-correlation, *Monthly Notices of the Royal Astronomical Society*, 2011, vol. 414, no. 1, pp. 596–601

Ware, R., Alber, C., Rocken, C., Solheim, F., Sensing integrated water vapor along GPS ray paths, *Geophysical Research Letters*, 1997, vol. 24, no. 4, pp. 417–420

Ware, R.H., Fulker, D.W., Stein, S.A., Anderson, D.N., Avery, S.K., Clark, R.D., Droegemeier, K.K., Kuettner, J.P., Minster, J.B., Sorooshian, S., SuomiNet: A real-time national GPS network for atmospheric research and education, *Bulletin of the American Meteorological Society*, 2000, vol. 81, no. 4, pp. 677–694

Weinberg, D.H., Mortonson, M.J., Eisenstein, D.J., Hirata, C., Riess, A.G., Rozo, E., Observational probes of cosmic acceleration, *Physics Reports*, 2013

Weinberg, S., *Cosmology*, vol. 1, 2008

Weniger, C., A tentative gamma-ray line from dark matter annihilation at the fermi large area telescope, *Journal of Cosmology and Astroparticle Physics*, 2012, vol. 2012, no. 08, p. 007

White, S.D., Navarro, J.F., Evrard, A.E., Frenk, C.S., The baryon content of galaxy clusters-a challenge to cosmological orthodoxy, 1993

Wiedner, M., Hills, R., Carlstrom, J., Lay, O., Interferometric Phase Correction Using 183 GHZ Water Vapor Monitors, *The Astrophysical Journal*, 2001, vol. 553, pp. 1036–1041

Wittman, D.M., Tyson, J.A., Kirkman, D., Dell'Antonio, I., Bernstein, G., Detection of weak gravitational lensing distortions of distant galaxies by cosmic dark matter at large scales, *Nature*, 2000, vol. 405, no. 6783, pp. 143–148

Zaldarriaga, M., Seljak, U., Gravitational lensing effect on cosmic microwave background polarization, *Physical Review D*, 1998, vol. 58, no. 2, p. 023 003

Zwicky, F., Spectral displacement of extra galactic nebulae, *Helv. Phys. Acta*, 1933, vol. 6, no. 110-127, p. 15

Zwicky, F., On the Masses of Nebulae and of Clusters of Nebulae, *The Astrophysical Journal*, 1937, vol. 86, p. 217